Fault reactivation and its effects on the petroleum systems of continental margins

Nathalia Helena Secol Mattos

Submitted in partial fulfilment of the requirements for the degree of Ph.D.

Cardiff University

July 2017

Fault reactivation and its effects on the petroleum systems of continental margins

Ph.D. project sponsored by Coordenação de Aperfeiçoamento de Pessoal de Nível Superior (CAPES – Brasil) (Ref. 99999.000877/2014-00)

Nathalia Helena Secol Mattos

Abstract

This research project uses high-quality seismic data from the Ottar Basin offshore Norway, Espírito Santo Basin offshore Brazil and Taranaki Basin offshore New Zealand. It investigates the geometry of multiple families of extensional faults and the effect(s) of fault growth on their seal competence. The main aims of this thesis are to investigate: a) the relationship between fault growth and deposition, b) the influence of fault reactivation in the compartmentalisation of strata around salt structures, and c) three distinct study areas as potential zones for enhanced fluid migration and seafloor seepage. Structural controls on three distinct petroleum systems were analysed based on the interpretation of the 3D geometry of seismic horizons, the mapping of fault displacements and throw distributions, and by modelling distinct faults taking into account present and past tectonic stresses.

The geometry and kinematics of the Samson Dome, offshore Norway, were investigated to propose a new evolutionary model for this salt structure, and to assess the timing(s) of salt uplift, salt collapse, and reactivation of adjacent faults. Faults were investigated using detailed displacement analyses and 3D models. Fault modelling took into consideration present-day *in situ* stresses, and also relative paleostresses. The results demonstrate an evolution occurring in three distinct stages, which were thoroughly discussed in this thesis. The Samson Dome is a structure where structural compartmentalisation is more important at depth, with dip-linked reactivated faults being preferential paths for fluid migration at shallow depths. However, their seal competence is enhanced 1100 ms below the sea floor, below which fluids can be trapped.

The geometry of fault families adjacent to distinct salt structures was assessed in the Espírito Santo Basin, offshore Brazil. Halokinesis is recorded from the Late Aptian to the Early Eocene, for four distinct salt structures, and controlled fault geometry and fluid flow patterns. The results in this thesis indicate a decrease in the seal competence of faults generated close to the studied salt diapirs. A conceptual model proposes that salt structures are linked by corridors of reactivated faults, which comprise preferential fluid-flow pathways from the South to the North-Northwest.

The Parihaka 3D survey of the Taranaki Basin was used to investigate the geometry of submarine channel systems formed in association with the reactivation of fault segments during the opening of the Northern Graben, a structure with regional expression offshore New Zealand. Three main drainage types were described around the Parihaka Fault. The results in this thesis suggest that the larger displacements observed led to the formation of two depocentres to the NE of the study area, which were progressively filled by submarine-channel and prograding deltaic units.

New results from this thesis include the assessment of the evolution of the Samson Dome, SW Barents Sea, and any controls of fault reactivation on the generation of structural compartments above this structure. This approach resulted in the recognition of the Samson Dome as a smaller seepage structure than previously considered in the literature. In the Espírito Santo Basin, faults reactivated by dip-linkage adjacently to salt diapirs and salt walls are the structures most favourable to record fluid leakage. In the Taranaki Basin, submarine channels may not use relay ramps between reactivated fault segments to reach hanging-wall depocentres. The results in this thesis can also be extrapolated to petroleum systems developed on continental margins worldwide.

Author note and status of publications

The results chapters presented in this thesis have been prepared as scientific papers for publication in international journals. The present status of publication at the time of the submission of thesis is as follows:

Chapter 4 has been published as Mattos, N. H., Alves, T. M., and Omosanya K. O., 2016, Crestal fault geometries reveal late halokinesis and collapse of the Samson Dome, Northern Norway: Implications for petroleum systems in the Barents Sea. Tectonophysics, v. 690, p. 79-96.

Chapter 5 has been under review in Tectonophysics as: Mattos, N. H., and Alves, T. M., Corridors of crestal and radial faults linking salt diapirs in SE Brazil.

Chapter 6 has been re-submitted after revision to Marine Geology as: Mattos, N. H., Alves, T. M., and Scully, A. M. Fault evolution as a control on Plio-Pleistocene submarine channel geometry in the Northern Graben, Taranaki Basin, New Zealand.

Although the articles are jointly co-authored with the project supervisor and others authors, the work presented in the publications is that of the lead author, Nathalia H. Mattos. Editorial work was provided by the author in accordance with a normal thesis chapter.

Acknowledgements

I would like to express my gratitude to all the people who have contributed in some way to the work presented in this thesis. Firstly I would like to thank my supervisor, Tiago M. Alves for his guidance, support, enthusiasm and encouragement throughout this project. I also acknowledge him for quickly reading my drafts and continuously offering advice which helped me in so many aspects of this work and in my overall development as a researcher. I am very grateful to Kamal'deen Omosanya for his constructive comments on my work and insightful conversations about academia. Davide Gamboa is thanked for all the support in the initial months of this research. Aisling Scully is thanked for the early-stage analysis in the New Zealand dataset. Gwen Pettigrew is thanked for being always available to help with the IT issues in the 3D Seismic Lab.

The Coordenação de Aperfeiçoamento de Pessoal de Nível Superior (CAPES – Brazil) is acknowledged for funding this PhD project. Jonathan Turner (BG Group) is thanked for providing the seismic dataset of the Barents Sea. CGG and the New Zealand Petroleum Board are also acknowledged for proving the data for the Espírito Santo and the Taranaki Basins, respectively.

Many thanks to the 3D Lab people: Aldina, Duarte, Chris, Ana, Tao Ze, Usman, Iqbal, James and Marco. A very special thanks to Nick and Chantelle, for the daily crosswords, tea and chats. To the Talybont Gate girls, Zhuldyz, Jikiung, Vasiliki, Malika and Damira, thanks for the amazing time during the first year. Nicola Russell and Teddy Hutton are thanked for letting me be part of their family here in Cardiff.

To my dear Cardiff friends Ana Forni, Renato Picelli, Luke Bratton and Gabriel Lins, thank you for all the fun, the excellent home-brewed beers, winter barbecue and for not letting me *going out on my own*. My Brazilian friends Lucas Cordeiro and Sayonara Soares will never be enough thanked for always being around and for helping me during the most difficult times, regardless of the distance or the time zones. Agradeço em especial aos meus pais Gilberto e Cristiane por todo o amor e incentivo dados à mim. Obrigada pela paciência e por sempre me permitirem ir além.

Table of contents

List of figures

List of tables

List of equations

1. Introduction and literature review

1.1. Rationale and aims

1.1.1. Rationale

To understand the genesis and evolution of sub-surface heterogeneities such as faults and joints is important because they constitute proof that important tectonic movements can affect the upper crust. Importantly, to address the often complex evolution of fault systems is also key to undertand their role in the entrapment and migration of fluids (Aydin, 2000; Biddle, 1985; Childs et al., 1997; Faulkner et al., 2010; Henriksen et al., 2011b; Jolley et al., 2010; Knipe et al., 1998; Smith, 1980; Walsh et al., 1998).

One of the hardest technical challenges of the petroleum industry is to economically produce hydrocarbons from reservoir intervals that are compartmentalised by faults and joints. Structural compartmentalisation may have significant impact on the volume of oil and gas produced from a field and, if not assessed in the first evaluation stages of a prospect, may result in the early relinquishment of economically-viable hydrocarbon accumulations (Caine et al., 1996; Jolley et al., 2010; Knipe et al., 1998). It is thus important to recognise the structural complexity that affects hydrocarbon reservoirs so that exploration and production geologists can determine the true volume of sub-surface oil and gas accumulations, as well as the presence of static and dynamic (flow) seals between each compartment.

The investigation of the mechanisms of fault formation is a fundamental aspect of assessing a potential reservoir, as faulted permeable units (sandstones) can either juxtapose other sandstones, favouring connectivity between compartments. In contrast

faults can juxtapose, or be limited by, impermeable intervals such as shales to form lateral barriers to fluid flow (Allan, 1989; Jolley et al., 2010; Knipe et al., 1998). Apart from the complex connectivity of strata juxtaposed by faults, it is also important to determine the timing(s) of fault growth with respect to (syn-tectonic) deposition within a sedimentary basin so that more reliable predictions of parameters such as the distribution of reservoir units, the quality of seal intervals, and main fluid pathways within (and between) reservoir intervals can be attained (Gartrell et al., 2004; Langhi et al., 2009; Wiprut and Zoback, 2002, 2000; Zhang et al., 2009).

Fault growth and reactivation are chiefly recorded in areas where the deposition of thick evaporite sequences is capable of influencing the structural evolution of sedimentary basins (Brun and Fort, 2011; Hudec and Jackson, 2007; Smit et al., 2008; Stewart, 2006; Vendeville, 2002; Vendeville and Jackson, 1992). The intrinsic instability of salt causes sedimentary basins with thick evaporite successions to be more susceptible to deformation during regional extensional or shortening events when compared to basins lacking thick evaporite successions (Hudec and Jackson, 2007; Jackson et al., 1994a; Vendeville, 2002). Therefore, halokinesis can result in the development of complex families of faults that can either constitute major structural compartments or, instead, comprise fluid-migration pathways in reservoir and seal units (Alves et al., 2009; Carruthers et al., 2013; Fiduk et al., 2004; Gamboa et al., 2010; Jackson et al., 1994a; Stewart, 2006; Talbot et al., 1991).

1.1.2. Aims of this research

This work assesses the geometry and growth histories of extensional faults located on three continental margins in order to understand the controls of fault growth and propagation in the generation of accommodation space for sediments, strata compartmentalisation, and associated fluid flow. The use of high-quality 3D seismic data, and supplementary 2D and well-log data, allowed a thorough investigation of the Ottar (Norway), Espírito Santo (Brazil), and Taranaki Basins (New Zealand) in terms of their stratigraphic and structural evolutions. Hence, this thesis addresses the following hypotheses, collectively or individually, for the three study areas:

a) The history of fault growth and propagation is strongly influenced by halokinesis in the Ottar and Espírito Santo Basins;
b) Fault evolution constitutes one of the main controlling factors on sediment deposition offshore New Zealand (Taranaki Basin);
c) There is a close relationship between fault reactivation and the degree of strata compartmentalisation around salt structures;
d) The study areas can be evaluated as potential fluid-flow (and seepage) zones;
e) Data from each of the study areas in this thesis can provide insights into the basin-scale evolution of continental margins, contributing to the analysis of seal unit competence and fluid migration in regions with similar structures.

The following section provides a summary of the relevant background literature concerning the three study areas addressed in this thesis. The thesis starts by revising the methods behind the analysis of fault geometry and displacements. . Salt tectonics and stress fields on continental margins are the main themes of Chapter 4 and Chapter 5. It continues by presenting a description of the geometry and evolution of submarine channel systems formed in tectonically active areas (Taranaki Basin), a theme explored in Chapter 6. The final topic of this literature review concerns the identification of distinct reservoir-compartmentalisation styles, an item common to the three core chapters of this thesis.

1.2. Fault geometry and displacement analyses

This section aims at providing a comprehensive literature review of the techniques used in displacement analyses, and the role of reactivation processes in fault growth. The mechanisms responsible for fault growth is a topic addressed in the three core chapters of this thesis.

1.2.1. Basic fault terminology

The terminology followed in this thesis is summarised in Figure 1-1. The along-strike dimension of fault planes along their lateral tips is called the length (L) of a fault, and is the longest dimension of the fault plane normal to the strike (H). These two terms are independent of the orientation of the slip vector and can be applied either to fault surfaces

on geological horizons, or to faults interpreted on 3D seismic data (Kim and Sanderson, 2005). When fault characteristics are compared for different fault populations, fault dimensions can be expressed as their maximum values L_{max} and H_{max}. Fault displacement decreases to zero towards the lateral-tip loops of an ellipse (fault surface) and increases to a maximum (D_{max}) in the centre of the fault (Figure 1-1; Childs et al., 2003; Cowie and Scholz, 1992a, 1992b; Kim and Sanderson, 2005; Walsh and Watterson, 1988).

1.2.2. Methods used in the analysis of fault displacement

A traditional method for analysing the displacement and propagation histories of growth faults is the Expansion Index (Bischke, 1994; Bouroullec et al., 2004; Jackson and Rotevatn, 2013; Lopez, 1990; Osagiede et al., 2014; Thorsen, 1963). This method consists of dividing the thickness of a unit deposited on the hanging-wall block of the fault by the thickness of the corresponding unit in the footwall block. The Expansion Index has been widely used to define periods of growth on normal faults, both at outcrop and on seismic data. However, the accurate measurement of the Expansion Index relies on the correct assignment of stratigraphic ages of units on the immediate footwall and hanging-wall (Lopez, 1990) and, significantly, on the resolution of the seismic data interpreted for the purpose of analysing fault growth (Osagiede et al., 2014). Additionally, as the Expansion Index is a ratio, no information on the slip rate is obtained through Expansion Indexes (Cartwright et al., 1998).

In this thesis, the primary tool used to document fault displacement is the throw-depth (T-z) method (Baudon and Cartwright, 2008a, 2008b; Cartwright and Mansfield, 1998; Mansfield and Cartwright, 1996; Omosanya and Alves, 2014; Peacock and Sanderson, 1991). This method consists of plotting the throw of horizons adjacent to a fault plane against their depth (Figure 1-2). Subtle variations in vertical throw distribution can be observed when T-z analyses are performed using a closely spaced interval (Baudon and Cartwright, 2008a). The relationship between fault throw (T) and depth (z) is widely used to estimate the degree of reactivation experienced by faults. Throw-depth (T-z) profiles for reactivated faults show abrupt variations in throw gradient and magnitudes, whereas minor changes and comparatively smaller throw values are obtained for non-reactivated faults (Baudon and Cartwright, 2008b). Further details on how this approach was applied to the study areas are described in *Section 3.5*.

1.2.3. Displacement-distance relationships

The relationship between displacement and distance along a fault trace governs fault initiation and growth mechanisms, as demonstrated for different types of faults (normal/strike-slip/reverse) from a wide variety of tectonic settings (Chapman and Williams, 1984; Cowie and Scholz, 1992b; Rippon, 1984; Walsh and Watterson, 1988; Williams and Chapman, 1983). Displacement-distance measurements can be obtained from fault surfaces (or traces) on seismic cross-sections, geological outcrops and topographic surfaces (Kim and Sanderson, 2005). This method consists of plotting fault displacement vs. the distance measured in the hanging-wall from an arbitrary reference point on the fault. This arbitrary point can be the fault width, height or, most commonly,

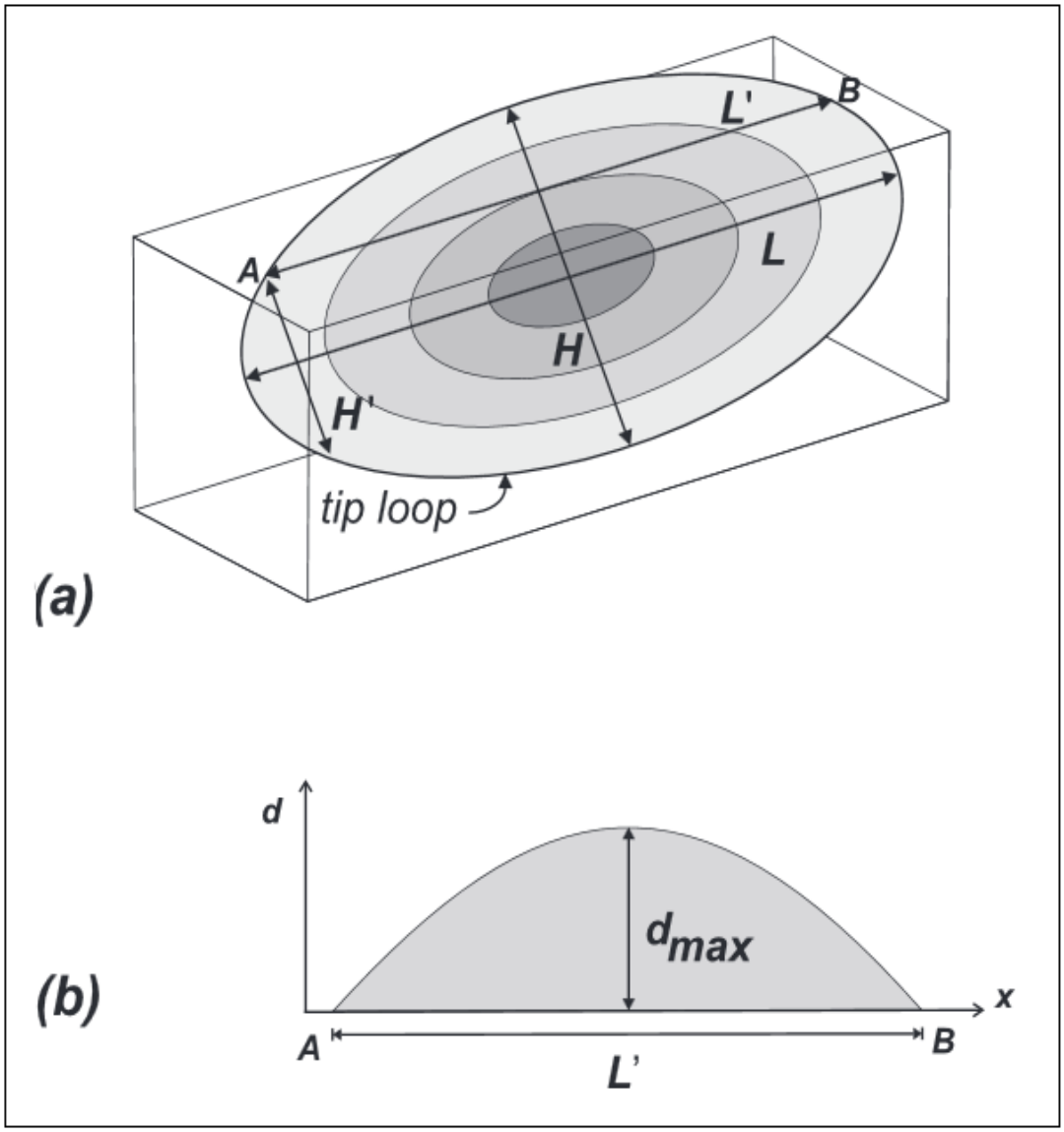

Figure 1-1: a) Schematic representation of displacement distribution on an elliptical fault surface with a specific length (L) and height (H). Displacement increases towards the fault centre, as reflected by the darker shades in the centre of the ellipsis. The fault intersects the upper surface of the block along line A-B. b) Displacement (d)-length (L) plot of fault trace along line A-B. Figure from Kim and Sanderson (2005).

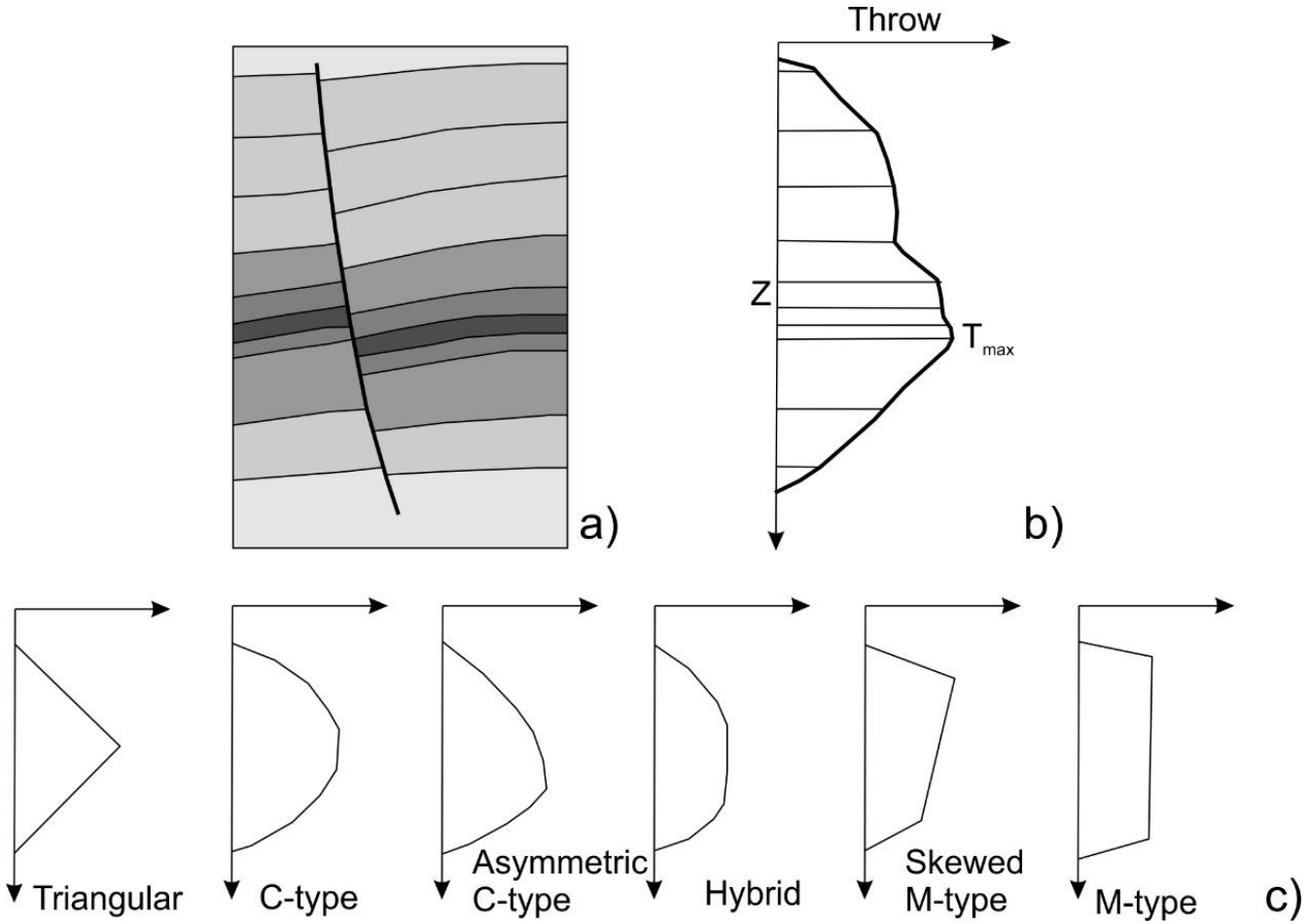

Figure 1-2: a) Illustrative sedimentary succession offset by a normal fault. b) Throw-depth (T-z) plot obtained for the fault shown in a). The throw (T) values are plotted on the x axis whereas the depth (z) is plotted along the y axis. c) Terminology used to characterise the type of throw profiles based on Muraoka and Kamata (1983). Modified from Baudon (2007).

the length of the fault (Chapman and Williams, 1984; Dawers and Anders, 1995; Muraoka and Kamata, 1983; Nicol et al., 2002; Peacock, 2002; Pollard and Segall, 1987).

Displacement-width (D-w) measurements suggest the occurrence of a systematic correlation between the width of a fault zone and displacement maxima, implying that increases in the thickness of faults' damage zones are proportional to fault displacement (Evans, 1990; Hull, 1988; Scholz, 1987). However, analyses considering fault width instead of distance along a fault plane as distance are not reliable as the displacement-width relationship of faults is usually not well constrained (Figure 1-3) (Evans, 1990).

In displacement-height (D-h) measurements, fault trace is the intersection line between the fault plane and a vertical seismic cross-section or outcrop normal to the fault strike. This measurement computes the true dip-slip values from normal faults (Muraoka and Kamata, 1983), thrust faults (Ellis and Dunlap, 1988), thrust-fold zones and linked-fault systems (Chapman and Williams, 1984; Williams and Chapman, 1983).

The displacement-length relationship (D-L or D-x, as used in this thesis) has a broader application in fault-growth analyses compared to the relationship between displacement and width or height. The use of displacement-length measurements can provide a basis for three-dimensional views of fault geometries (Cowie and Scholz, 1992a, 1992c), and allows the calculation of total strain in a faulted rock (Scholz and Cowie, 1990). The assessment of the kinematic relationship between faulting and folding can also be made through displacement-length analyses (Chapman and Williams, 1984; Muraoka and Kamata, 1983; Nicol et al., 2002; Peacock, 1991a, 1991b). The most significant use of displacement-length plots, however, is to provide insight into the mechanism of initiation,

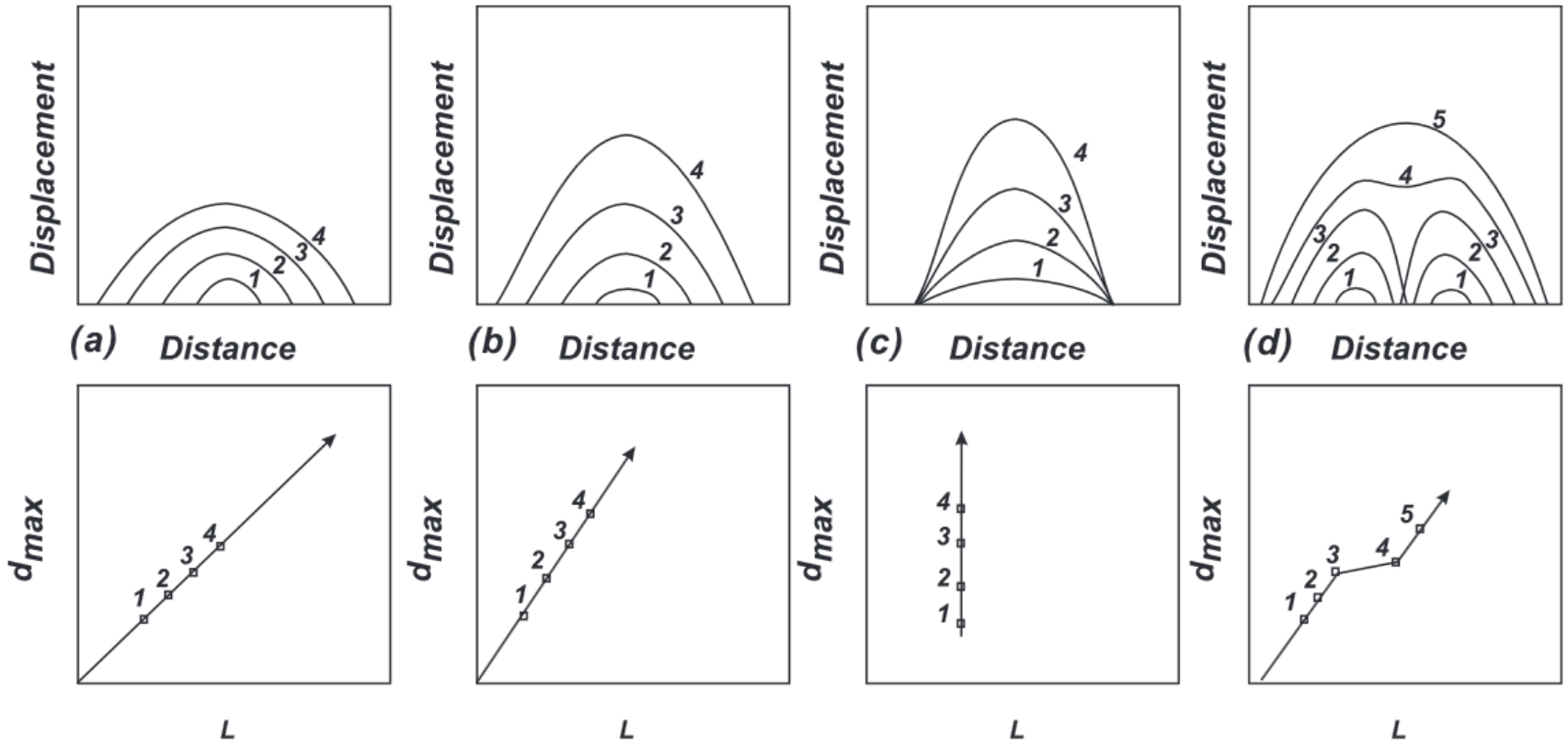

Figure 1-3: Fault growth models based on the displacement-distance relationships. a) Constant d_{max}/L ratio model. b) Increasing dmax/L ratio with fault growth. c) Constant length model of Walsh et al. (2002), with a fast increasing at the early stages of fault growth followed by a constant growth as the displacement accumulates. d) Fault linkage model, with faults growing isolated at the early stages and then linking to produce additional fault length (Figure from Kim and Sanderson, 2005).

growth and evolution of faults through time (Figure 1-3) (Cowie and Scholz, 1992a, 1992b, Kim et al., 2001a, 2001b; Kim and Sanderson, 2005; Peacock and Sanderson, 1995; Walsh and Watterson, 1988; Watterson, 1986). The two end-members of fault growth models are the constant d_{max}/L ratio model (Figure 1-3a), usually applied for small and isolated faults, and the fault linkage model (Figure 1-3d), where initially isolated faults propagate towards each other and link to produce a larger fault (Cartwright et al., 1995; Fossen and Rotevatn, 2016; Kim and Sanderson, 2005; Peacock and Sanderson, 1991; Walsh et al., 2003). Intermediate models include the increasing of the d_{max}/L ratio with the fault growth (Figure 1-3), and the constant length model, in which the fault length increases at an early stage and remains constant while the displacement increases (Figure 1-3c; Walsh et al., 2002).

1.2.4. Scaling laws

The apparent scaling of fault dimensions has been used to corroborate fault growth models by radial propagation. These models take into acount an idealised blind fault with dimensions that increase proportionally to the elliptical slip events (Cartwright et al., 1995; Cowie and Scholz, 1992a; Walsh and Watterson, 1988; Watterson, 1986). The relationship between the maximum cumulative displacement on a fault (d_{max}) and the maximum linear trace length can be expressed as (Equation 1-1):

$$d_{max} = cL^n$$

Equation 1-1

The exponent value n ranges from 0.5 (Fossen and Hesthammer, 1997) to 2 (Walsh and Watterson, 1988; Watterson, 1986). Intermediate values for this same exponent include n = 1 (Cowie and Scholz, 1992a, 1992b; Dawers et al., 1993; Dawers and Anders, 1995) and n = 1.5 (Gillespie et al., 1992). The value of the exponent is important since n = 1 defines a linear scaling law and n ≠ 1 a scale-dependent geometry. The value c is a constant of fault displacement at the unit length; when n = 1, c is the constant ratio d_{max}/L. Exponent values n ≠ 1 imply that the difference between consecutive slip events on a fault is not a constant, but related to the number of slip events that have occurred along the fault (Cowie and Scholz, 1992).

Multiple authors suggest that faults have a constant d_{max}/L ratio for individual datasets (Cowie and Scholz, 1992a; Dawers et al., 1993; Dawers and Anders, 1995; Peacock and Sanderson, 1996; Walsh and Watterson, 1988). The combination of discrete datasets with a limited range of length scales for a displacement-length analysis, however, can lead to misinterpretations, as important scatter can be observed in all d_{max}/L plots (Cowie and Scholz, 1992a; Kim and Sanderson, 2005; Torabi and Berg, 2011). Considering a wide range of factors controlling the d_{max}/L ratio, Kim and Sanderson (2005) compiled data from normal, strike-slip and thrust faults (Figure 1-4). The authors aimed at addressing how the different types of faults behave in relation to their displacement and length. From this plot, it was possible to conclude that the d_{max}/L ratio for strike-slip faults is slightly

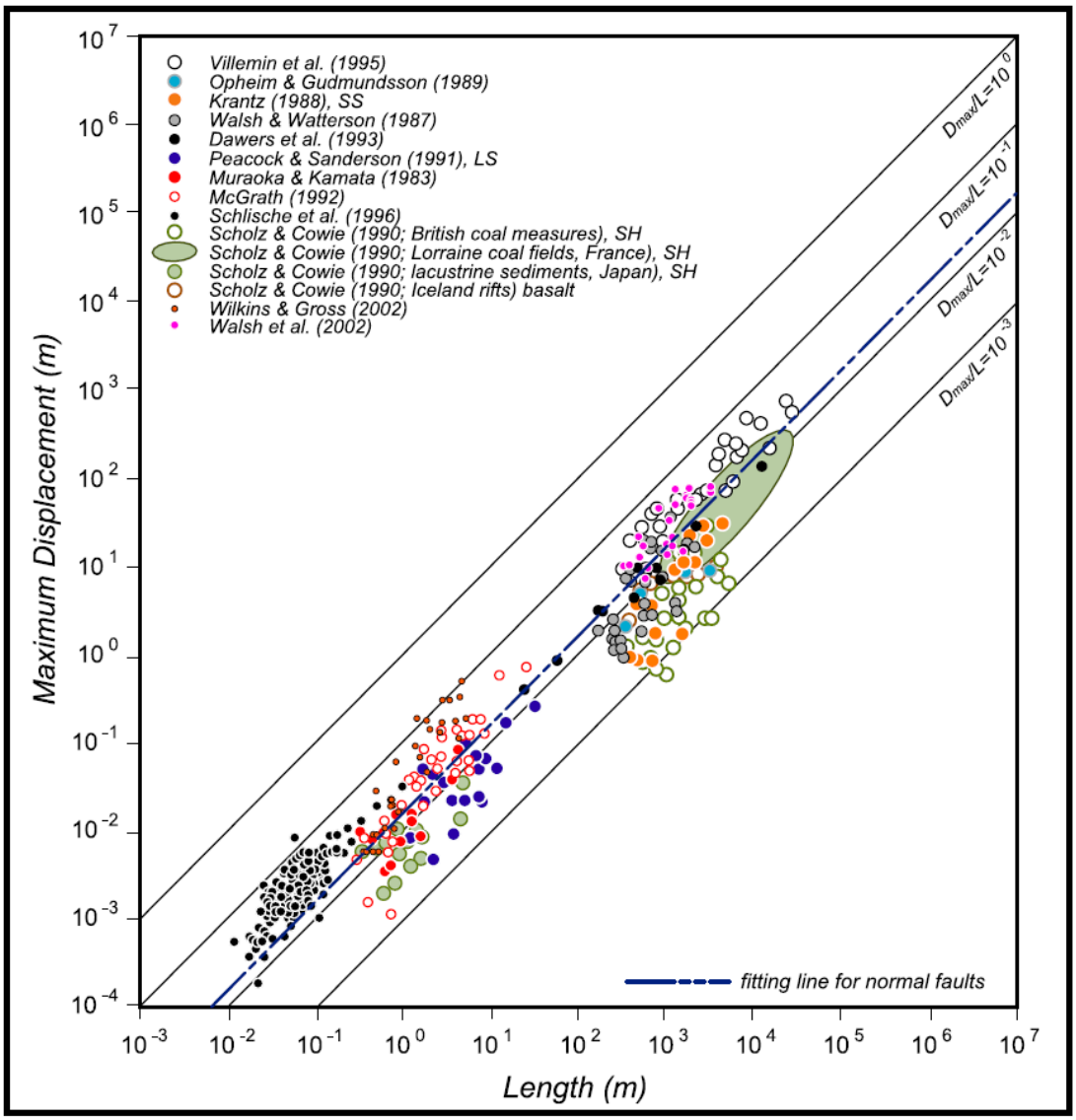

Figure 1-4: Compilation of previously published maximum displacement (d_{max}) vs. fault length (L) for normal, thrust and strike-slip faults. SS-sandstones; LS-limestones; and SH-shale. Figure from Kim and Sanderson (2005).

higher than for thrust and normal faults (Kim and Sanderson, 2005) (Figure 1-4). The reason for this higher d_{max}/L ratio for strike-slip faults may be related to the measurement of fault length being systematically taken in directions parallel to the slip direction. In addition, Figure 1-4 demonstrates that the d_{max}/L ratio slightly decreases with fault length. This characteristic probably results from different fault growth mechanisms at various scales. Factors that contribute to the scattering in d_{max}/L plots include:

- The nature of the log-log plots on which displacement and length data are presented (Gillespie et al., 1992);
- Sampling and measurement errors (Gillespie et al., 1992; Walsh and Watterson, 1988);
- Variations in mechanical properties and tectonic settings in the host-rock (Cowie and Scholz, 1992a; Wilkins and Gross, 2002);
- The type of fault(s), including position and measurement direction(s) (Kim and Sanderson, 2005);
- Earthquake rupture and slip/propagation histories of faults (Kim and Sanderson, 2005);
- Mechanical anisotropy and stratigraphy in the rock volume offset by faults (Bürgmann et al., 1994; Kim and Sanderson, 2005; Schultz and Fossen, 2002).
- Complex relationships between fault damage zones width and fault displacement (Faulkner et al., 2010; Mitchell and Faulkner, 2009).

In addition to these factors, scattering in d_{max}/L plots has also been attributed to fault propagation (Peacock and Sanderson, 1996), fault reactivation (Kim et al., 2001b), and to the interaction and overlapping of fault segments (Bürgmann et al., 1994; Cartwright et al., 1995; Peacock, 1991b; Peacock, 2002; Peacock and Sanderson, 1991; Willemse et al., 1996).

Torabi and Berg (2011) thoroughly revised the relationships between maximum displacement and length for faults in different tectonic settings to suggest that the d_{max}/L ratio is higher for small and large faults, while for medium-sized faults this ratio is smaller. According to the same authors, larger d_{max}/L ratios for large faults can result from the accumulation of displacement and length from the smaller fault segments linked to form a large fault. This is in agreement with previously published works in which the displacement-length ratio is expected to be higher for areas of overlapping faults segments than for fault segments that do not interact (Dawers and Anders, 1995; Peacock and Sanderson, 1991; Kim and Sanderson, 2005). Fault core thickness and the damage zone width should also be taken into account when assessing the d_{max}/L ratios for the fault system, suggesting the existence of a hierarchical distribution of faults and implying that small, medium and large-sized faults should be considered separately in a fault system (Torabi and Berg, 2011).

1.2.5. Fault growth mechanisms

In contrast to models that consider faults as isolated slip surfaces, most faults on Earth are complex structures that result from bifurcating slip surfaces, or from the overlapping,

coalescence and linkage of individual segments (e.g. Cartwright et al., 1995; Ellis and Dunlap, 1988; Peacock and Sanderson, 1991; Segall and Pollard, 1983, 1980; Trudgill and Cartwright, 1994). Fault segmentation and linkage may affect displacement distribution(s) along the fault length and consists of one of the many factors that cause scattering in maximum displacement with fault length (Bürgmann et al., 1994; Cartwright et al., 1995; Childs et al., 1995; Peacock, 1991b; Peacock, 2002; Peacock and Sanderson, 1991; Willemse et al., 1996).

Early displacement analyses carried out on strike-slip faults in granitic rocks of different sizes, suggest that large segmented faults are formed by the nucleation of smaller individual fractures in a single sub-parallel array (Segall and Pollard, 1983). An analysis conducted on thrust faults (Ellis and Dunlap, 1988) describe how three (initially) independent faults were linked through their lateral tips (Figure 1-5). The occurrence of a displacement maximum characterises areas of nucleation of faults, and a displacement minimum indicates the area of segment linkage. Kinematic analyses of displacement variations due to segment linkage, for distinct normal fault zones (Peacock and Sanderson, 1991), suggest that faults evolve by initially developing isolated structures, each with an approximately linear profile (Figure 1-6). Displacement transfer between fault segments is accommodated by bed rotation, a process leading to the development of a relay ramp, which is then faulted. Relay ramps can be breached if the fault cuts the ramp, resulting in a composite fault with an along-strike bend. The occurrence of relay ramps at oversteps and linkage points is usually reflected as a minimum in total fault displacement (Peacock and Sanderson, 1994).

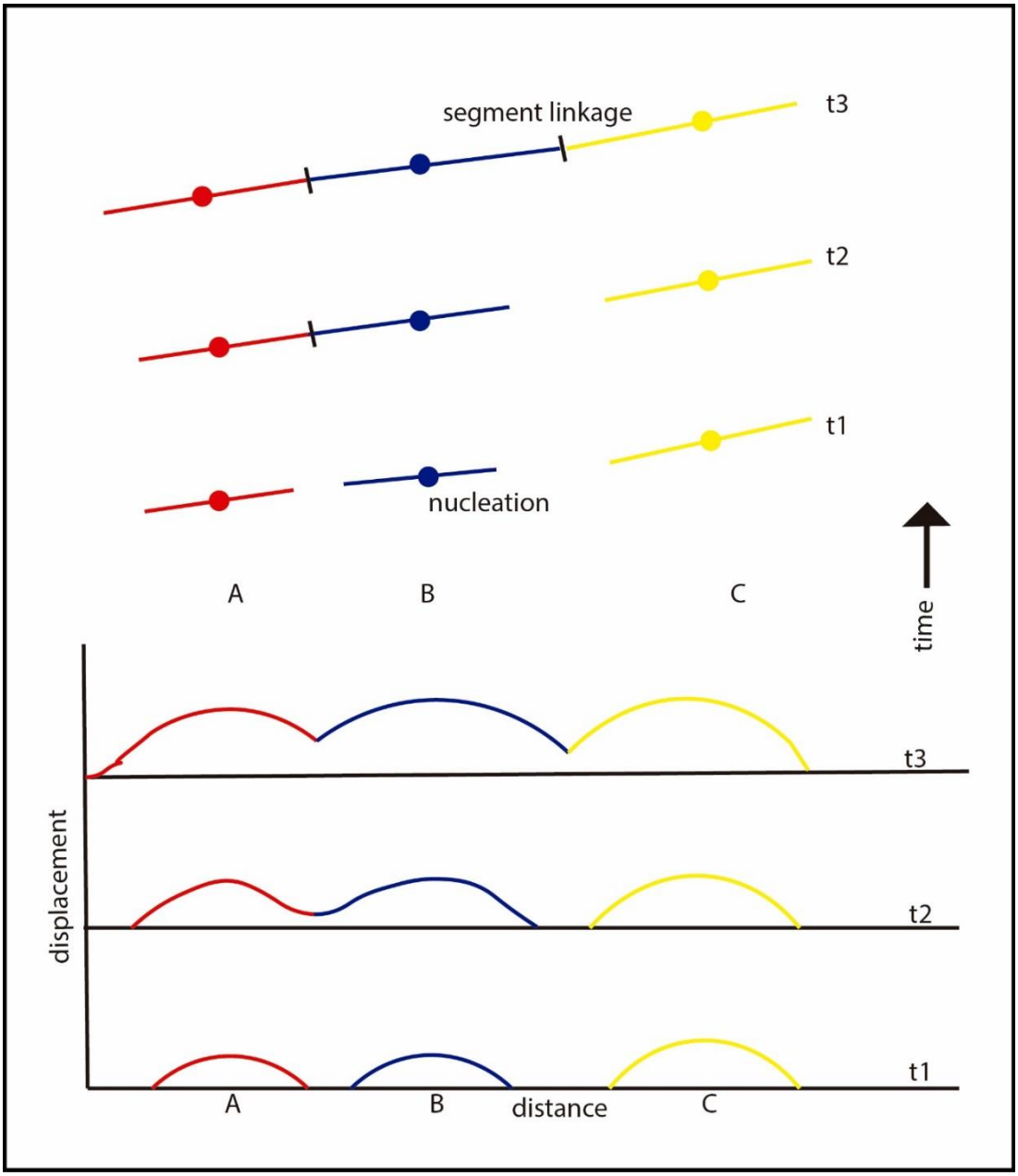

Figure 1-5: Schematic representation of a thrust fault development. Interaction of the lateral tips in map view, and on displacement-distance plots, subsequently link three initially-independent faults segments (A, B and C). Adapted from Ellis and Dunlap (1988).

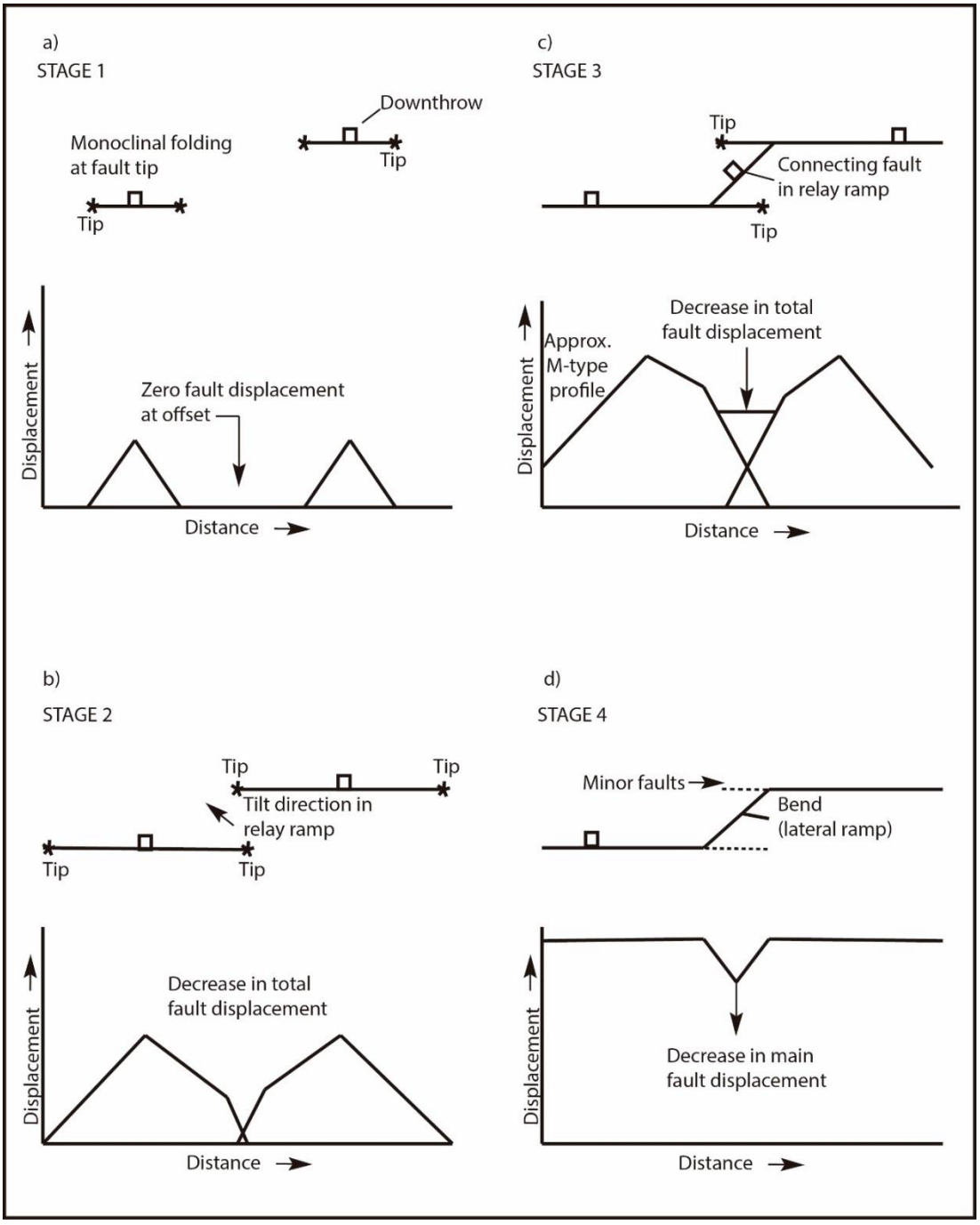

Figure 1-6: Diagrams illustrating four stages of linkage development through a relay zone and corresponding shapes of displacement-distance plots. Figure from (Peacock (1991) and Peacock and Sanderson (1991).

As large fault zones usually result from the coalescence and linkage of smaller faults, the fault growth model by linkage indicates a change in the displacement patterns described for idealised blind faults (Figure 1-7; and also Cartwright et al., 1995; Dawers and Anders, 1995; Mansfield and Cartwright, 2001; Martel and Boger, 1998; Peacock and Sanderson, 1991; Peacock, 1991; Trudgill and Cartwright, 1994). A fault growth model by segment linkage was suggested using maximum displacement (D_{max}) and length (L) measurements for faults in the Canyonlands Grabens region, Utah (Cartwright et al., 1995). This study discussed the displacement distribution near observed fault tips and suggested that the observed scatter in displacement-length relationships resulted from fault growth through (largely) sequential segment linkage. Similar conclusions were obtained from analogue modelling analyses undertaken by Mansfield and Cartwright (2001).

Linkage regions are represented by anomalies in displacement values when plotting displacement-distance profiles. These anomalies consist of elongated sub-vertical zones, with the long axis being sub-parallel to the slip direction (Childs et al., 1993, 1995). As two sub-parallel faults propagate towards each other, the stress fields at the fault tips increase and displacement is accumulated near them, resulting in lateral tips within an overlap zone with steeper displacement gradients (Cartwright et al., 1995; Mansfield and Cartwright, 2001; Peacock, 1991a; Peacock and Sanderson, 1991; Walsh and Watterson, 1988). Apart from these fault tips, linkage of individual fault segments is also likely to occur in the dip direction, as suggested by some studies on fault linkage (Ellis and Dunlap, 1988; Muraoka and Kamata, 1983).

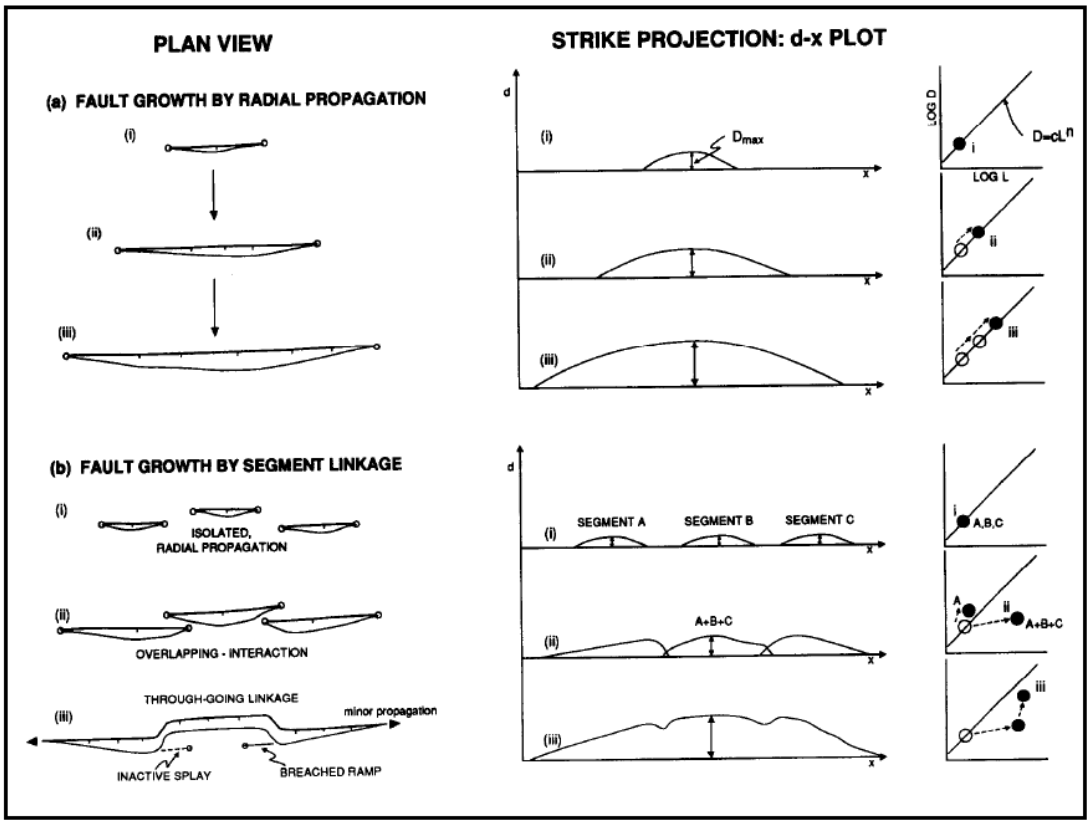

Figure 1-7: Comparison of two different fault growth models. a) Fault growth by radial propagation and b) Fault growth by segment linkage. Three stages of growth evolution are compared for both models in plain view, on a displacement-distance plot and on a log-log plot of maximum displacement (D) against maximum length (L). The radially propagating fault follows a linear growth path whereas the linked fault follows a step-like path. Figure from Cartwright et al. (1995).

Fault segments therefore grow by propagation, overlap and later linkage in the dip direction and are characterised by displacement anomalies with the long axis orthogonal to the slip direction (Mansfield and Cartwright, 1996). Fault dip-linkage results in relay structures sub-parallel to the fault strike. However, zones of dip-linkage between two or more (originally independent) segments are unlikely to be preserved in the geological record since the linkage points tend to be destroyed during the fault growth (Childs et al., 1996). These structures may be recognised as displacement minima anomalies in seismic data when good lateral and vertical resolution, associated with high sampling density, are acquired from discrete faults (Mansfield and Cartwright, 1996).

1.2.5.1. The coherent fault growth model

Fault linkage models mostly involve the nucleation and propagation of discrete fault segments followed by overlap, interaction and formation of relay ramps or bends, as summarised in the previous section. This "isolated fault model" (Walsh et al., 2003) is widely endorsed by several authors (Cartwright et al., 1995; Childs et al., 1993; Dawers and Anders, 1995; Mansfield and Cartwright, 1996; Peacock and Sanderson, 1991) because of the 2-D nature of the data in map or cross-section, based on the assumption that fault propagation occurs within the self-contained fault plane. More recently, the widespread use of seismic data to evaluate fault growth has highlighted the importance of out-of-plane fault propagation. An alternative model for fault linkage was suggested by Childs et al. (1995), and Childs et al. (1996), and denominated as "the coherent fault model" (Figure 1-8).

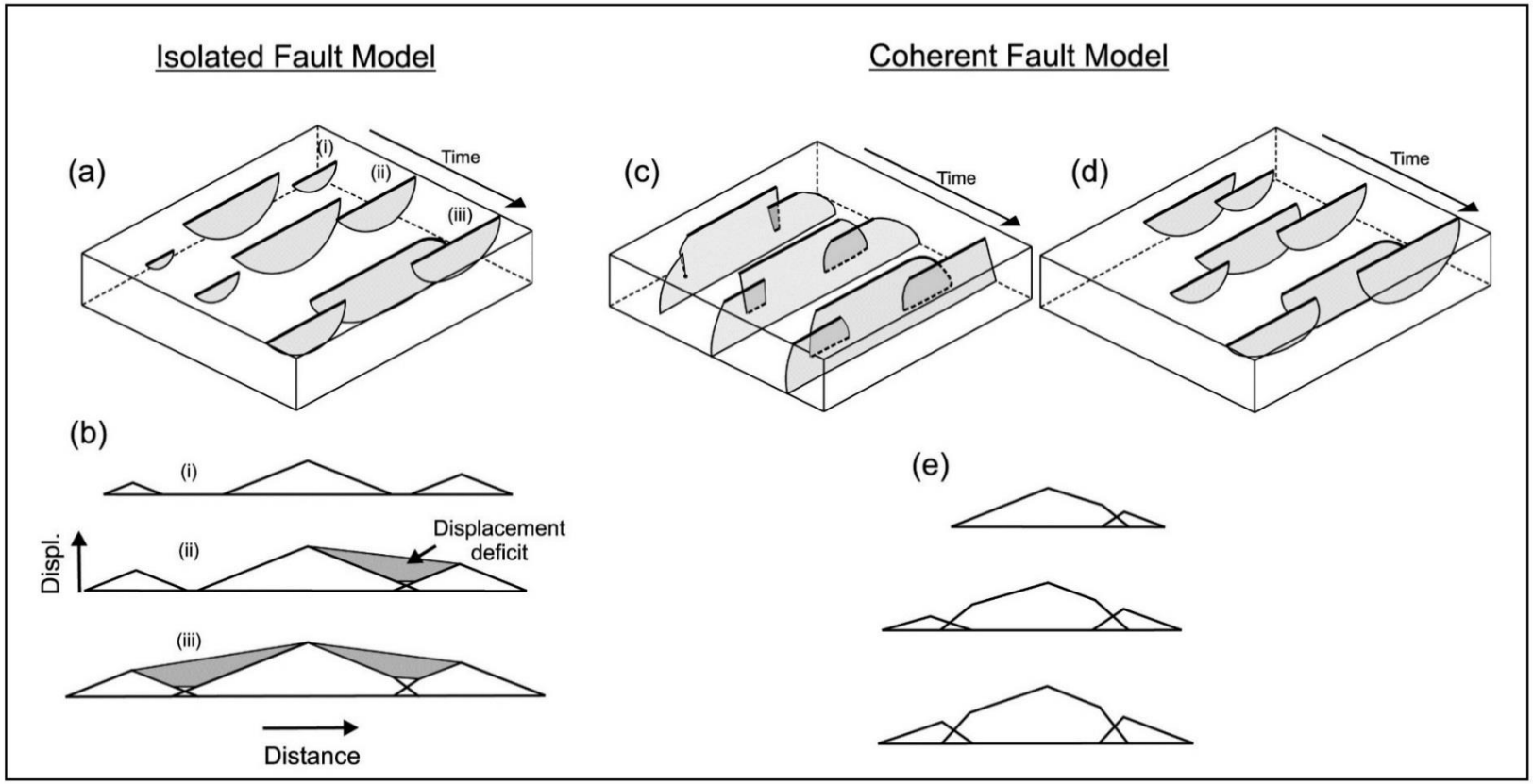

Figure 1-8: Schematic comparison between the "isolated fault" and the "coherent fault' models. The block diagrams (a, c and d) show the growth stages of a segmented fault array (i–iii). The displacement-distance plots (b and e) are for fault traces on the upper surfaces of the block diagrams (bold lines). The coherent fault model is illustrated for hard-linked (c) and soft-linked (d) fault segments. Figure taken from Walsh et al. (2003).

In the coherent fault model, segments of a fault array are thought to be kinematically related since their initiation, and later during fault growth and propagation (Childs et al., 1996, 1995; Walsh et al., 2003). Fault segmentation may occur either by fault surface bifurcation or by stepping during the propagation of fault segments. Segmented fault arrays generated by these processes may be either "hard-linked" or "soft-linked" to other fault segments or the main surface (Walsh et al., 2003).

Differences between the "isolated fault model" and the "coherent fault model" are best constrained for synsedimentary faults, particularly in areas where sedimentation rates are higher than fault displacement rates. The discrimination between both fault models can be attained through different methods, including the analysis of the 3D propagation and geometry of an ideal elliptical fault, the spatial organisation and the aggregate displacement patterns of segmented fault arrays (Walsh et al., 2003). The existence of the "coherent fault model" does not mean the obsolescence of the "isolated fault model". In fact, fault segmentation can be controlled by multiple factors, including the stratigraphic and material properties of the faulted sequence; thus indicating that both fault growth mechanisms can occur in nature, even in the same geological setting, depending on the fault array evolution and system considered (Fossen and Rotevatn, 2016). In summary, isolated fault growth results from the nucleation of embryonic faults, considering the existence of boundary conditions to distribute the strain homogeneously for nucleation, as observed both in sandbox models, representing the sand overlying a relatively viscous material such as silica gel (Cowie et al., 2000; Soliva and Schultz, 2008), and in the nature, with sandstones overlying shale or salt units (Trudgill and Cartwright, 1994). The coherent fault model most often results from the upward propagation of a reactivating

buried fault with a localised strain in the overburden above the fault (Childs et al., 2009; Giba et al., 2012).

1.3. Salt tectonics

1.3.1. Definition of salt and mechanics of salt flow

Sedimentary basins recording the deposition of salt (or evaporite) layers are more susceptible to deformation than basins formed by a sequence of non-evaporitic rocks (Fossen, 2010). Evaporites can be found in cratonic basins, syn-rift basins, passive continental margins and foreland basins (Hudec and Jackson, 2007). Salt layers in sedimentary sequences contain variable amounts of evaporites, including halite, gypsum, anhydrite, high-grade K- and Mg-rich evaporites such as sylvite and carnallite, and non-evaporitic minerals such as clays (Fossen, 2010) and carbonates (Warren, 2006). The mineral halite (NaCl) is considered as pure rock salt and has a density of 2.160 g/cm^3 (Talbot and Jackson, 1987).

Salt bodies have fundamentally distinct physical and rheological properties when compared to siliciclastic and carbonate rocks (Weijermars et al., 1993). After the first 100-200 m of burial, salt becomes incompressible and does not change its density with increasing thickness of overburden rocks. Conversely, compaction is an imperative process in siliciclastic units, as increasing burial depths cause sandstones and shales to lose their effective porosity and become denser (Hudec and Jackson, 2007; Talbot and Jackson, 1987). The different behaviours of salt and siliciclastic rocks when buried results

in an inversion in density as the siliciclastic overburden becomes denser than the salt. Therefore, the salt buried under thicker overburden units becomes buoyant below a certain threshold depth (Hudec and Jackson, 2007).

Density inversion causes the salt-bearing sedimentary basin to become unstable, and subsequently prone to lose its potential energy. When both the salt and overburden densities are similar, neutral buoyancy is reached. The neutral buoyancy for a carbonate overburden occurs beneath a depth of 650 m. For the buoyant salt to rise to the surface, the overburden density must exceed the salt density, which for a siliciclastic overburden occurs at a burial depth ranging between 1600 to 3000 m (Nelson and Fairchild, 1989).

When assessing the driving forces for halokinesis, differential overburden loading is the primary mechanism inducing salt movement from high- to low-pressure zones. This mechanism controls the generation of pressure heads (Figure 1-9a) and elevation heads (Figure 1-9b) imposed on a salt layer (Hudec and Jackson, 2007). Halokinesis can therefore be driven by three types of loading. The first type, gravitational loading, results from a combination of the weight of the overburden rocks and any gravitational forces acting on the salt layer, causing the salt to flow from areas with a high pressure head to areas with low pressure (Hudec and Jackson, 2007). Displacement loading occurs when one of the flanks of a salt body moves towards (or away) from the other flank during regional shortening or extension. Thermal loading occurs when the volume of salt changes due to temperature variations in a sedimentary basin. When the salt body is heated, it expands and becomes buoyant, producing convection cells within the salt layer.

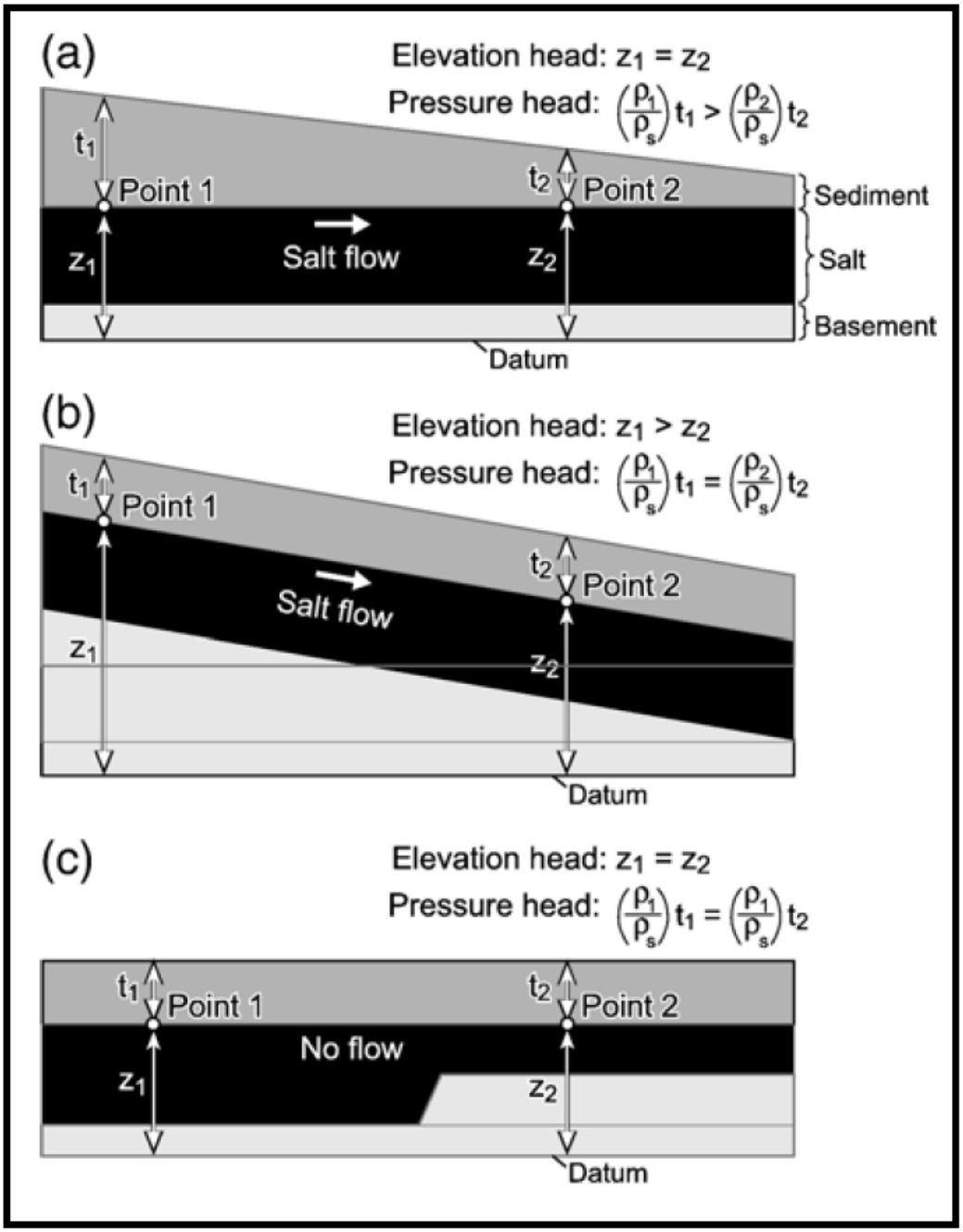

Figure 1-9: Differential overburden loading is the main driving force of halokinesis. A) When an overburden has variable lateral thickness, a pressure head will be formed from Point 1 to Point 2 and salt will flow from left to right along the pressure gradient. No elevation head will be formed since the salt layer is tabular. B) When the overburden with uniform thickness is above a tabular but inclined salt layer, no pressure head will be produced, and an elevation head will be formed with salt flowing from Point 1 to Point 2. C) When a uniform thickness overburden is over a flat salt layer no pressure or elevation head will be formed, even though the salt thickness varies. Figure from Hudec and Jackson (2007).

The salt may remain static in the subsurface if the resisting forces that oppose salt flow are dominant in relation to the driving forces. The two dominant resisting forces in nature are the strength of the overburden, and the boundary friction that occurs within the salt layer (Hudec and Jackson, 2007). The first resisting force is associated with the occurrence of thick sedimentary roofs above the salt layer, which are unlikely to be deformed by salt unless the salt flow is accompanied by an extensional or shortening event. Boundary friction limits the ability of salt to flow due to boundary drag along the top and the bottom surfaces of the salt layer (Alves et al., 2017).

1.3.2. Diapir-growth mechanisms

For the salt to pierce its overburden strata completely, or partially, to form a diapir, the rocks above it must be removed or displaced. The ascension and emplacement of salt through the roof rocks have been extensively discussed in the literature (e.g. Berner et al., 1972; Hossack, 1995; Schultz-Ela et al., 1993; Talbot et al., 1991; Talbot and Jackson, 1987; Vendeville and Jackson, 1992; Worrall and Snelson, 1989). Three main mechanisms for salt diapirism have been proposed by this and other work: active diapirism, passive diapirism and reactive diapirism (Figure 1-10).

Reactive diapirism requires regional extension to occur. Diapirism is triggered when the salt progressively pierces an initial graben or half-graben. As extension continues, overburden rocks are thinned and the salt moves to fill the created space (Schultz-Ela et al., 1993; Vendeville and Jackson, 1992). Reactive diapirs (Figure 1-10a) are elongated and strike orthogonally to the extension direction. These extensional forced generate new

faults in the older fracture zone above the diapir crest (Jackson et al., 1994a). The structural style of reactive diapirism is controlled by the relative ratios of sediment aggradation and regional extension. As extension ceases or slows, salt movement and associated creation of accommodation space also terminate.

As extension and reactive diapirism cause the diapir to become sufficiently tall, and the roof sufficiently thin, the pressure at the diapir crest results in its intrusion into overburden rocks (Schultz-Ela et al., 1993). Salt intrusion marks the transition between reactive and active diapirism (Figure 1-10b). One of the most distinctive features of diapirs formed actively is their arched overburden. The intrusion of salt forces its arched roof to form a central graben flanked by normal and reverse faults. The normal faults in the central graben propagate downward with new faults being created downwards, while reactive faults propagate inwards (Jackson et al., 1994a). A thick and arched roof above a diapir indicates that buoyancy alone did not provide enough upward force to raise thick roofs, and that salt diapirs were instead squeezed. Squeezed salt diapirs (Figure 1-10c) grow by the displacement of salt from the stem to the head of the diapir, and downwards back to the source layer (Dooley et al., 2009). The most diagnostic feature of squeezed, active diapirs is the occurrence of a large bulbous head with a narrow stem.

Active diapirism is controlled by gravitational forces acting on the salt, in contrast to extensional controls that act on the salt during reactive diapirism. Active diapirism can continue even if the regional extension ceases to act on a evaporite body (Vendeville and Jackson, 1992). If regional extension ceases, active diapirs will be surrounded by radial faults. In contrast, if extension follows the piercement of overburden units by salt, sub-

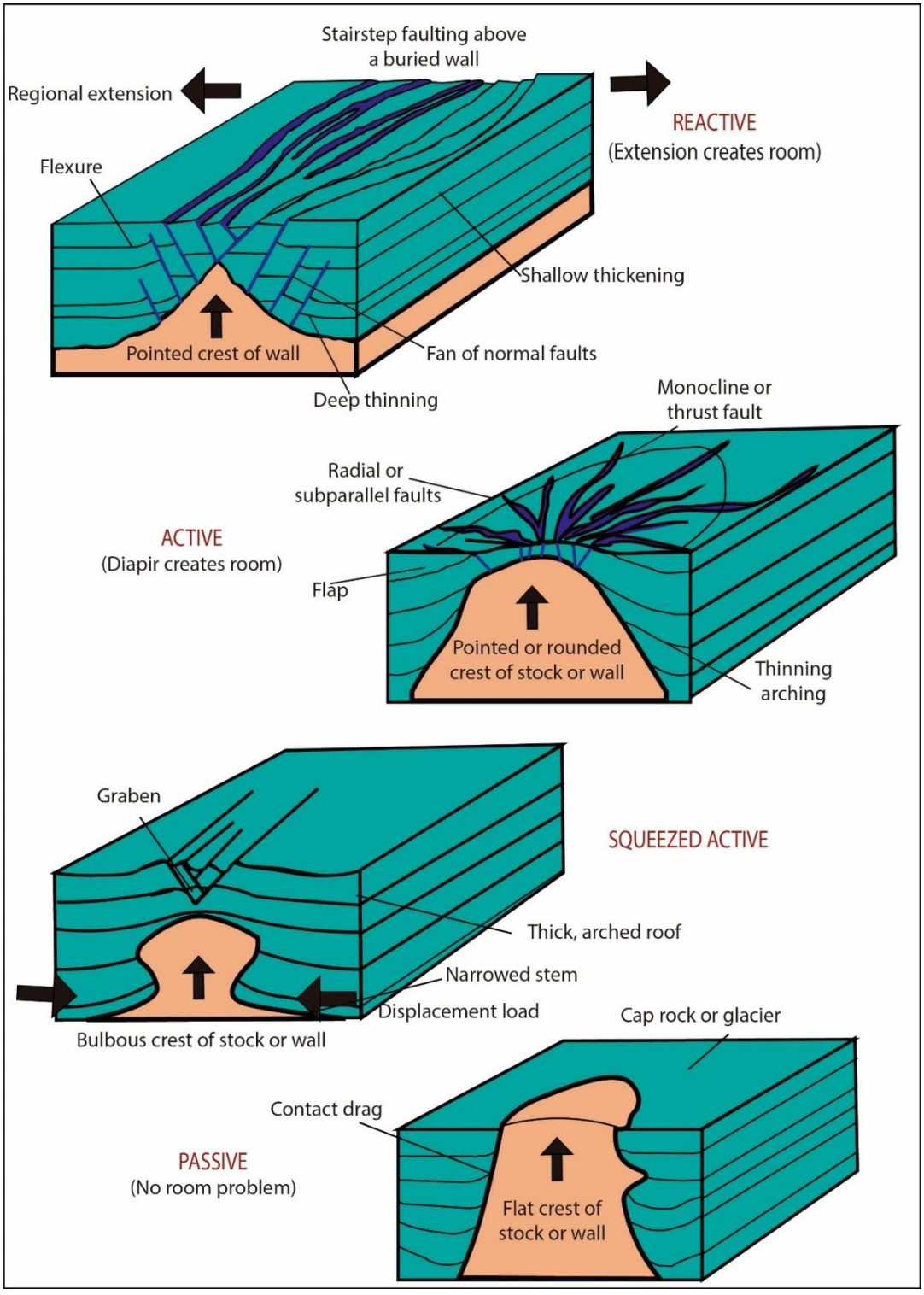

Figure 1-10: Four models of salt diapirism and their characteristic features. a) Reactive diapir. b) Active diapir. c) Squeezed Active diapir. d) Passive diapir.

parallel faults will surround the diapirs (Withjack and Scheiner, 1982). As an active diapir breaks through its thin and weak roof, the salt will rise first as a narrow crest to later develop its full width, becoming a passive diapir.

When a diapir emerges at the surface, it becomes passive. The salt accumulated around the diapir thins over the crest and remains fixed near the sediment surface. Passive diapirs are characterised by the occurrence of minor to negligible radial faults around the flanks, and drag folds, depending on the relative lithology (composition) of the post-salt overburden (Jackson et al., 1994a) (Figure 1-10d). Variations in sedimentation rates on the flanks of passive diapirs depend on the balance between aggradation and the rate of salt (diapiric) rise. For example, if a diapir rises faster than surrounding sediments can aggradate, the salt will overflow the diapir margins and will widen upwards.

1.3.3. Salt-related structures

Once the driving forces of diapirism overwhelm the resisting forces, upwards movement of the salt through the overburden is set to begin. Salt piercement causes the roof rocks to be carried upwards by the salt, and a variety of structures related to halokinesis are formed as a consequence (Jackson et al., 1994b). The resulting salt structures can be categorised according to their forms, sizes, relationship to host and overburden rocks, and by considering any relationships between these structures and regional deformation styles (Figure 1-11).

A full detailed account of how these structures are classified into distinct groups and sub-groups is given in Jackson and Talbot (1994). The term salt diapir is employed for all the salt-related structures in Jackson and Talbot (1994) regardless of the mechanism by which the salt pierced the overburden. However, different salt geometries may result from distinct modes of salt emplacement. The largest and most mature groups of salt structures comprise salt-wall canopies and salt-stock canopies, whereas the least mature salt structures include salt rollers, salt anticlines and salt pillows (Figure 1-11).

Salt-rich passive continental margins are dominated by extensional forces, which result in the formation of immature salt structures such as salt anticlines, salt pillows and rollers associated with large faults in upper slope regions (Alves, 2012; Rowan et al., 1999). At the transition zone separating the extensional upper-slope from the compressive lower-slope domains, dominant salt structures include salt walls, whereas in the compressive lower slope domain include mature salt structures such as thrust, allochthonous salt sheets and canopies (Brun and Fort, 2004). The salt diapirs studied in Chapters 4 and 5 fall under the extensional to transitional domains, and include 3D geometries such as salt anticlines, salt rollers and salt walls (Figure 1-11).

1.3.4. Salt-related faults

Once salt bodies start moving (vertically) away from its source layer, the post- or supra-salt sedimentary overburden is deformed. Seismic-scale deformation due to halokinesis and salt diapirism may be either brittle, resulting in the development of

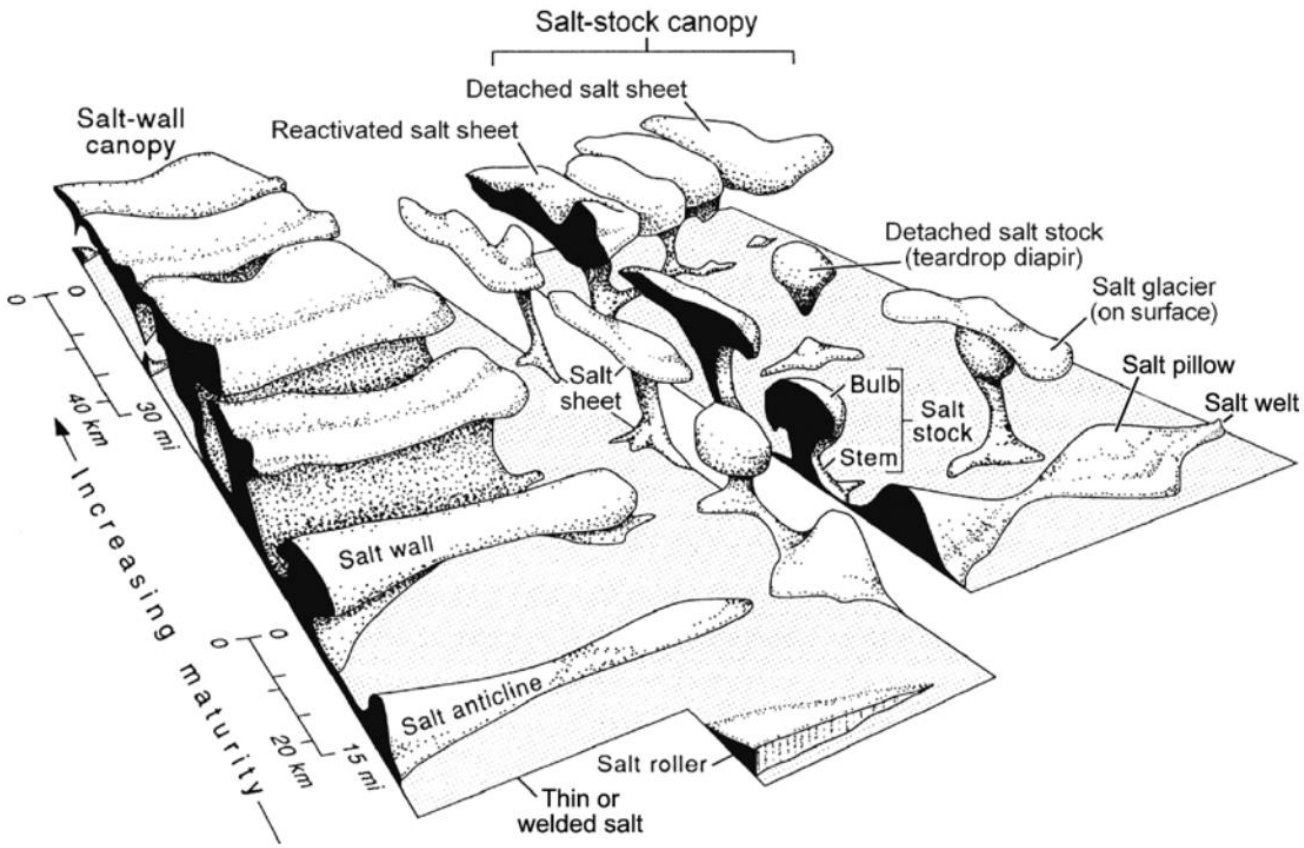

Figure 1-11: Block diagram showing the main shapes of the salt structures relative to increasing structural maturity and size. In the upper slope domain, predominant salt structures include salt rollers, salt pillows and salt anticlines. In the transitional domain, salt walls predominate, whereas the lower slope domain is dominated by mature salt structures such as canopies. From Hudec and Jackson (2007).

fractures and faults, or ductile recording the formation of folds due to the arching and buckling of the roof rocks. This section aims to give an overview of the fault families that are formed around salt diapirs.

Dome-related fault patterns are typically defined as synthetic normal and reverse faults with an approximately radial pattern in map view (Schultz-Ela et al., 1993; Withjack and Scheiner, 1982). However, when recognising and assessing salt-dome fault patterns it must be stressed that a salt dome may be affected by subsidence caused by extensional collapse (Jackson et al., 1994a; Vendeville and Jackson, 1992) or solution collapse (Clark et al., 1999). Fault families associated with dome formation are commonly classified based on their map view with respect to the diapir, and by the sense of displacement and dip orientation (Alsop, 1996; Alsop et al., 2000; Davison et al., 2000; O'Brien and Lerche, 1988; Stewart, 2006; Yin and Groshong, 2007). The most common dome-related fault patterns documented in the literature are radial normal faults (Figure 1-12a to 12d), concentric normal faults, and concentric reverse faults (Figure 1-12e and 12f).

1.3.4.1. Radial faults

Radial normal faults comprise the simplest and most common arrangement of extensional faults around salt domes (Yin and Groshong, 2007) (Figure 1-12a to d). These structures may also be found in many other geological structures resembling circular domes such as igneous plutons and calderas (Acocella et al., 2004; Chadwick and Dieterich, 1995; Holohan et al., 2008; Walter and Troll, 2001), gneissic domes

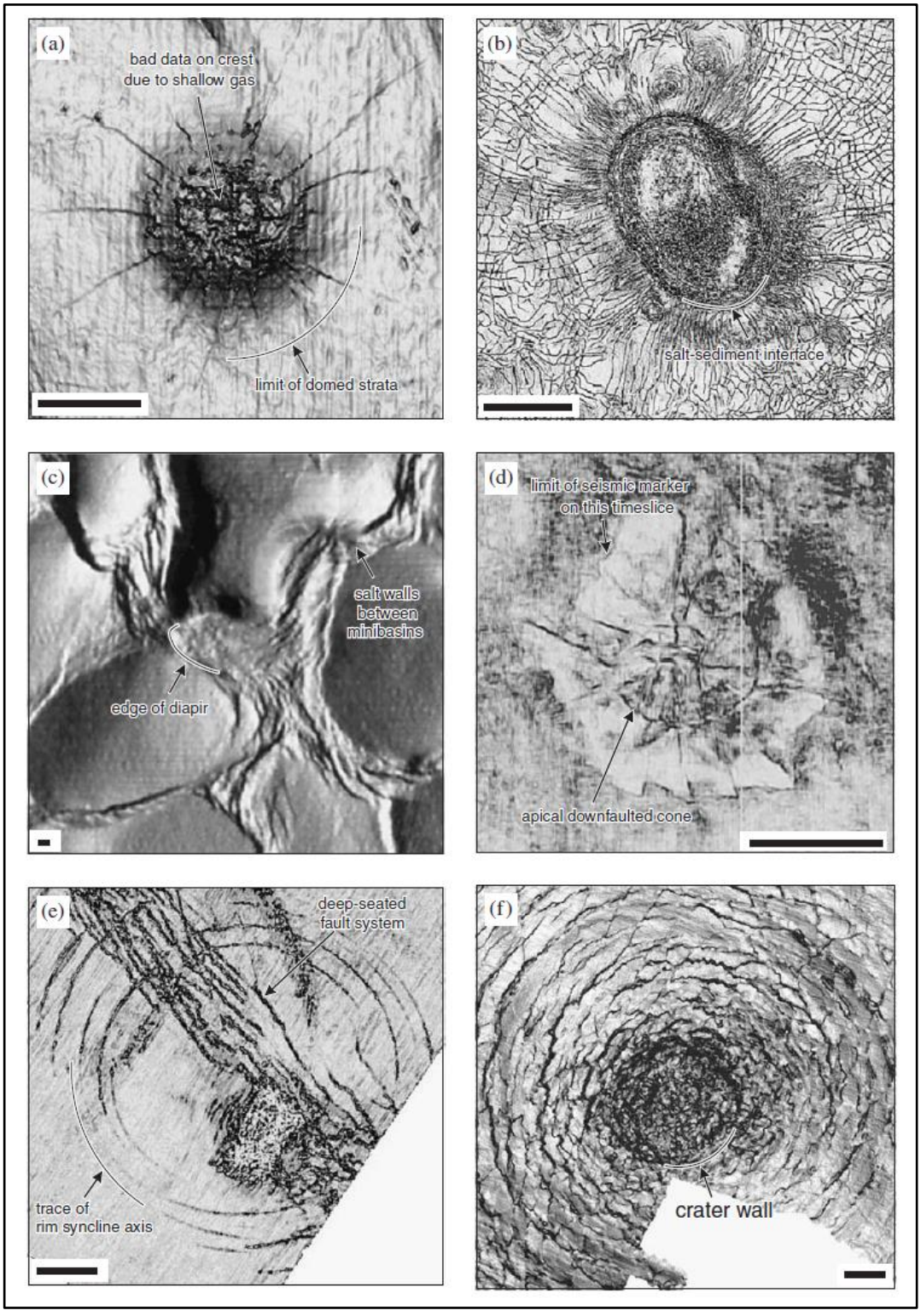

Figure 1-12: 3D seismic attribute slices with radial and concentric faults for different geological settings. a) Radial faults in domed sediments above salt diapirs; b) radial faults adjacent to salt diapir; c) diapirs at wall intersections separating sedimentary minibasins; d) radial faults and crestal conic graben; e) concentric faults around rim syncline associated with mud withdrawal, f) concentric faults around a cylindrical void. Figure from Stewart (2006).

(Yin, 2004), mud volcanoes (Neurauter and Roberts, 1994), and mud diapirs (Hansen et al., 2005).

The arching of overburden rocks, caused by the diapir's forceful intrusion, is responsible for the formation of radial faults (Schultz-Ela et al., 1993; Stewart, 2006; Vendeville and Jackson, 1992). These faults are typically limited to the arched area of the sedimentary roof and occur in a variety of extension directions. This latter characteristic results in the development of faults with different azimuths (Alsop et al., 2000; Withjack and Scheiner, 1982; Yin and Groshong, 2007).

Analogue models for radial faults indicate that the magnitude of extension is proportional to the stretch height of the overburden, and displacement accumulates preferentially at the flanks or the apex of the dome, decreasing to zero away from the dome crest (Withjack and Scheiner, 1982; Yin and Groshong, 2007). As a result, fault throw in radial faults increases towards the crest of the dome and is negligible at the dome's edge (Yin and Groshong, 2007) (Figure 1-12d). The most accepted kinematic model for the formation of radial and concentric faults proposes that doming or uplift of the diapir flanks occurs in distinct scenarios, and notably apart from the arching caused by the forceful intrusion of salt (Stewart, 2006). Doming can also occur as sediment compacts over the salt diapirs' incompressible heads. Finally, doming can be associated with passive diapirism as the strata that partially cover the diapirs' head are folded and rotated to form a drag fold.

1.3.4.2. Concentric normal faults

Concentric normal faults can be subdivided into two distinct groups based on their dip. The first group comprise faults that dip away from the salt diapir. The faults are formed to accommodate the folding of competent strata, which then subside around the incompressible and buoyant salt (Alsop et al., 2000). The stretching component of extensional concentric faults is accommodated in the radial direction. The second group of concentric normal faults dip towards the salt diapir and are associated with crestal collapse. A diapir falls or collapses when the tilted salt layer is above the regional datum and become unstable (Stewart, 2006).

1.3.4.3. Concentric reverse faults

Reverse concentric faults are developed due to the radial compression of the overburden units resulting from a rapid increase in diapir volume and radius (Davison et al., 1993). Such an increase in the diapir radius result from the shallow extrusion or squeezing of the diapir. Reverse concentric faults are thus formed to accommodate the resulting shortening and to align it tangentially to the diapir. As the strata are overturned, pre-existing extensional concentric faults are rotated and reactivated as reverse faults, becoming curved as the fault plane propagates (Davison et al., 1993).

1.4. The regional stress field

From the perspective of hydrocarbon exploration, the knowledge of *in situ* rock stresses is important so we can understand reservoir behaviour, estimate hydrocarbon retention within the reservoir, and assess borehole stability (Fejerskov et al., 2000; Lindholm et al., 1995). Stress fields can be inferred from the relationship between the strain (deformation) and bedrock rheology. Tectonic stresses comprise the horizontal components of the *in situ* stress field, which deviate from a reference state in scales ranging from plate-wide to local. *In situ* stresses are also affected by natural and anthropogenic processes, including drilling and mining (Engelder, 2014). On the Earth's surface, the main sources of information on crustal-scale stresses derive from fault inversion methods, including the Anderson's theory of faulting (Anderson, 1942), the Wallace and Bott hypothesis (Bott, 1959; Wallace, 1951), the Numeric Dynamic Analysis (Sperner et al., 1993) and Direct Stress Inversions (Angelier, 1994, 1990). *In-situ* stress measurements, including earthquake focal mechanisms, borehole breakouts and drilling-induced fractures, provide the magnitude and orientation of present-day *in situ* stresses and are used in the World Stress Map (Heidbach et al., 2008).

The World Stress Map (WSM) consists of a global compilation of publicly available *in situ* stress data (Heidbach et al., 2008). Different sources of stress information, such as earthquake focal mechanisms, borehole breakouts and drilling-induced fractures, are complemented by *in-situ* stress measurements that include overcoring, hydraulic fracturing and borehole slotter data. Earthquake focal mechanisms are most frequent along plate boundaries, where earthquakes are

common. Breakouts, hydraulic fractures and overcoring tend to be found at shallower levels. Structural data from fault-slip analyses and alignments of magmatic vents also indicate modern and paleostresses.

Many of present-day structures are not recently formed but inherited from past deformation events adjusted to the present-day stress field. For these structures as important as the present-day quantification of *in-situ* stress(es), is the measurement of paleostress. This section aims to discuss the main methods for indirect determination of paleo- and modern stress tensors.

1.4.1. The Anderson faulting theory

The most simple approach used in paleostress inversion provides a first order estimate of principal stress orientations from large-scale fault patterns, without quantifying any kind of stress anisotropy (Anderson, 1942). The Anderson scheme for relative stress magnitudes classifies an area as being characterised by normal, strike-slip or reverse faulting (Figure 1-13). This classification depends on whether the crust is extending, rock blocks slide past one another in strike-slip structures, or reverse faults form due to compression on the Earth's crust (Anderson, 1942). The Anderson classification scheme is also used to estimate principal horizontal-stress magnitudes in relation to observed vertical stresses. For normal faulting regimes, the vertical stress σ_v is the maximum principal stress (σ_1), for strike-slip regimes the intermediate principal stress (σ_2), and for reverse faulting regimes the least principal stress (σ_3) (Zoback, 2010).

Criticisms of Anderson faulting theory often highlight key limitations that are inherent to its application. The magnitude of the principal stresses at any depth are controlled by the crust's strength at depth. Thus, the precise value of each stress magnitude cannot be determined by this method. The Andersonian fault theory is also only valid for relatively new structures with pure dip-slip or pure strike-slip movement. In situations where slip occurs along a pre-existing discontinuity, where the orientations are not dependent on the current stress state, the Anderson faulting theory cannot be applied (Zoback, 2010).

1.4.1.1. Vertical stress magnitude

Based on the Anderson faulting theory, the principal stresses can be estimated when their orientations are known (Zoback, 2010). For offshore areas, the magnitude of σ_v is equivalent to the integration of the rock densities from the surface to the depth of interest, adding water depth (Equation 1-2).

$$\sigma_v = \rho_w g z_w + \int_{z_w}^{z} \rho(z) g \, dz \approx \rho_w g z_w + \rho_o g (z - z_w)$$

Equation 1-2

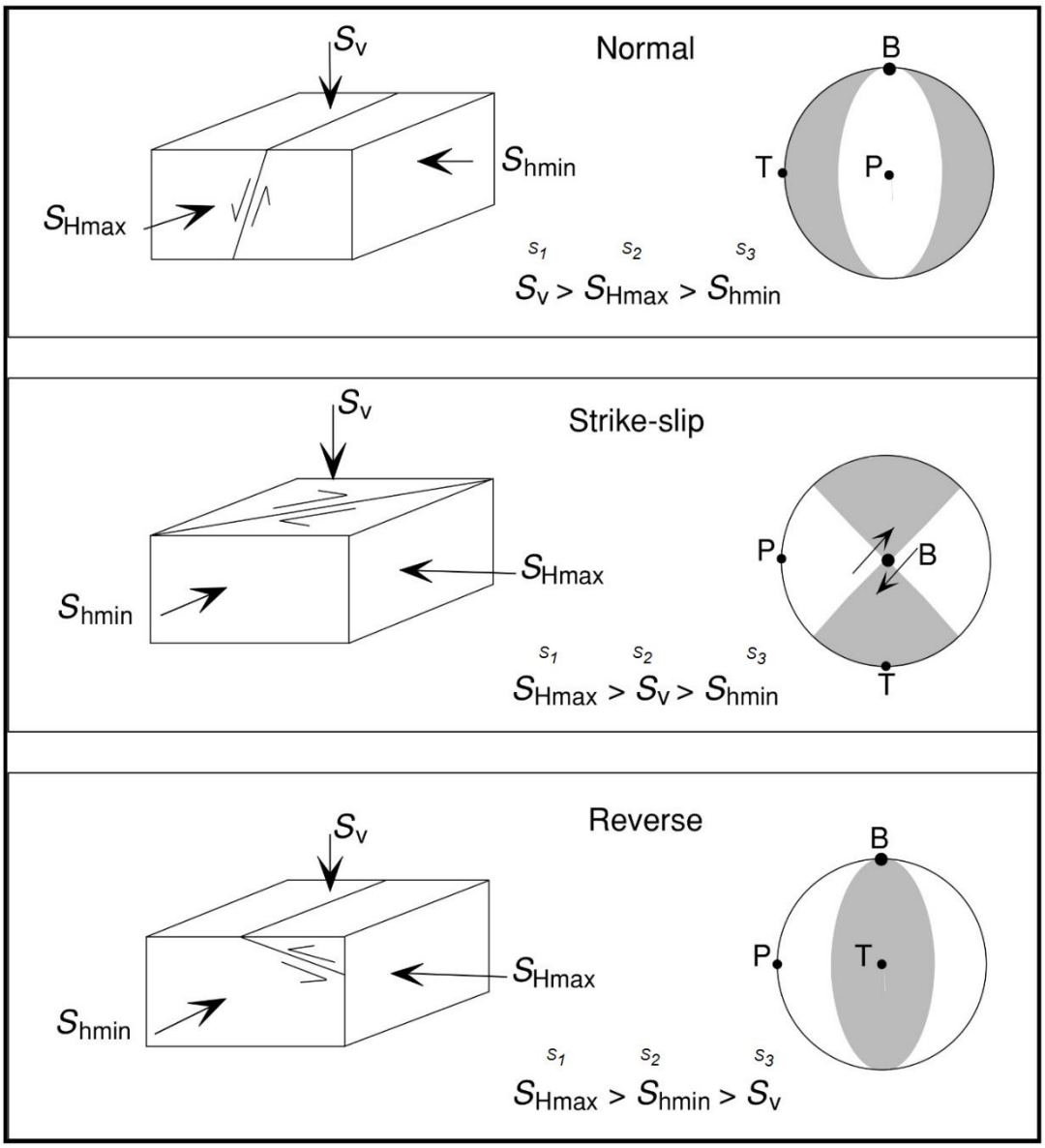

Figure 1-13: Anderson classification scheme for relative stress magnitudes in three different tectonic settings: normal; strike-slip and reverse faulting regions. Relative stress magnitudes are indicated to each fault regime. Modified from Zoback (2010).

In Equation 1-2, $\rho(z)$ is the density as function of depth, g is the gravitational acceleration, ρ_o is the mean overburden density, ρ_w the water density and z_w the water depth (Jaeger et al., 2009). Sea water has an approximate density of 1 g/cm^3 and the hydrostatic pressure increases at a rate of 10 MPa/km. Considering that most siliciclastic rocks have an average density of 2.3 g/cm^3, Equation 1-2 results in a principal stress that increases with depth at a rate of ~23 MPa/km (Zoback, 2010) as shown by Equation 1-3:

$$\sigma_v = 23z$$

Equation 1-3

1.4.1.2. The minimum and maximum horizontal stresses

Stress fields can be described in terms of the stress difference ratio (Φ), where σ_1 is the maximum stress, σ_2 the intermediate stress and σ_3 the least principal stress (Equation 1-4; Morris et al., 1996):

$$\Phi = \frac{\sigma_2 - \sigma_3}{\sigma_1 - \sigma_3}$$

Equation 1-4

When the value of Φ is known together with the ratio between the known vertical stress and either σ_{Hmax} or σ_{hmin}, Equation 1-4 can be used to calculate the minimum and maximum horizontal stress components. In most cases, however, the ratio between the vertical and horizontal stress is unknown. One manner to solve this problem is applying the Eaton (1969) equation, that considers the Earth as an elastic body and relates the horizontal stress $\sigma_{(H\ or\ h)}$ to the vertical stress σ_v and the Poisson ratio *v* as expressed in Hooke's law by Equation 1-5.

$$\sigma_{H\ or\ h} = \left(\frac{v}{1-v}\right)(\sigma_v - P_f) + P_f$$

Equation 1-5

Eaton (1969) assumed that all independent variables in Equation 1-5 were a function of the overburden properties. If an instantaneous overburden stress is applied to a poroelastic space, the rock body will experience an equal increase in horizontal stress in all directions, causing the so-called Poisson Effect. To deviate from the increase in the horizontal stress resulting from an increase in vertical stress with no lateral strain, Eaton (1969) replaced the Poisson ratio *v* by a depth-dependent empirical value. This empirical value varies from 0.25 at shallow depths (~300 m) to 0.45 at depths of 3000 m or more. Where pore fluid pressures (P_f) values are close to hydrostatic, Eaton (1969) argued that a constant Poisson ratio of 0.25 would fit well into the equation, and thus Equation 1-5 can be simplified to:

$$\sigma_{H\ or\ h} = \frac{0.25}{0.75}\sigma_v = 0.33\sigma_v$$

Equation 1-6

In extensional regimes, the principal stress is approximately horizontal and is smaller than the vertical stress. For compressional areas, the opposite is true. Equation 1-5 and Equation 1-6 are based on an idealised model for regions experiencing extension, and if they were true for every rock unit in the Earth's crust, reverse faults would not exist.

Considering all possible stress states, alternative models for estimating stress conditions when no information on horizontal stress magnitudes is available from the literature are given by Jaeger et al. (2009), Peška and Zoback (1995) and Zoback et al. (2003). The latter authors assume that one of the principal stresses is vertical, and the stress state within the crust is in frictional equilibrium, and use information on pore pressure (P_f) and the coefficient of frictional sliding (μ) on the plane of weakness. Considering that σ_1 is the maximum principal stress and σ_3 the least principal stress, the effective principal stress ratio given by Jaeger et al. (2009) is given by Equation 1-7:

$$\frac{\sigma_1 - P_f}{\sigma_3 - P_f} = (\sqrt{\mu^2 + 1} + \mu)^2$$

Equation 1-7

The coefficient of frictional sliding (μ) on the plane of weakness can range from 0.6 to 1.0, according to laboratory experiments (Byerlee, 1978). Shear tests on different types of rock indicate that shear failure is defined by a frictional coefficient of 0.85, if the normal stress on the failure plane is below 200 MPa. This indicates a crustal depth ranging from 1 to 5 km. At crustal depths between 5 and 6 km, the normal stresses imposed on the failure plane exceed 200 MPa, and a frictional coefficient of 0.6 defines the shear failure.

To predict the limiting stress magnitudes using Equation 1-7, it is necessary to use the Anderson faulting theory to determine the relationship between the principal stresses (σ_v, σ_{Hmax} or σ_{hmin}) and σ_1, σ_2 and σ_3. The maximum difference in the magnitude of the principal stresses depends on the depth, local pore pressure, and on whether we are in the presence of an extensional (Equation 1-8), strike-slip (Equation 1-9) or compressive (Equation 1-10) environment (Zoback et al., 2003), such as:

$$Normal\ faulting: \frac{\sigma_1}{\sigma_3} = \frac{\sigma_v - P_f}{\sigma_{hmin} - P_f} \leq \left(\sqrt{\mu^2 + 1} + \mu\right)^2$$

Equation 1-8

$$Strike - slip\ faulting: \frac{\sigma_1}{\sigma_3} = \frac{\sigma_{Hmax} - P_f}{\sigma_{hmin} - P_f} \leq \left(\sqrt{\mu^2 + 1} + \mu\right)^2$$

Equation 1-9

$$Reverse\ faulting: \frac{\sigma_1}{\sigma_3} = \frac{\sigma_{Hmax} - P_f}{\sigma_v - P_f} \leq \left(\sqrt{\mu^2 + 1} + \mu\right)^2$$

Equation 1-10

As stress accumulated in the crust is limited by the frictional strength of faults, it is possible to estimate the range of possible stress states at any given depth and pore pressure using stress polygons (Moos and Zoback, 1990; Zoback et al., 1987). These stress polygons combine the Coulomb Faulting Theory and the Anderson classification scheme for relative stress magnitudes for normal, strike-slip and compressive faulting regimes. Moos and Zoback (1990) illustrated the range of possible stress state for a case considering a depth of 5 km in continental crust, average density of 2600 kg/m^3, and a frictional coefficient of 0.8 (Figure 1-14).

Figure 1-14 shows vertical and horizontal lines corresponding to σ_v values that separate the fields of normal (NF), strike-slip (SS) and reverse faults (RF). The vertical line, indicating the lowest value of σ_{hmin}, is the failure boundary for normal faults, where $\sigma_1=\sigma_v$ and $\sigma_3=\sigma_{hmin}$. The horizontal line constraining the greatest value for σ_{Hmax} is the failure boundary for reverse faulting, where $\sigma_1=\sigma_{Hmax}$ and $\sigma_3=\sigma_v$. The steep line indicates the allowable stress states for strike-slip faulting, where $\sigma_1=\sigma_{Hmax}$ and $\sigma_3=\sigma_{hmin}$.

1.4.1.3. Stress inversion

Alternative methods to estimate paleostress values include the Wallace and Bott Hypothesis (Bott, 1959; Wallace, 1951); the Direct Stress Inversion (DSI) Method (Angelier, 1990); and the Numeric Dynamic Analysis (NDA, Spang, 1972; Sperner et al., 1993).

The Wallace and Bott Hypothesis uses field paleostress indicators, including fault orientations and slip directions inferred from slickensides (Bott, 1959; Wallace, 1951). The prediction of the slip direction along a plane of known orientation is possible when one assumes that slip takes place parallel to the direction of maximum shear stress.

The Direct Stress Inversion (DSI) method (Angelier, 1990) is a sophisticated version of the Wallace and Bott Hypothesis, and allows for the calculation of the shear stress on a fault when the slip direction is known. The stress tensor is calculated through a least square algorithm that minimises the sum of the angles between the slip vectors and the calculated shear stress for all faults. Limitations of this method arise from the sensitivity of the method to heterogeneities in the input data.

The Numeric Dynamic Analysis (NDA, Spang, 1972; Sperner et al., 1993) is an inversion method initially applied to calculate stress from twin lamellae in calcite crystals. In this method, the orientations of compressional (P), tensional (T) and neutral (B) axes for each fault are established together with the failure angle (Θ). The failure angle is the angle between the P-axis and the fault surface. Considering that P coincides with a positive (+1) σ_1 and T coincides with a negative σ_3 (-1), it is possible to calculate a reduced stress tensor for a set of fault slip data.

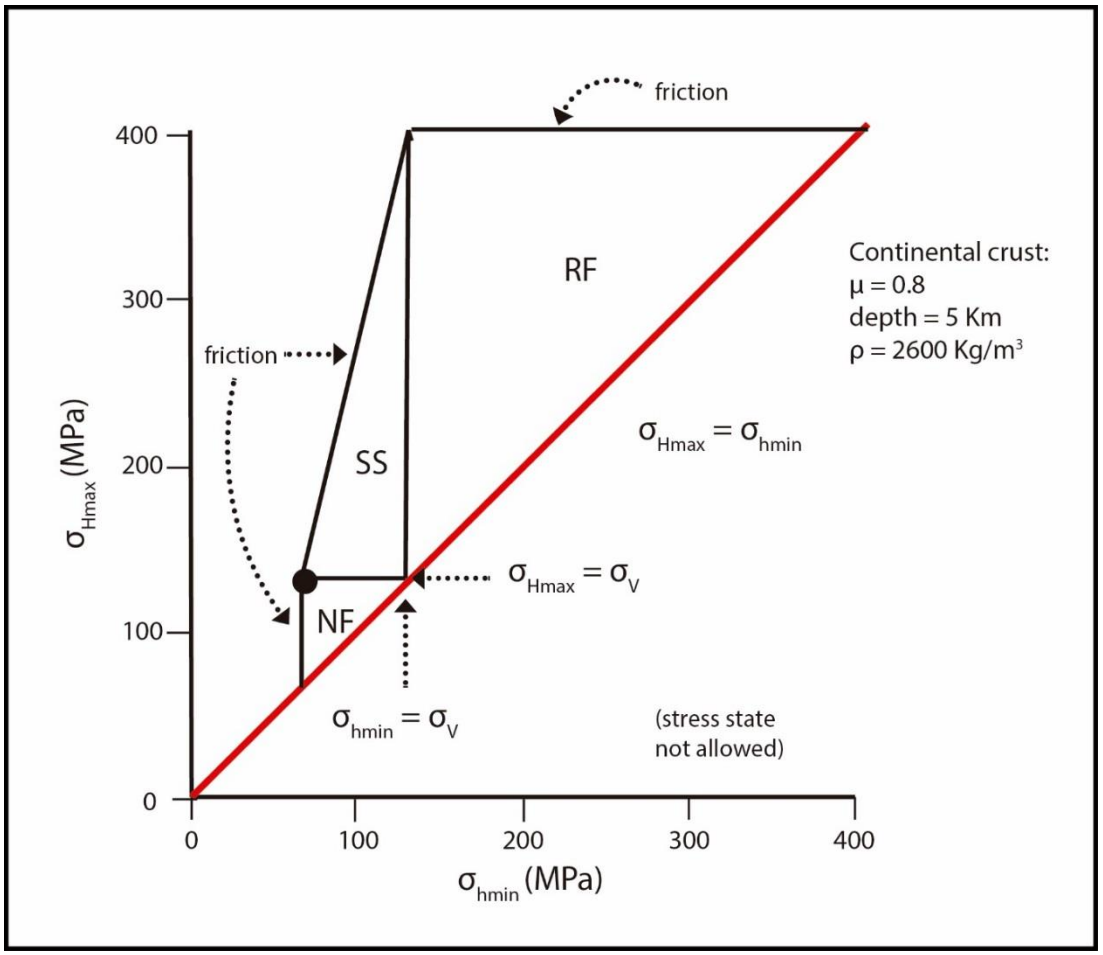

Figure 1-14: Stress polygon showing the permitted horizontal stresses σ_{Hmax} and σ_{hmin} in the continental crust. For this particular case, the continental crust is assumed to be sedimentary with an average density of 2600 kg/m^3, frictional coefficient of 0.8, a depth of 5 km and approximately hydrostatic pore pressure conditions (Pf = 0.43 σ_V). The vertical line indicating the lowest value of σ_{hmin} is the failure bound for normal faults, where $\sigma_1=\sigma_v$ and $\sigma_3=\sigma_{hmin}$. The horizontal line constraining the greatest value for σ_{Hmax} is the failure bound for reverse faulting, where $\sigma_1=\sigma_{Hmax}$ and $\sigma_3=\sigma_v$. The inclined line limits the allowable stress states for strike-slip faulting, where $\sigma_1=\sigma_{Hmax}$ and $\sigma_3=\sigma_{hmin}$. Modified from Moos and Zoback (1990).

More recently, researchers refined the inversion methods previously mentioned to provide a more reliable technique (Morris et al., 1996; McFarland et al., 2012; Sippel et al., 2010; Žalohar and Vrabec, 2007). In particular, the paleostress inversion method of McFarland et al. (2012) is based on the relationship between slip tendency values and the displacement measured for a set of faults. In this method, a fault is likely to slip when the shear stress is equal or greater than the normal stress acting on a fault surface (Morris et al., 1996). M^{c}Farland et al. (2012), nevertheless, highlight two important criteria that need to be taken into account when assessing the quality of fit for the inverted stress tensors. They are: a) a positive relationship is expected between slip tendency and displacement, and b) small displacements with large slip tendency are more plausible than large displacements with small slip tendency, i.e., surfaces may have started slipping at different points.

Slip tendency (T_s) comprises the likelihood that a fault will slip, computed as the ratio of shear (τ) to normal (σ_n') stresses on a fault plane, as shown in Equation 1-11 (Morris et al., 1996). Slip tendency has no units and is mathematically described as:

$$T_s = \frac{\tau}{\sigma_n'}$$

Equation 1-11

Slip tendency depends on the stress field and orientation of a fault surface. A fault will slip depending on the cohesive strength and the coefficient of static friction (μ) of its surface. Slip tendency can be estimated quantitatively on colour-scaled 3D maps of fault

planes, with values varying from 0 (no slip) to 1 (slip occurs) (Figure 1-15a). For a cohesionless fault surface, a slip will occur when the resolved shear stress (τ) is equal or surpasses the frictional resistance to sliding (F), as shown in Equation 1-12 (Morris et al., 1996):

$$F \leq \tau = \mu\sigma_n$$

Equation 1-12

In addition, the fluid transmissivity of faults can be modelled by estimating a Leakage Factor (L). Faults that either constitute migration conduits for fluids in the subsurface, or act as local seals, can be estimated quantitatively on colour-scaled 3D maps of fault planes (Figure 1-15b). The likelihood for a cohesive surface to transmit fluids is defined as the ratio of the fluid pressure (P_f), considered to be hydrostatic and obtained through vertical stress data (Zoback, 2010), to the difference between the effective normal stress (σ_n') and the tensile strength (T) of a fault zone (Midland Valley Move Application, 2015) such as (Equation 1-13):

$$L = \frac{P_f}{(\sigma_n' - T)}$$

Equation 1-13

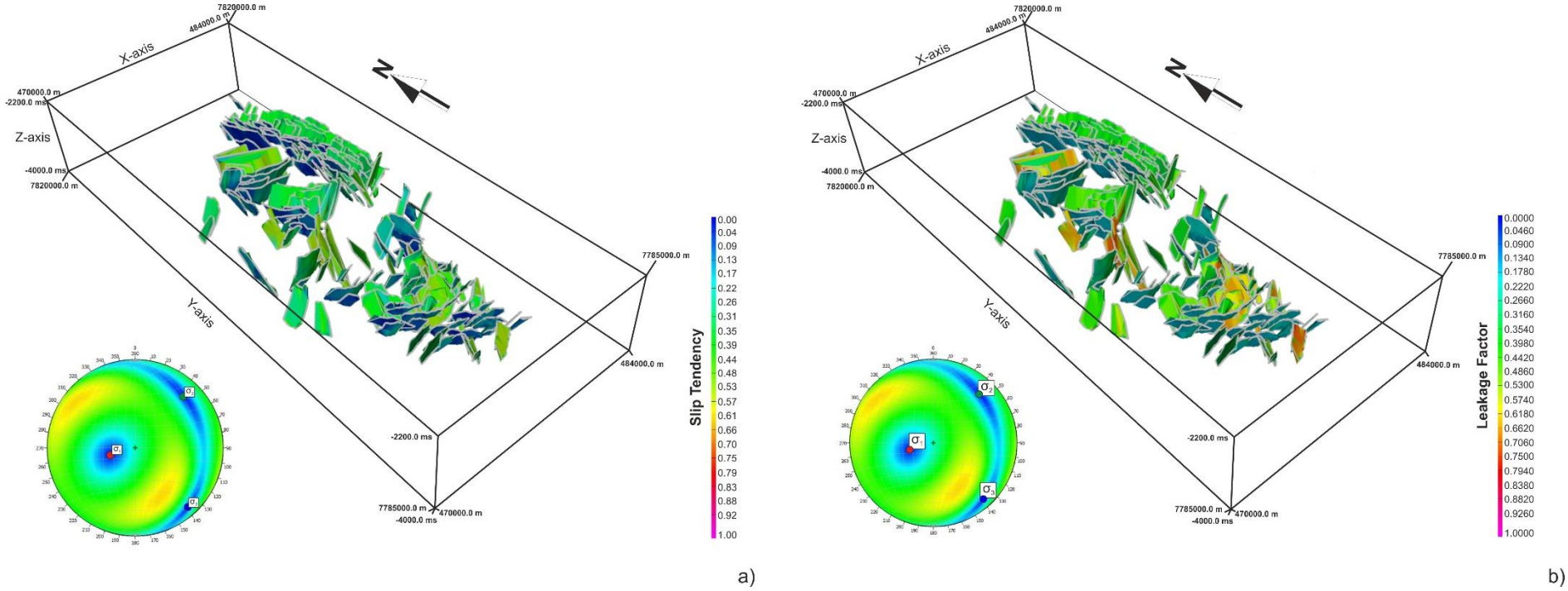

Figure 1-15: a) Slip tendency model for a group of faults based on the stress field and orientation of the fault surfaces. Slip tendency values vary from 0 to 1.0. b) Leakage factor model for a group of faults indicating the likelihood for a cohesive surface to transmit fluids.

1.5. Submarine channels

The aim of this section is to introduce submarine channels as specific depositional (and erosional) features, and to summarise the main controls on the deposition of turbidite flows in their interior. The influence of fault reactivation in the development and evolution of submarine channel systems off New Zealand is the theme of Chapter 6.

1.5.1. Definitions

Submarine channels are the primary depositional element of deep-water continental margins. Self-incised submarine channels are conduits for sediment transported by turbidite flows. They link fluvio-deltaic systems from the proximal shelf edge to distal continental slopes and oceanic basins (Babonneau et al., 2002; Clark and Pickering, 1996; Mayall et al., 2006; Mutti and Normark, 1991; Normark and Piper, 1991; Pirmez et al., 2000). Turbidite flows consist of episodic density currents that are characterised by turbulent sediment suspension within the flow. The primary controls on the type(s) and density turbidite flows include the steepness of the continental slope, sediment type and supply, basin physiography, climate and sea-level variations (Bouma, 2004; Normark et al., 1993; Posamentier and Walker, 2006).

Submarine channel systems typically extend for kilometres from the shoreline and the continental shelf, and are commonly found in distal slope areas at water depths of over 4000 m (Babonneau et al., 2002; Galloway, 1998; Normark et al., 1979; Prather, 2003). A submarine channel system is characterised, in its proximal part(s), by the presence of canyons with a deeply incised V-shaped geometry that feed the channel-levee system downslope through turbidity currents (Babonneau et al., 2002; Damuth et al., 1988; Green, 2009) (Figure 1-16). These turbidity currents tend to be confined within high-relief canyon walls. The intermediate portion of the submarine channel system comprises the upper and lower channel-levee systems. The upper channel-levee system occurs between the upper fan-valley and the middle fan-valley, and the geometry of this system may vary from an intensely eroded V-shape to a less eroded U-shape (Babonneau et al., 2002; Jegou et al., 2008; Savoye et al., 2009). The lower channel-levee system occurs between the middle fan-valley and the lower fan, and consists of a well-developed channel-levee system with a channel width of up to 1.5 km, and a channel depth of up to 150 m (Babonneau et al., 2002; Savoye et al., 2009). Channel-levee systems terminate on the basin floor with the formation of stacked, small-scale frontal splay complexes (Jegou et al., 2008; Straub et al., 2009; Wynn et al., 2002) (Figure 1-16). Submarine channels in the frontal splay complexes tend to be shallow and show low-relief levees (Normark et al., 1993; Posamentier and Walker, 2006).

The morphology of a submarine channel may range from narrow-straight to deeply incised channels with large widths, with the levees being well- to poorly-developed (Gee et al., 2007). Rates of deposition and sediment supply in a submarine channel, as well as its geometry, are primarily dependent on tectonic activity and *exogenous* parameters as climate and sea-level variations (Bouma, 2004; Kolla, 2007; Qin et al., 2017, 2016;

Shepard and Emery, 1973; Wood, 2007). Variations in channel sinuosity are also related to the flow density and velocity, seafloor topography, sediment volume and thickness (Kane et al., 2008; Kolla et al., 2007, 2001; Peakall et al., 2007).

1.5.2. Evolution of submarine channel systems

The evolution of submarine channel systems can be assessed by their infill histories, which result from the consecutive erosion, deposition, and avulsion or abandonment of the channels (Abreu et al., 2003). Highly active channel systems are characterised by the deposition of coarse-grained sediments, whereas fine-grained sediments predominate in submarine channels of relatively moderate activity (Mayall et al., 2006; Normark et al., 1993; Pirmez et al., 2000). Four main depositional facies groups are found in channel-fill deposits: basal lags, slumps and debris flows, stacked sand-rich channels and channel-levees (Deptuck et al., 2003; Mayall et al., 2006; Mayall and Stewart, 2000; McHargue et al., 2011).

Basal lags mainly comprise coarse-grained sediments such as conglomerates and sand. Mudclast conglomerates are also commonly found in the channel bases, reflecting significant erosion of the channel base (Mayall et al., 2006). Slumps and debris flows comprise a facies association common in the erosional stages of channel development and can be composed of fine-grained sediments (Mayall et al., 2006; Posamentier and Kolla, 2003). These deposits can either derive from the long-distance transport of sediment from upper-slope areas, or represent the collapse of the channel walls (Mayall et al., 2006).

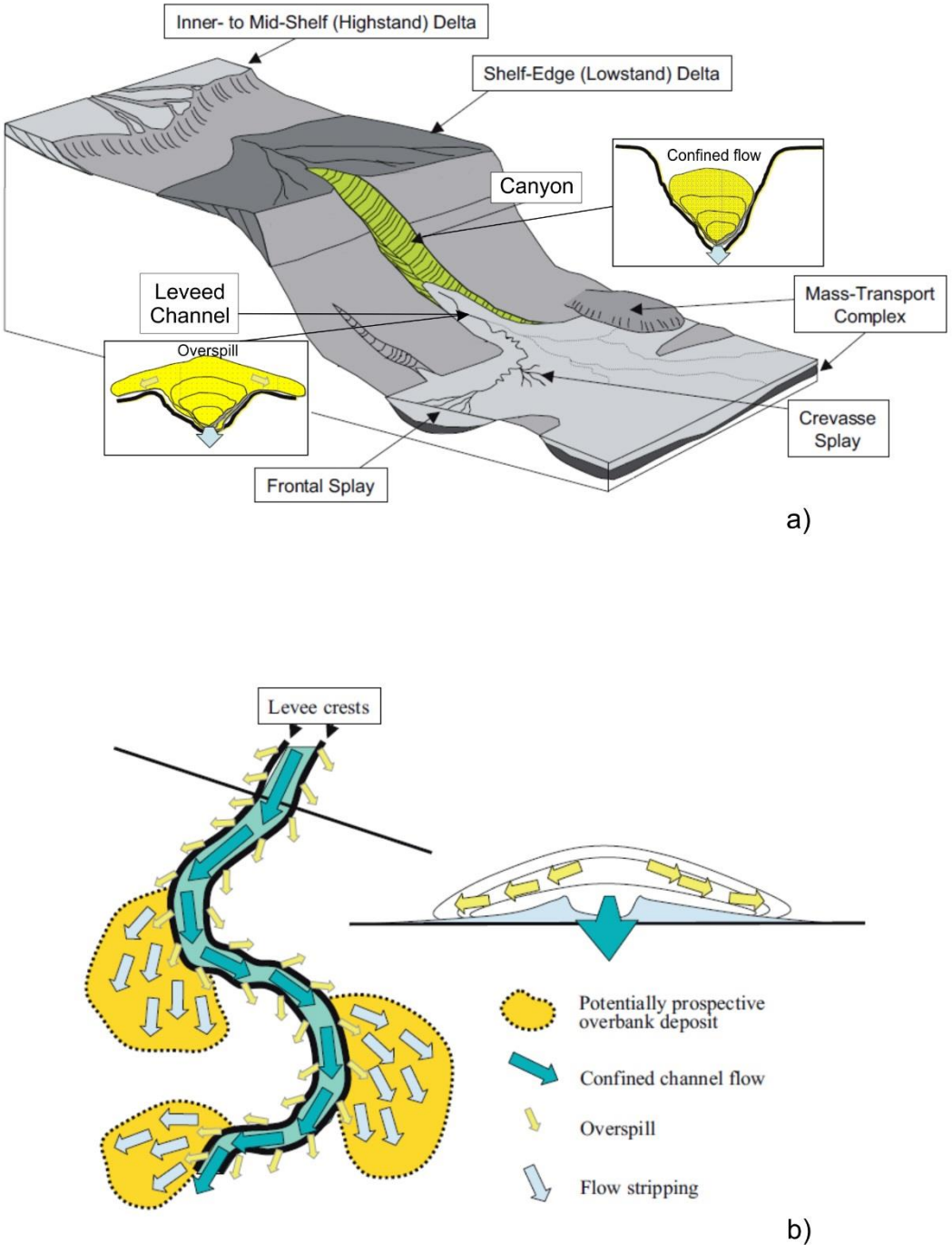

Figure 1-16: a) Diagram representing continental shelf to deep-water physiography, with the canyon in the proximal region, the levee channels in intermediate areas of the continental slope, and the frontal play in the distal basin. The flow is confined to the canyons due to the occurrence of high-relief canyon walls. A decrease in the channel walls relief is observed with distance, resulting in the formation of channel-levee systems in intermediate regions and frontal splay deposits distally. b) Cross-sectional representation of a sediment gravity flow through a leveed channel. The dark blue arrows represent the confined channel flow within the channel walls, delimited by the levee crests, whereas the light-yellow arrows represent the spill over the levee crests. The yellow circles represent prospective overbank deposits, with the blue arrows reflecting deposition in the overbank. Modified from Posamentier and Walker (2006).

Stacked sand-rich channels are the most important element of the channel infill in terms of its reservoir potential, as they comprise the vertical stacking of a series of individual channels rich in sands (Mayall et al., 2006). Finer sediments are generally deposited towards the channel margins (McHargue et al., 2011). The final stage of the channel fill is in most cases represented by the deposition of fine-grained sediments in association with the development of highly sinuous leveed channels with complex architectures (Deptuck et al., 2007; Mayall et al., 2006). In essence, the relative amount of mudstones increases in the channel fill with the progressive abandonment of submarine channels (McHargue et al., 2011).

Submarine channels are organised following specific hierarchical frameworks, in which large channel complexes are filled by channels of lesser orders. The smallest order is represented by a single channel (Abreu et al., 2003; Mayall et al., 2006; Sprague et al., 2002) (Figure 1-17). Submarine channels' hierarchical frameworks are identified based on: a) the geometry of channel fill strata, b) the vertical and lateral channel stacking patterns, and c) the relative distribution of their bounding surfaces (Abreu et al., 2003; Clark and Pickering, 1996; Mayall et al., 2006; Sprague et al., 2002). Confined channels tend to exhibit important vertical stacking, whereas sinuous and less confined channels tend to show lateral stacking (Abreu et al., 2003; Clark and Pickering, 1996). Differing stacking patterns in submarine channels can result from gradual to abrupt shifts in their position(s). Gradual shifts occur in sinuous channels during the migration of meanders, resulting in the formation of Lateral Accretion Packages (LAPs; Abreu et al., 2003).

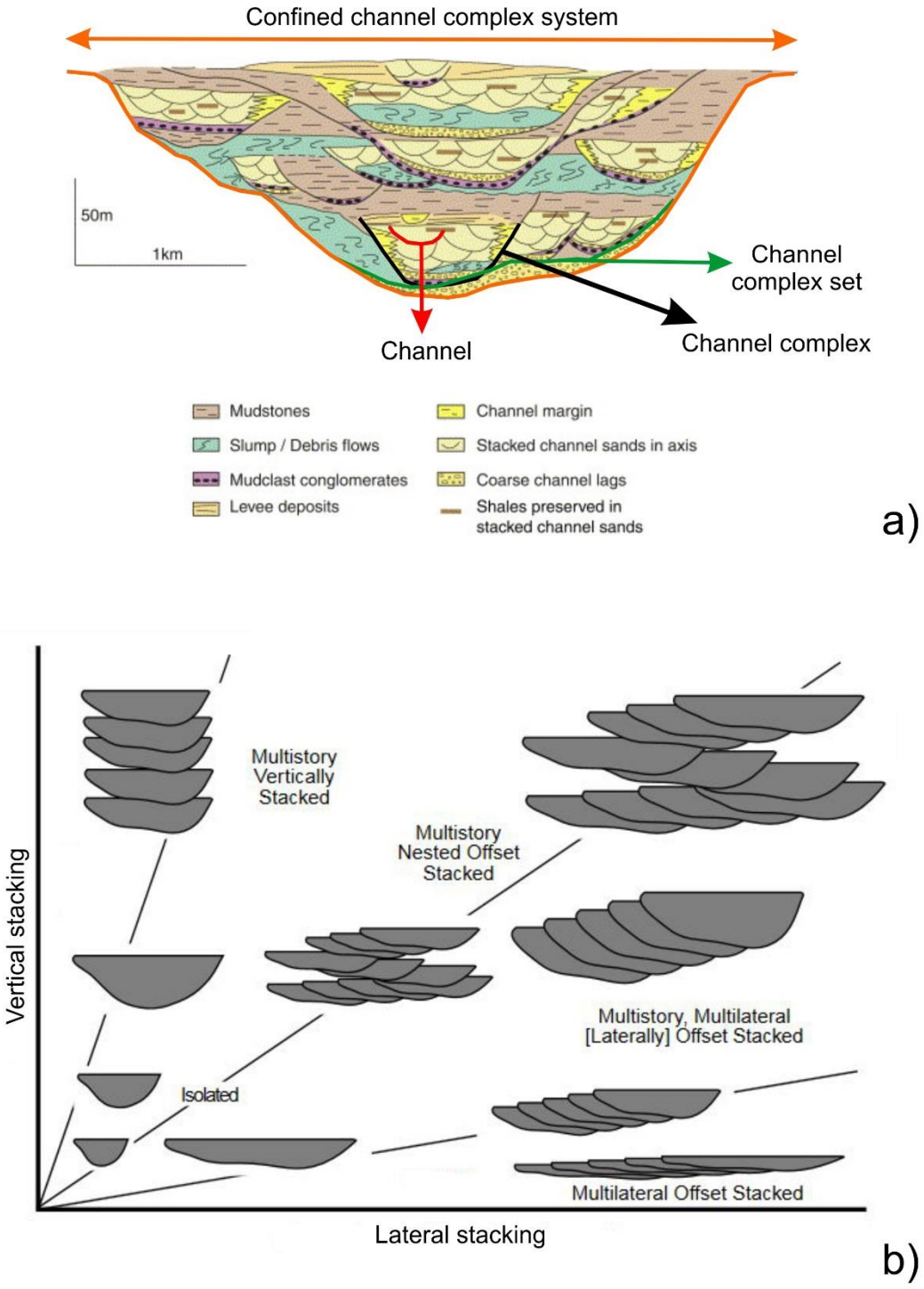

Figure 1-17: a) Hierarchical arrangement of channel complexes. The red arrow and contour represent the smallest order in the channel complex hierarchy, whereas the black arrow represent a complex comprising individual channels. The green arrow and contour represent a set of channel complexes and the orange contour and arrow represent the confined channel complex system that is formed different channel complex sets (Modified from Mayall et al., 2006). b) Channel stacking arrangement resulting from gradual and abrupt shifts in the position of the channel (Modified from Clark and Pickering, 1996).

Abrupt shifts, in contrast, are created by channel avulsion. A channel system can be dominated by either vertical or lateral stacking, although it is common the simultaneous occurrence of both patterns, with expected variations occurring along a single submarine channel (Abreu et al., 2003; Mayall and Stewart, 2000; Qin et al., 2016, 2017).

1.6. Reservoir compartmentalisation

The reservoir is one of the main elements of a petroleum system, consisting of rocks that are able to receive, accommodate and transfer fluids. It constitutes the principal target of hydrocarbon exploration (Biddle and Wielchowsky, 1994; Morse, 1994; North, 1985). The properties and external geometry of a reservoir rock are controlled by the depositional environment, structure and diagenesis (Ainsworth, 2010; Bjørlykke, 2014). The processes occurring within the depositional environment are reflected on the compositional and textural properties of sedimentary rocks and, consequently, on their porosity and permeability, which are the main factors considered during the evaluation of the reservoir potential (Ainsworth, 2006, 2005; Clark et al., 1996; Ehrenberg and Nadeau, 2005). The porosity controls the capacity for storing fluid, whereas permeability controls the ability of the reservoir rock to transmit fluids (Slatt, 2006).

The porosity and permeability of reservoir-prone lithologies are affected by compaction and diagenetic processes, which are capable to modify the original textures of siliciclastic and carbonate rocks (Bjørlykke, 2014; Slatt, 2006). The quality of the reservoir can be either enhanced or reduced depending on the degree of alteration of its

original components, as well as on the influence of other factors such as the precipitation of clay in pore spaces (Allen and Allen, 2013; Slatt, 2006).

Reservoirs are usually compartmentalised, regardless of their depositional environment (Slatt, 2006). The complexity of a reservoir within the sedimentary basin is enhanced by the occurrence of a network of compartments isolated by seal units (Fox and Bowman, 2010; Jolley et al., 2010; Larue and Hovadik, 2006). Compartmentalisation in sedimentary basins is generally recognised through the detection of isolated underpressured or overpressured compartments on well data (Finkbeiner et al., 2001; Hao et al., 2015; Webster et al., 2011). Reservoir complexity can also be assessed by differences in the chemical fingerprints of different compartments (Barclay et al., 2000; Bhullar et al., 1998). While borehole and geochemical data often provide insights into the compartmentalisation of reservoirs, the use of 2D and 3D seismic data can provide a basin-scale overview of stratigraphic and structural compartments (Leveille et al., 1997; McKie et al., 2010; Milkov et al., 2007).

Compartments are structural, stratigraphic or diagenetic boundaries that can occur at variable scales and constitute barriers or baffles to fluid flow. Hence, they compromise the connectivity of strata within a reservoir (Ainsworth, 2010; Bradley and Powley, 1994; Jolley et al., 2010; Knipe et al., 1998; Larue and Hovadik, 2006). A mixed compartment is commonly found in modern reservoirs and comprises two or three seal boundaries occurring concomitantly (Ainsworth, 2010).

Compartments can also be classified in terms of their sealing potential and fluid mobility (Ainsworth, 2010, 2005; Bradley and Powley, 1994; Jolley et al., 2010; Lee and Deming, 2002) (Figure 1-18). A static compartment is completely sealed and does not

allow fluid transference between adjacent strata, whereas a dynamic compartment allows a slow fluid mobility due to the presence of low permeability baffles (Lee and Deming, 2002). A closed compartment has barriers or baffles on all four directions, whereas an open compartment has barriers on three directions and a permeable feature in one direction. Compartmentalisation can also be vertical or lateral according to the position of continuous impermeable barrier(s) (Ainsworth, 2010, 2005; Jolley et al., 2010; Knipe et al., 1998; Larue and Hovadik, 2006).

1.6.1. Stratigraphic compartmentalisation

Stratigraphic compartmentalisation is related to the architecture of depositional systems, a characteristic controlled by factors such as accommodation space, sedimentation rate, and sea-level changes (Ainsworth, 2010; Clark et al., 1996) (Figure 1-18b). High accommodation-sedimentation ratios during sea-level rise will create vertical compartments, whereas low accommodation-sedimentation ratios will create both vertical and lateral compartments (Ainsworth, 2010). For confined reservoir architectures such as those of channel systems, the primary control on compartmentalisation is the degree of evolution of the channel (Labourdette et al., 2006; Larue and Hovadik, 2006; Mayall et al., 2006). In these channel systems, the occurrence of shale drapes can compromise the connectivity between vertically stacked sand bodies (Slatt, 2006), whereas recurrent erosive flows can enhance vertical connectivity (Labourdette et al., 2006). Channel-levee systems have partially unconfined architectures,

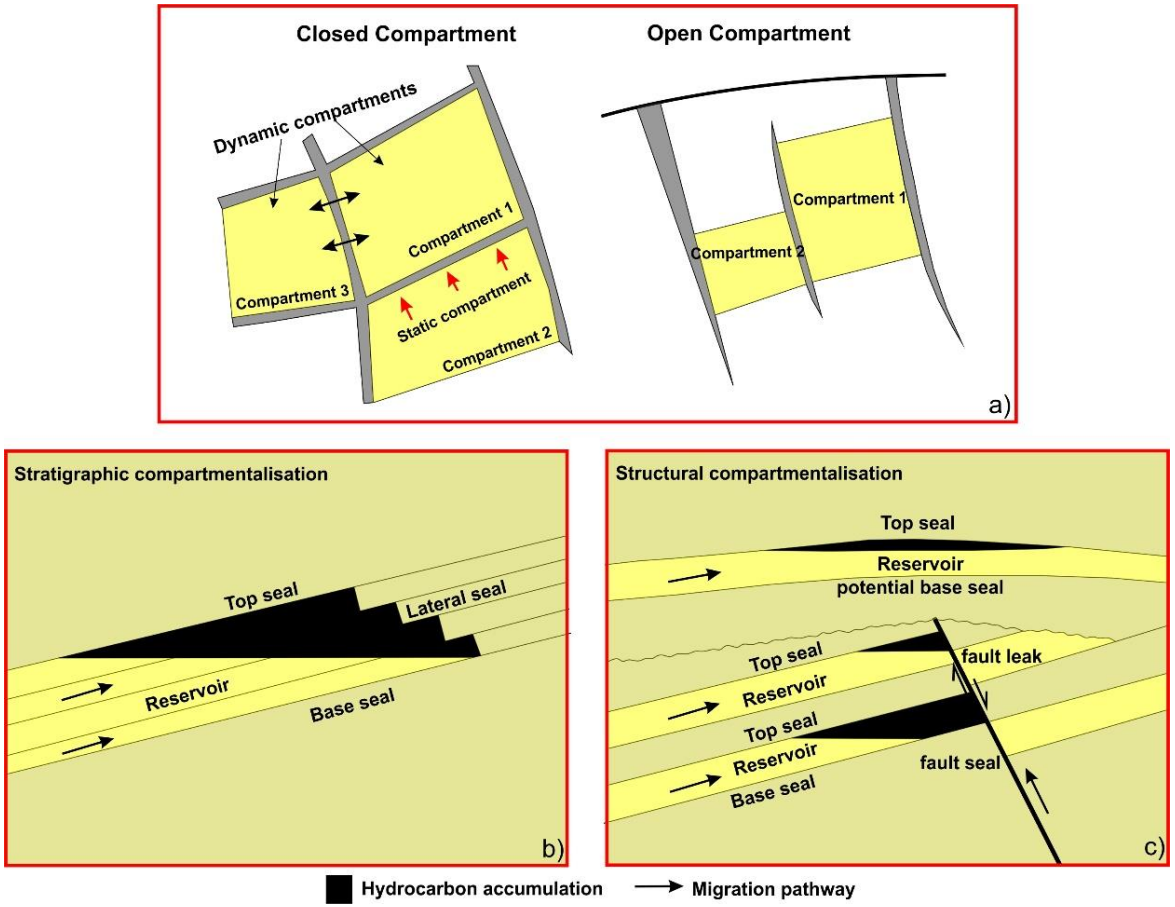

Figure 1-18: a) Representation of closed and open compartments, and the key concepts of static and dynamic compartments within a reservoir. Figure modified from Gamboa (2011). b) Representation of stratigraphic compartmentalisation resulting in hydrocarbon accumulations sealed by basal, lateral and top seals. c) Representation of structural compartmentalisation showing a fault acting both as a seal and main fluid pathway. The black areas represent hydrocarbon accumulations and the arrows indicate fluid migration pathways. Figures b and c modified from Biddle and Wielchowsky (1994).

with reservoir-prone lithologies occurring both in the channelised portions and in overbank strata, thus increasing the complexity of stratigraphic compartments.

1.6.2. Structural compartmentalisation

Structural compartments result from syn- to post-depositional deformation of reservoirs units, and result in the creation of structures such as folds and faults (Biddle and Wielchowsky, 1994) (Figure 1-18c). The presence of these structures affect the accumulation and flow of fluid in different forms (Ainsworth, 2006). Structural compartmentalisation dominated by folds generally derives from tectonic deformation of depositional features (strata). However, primary depositional effects such as gravity-induced slumping and sediment compaction can also result in folded compartments (Biddle and Wielchowsky, 1994; Clark et al., 1996). The accumulation of fluids in folded compartments is generally associated with the geometry of the deformed strata, as fluids tend to migrate towards the fold crests (Clark et al., 1996; Ingram et al., 2004).

The complexity of reservoir compartments increases with the presence of faults and fracture arrays (Jolley et al., 2010, 2007; Knipe et al., 1998). In parallel, the degree of compartmentalisation of a reservoir depends on factors such as the size and shape of compartments, reflected by a) distinct fault densities, and b) the occurrence of different fault families. It is thus important to investigate the geometry of different fault arrays to determine the impact of these structures in the location of hydrocarbon accumulations within a sedimentary basin, as well as to assess the existence of static

or dynamic flow connectivity between adjacent compartments (Knipe et al., 1998). Faults result from the displacement of a surface due to compressive or extensional stresses and can either affect the viability of a reservoir by enhancing the connectivity of individual compartments, or act as seals to fluid flow within reservoir strata (Caine et al., 1996; Jolley et al., 2010; Knipe et al., 1998). A sealed fault, i.e. fault with low porosity and permeability, will act as a barrier or baffle within more permeable reservoir units, and will compromise fluid flow between adjacent compartments (Figure 1-18) (Biddle and Wielchowsky, 1994; Jolley et al., 2007; Knipe et al., 1997). Conversely, a non-sealed fault will result in a relative increase in the connectivity and constitute a conduit for fluid flow.

The occurrence of lithologic units overlying salt structures increases the complexity of hydrocarbon reservoirs (Ainsworth, 2006; Clausen et al., 2014; Stewart, 2006). The instability of salt causes sedimentary basins rich in salt to be more susceptible to deformation during regional extensional or shortening events when compared to basins lacking salt (Hudec and Jackson, 2007; Jackson et al., 1994a; Vendeville, 2002). Halokinesis is an important factor in reservoir configuration not only because the displacement of salt leads to the development of faults, but also because faults may cross-cut reservoir intervals to develop major structural compartments or act as fluid pathways (Alves et al., 2009; Carruthers et al., 2013; Gamboa et al., 2010; Guerra and Underhill, 2012; Jackson et al., 1994b; Schultz-Ela et al., 1993; Stewart, 2006; Talbot et al., 1991).

1.6.3. Diagenetic compartmentalisation

Diagenetic processes such as compaction and cementation affect the internal properties of rocks such as porosity and permeability and, consequently, their quality as reservoirs (Slatt, 2006). Diagenetic reactions occurring within a sedimentary basin can be either localised or basin-wide. Localised reactions will affect the porosity and permeability of the rocks and consequently the capacity of retaining fluid flow at variable scales, whereas basin-wide diagenesis will have a greater impact on fluid flow paths and areas of potential fluid accumulation (Clark et al., 1996).

Mechanical compaction is chiefly controlled by the effective stress imposed on a volume of rock and occurs when the load of a sedimentary succession causes the subjacent units to rearrange their grain contacts, leading to a reduction in pore space (Gutierrez and Wangen, 2005). The degree of compaction in sedimentary rocks varies as a function of their composition and burial depth. Ductile rocks such as mudstones and shales are highly compacted due to the sudden removal of porosity, whereas sands and sandstones are more resistant (Bjørlykke and Høeg, 1997). The breakdown of rock grains and minerals during mechanical compaction can provide a trigger to chemical diagenesis (Slatt, 2006). Cementation is a diagenetic process resulting from mineral precipitation in pore spaces, reducing or eliminating porosity and thus reducing the fluid flow capacity. In turn, the dissolution of unstable cements such as carbonates or feldspars can result in the creation of secondary porosity and permeability (Slatt, 2006).

1.7. Thesis layout

This thesis is divided into eight chapters. The present chapter (Chapter 1) contains an introduction to the thesis, including its rationale and aims. Chapter 1 also presents a literature review of the key concepts covered in this thesis. The literature review is followed by the Geological Settings (Chapter 2) of the three areas covered in this thesis. The order of appearance of the study areas in Chapter 2 reflects the order of the remaining data-analysis chapters. Chapter 3 presents the Methods used in the thesis, and includes a description of 3D seismic acquisition methods, the parameters of the datasets used in this research, and the way(s) they were interpreted. Quantitative methods used in structural analyses are also described in Chapter 3. Chapter 4 concludes on the geometry and kinematics of the Samson Dome, Barents Sea, and the observed increase in the sealing potential of faults with depth. Chapter 5 evaluates the timing of formation of faults adjacent to salt structures in the Espírito Santo Basin, Brazil, and the importance of fault corridors to fluid flow in this same basin. Chapter 6 investigates the effect of a reactivated fault zone in the evolution of a submarine channel system in the Taranaki Basin, New Zealand. Chapter 7 provides a summary of major findings and a discussion of the wider results in this thesis. Final conclusions are presented in Chapter 8.

2. Geological setting of the studied areas

2.1. Introduction

The aim of this chapter is to review the geological setting of the three study areas. The main topics to be covered here include a description of the main characteristics of each of the three sedimentary basins, and their tectono-stratigraphic evolutions. In this chapter, the order of appearance of key sedimentary basins follows the order of the core result chapters in the thesis. The geological setting of the Barents Sea comprises an overview of the in-situ stress conditions in that same region. The geological setting of the Espírito Santo Basin includes a detailed review of the stratigraphy of this basin. The tectonic evolution of the Taranaki Basin is followed by a description of the Cape Egmont Fault Zone and the Miocene – Quaternary stratigraphy for the Northern Taranaki Graben.

2.2. Barents Sea, Norway

The Barents Sea is an epicontinental sea located in northernmost Europe, with an area of ~1.3 million km^2 and an average water depth of 300 m (Doré, 1995). The northern limits of the Barents Sea are the Svalbard Archipelago and Franz Josef's Land, and its eastern boundary is Novaya Zemlya (Figure 2-1a). To the south, the Barents Sea is bounded by the Norwegian Mainland and the Kola Peninsula (Barrère et al., 2009; Doré, 1995; Faleide et al., 1993, 1984; Henriksen et al., 2011b; Vorren et al., 1991) (Figure 2-1a).

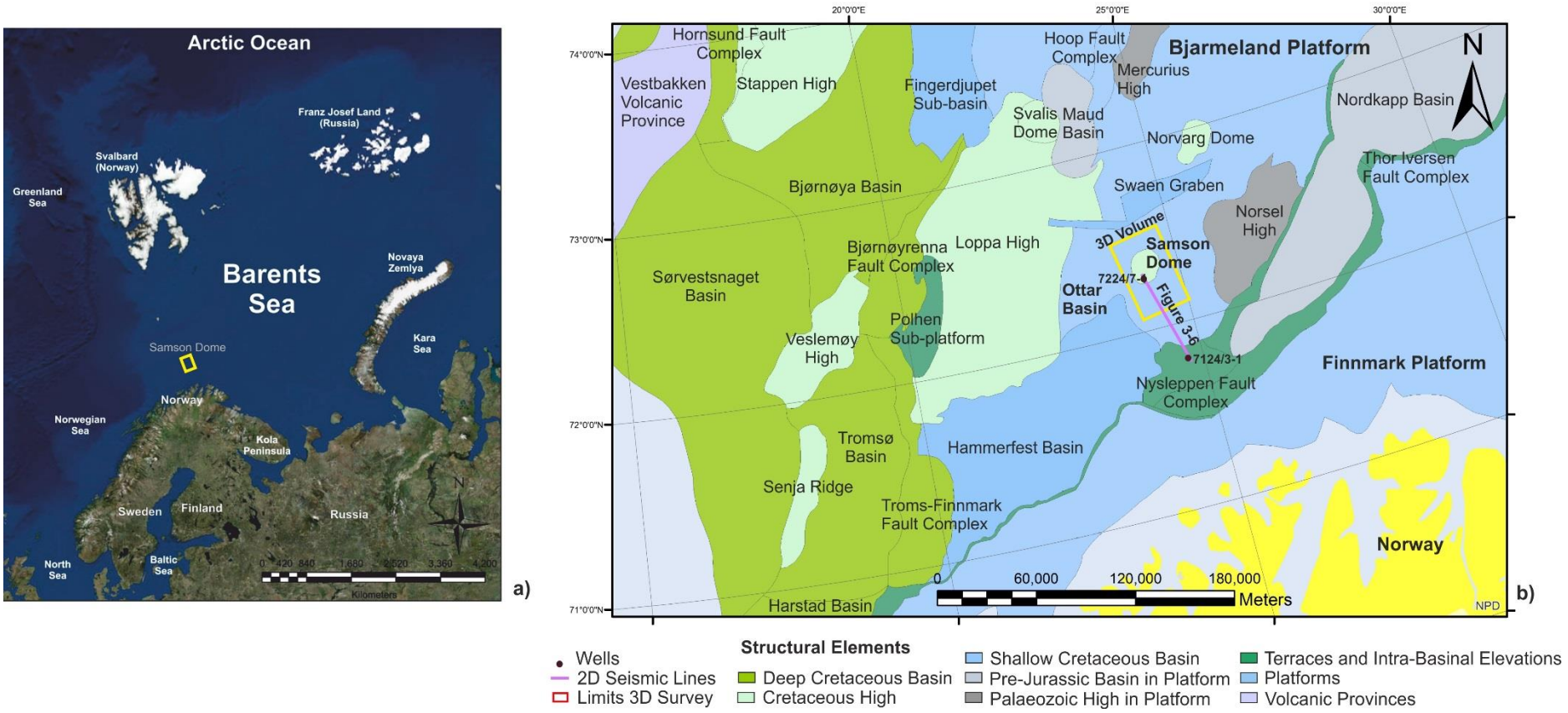

Figure 2-1: a) Location map of the Barents Sea and its main structural boundaries. The Barents Sea is limited to the west by the Norwegian Sea, to the north by the Svalbard Archipelago (Norway) and Franz Josef's Land (Russia), to the east by Novaya Zemlya and to the south by the Norwegian Mainland and the Kola Peninsula. b) Detailed location map of the Barents Sea highlighting main structures at a regional scale. The location of the 3D seismic cube and 2D seismic line used in this work are shown on the map. The map in b) was modified after the Norwegian Petroleum Directorate FactMaps (2015).

The Barents Sea comprises several platforms, structural highs and basins, formed at different stages during the Late Paleozoic and Mesozoic (Doré, 1991; Gabrielsen, 1984; Nøttvedt et al., 1993; Ritzmann and Faleide, 2007). One of these basins, the Ottar Basin, comprises a 170 km-long and 50-80 km-wide depocentre developed during Late Devonian–Middle Carboniferous rifting (Breivik et al., 1995; Dengo and Røssland, 2013; Gudlaugsson et al., 1998; Jensen and Sørensen, 1992). The Ottar Basin is bounded by the Norsel High to the southeast and by the Hammerfest Basin to the southwest (Figure 2-1b). Its northwest limit coincides with the Loppa High, the Maud Basin, and the Mercurius High, whereas the Ottar Basin is bounded by the Nordkapp Basin to the northeast (Figure 2-1b). The Ottar Basin comprises the Swaen Graben and two salt structures, the Norvarg and Samson Domes (Gudlaugsson et al., 1998).

In map view, the Samson Dome has been described as having an elliptic to circular geometry, with a diameter of ~18 km. It exhibits a radial fault pattern generated by extension in post-salt Mesozoic sequences (Gabrielsen et al., 1990), and was later reactivated during the Late Cretaceous and Early Tertiary (Breivik et al., 1995). Data in Gabrielsen et al. (1990) and Breivik et al. (1995) reveal a lenticular evaporite body at depth, with a maximum thickness of 3.5 km and an estimated volume of 500-600 km^3 (Figure 2-2). Breivik et al. (1995) suggested that the primary reason for the very moderate salt movement recorded above the Samson Dome was the presence of thick and competent overburden rocks (i.e., Lower Permian carbonates and Upper Permian silicified strata) above Upper Paleozoic evaporites.

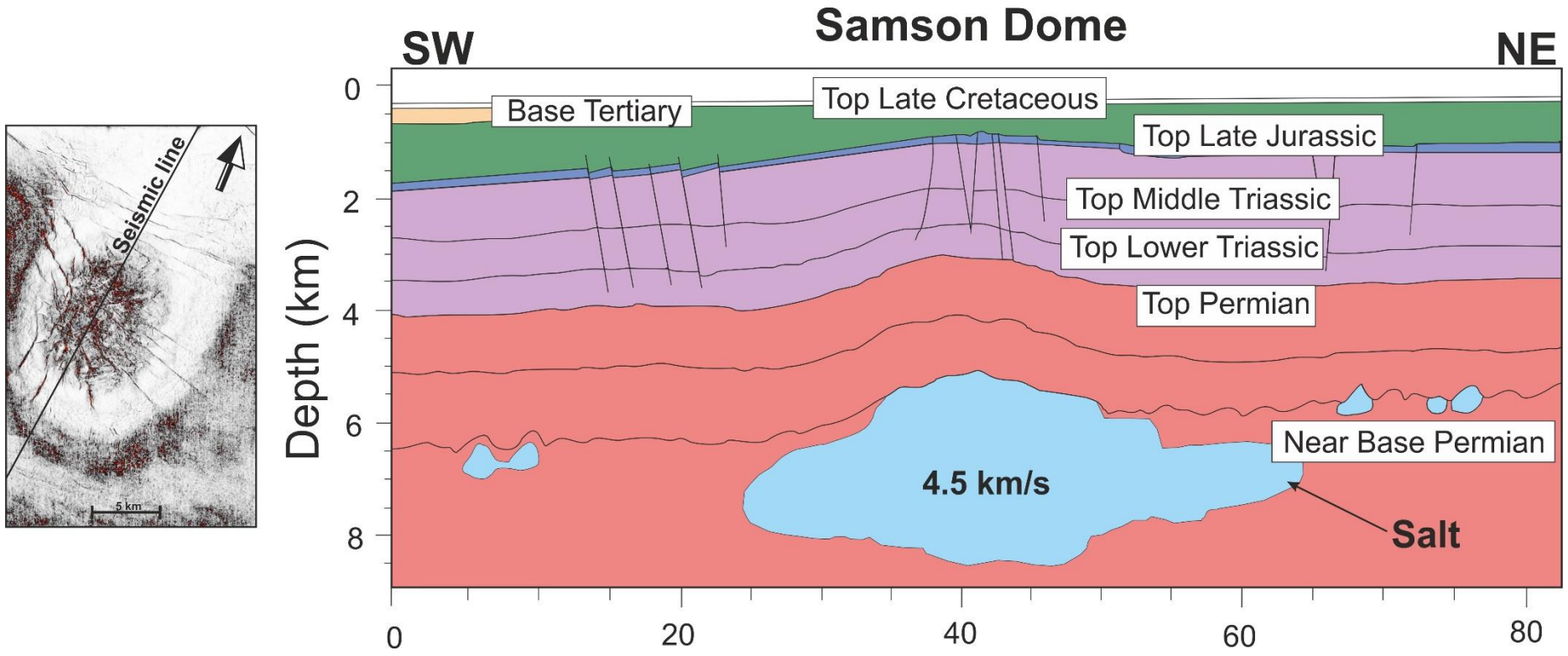

Figure 2-2: Interpretation of a SW-NE seismic line across the Samson Dome showing the bottom depth of this salt anticline at a depth of ~8.5 km. This salt structure has been interpreted as a salt body with a maximum thickness of 3.5 km and an estimated volume of 500-600 km^3. The estimated p-wave velocity of the salt body is ~4.5 km/s. Figure modified from Breivik et al. (1995).

2.2.1. Tectonostratigraphic evolution of the Barents Sea

The Caledonian Orogeny deformed the crystalline basement of the Barents Sea from Late Silurian to Early Devonian (Faleide et al., 1984; Gernigon and Brönner, 2012; Gudlaugsson et al., 1998). Compression during the Caledonian Orogeny was followed by rifting in the Mesozoic, and continental breakup of the Northern Atlantic Sea between Norway and Greenland during the Cenozoic (Faleide et al., 2008; Gabrielsen et al., 1990; Gee et al., 2008; Gernigon et al., 2014; Glørstad-Clark et al., 2010). The Caledonian Orogeny played a significant role in influencing the location and orientation of sedimentary basins in the Barents Sea (Breivik et al., 2002; Faleide et al., 1993; Gernigon and Brönner, 2012; Gudlaugsson et al., 1998; Ritzmann and Faleide, 2007; Worsley, 2008). Extension, rifting and plate separation marked the early stages of the Caledonide Orogen in Scandinavia during the breakup of Rodinia in the Neoproterozoic (Cocks and Torsvik, 2005; Soper et al., 1992; Torsvik et al., 1996).

The development of the Caledonide Orogen began with subduction of the Iapetus Ocean margins from Late Cambrian to the Early Ordovician (Finnmarkian event; Roberts, 2003). Orogenesis continued during the Early Ordovician, and recorded the obduction of ophiolites in Central Norway (Trondheim event). The Taconian event, dated as Middle to Late Ordovician, marked the beginning of anticlockwise rotation of Baltica away from Siberia. This was followed by the Scandian event, which witnessed the closure of the Iapetus Ocean in the Middle Silurian to Early Devonian

(Faleide et al., 1984; Gee et al., 2008; Gudlaugsson et al., 1998; Ritzmann and Faleide, 2007; Roberts, 2003; Soper et al., 1992).

From Early to Middle Devonian, gravitational collapse of the Caledonian Mountain Chain resulted in widespread extension in the western Barents Sea (Faleide et al., 1996; Roberts, 2003; Worsley, 2008). Despite the lack of information regarding the development of sedimentary basins at this stage (Gabrielsen et al., 1990; Gudlaugsson et al., 1998), the western Barents Sea suggestively acted as a transfer zone linking Norway and Greenland during this first episode of Atlantic rifting (Doré, 1991; Gudlaugsson et al., 1998).

From Late Devonian to Mid Carboniferous, the western Barents Sea recorded multiple episodes of extension, which led to the development of a complex system of rift basins limited by structural highs (Dengo and Røssland, 2013; Faleide et al., 1984; Gabrielsen et al., 1990; Nøttvedt et al., 1993). In particular, Middle Carboniferous rifting was accompanied by important strike-slip tectonics, with several NE-trending basins being developed above NE-trending horsts and grabens that followed the structural fabric of the Caledonian basement (Gudlaugsson et al., 1998; Worsley, 2008). Large-scale basins, such as the Nordkapp, Bjørnøya, Tromsø, Hammerfest, Maud and Ottar Basins, were generated at this time (Figure 2-1) (Dengo and Røssland, 2013; Faleide et al., 1993; Gabrielsen et al., 1990; Gudlaugsson et al., 1998).

An expansion in the sea area off northern Norway occurred in the Late Carboniferous, but tectonic activity diminished soon after until the Early Permian. In such a setting, the deposition of evaporites marks the end of rifting and the beginning of thermal subsidence in the region (Dengo and Røssland, 2013). As the Barents Sea

moved further north during the Middle Permian, within a semi-arid climatic belt, it favoured the development of a post-rift carbonate platform dominated by warm-water limestones and evaporites (Elvebakk et al., 2002; Faleide et al., 1984; Gudlaugsson et al., 1998; Johansen et al., 1993; Stemmerik, 2000). The closure of the Uralian Sea during the Late Permian, however, affected the entire Barents Shelf. This increased subsidence rates and changed depositional stacking patterns from carbonates and evaporites to clastic, organoclastic and cherty sediments (Alves, 2016; Johansen et al., 1993; Worsley, 2008). Late Permian subsidence, together with the marked influence of extensional events in the western Barents Sea, resulted in the full establishment of the area currently named as *Bjarmeland Platform* (Breivik et al., 1995).

During the Mesozoic, the Barents Sea was affected on its northern and western borders by the break-up of the Laurasian supercontinent, with subsequent opening of the Eurasian Basin and Norwegian-Greenland Sea (Faleide et al., 1993). The climate became humid, resulting in the deposition of large amounts of non-marine, nearshore and shallow-marine sediments derived from the Uralian Orogen (Glørstad-Clark et al., 2010; Johansen et al., 1993). Strata in the western Barents Sea were, at this time, deposited during successive episodes of transgression and regression in sea-level (Smelror et al., 2009).

Tectonic activity in the western Barents Sea was relatively moderate during the Triassic, and the region became a shallow-water siliciclastic shelf at this time (Klausen et al., 2015; Klausen and Mørk, 2014; Mørk and Elvebakk, 1999). The first salt movements in the Ottar Basin took place from Middle Triassic to Late Triassic, resulting from gravitational instability generated by: a) loading gradients imposed by

a NW-prograding shelf, and b) the reactivation of basement faults (Breivik et al., 1995). Passive margin subsidence, active faulting along the western margin of the Barents Sea (including the Bjarmeland Platform), and variations in sediment supply affected the relationship between sedimentary infill and accommodation space during the Triassic (Gabrielsen et al., 1990; Glørstad-Clark et al., 2010; Klausen et al., 2015; Smelror et al., 2009). During the Middle Triassic, the western Barents Sea records the development of a marine shelf where organic-rich mudstone accumulated in restricted anoxic conditions (Smelror et al., 2009). In the Late Triassic, another extensional event took place in the Barents Sea, resulting in the formation of an extensive coastal plain (Faleide et al., 1984; Glørstad-Clark et al., 2010; Klausen and Mørk, 2014; Smelror et al., 2009).

The Jurassic was marked by a major rifting episode. Early Jurassic deposition in the Ottar Basin started with sandstones and subordinated shales (Tubåen Formation) in a high-energy (transitional) marine setting (Dalland et al., 1988). Depositional environments in the basin evolved from tidal flats to floodplains in the Pliensbachian, as indicated by the deposition of interbedded siltstones, sandstones, shales and claystones in the Nordmela Formation (Figure 2-3). During the Middle Jurassic, rifting affected the entire North Atlantic opening a large marine gateway from the North Sea (and further south) to the study area. This event is recorded by the deposition of well-sorted and mineralogically mature sandstones in the Stø Formation (Faleide et al., 2008). The Middle and Late Jurassic were dominated by regional extension and development of relatively minor strike-slip fault systems. Block faulting occurred in the Middle Jurassic and increased during the Late Jurassic and Early Cretaceous,

culminating in the formation of large basins bounded by salt structures and major structural highs (Gabrielsen et al., 1990) (Figure 2-3).

The Cretaceous started with intense rifting and associated tectonic subsidence in the western Barents Sea, whereas its eastern part remained relatively stable (Faleide et al., 1993). Rifting resulted in the (structural) decoupling of the Harstad, Tromsø and Bjørnøya basins from the remainder of the Barents Sea (Smelror et al., 2009). In the Late Cretaceous, rifting in the North Atlantic led to the reactivation of normal faults on the western margin, together with local compression and uplift on the Svalbard Platform (Faleide et al., 1993, 1984; Gabrielsen et al., 1990). Tectonic subsidence, however, continued in other parts of the Barents Sea to the east of the Svalbard Platform. The sedimentary infill came both from source areas in the eastern and the northern Barents Sea, which were uplifted at this time (Johansen et al., 1993; Smelror et al., 2009).

At the Cretaceous-Paleogene boundary, extension between Norway and Greenland was replaced by strike-slip deformation, a change resulting in the formation of the Sørvestsnaget Basin (Breivik et al., 1998) (Figure 2-1). The final stage of lithospheric breakup between Norway and Greenland occurred around the Paleocene-Eocene boundary, with subsequent opening of the Norwegian-Greenland Sea at 55-54 Ma (Faleide et al., 2008). The opening of the Norwegian-Greenland Sea resulted in the salt diapirism through normal faults in the Sørvestsnaget Basin (Perez-Garcia et al., 2013). During the Eocene, deep-marine conditions predominated in the western Barents Sea, as recorded by the deposition of sands from submarine fans (Safronova et al., 2014). From the Middle Miocene to the present day, the Barents Sea was uplifted

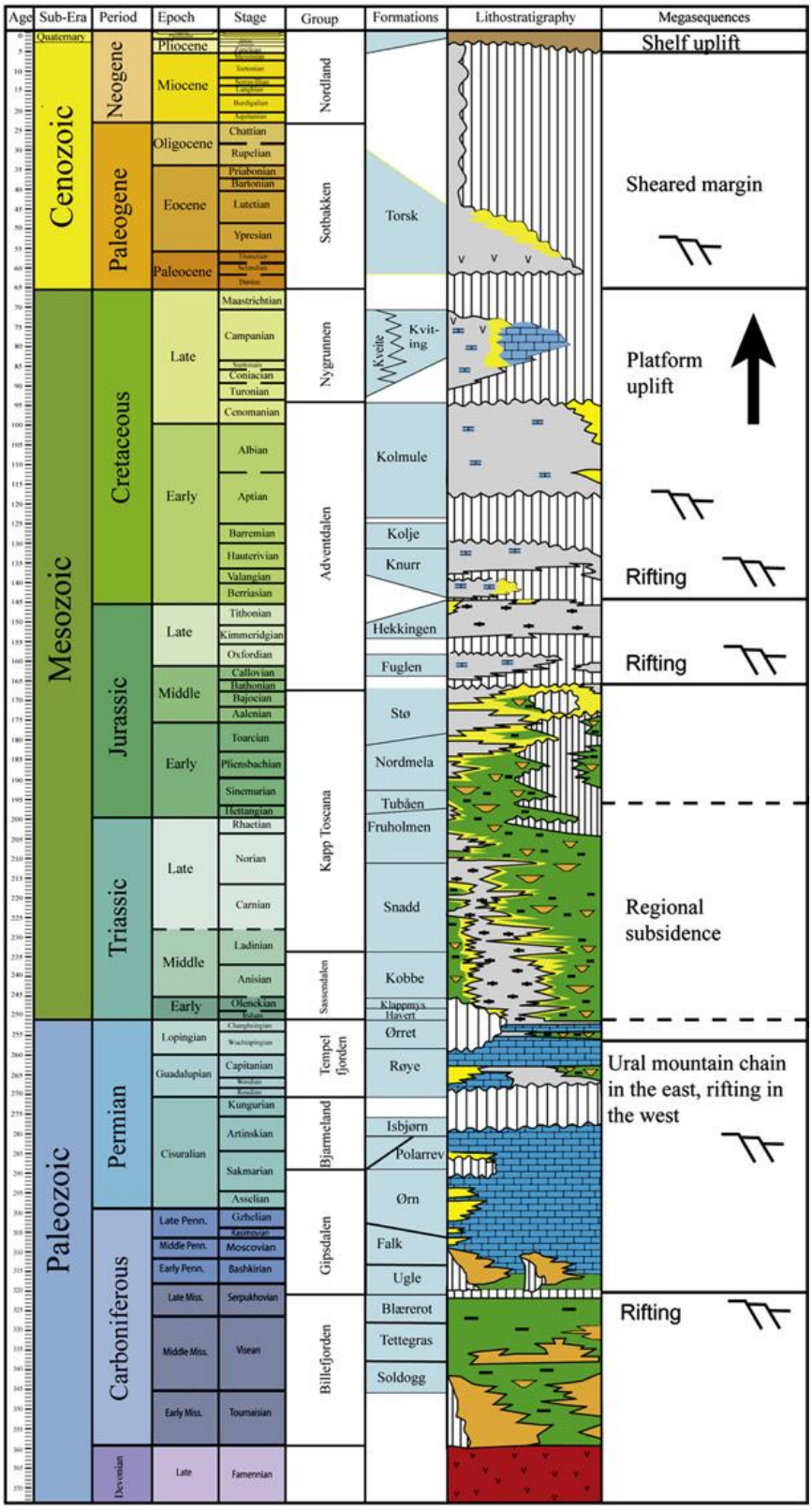

Figure 2-3: Stratigraphic column of the Western Barents Sea. Modified from Glørstad-Clark et al., (2010).

in its eastern part (Dengo and Røssland, 2013). This uplift is also associated with glacial erosion of the Barents Shelf during the Pliocene-Pleistocene (Faleide et al., 2008).

2.2.2. In-situ stress conditions in the Barents Sea

At present, regional data record NW-trending strike-slip to maximum compressive stresses in the central and western parts of the European Plate. The average azimuth of these stresses approaches 140° (Gölke et al., 1996; Klein and Barr, 1986; Müller et al., 1992). Exceptions to this regional stress distribution are found in Scandinavia (Bungum et al., 1991; Müller et al., 1992; Ranalli and Chandler, 1975; Stephansson, 1993). Earthquake focal mechanisms and borehole data from the Finnmark Platform indicate compressional stress regimes at shallow depths, with reverse faults responding to a maximum horizontal stress σ_H trending either N-S or E-W (Figure 2-4).

The existence of focal mechanisms for only five (5) earthquakes, the small seismological coverage and the low number of stress measurements makes it difficult to draw any conclusion about the general stress orientation and the tectonic regime in the broader region that forms the Barents Sea (Brudy and Kjørholt, 2001; Lindholm et al., 1995, 2000). Nonetheless, the analysis of borehole breakouts (Fejerskov et al., 2000; Gölke and Brudy, 1996), regional earthquake focal mechanisms (Lindholm et al., 2000) and borehole measurements (Fejerskov et al., 2000) for the western Barents

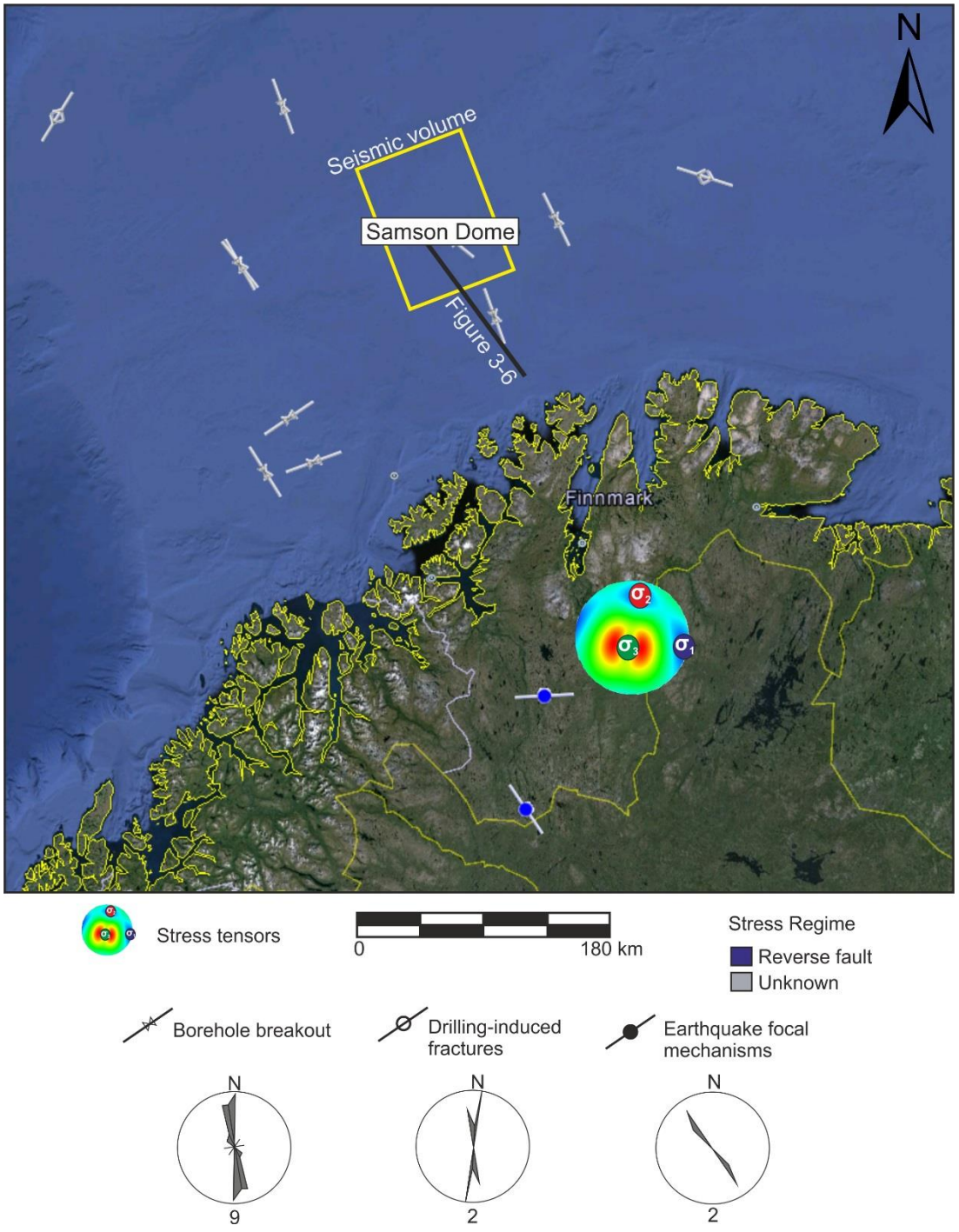

Figure 2-4: Present-day stress data for the Barents Sea and Finnmark. Stress tensors for the Finnmark Platform, used as a reference data in the assessment of slip tendency and leakage factor values for faults in the study area. Rose diagrams show the azimuth of the maximum stress σ_{Hmax} for each measurement technique. Stress data compiled from the World Stress Map (Heidbach et al., 2008).

Sea indicate a N-S maximum horizontal stress direction and a mean σ_H azimuth of N177.24°±46.91°E (Figure 2-4). The broad standard deviation recorded for the average σ_H azimuth results from the scatter of stress data obtained for the region. In-situ stress data indicate a clockwise rotation of the stress azimuth from WNW-ESE in the North Sea, to NW-SW in the Norwegian Sea and N-S in the Barents Sea (Figure 2-4). This stress-azimuth rotation suggests ridge push to be the principal stress-generating mechanism in the western Barents Sea (Lindholm et al., 2000). Another possible explanation for the different stress azimuths recorded in Finnmark and the Barents Sea, compared to the general NW-SE trend for Europe, relates to the superposition of local stresses on regional stress fields (Gölke and Brudy, 1996). Sources of local stress include the influence of local structures such as salt anticlines, salt diapirs, faults and folds, and lateral variations in rock properties at depth (Brudy and Kjørholt, 2001; Fejerskov et al., 2000).

2.3. Espírito Santo Basin, Brazil

The Espírito Santo Basin comprises a rift basin developed in the southeastern continental margin of Brazil during the Late Jurassic-Cretaceous (Figure 2-5). This basin covers an offshore area of about 200,000 km^2, while the continental area of the basin is around 18,000 km^2 (Mohriak, 2003). Its northern limit is the Abrolhos Bank, a Paleogene volcanic plateau that separates Espírito Santo from the Cumuruxatiba Basin (Mohriak, 2005). The Vitória-Trindade High separates the Espírito Santo Basin from the Campos Basin to the south (França et al., 2007) (Figure 2-5).

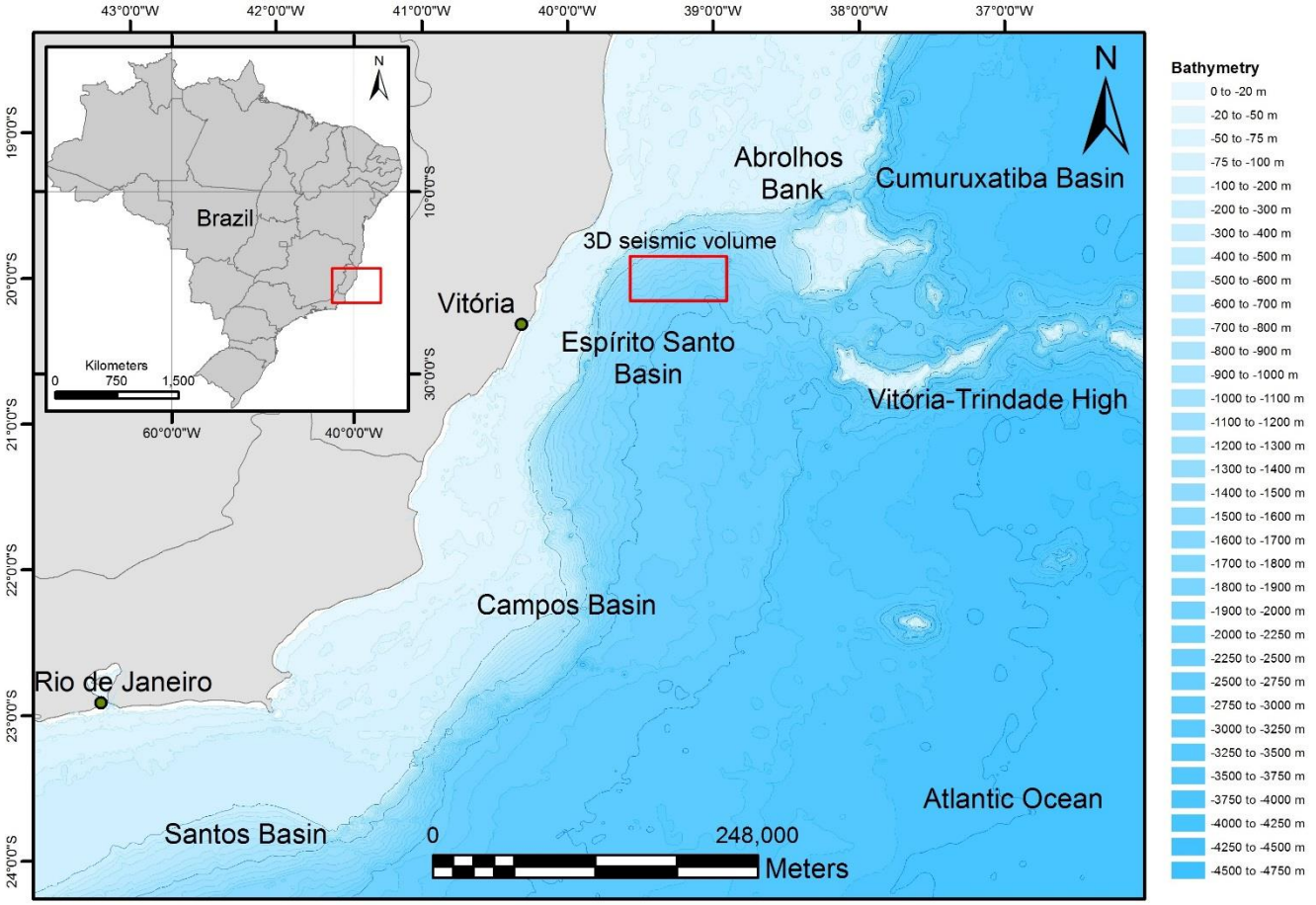

Figure 2-5: Location map of the Espírito Santo Basin and its main boundaries. The Espírito Santo Basin is limited to the north by the Abrolhos Bank and to the south by the Vitória-Trindade High. The location of the 3D seismic cube is indicated by the red polygon

The structural framework of the Espírito Santo Basin reflects the development of the South Atlantic Ocean during Late Jurassic – Cretaceous lithospheric extension (Chang et al., 1992; Fiduk et al., 2004; Mohriak, 2003; Ojeda, 1982) (Figure 2-6). Structures developed in the Espírito Santo Basin at this time include horsts, grabens and a series of salt-related structures; salt diapirs, salt rollers and rollovers, turtle anticlines, salt rafts and salt walls (Alves, 2012; Fiduk et al., 2004; Mohriak et al., 2008).

Halokinesis, and the consequent development of salt structures in the Espírito Santo Basin, started in the Late Aptian-Early Albian and were driven by the combination of differential sediment loading, gravity spreading and downslope thin-skinned gravitational gliding above Aptian evaporites (Demercian et al., 1993; Fiduk et al., 2004). Halokinesis generated structures such as salt rollers, vertical salt diapirs with overhangs, allochthonous salt tongues along contractional folds, salt canopies and tongues, turtle anticlines and extensive salt nappes (Fiduk et al., 2004).

The growth of salt structures in the Espírito Santo Basin continued through the Cenozoic as a result of: a) continuous sediment input onto the continental slope, and b) the influence of the regional magmatism that created the Abrolhos Plateau, inducing local uplift and deformation of pre-existent salt structures (Fiduk et al., 2004).

2.3.1. Tectonic evolution of the Espírito Santo Basin

The tectonic development of the Espírito Santo Basin is similar to the general

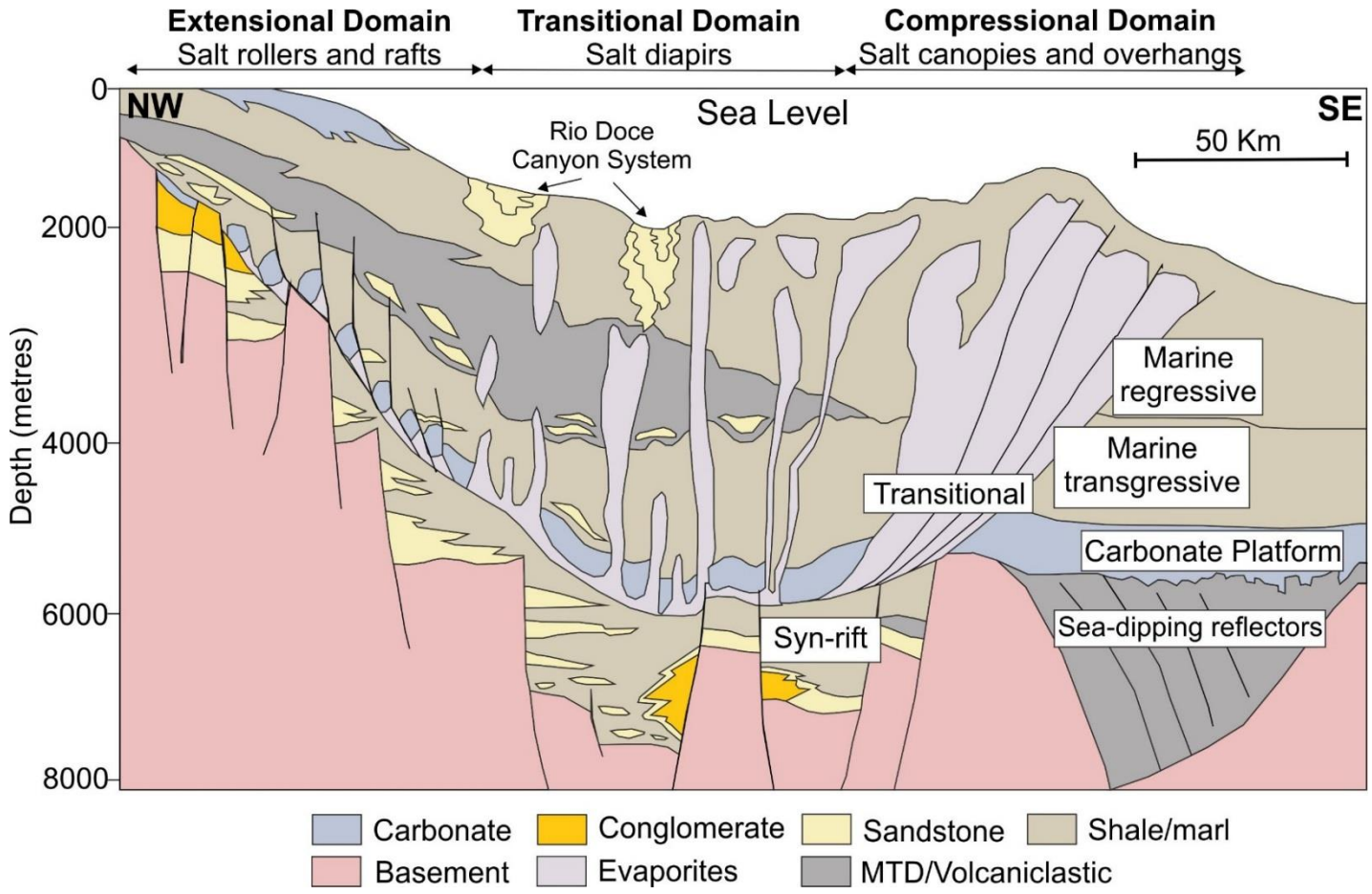

Figure 2-6: Simplified regional section of the Espírito Santo Basin showing major depositional sequences and structures across three salt domains (extensional, transitional and compressional). Modified from Fiduk et al. (2004) and Gamboa (2011).

evolution of passive continental margins in the South Atlantic, including the Campos and Santos Basins, two of the most prolific hydrocarbon-bearing basins in Brazil (Bruhn et al., 2003; Cobbold et al., 2001; Guardado et al., 2000; Milani et al., 2003). The four evolutionary stages of the Espírito Santo Basin comprise pre-rift, syn-rift, transition and drift stages (Cobbold et al., 2001; Ojeda, 1982). These evolutionary stages correlate with five depositional megasequences: pre-rift, rift, transitional, transgressive marine and regressive marine (Fiduk et al., 2004; Mohriak et al., 1998).

The pre-rift stage corresponds to the intracratonic phase of the Gondwana supercontinent, before Late Jurassic – Early Cretaceous rifting of the South Atlantic (Cainelli and Mohriak, 1999). At this time, large sag basins were developed in the interior of cratons and filled with Palaeozoic shallow-water sediments (Mohriak, 2003; Mohriak et al., 2008; Ojeda, 1982). Tectonic subsidence associated with an early stretching event occurred before the main rift phase and resulted in the development of a regional sag basin denominated Afro-Brazilian Depression (Garcia, 1991). Fluvial and alluvial sediments filled this depression together with localised evaporite deposits (Chang et al., 1992). Offshore SE Brazil, however, these deposits are absent, and pre-rift units from the Pelotas to Espírito Santo Basins are associated with the Serra Geral magmatic event, initiated in the Paraná Basin and reaching continental shelf basins during the Late Jurassic-Early Cretaceous (Cainelli and Mohriak, 1999; Mohriak, 2003).

The syn-rift stage occurred during the Late Barresian to the Early Aptian in the Espírito Santo Basin (Fiduk et al., 2004; Mohriak, 2003) (Figure 2-7a). This phase is characterised by important tectonic movements and by the formation of the East Brazil

Rift System, itself associated with divergent motion between South America and Africa (Chang et al., 1992; Demercian et al., 1993; França et al., 2007; Ojeda, 1982). The East Brazil Rift System extends for 3,500 km along the Brazilian continental margin and, in the Espírito Santo Basin, is limited to the West by an E-trending normal fault system (Mohriak, 2003). In its interior, the syn-rift megasequence consists of fluvial and lacustrine strata accumulated in narrow, fault-controlled depocentres generated between the Espírito Santo and Sergipe/Alagoas Basins (Cainelli and Mohriak, 1999). Three main lithologic facies are recognised in the syn-rift megasequence: 1) alluvial fans, fan deltas and transitional deposits, 2) lacustrine shales and marls, and 3) lacustrine pelecypod limestones (*coquinas*) (Cainelli and Mohriak, 1998).

The end of continental rifting during the Aptian marks a transitional phase between syn-rift and the marine drift stages (Mohriak, 2003; Ojeda, 1982) (Figure 2-7b). The depositional setting of the transitional megasequence is characterised by the formation of a narrow and elongated basin, in an arid climate with little water circulation. This setting allowed the precipitation of thick evaporite sequences on both the South American and West African continental margins (Chang et al., 1992; Demercian et al., 1993; França et al., 2007; Mohriak, 2003; Ojeda, 1982). The transitional evaporitic megasequence comprises the main seal interval above the syn-rift sequence (Mohriak, 2003).

Continuing divergence between South America and West Africa, with increasing thermal subsidence, marked the drift stage (Late Cretaceous to the Holocene; Bruhn and Walker, 1997; Cainelli and Mohriak, 1999). An open marine setting predominated

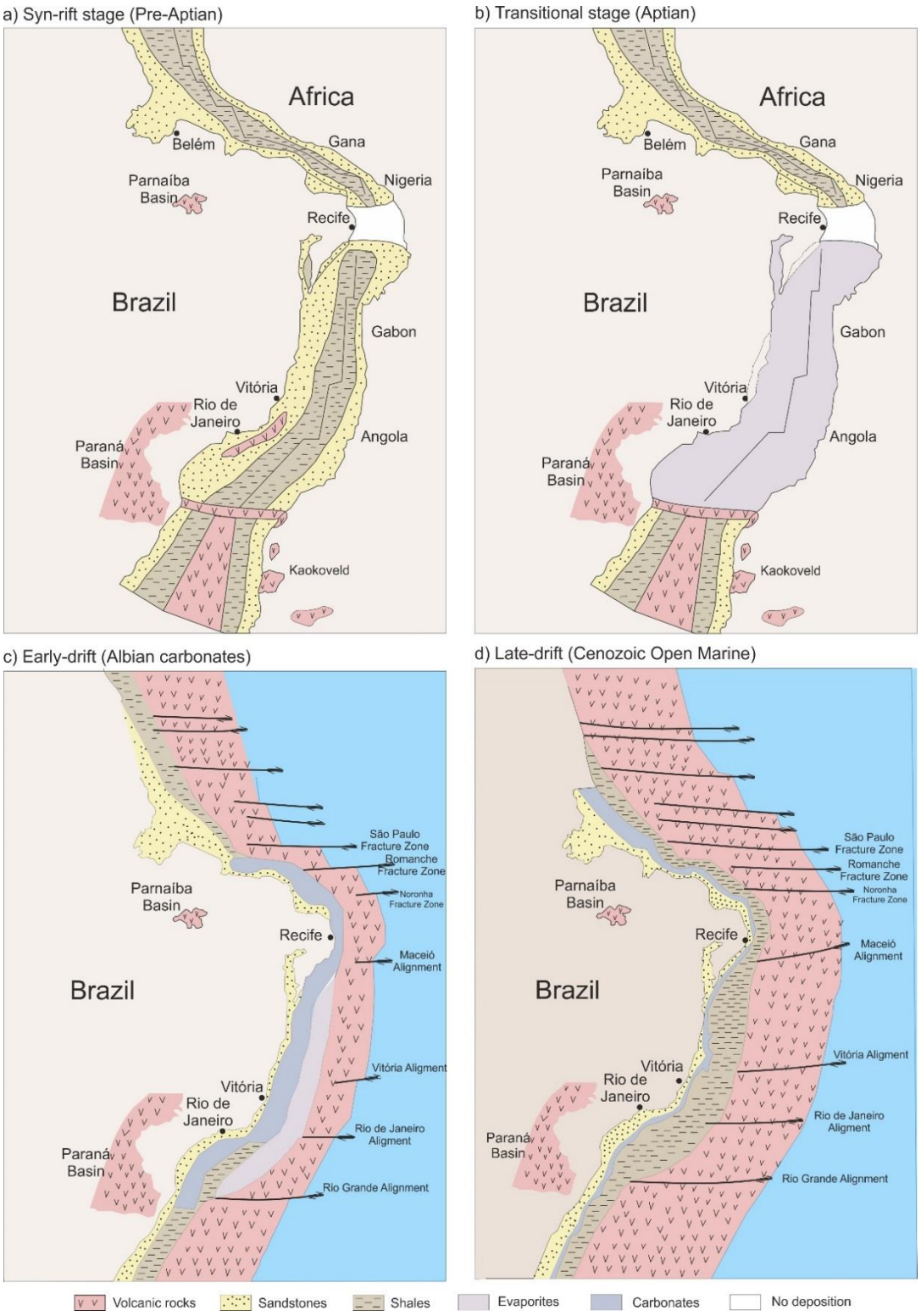

Figure 2-7: Paleogeographic evolution of SE Brazil showing four main tectonic stages. a) Syn-rift stage, characterised by continental deposition; b) Transitional stage, with deposition of evaporites in a restricted basin developed at the end of the Aptian; c) Early drift stage, with the development of carbonate platforms and d) Late drift stage, reflecting open marine sedimentation. Modified from Ojeda (1982).

at this time, as continuous subsidence resulted in the cessation of topographic barriers to ocean circulation (Mohriak, 2003). An evaporitic (transitional) megasequence evolved gradually towards marine strata during the drift stage (Cainelli and Mohriak, 1998). As a result, two megasequences comprise the drift stage, the Early Drift Transgressive megasequence and the Late Drift Regressive megasequence (Cainelli and Mohriak, 1998; Fiduk et al., 2004; Ojeda, 1982).

In the Espírito Santo Basin, the Early Drift Transgressive megasequence is subdivided into two transgressive stratigraphic sequences (Figure 2-7c). The lower sequence corresponds to the Barra Nova Group and comprises alternating sand-rich units (Albian) and Albian-Cenomanian carbonates (Asmus et al., 1971; Demercian et al., 1993; França et al., 2007). The top of this Group records a change in basin configuration; in the central part of the basin were formed a series of tectonic rafts, while an unconformity associated with the incision of the Regência and Fazenda Cedro paleocanyons is observed in the continenal portion of this basin (França et al., 2007). The upper transgressive sequence, deposited between the Cenomanian and the Ypresian, represents a phase of relative deepening of the Espírito Santo Basin marked by the drowning of the Regência carbonate platform (Albian). Strata in this sequence consists of dark shales, turbiditic sandstones and carbonate breccias (Cainelli and Mohriak, 1998; França et al., 2007).

The Late Drift Regressive megasequence (Figure 2-7d), deposited from the Meso-Eocene (Lutetian) to present-day, reflects a tectonic phase marked by: a) uplift of hinterland mountain ranges such as Serra do Mar and Serra da Mantiqueira, b) development of the Abrolhos Plateau, and c) continuous halokinesis in the Espírito

Santo Basin (Cainelli and Mohriak, 1999; Cobbold et al., 2001; França et al., 2007). The presence of a magmatic hot-spot in the Vitória-Trindade region, associated with the reactivation of ancient rift structures, culminated in a magmatic event (Abrolhos Volcanism) that involved two-thirds of the Espírito Santo Basin. It also led to the development of the Abrolhos Plateau, a volcanic bank with an area of 30,000 km^2 (Fainstein and Summerhayes, 1982; França et al., 2007). The intense tectonism recorded at this time resulted in a regional sea-level drop, which is signed by a regional Paleocene unconformity (Cobbold et al., 2001; Demercian et al., 1993; França et al., 2007).

The Late Drift Regressive megasequence can be divided into four second-order stratigraphic sequences (França et al., 2007). The first sequence, comprising Paleocene to lowest Eocene shales and sandstones, was deposited with a clear offlap pattern in proximal areas of the margin and reflects the uplift of the basin margins. The erosion of the Serra do Mar and Serra da Mantiqueira, combined with the Abrolhos volcanic phase, resulted in the deposition of a mixed siliciclastic and volcaniclastic unit (Figueiredo and Mohriak, 1984; França et al., 2007; Mohriak, 2003). Carbonates also occur in this sequence, particularly over the Abrolhos Plateau.

The second sequence is limited at its top by an angular unconformity, denominated Pre-Late Eocene Unconformity (França et al., 2007). In the third sequence, sediment was mainly transported to the Espírito Santo Basin by turbidity flows associated with submarine fans and channel systems, and by debris flows reflecting widespread slope instability (Cainelli and Mohriak, 1998; Figueiredo and Mohriak, 1984; França et al., 2007; Mohriak, 2003). The fourth sequence consists of channelised turbiditic

sandstones in the proximal part of the basin, and shales in more distal parts (França et al., 2007).

2.3.2. Stratigraphy of the Espírito Santo Basin

The stratigraphy of the Espírito Santo Basin has recently been reviewed and summarised in light of the updated Espírito Santo Basin Stratigraphic Chart of França et al. (2007). The Espírito Santo Basin sedimentary succession comprises, in chronostratigraphic order, the Nativo, Barra Nova, and Espírito Santo Groups (Figure 2-8).

The Nativo Group (*cf.* Asmus et al., 1971) consists of Valanginian to Aptian strata deposited unconformably over a Pre-Cambrian basement (Figure 2-8). The Nativo Group includes the Cricaré and Mariricu Formations, which comprise continental siliciclastic rocks interbedded with extrusive magmas, volcaniclastic material and tuffs (Asmus et al., 1971; Chang et al., 1992; França et al., 2007; Mohriak, 2003; Ojeda, 1982). The top of the Nativo Group comprises an evaporitic sequence. The Cricaré Formation (*cf.* Vieira et al., 1994) comprises sandstones and feldspar-rich conglomerates (Jaguaré Member), interbedded with grey shales, pelecypod limestones and marls of the Sernambi Member, and volcaniclastic rocks of the Cabiúnas Formation. The Cricaré Formation is separated from the Mariricu Formation by a regional unconformity, the Pre-Alagoas Unconformity (Dias, 2005; França et al., 2007; Vieira et al., 1994). The Mariricu Formation, of Aptian age, comprises the

Mucurí and Itaúnas Member (França et al., 2007). The basal Mucurí Member is composed of sandstones and conglomerates intercalated with shales and siltstones deposited by alluvial and fluvio-deltaic systems (Vieira et al., 1994). The intermediate sequence of the Mucurí Member includes fine to very fine sandstones and marks the transition to the Itaúnas Member, which was deposited over an unconformity that marks the top of the Late Aptian sequences (França et al., 2007). The Mucurí Member reflects the very first marine incursions, under restricted water circulation, recorded in the Espírito Santo Basin (Chang et al., 1992; Demercian et al., 1993; França et al., 2007; Vieira et al., 1994). In contrast, the Itaúnas Member comprises limestones and anhydrite deposited in the proximal parts of the basin, and halite in the central part of the Espírito Santo Basin. Carbonate and evaporites are intercalated with thin shales (Vieira et al., 1994).

The Barra Nova Group (Vieira et al., 1994) includes the São Mateus and Regência Formations, which were deposited from the Albian to the Cenomanian on a shallow shelf, over the Itaúnas Member evaporitic sequence (França et al., 2007). The São Mateus Formation consists of sandstones deposited in a proximal marine setting over a succession of shales, siltstones, and carbonates (Figure 2-8). The Regência Formation (Asmus et al., 1971) includes a relatively thick carbonate sequence comprising limestones, carbonate mudstones, and wackestones with ostracods, gastropods and pelecypods fragments deposited in distal parts of the Espírito Santo Basin. The Barra Nova Group is bounded at its top by the Pre-Urucutuca unconformity (França et al., 2007).

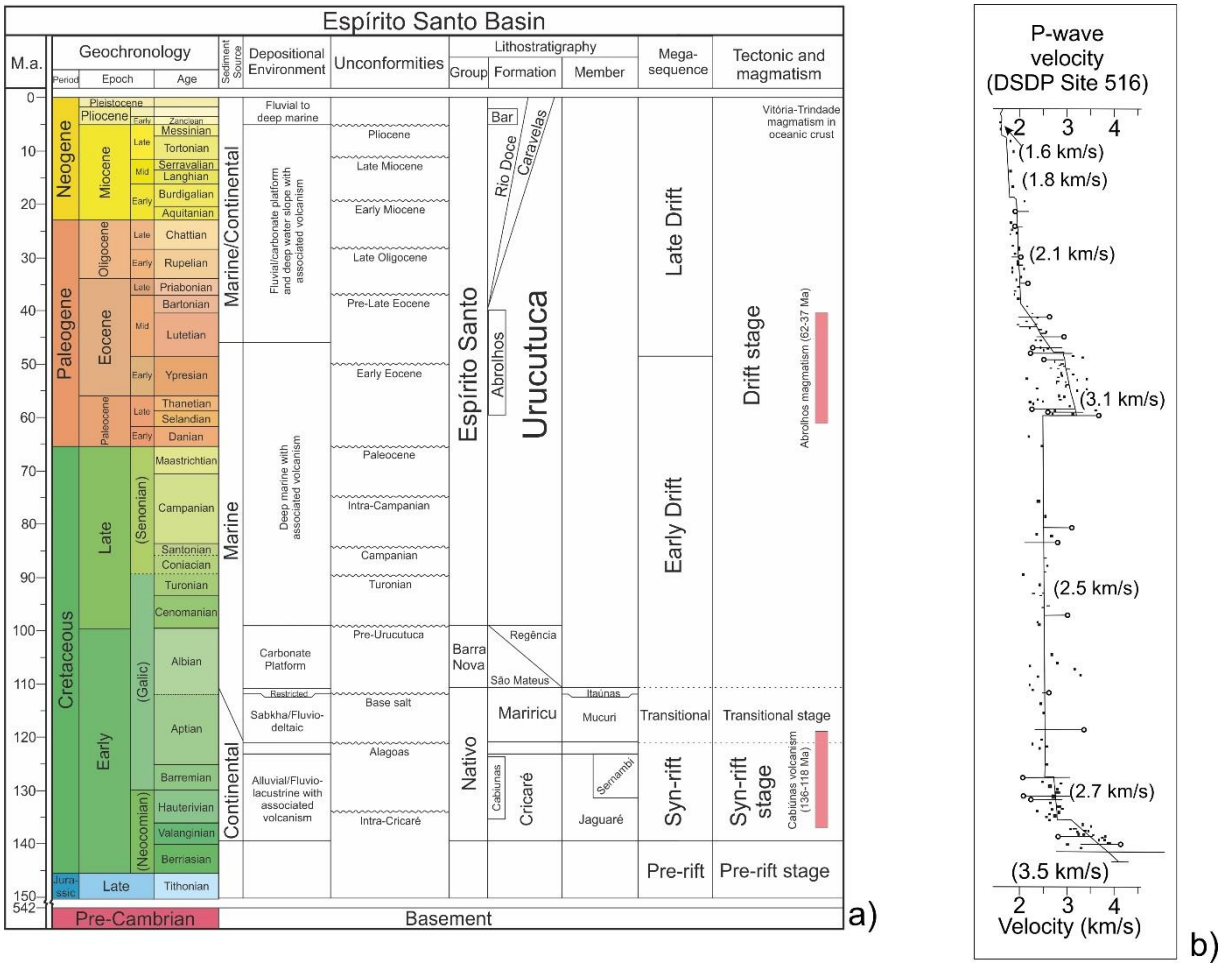

Figure 2-8: Stratigraphic column of the Espírito Santo Basin highlighting the sediment sources and depositional environments that resulted in four tectonic stages and five depositional megasequences in the basin (Modified from França et al., 2007).Velocity data for well DSDP Site 516 for the Rio Grande Rise compiled from Barker et al. (1983).

The Espírito Santo Group reached a maximum thickness of 6,600 m from the Cenomanian to Recent. This group is sub-divided into five formations, the Urucutuca, Abrolhos, Caravelas, Rio Doce and Barreiras Formations (Figure 2-8). The Urucutuca Formation comprises shales interbedded with conglomerates, limestones, and sandstones, which were deformed from the Cenomanian to the Coniacian by the salt tectonics in proximal parts of the Espírito Santo Basin. On the distal margin, dark shales and sands have been described (Cainelli and Mohriak, 1998; França et al., 2007). The Urucutuca Formation (Coniacian to Campanian) grades into sandy turbidites sourced by the Fazenda Cedro and Regência paleocanyons (França et al., 2007). During the Campanian-Maastrichtian, the Urucutuca Formation deposited turbidites at its base and predominantly shales and sandstones in the proximal part of the basin. Marls occur in the distal part of the Espírito Santo Basin. From the Selandian to the Bartonian, the volcaniclastic Abrolhos Formation became interbedded with thick turbidites in channelised bodies whose distribution was controlled by halokinesis (Cainelli and Mohriak, 1998; Figueiredo and Mohriak, 1984; França et al., 2007; Mohriak, 2003).

The Caravelas Formation (Asmus et al., 1971) consists of turbidites, calcarenites and calcareous mudstones deposited on a carbonate shelf of Bartonian to Recent age. This formation is deposited over the volcanic rocks of the Abrolhos Formation and interfingers with the Urucutuca and Rio Doce Formations (see Alves, 2010).

The Rio Doce Formation consists of sandstones interbedded with shales and siltstones deposited in continental to shallow-marine environments (França et al., 2007). During the Pliocene, the Rio Doce Formation interfingered with the Caravelas Formation in distal parts of the shelf, whereas in proximal parts of the basin the Barreiras Formation is

intercalated with the Rio Doce Formation. The Barreiras Formation consists of varied strata (shales to conglomerates) deposited in fluvial and alluvial environments (Vieira et al., 1994).

2.4. Taranaki Basin, New Zealand

The Taranaki Basin is a Cretaceous-Holocene sedimentary basin located on the northwest margin of New Zealand (Figure 2-9). This asymmetric basin extends through an offshore area of ~100.000 km^2 (King and Thrasher, 1996). The Taranaki Fault, a reverse fault related to convergence between the Australian (west) and Pacific (east) tectonic plates (Baur, 2012; Holt and Stern, 1991), bounds the Taranaki Basin to the east. Its western limit is the Challenger Plateau whereas, in the south, the Taranaki Basin merges with the sub-basins of the South Island. To the northwest, this basin terminates in the New Caledonian Basin (King and Thrasher, 1996).

The Cape Egmont Fault Zone divides the Taranaki Basin into two tectonically-distinct regions: the relatively undeformed Western Stable Platform, and the tectonically active Eastern Mobile Belt (King and Thrasher, 1996; Nodder, 1993) (Figure 2-9). The Eastern Mobile Belt has a complex deformation history (Armstrong et al., 1998; Kamp et al., 2004b; King and Thrasher, 1996; Knox, 1982), comprising the Northern and the Central Grabens to the north, and the Southern Inversion Zone to the south (Figure 2-9). A buried Miocene volcanic centre trending N-S along the North Taranaki Graben (Mohakatino

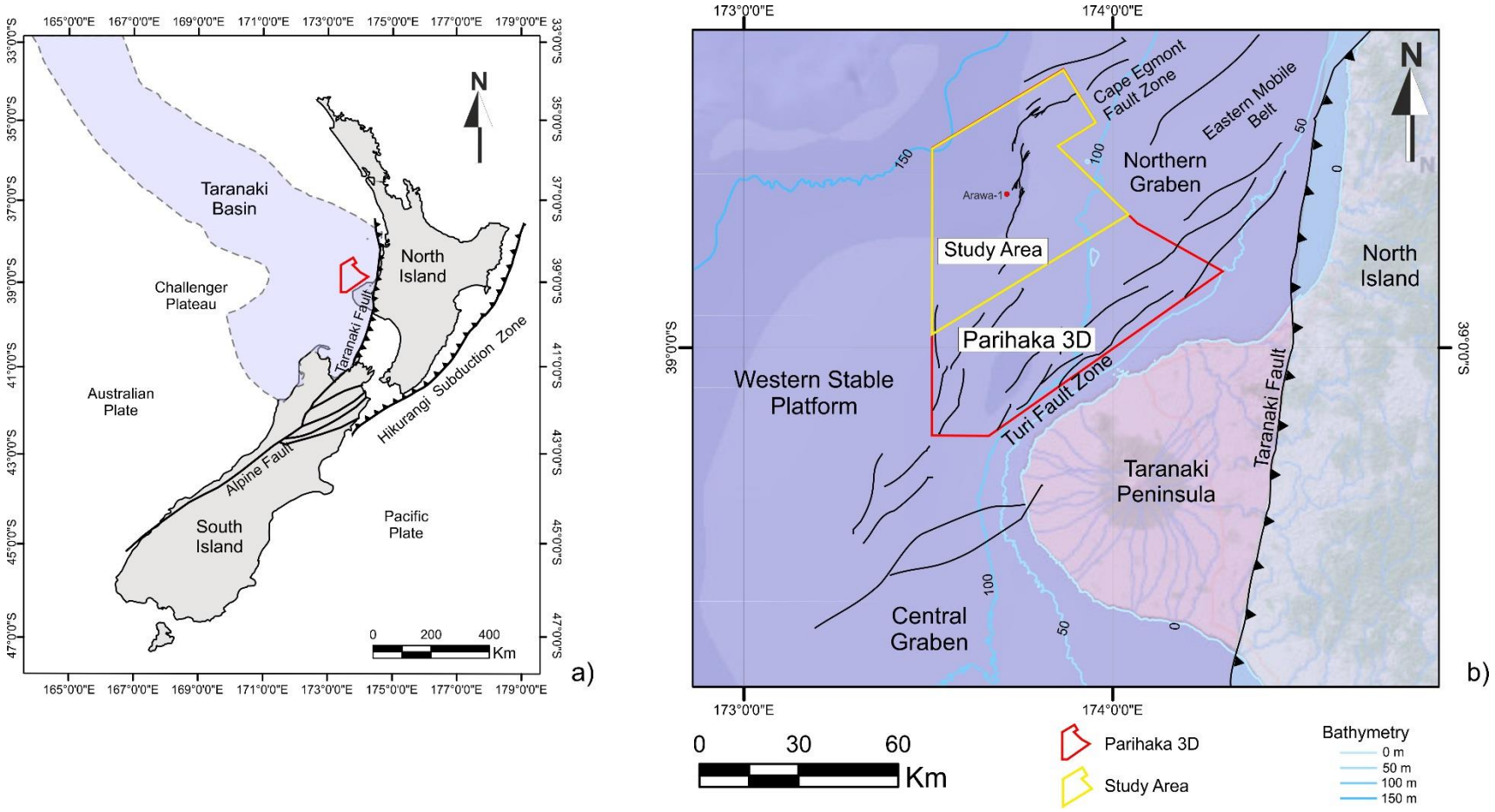

Figure 2-9: a) Regional location map of the New Zealand and its main structural boundaries. The Taranaki Basin is limited at east by the Taranaki Fault and at west by the Challenger Plateau. To the south, the Taranaki Basin is limited by the South Island. The 3D seismic cube is delimited by the red polygon. b) Detailed location map of the Northern Graben showing the main structures at a local scale. The study area occurs between 100 and 150 m below the sea-level. The study area is delimited by the yellow polygon.

Volcanic Centre) is observed in the Northern and Central Grabens (Hansen and Kamp, 2004a; Neall et al., 1986; Stagpoole and Funnell, 2001). The study area is, therefore, located in the North Taranaki Graben, a structure progressively developed during the Pliocene (Giba et al., 2010; Hansen and Kamp, 2004a; King, 2000; King and Thrasher, 1996; Stern et al., 2006).

2.4.1. Tectonic evolution of the Taranaki Basin

The evolution of the Taranaki Basin was marked by rifting and passive margin development from Late Cretaceous to the Early Eocene (Giba et al., 2010; King, 2000; King and Thrasher, 1996). Extension in the Taranaki Basin was concomitant with basin subsidence and compressive episodes related to important tectonic movements between the Australian and Pacific plates along the Hikurangi Trough subduction zone (Holt and Stern, 1991; King and Thrasher, 1996; Nicol et al., 2005; Stagpoole and Nicol, 2008). The Late Paleogene marked the end of the passive-margin stage of the Taranaki Basin, and the beginning of a phase of subsidence that mostly affected the eastern areas close to the Taranaki Fault (Figure 2-9). During the earliest Miocene, the subsidence phase was replaced by compression resulting from westward thrusting along the Taranaki Fault (Kamp et al., 2004a, 2004b; King, 2000; King and Thrasher, 1996; Nicol et al., 2004). From Miocene to the Pliocene-Pleistocene concomitant shortening in the south, and extension in the north, took place in the Taranaki Basin (Giba et al., 2010; Stagpoole and Nicol, 2008). In parallel, andesitic volcanic complexes were active in the Taranaki Basin

from ~ 12 Ma to 6 - 4.8 Ma, resulting in the formation of the Mohakatino Volcanic Centre (Hansen and Kamp, 2004a).

Back-arc extension, generated in response to clockwise rotation of the Hikurangi Trough to the east during the Early Pliocene, led to the formation of the Northern Graben, a NNE-SSW fan-shaped graben delimited by the Cape Egmont Fault Zone to the west and by the Turi Fault Zone to the east (Giba et al., 2010; King, 2000; King and Thrasher, 1996).

2.4.2. The Cape Egmont Fault Zone

The Cape Egmont Fault Zone (CEFZ) extends for more than 200 km along the western portion of the Taranaki Basin. It shows a width of 15 – 20 km and comprises a series of normal, reverse and en echelon faults revealing complex reactivation from Cretaceous to Recent times (Nodder, 1993). One of the main faults developed at the Cape Egmont Fault Zone is the Parihaka Fault, a complex structure comprising four individual fault segments, 8 to 15 km-long, resulting in a total length of approximately 50 km (Giba et al., 2012) (Figure 2-10). Segments S1 and S2, to the south of the CEFZ, strike NNW to SSE and are nearly continuous, evidencing hard-linkage at Late Cretaceous level. The Early Pliocene (3.7 Ma) back-arc extension that culminated in the development of the Northern Graben resulted in the reactivation of segments S1 and S2 (with a maximum vertical displacement of 600 m), and in the concomitant formation of NE-striking segments S3 and S4 to the north of the CEFZ. Fault reactivation to the south ceased during

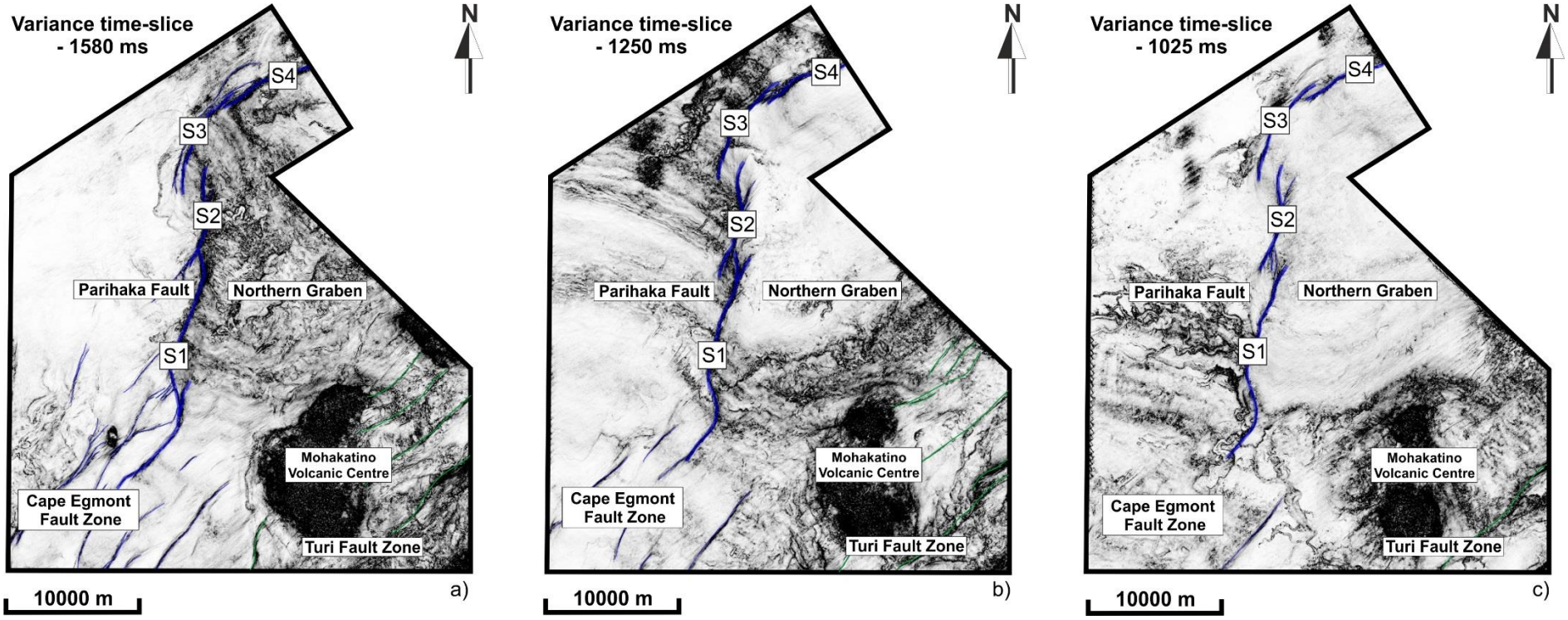

Figure 2-10: Variance time-slices at a) -1580 ms, b) -1250 ms, and c) -1025 ms showing the configuration of the Cape Egmont Fault Zone. The Parihaka Fault is the most distinctive structure of this seismic volume and is the object of study of Chapter 4. This fault comprises four segments named S1 to S4. The current configuration of the Parihaka Fault observed in these time-slices is related to the back-arc extension that culminated in the formation of the Northern Graben during the Early Pliocene, with the reactivation of S1 and S2 and the formation of S3 and S4. Relay ramps between segments S1 and S2, S2 and S3 and S3 and S4 are observed in these time slices. Segments S1 and S2 show high linkage at -1580 ms, whereas at -1025 ms these segments show soft linkage.

the Pleistocene, whereas to the north faulting continued into the Holocene, resulting in vertical displacements of up to 1450 m for the NE-striking segment S4 (Giba et al., 2012). In Quaternary strata, breached or unbreached relay zones were developed between the Parihaka Fault segments according to the coherent fault growth model of Walsh et al. (2003) (Figure 2-10). Variations in fault strike results in the rotation of the fault surface. For segments S3 and S4, the growth of the Parihaka Fault was accommodated by later displacement and rotation of the relay zones (Giba et al., 2012).

2.4.3. Miocene – Quaternary stratigraphy of the Taranaki Basin

The Miocene – Quaternary lithostratigraphy of the Taranaki Basin is shown in Figure 2-11. Miocene units are associated with the regressive Wai-ti Group, which was deposited during passive-margin extension concomitant with plate subduction (King and Thrasher, 1996). The prograding units of the Pliocene-Pleistocene Rotokare Group were deposited during the back-arc extension phase of the Taranaki Basin. They include fan deposits of the basal Mangaa Formation and large volumes of shelf and slope sediments of the Giant Foresets Formation (Hansen and Kamp, 2002). The interval of interest to this study is included within the Giant Foresets Formation, a ~2000 m-thick unit characterised by the occurrence of clinoforms and incised submarine channels (Hansen and Kamp, 2002; King and Thrasher, 1996; Salazar et al., 2015). The high sedimentation rates of the Giant Foresets Formation were capable of preserving the growth history of the main fault

segments of the Parihaka Fault during the Pliocene-Pleistocene (King and Thrasher, 1996).

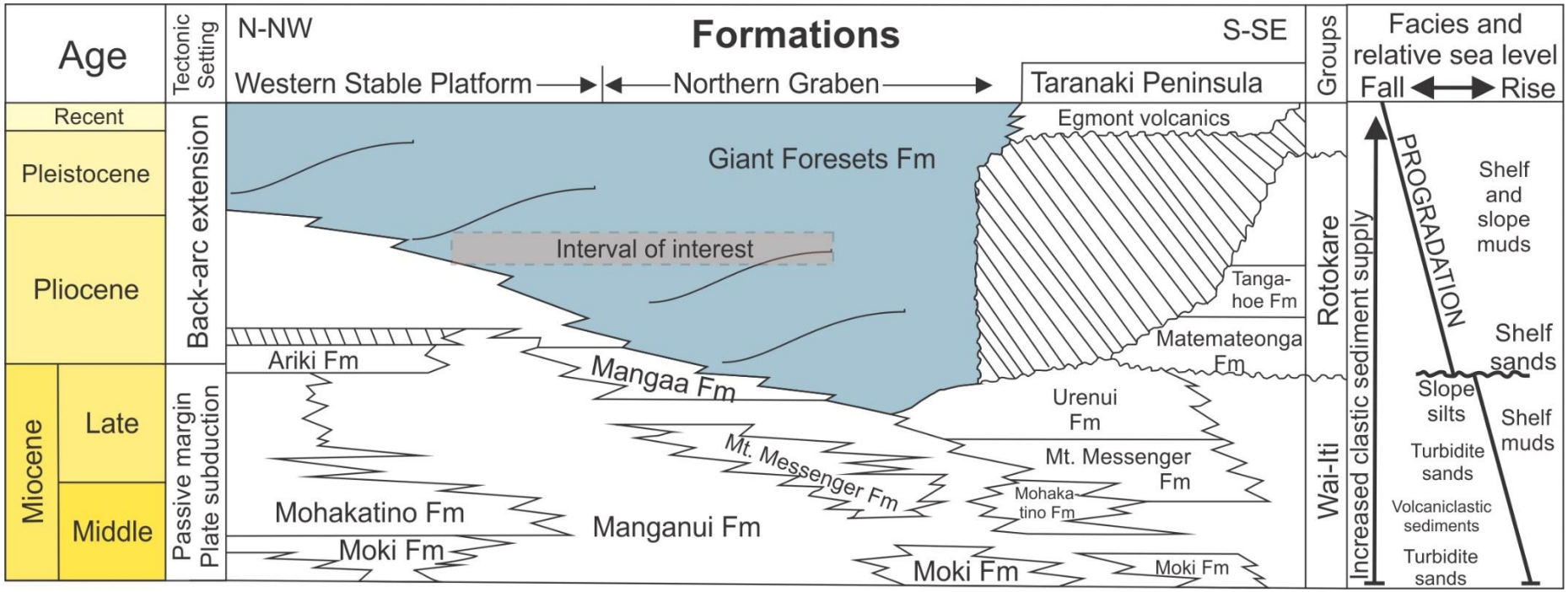

Figure 2-11: Stratigraphic column highlighting depositional facies and relative sea-level changes in the Taranaki Basin from Miocene to Recent. The interval of interest of this thesis occurs within the Giant Foresets Formation, and is highlighted in this figure. Modified from King and Thrasher (1996).

3. Data and methods

3.1. Introduction

This PhD thesis was chiefly based on the observation, interpretation and analysis of 3D seismic cubes. Well data and 2D seismic lines were also used for specific purposes and will be further described in Section *3.3.* In essence, the aims of this chapter are: a) to provide an overview of seismic acquisition and the nature of the seismic waves, b) to outline the specifications and parameters of each of the seismic surveys used in this thesis, c) to describe the methods used to interpret and analyse seismic horizons and fault families, and d) to provide an overview of the methods used in the structural analysis of interpreted faults. The methods described here were applied in, at least, two of the results chapters. Specific methods applied for individual chapters, such as, stratigraphic juxtaposition analysis (Chapter 5), and channel mapping and channel morphology analyses (Chapter 6) are described in their corresponding chapters.

3.2. Three-dimensional (3D) seismic data

Three-dimensional (3D) seismic data is considered a primary tool in the investigation of geological features associated with hydrocarbon accumulations. In addition, regional tectonics, depositional systems and processes and the occurrence of igneous systems can also be assessed using 3D seismic data (Cartwright, 2007).

In comparison to 2D surveys, 3D seismic data produces a volume. While data recorded in 2D images geological features along a vertical plane, 3D seismic data consists

of multiple closely-spaced lines without spatial aliasing problems (Davies et al., 2004). Increasing vertical and horizontal resolutions result from the acquisition of 3D seismic data, as data volume will consist of lines, planes and slices that can be extracted and interpreted in both horizontal and vertical directions to discern depositional and structural features (Brown, 2011; Davies et al., 2004; Yilmaz, 2001).

3.2.1. 3D seismic acquisition

The principles behind 3D seismic acquisition are based on the production and reflection of a seismic signal. Offshore seismic surveys use airgun arrays, water guns, or other controlled sources near a survey vessel to produce the acoustic (sound) pulse, and streamers of hydrophones as data receivers (Figure 3-1). The length of receiver cables is dependent on the depth of the surveyed area (Bacon et al., 2007), and the end of these cables are attached to a tail buoy. The shooting, or inline, direction is coincident with the ship track, and common trace spacing varies from 12.5 to 25 m. The crossline direction is perpendicular to the inline direction, and trace spacing normally varies from 25 to 50 m (Yilmaz, 2001).

An acoustic pulse (compressional or P-wave) is produced and penetrates the surface. Below the sea floor, geological interfaces with different seismic velocities and densities reflect the propagated sound, which is recorded by hydrophones (Bacon et al., 2007; Zhou, 2014). The time taken for a seismic signal to travel from the source (airgun) down to the reflector and back, is measured as two-way travel time (TWTT), in seconds or

milliseconds. These TWTT values can be converted to depth when the propagation velocities of seismic energy are also measured (Bacon et al., 2007).

3.2.2. Nature of seismic waves

Seismic waves are a disturbance transmitted as a set of wave motions that propagate through compressional or elastic displacements from a seismic source to a medium, without transfer of mass (Kearey et al., 2013; Liner, 2004; Lowrie, 2007). The acquisition of marine seismic data is mainly concerned with the detection of compressional reflected at subsurface geological boundaries (Kearey et al., 2013). The mechanics of compressional waves, also referred as longitudinal waves, involves oscillation about a fixed-point that is parallel to the direction of wave propagation (Kearey et al., 2013; Liner, 2004).

The main parameters of compressional waves propagating through a fluid or solid are velocity and frequency. Velocity (v), also referred in the literature as wave speed (Liner, 2004), is the magnitude and direction in which seismic waves travel across the geological interfaces. The seismic velocity varies depending on physical properties of the rocks such as composition (lithology), texture, degree of cementation, temperature, pressure variations with depth, and other factors such as porosity, pore fluids, mineralogy, fractures, elastic moduli and density of the rocks. Seismic velocity tends to increase with confining pressure and depth, and with increasing compaction and cementation in subsurface strata (Kearey et al., 2013; Liner, 2004).

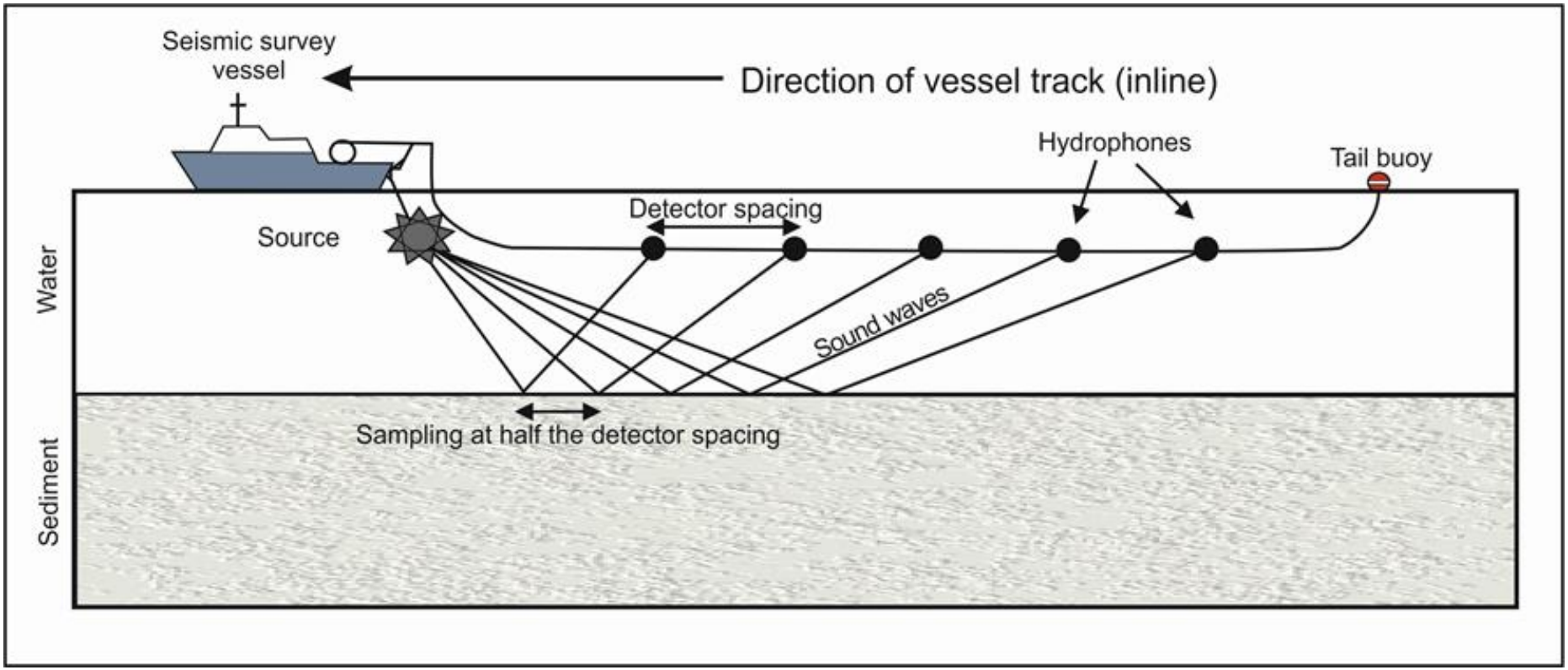

Figure 3-1: Schematic representation of 3D offshore surveys. The shooting direction of the sound waves is coincident with the vessel track line. Sound waves travel through the water into the sediment layers and are reflected back to the hydrophones, where they are acquired. Modified from Bacon et al. (2007).

Frequency (f) is defined as the number of seismic wave cycles that go through a fixed point in a given unit of time. Frequency tends to decrease with depth, due to the preferential attenuation of higher-frequency waves as they propagate through the rocks. The most common result of frequency decay with depth is a noticeable decrease in vertical resolution (Brown, 2011).

The partition of energy between transmitted and reflected P-waves depends on the intrinsic properties of the geological interfaces, and is commonly denominated as impedance (Lowrie, 2007). The product between the rock density (ρ) and the P-wave velocity (V) defines the acoustic impedance (Z) of a rock layer (Equation 3-1):

$$Z = \rho \times V$$

Equation 3-1

A sandy interval underlying a shale is a typical interface between two layers of contrasting impedance (Figure 3-2). When a seismic wave reaches the interface of these contrasting layers, some of its energy is reflected towards the surface, and some is reflected downwards (Brown, 2011; Kearey et al., 2013). Sands have a lower impedance than shales in relatively young successions; for older rocks, the impedance of sands is higher compared with shales, as they are more compacted (Brown, 2011).

Variations in acoustic impedance across seismic interfaces are recorded as wavelets. The amplitude of a wavelet is the measure of its size normal to the propagation direction

of the wave. Relative increases in acoustic impedance are shown as peaks, thus representing positive amplitudes in a wavelet. Negative amplitudes are displayed as troughs and denote a decrease in impedance (Hart, 1999). In variable wiggle displays, peaks are shown in black and troughs in white.

The 'SEG (Society of Exploration Geophysicists) normal polarity classification' (Brown, 2011) suggests displaying waves as peaks and troughs and is the convention used for Chapters 4 and 6 (Figure 3-3a and b). The use of a gradational colour scheme to show variable acoustic impedances is preferred, rather than using contrasting colours, so one can interpret amplitude trends and patterns (Brown, 2011; Hart, 1999). In Chapters 4 and 6, gradational black is used to highlight peaks and gradational red to highlight troughs (Figure 3-3c). White coloured areas on seismic profiles indicate zero amplitudes, or 'zero crossings'. In Chapter 5 polarity display follows the standard European convention for a zero-phase wavelet, with peaks of acoustic impedance shown as grading red reflections on seismic profiles, and relative lows in acoustic impedance shown as grading blue seismic reflections.

The periodical wave motion is described by its phase. Seismic surveys can be of maximum, minimum and zero-phase data; with the latter being the preferred data type in seismic interpretation (Brown, 2011). In the zero-phase data, the wavelet is symmetrical, with the maximum amplitude of the energy concentrated at the crest. The wavelet symmetry minimises the ambiguity when the interpreter relates the observed waveforms to subsurface interfaces. Horizon tracking completed at the centre of the wavelet is also an advantage of the zero-phase data, as it coincides with the (subsurface) interface that caused the reflection.

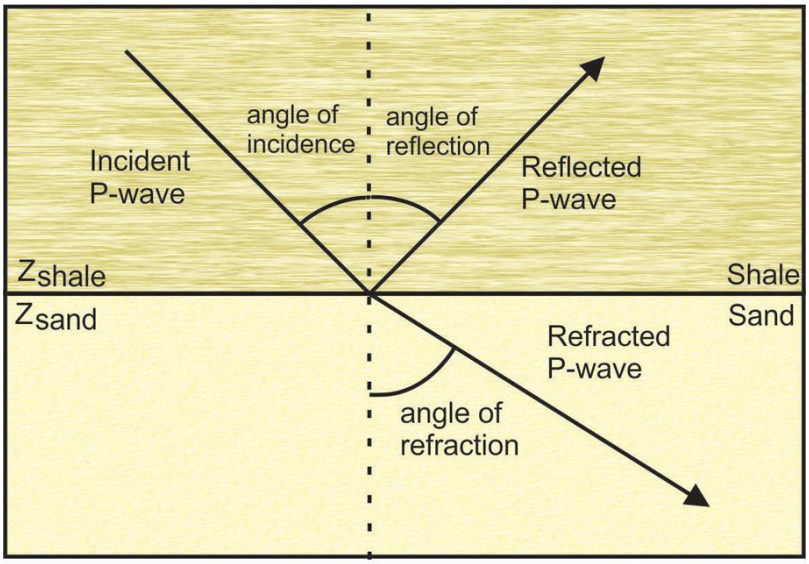

Figure 3-2: Reflected and refracted wave paths as a P-wave meets an interface between shale and sand with contrasting impedances. The angle of the reflected wave is the same as the incident wave. The angle of refraction may vary according to the velocity of the medium, represented by the sand. Modified from Kearey et al. (2013).

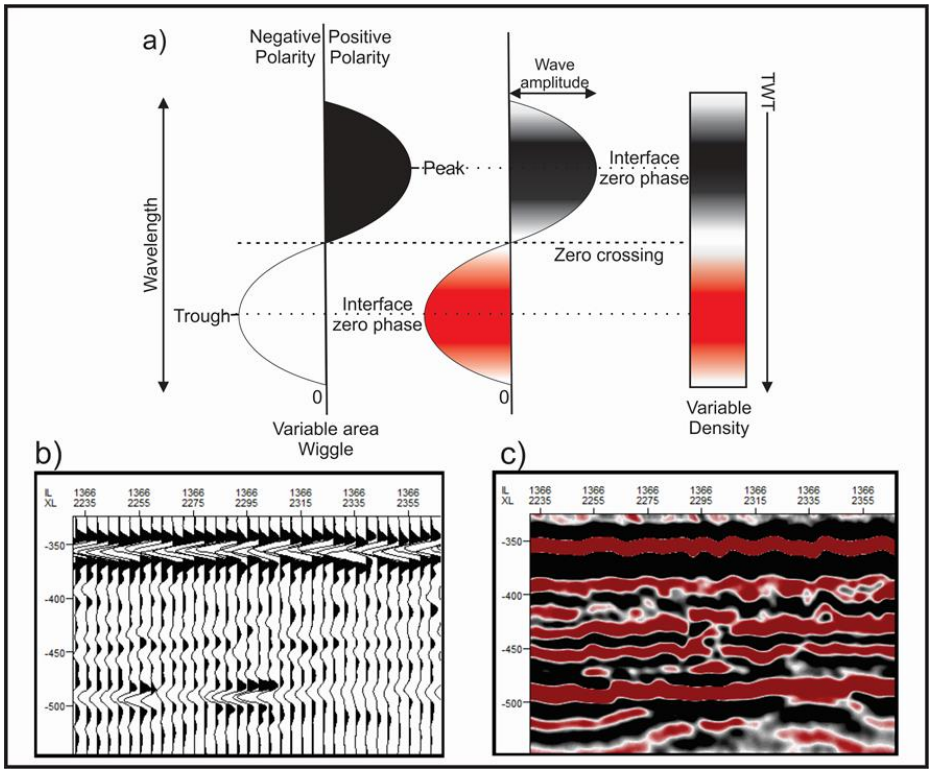

Figure 3-3: Society of Exploration Geophysicists (SEG) normal polarity classification. a) Variable area wiggle with peaks (in black) representing an increase in impedance and positive amplitudes of a wavelet. The troughs (in white) represent negative amplitudes and decreases in acoustic impedance. In the variable density display, colour-coded voxels indicate the peaks in black, troughs in red and zero amplitude areas in white (Modified from Hart, 1999 and Brown, 2011). b) Random seismic transect of the study area in the variable area wiggle trace. c) The same seismic transect as a variable density display, allowing an easier interpretation of the data.

3.2.3. Seismic resolution

Seismic resolution is one of the key parameters used to assess the quality of seismic data, and is related to the ability to recognise two points that are close to each other, and still can be detected (Yilmaz, 2001). In other words, seismic resolution is the measurement of how small a geologic feature, such as the thickness of a sedimentary bed, or a fault, can be distinguished in a seismic dataset (Zhou, 2014).

Vertical resolution, also called temporal or depth resolution, quantifies the closeness of two reflections, one at the top and other at the bottom of a rock layer, that can be distinguished (Yilmaz, 2001). The vertical resolution is determined along the direction of wave propagation by a reflected pulse-length on the seismic profile, and it is measured in terms of wavelength (Kearey et al., 2013).

Seismic wavelength varies from around 40 m in the shallower parts of seismic volumes and 250 m at depth (Brown, 2011). These values show an increasing tendency with depth since the velocity becomes higher at depth due to the effects of sediment compaction, and frequency decreases progressively due to wave (signal) absorption (Kearey et al., 2013). As the resolution decreases with increasing wavelength, it is noted that the resolution deteriorates with depth.

Sheriff and Geldart (1995) stated that the maximum possible resolution for a reflected pulse, represented as a wavelet, varies between one-quarter ($\lambda/4$) and one-eighth ($\lambda/8$) of the dominant wavelet wavelength. Typically, one-quarter of the wavelength is assumed by many authors as the preferred maximum resolution (Brown, 2011; Hart, 1999; Kearey et al., 2013; Liner, 2004; Lowrie, 2007; Yilmaz, 2001; Zhou, 2014). The threshold for

vertical resolution may depend on the noise level of the data allowing, for example, rock layers with a thickness of up to λ/30 to be detected (Yilmaz, 2001). However, the seismic amplitude and frequency may vary below the conventional limits of the seismic resolution, indicating the possibility of recovering the frequency beyond the seismic data bandwidth and inferring layer thicknesses below the seismic sample rate (Chopra et al., 2006).

The detection of smaller features on seismic data can be achieved by increasing the dominant frequency of the stacked seismic data, either by recording or by processing the raw seismic data (Yilmaz, 2001). During the recording of seismic data, it is necessary to use adequate receiver arrays and antialiasing filters in order to prevent and reduce the loss of high-frequency signal due to the statics. During the processing of the obtained data, the primary concern is the removing of any statics that can reduce the high-frequency signal before stacking the data and with the preservation and display of the high-frequency signal. Deconvolution is the tool used to ensure that the high-frequency signal is displayed on the stacked data.

The horizontal or lateral resolution defines how close two points can be and still be recognised as two individual features, rather than one (Yilmaz, 2001). Compared to the vertical resolution, the quantification of horizontal resolution in more complex, as it is necessary to consider the detector (hydrophone) spacing and the properties of seismic waves (Kearey et al., 2013). The detector spacing is related to the position of the hydrophones as previously discussed in the section "Seismic Acquisition". Receivers must be kept closely from each other to make sure the reflection will be reliably correlated, as horizontal resolution decreases with reflection depth. From Figure 3-4 it is

noted that reflections must be spaced at a distance that is equal to half the detector spacing. The seismic waves properties, such as the dominant frequency, the depth of the reflecting interface, and the velocity above the reflector, must be considered when quantifying horizontal resolution (Kearey et al., 2013; Yilmaz, 2001).

The seismic reflection method is better described when considering an infinite number of rays travelling down onto a horizontal reflector through a circular area called the Fresnel Zone (Figure 3-5). The Fresnel Zone is also the horizontal resolution limit of the seismic data, defined by the energy that returns to the seismic detector within one-half of the wavelength of the primary wave front. This is the half-wavelength constructive condition necessary to reflect a coherent seismic signal (Kearey et al., 2013; Liner, 2004; Zhou, 2014).

The size of the Fresnel Zone is related to the reflector depth. The dominant frequency tends to be lower with depth after considering the effects of absorption. This leads to an increase in wavelength and in velocity of seismic waves with depth, which consequently results in a lower seismic resolution (Brown, 2011; Kearey et al., 2013; Liner, 2004). The width of the Fresnel Zone is related to the dominant wavelength λ of the source, and to the reflector depth z such as (Equation 3-2):

$$w = \sqrt{2z\lambda}$$

Equation 3-2

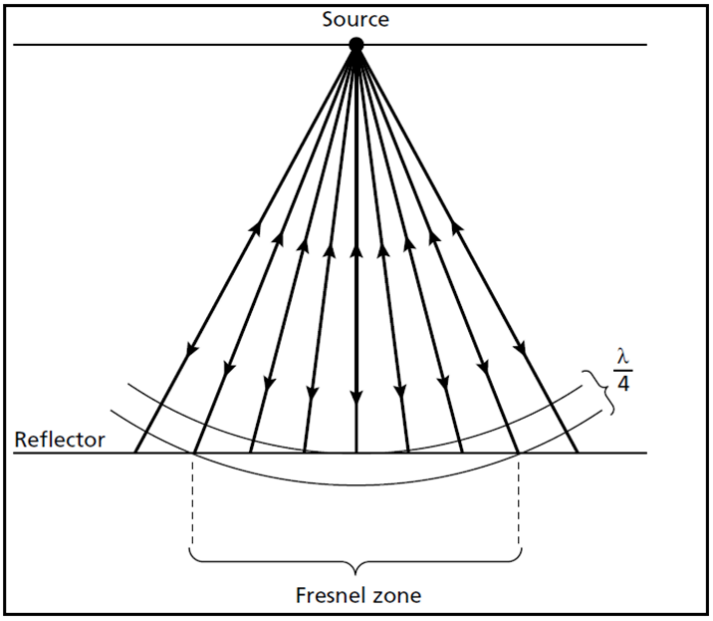

Figure 3-4: The Fresnel Zone, or the horizontal resolution of the seismic data. The energy that returns to the seismic detector is half the wavelength of the detector spacing. Figure from Kearey et al., (2013).

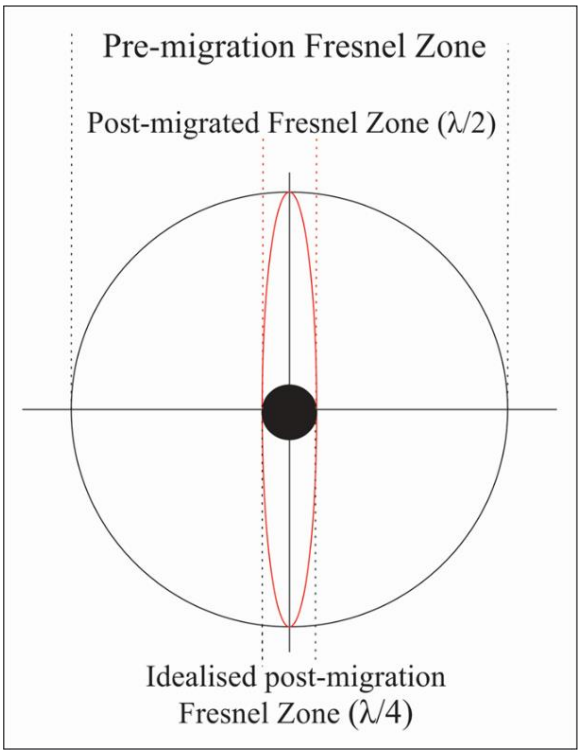

Figure 3-5: The large circle represents the Fresnel Zone prior to data migration. The oval red form is the Fresnel Zone after migration, which shows the wavelength reduced by half. The black dot located in the centre of the circle represents the idealised post-migration of the Fresnel Zone, with the wavelength reduced by a quarter. Modified from Brown (2011).

The limit of the receiver's horizontal resolution is also represented by the width of the Fresnel Zone, as closely spaced features separated at depth by a distance smaller than the Fresnel Zone cannot be distinguished (Liner, 2004). The lateral resolution limits of the Fresnel Zone apply to seismic data that are not migrated.

Seismic data must be processed and migrated to produce a 3D volume or cube, which will be further interpreted. Data processing consists in the collection of seismic reflection events falling into the same area, the common midpoint (CMP) gather, to create a CMP stack that will improve the signal-to-noise ratio (Yilmaz, 2001; Zhou, 2014). Migration of the stacked seismic data is another essential step in the processing sequence and involves the movement of dipping events to their correct position, rather than their recorded location. In addition, data migration focuses seismic energy that is spread over the Fresnel zone and collapses diffraction patterns from points and edges (Bacon et al., 2007). The Fresnel Zone is, thus, ideally reduced to a circle with a radius of a quarter the wavelength, as showed in Figure 3-5. In practice, however, it is more likely for the Fresnel Zone to be reduced to approximately half of the radius (Brown, 2011). Data improvements resulting from the migration of seismic data include a reduction in noise and a relative increase in horizontal resolution.

3.2.4. Time-depth conversions

The vertical scale of 3D seismic volumes is usually recorded in milliseconds (ms) two-way time (TWTT). In order to convert TWTT into true depth (D), the one-way travel

time distance (TWTT/2; in seconds) must be multiplied by the P-wave velocity (V) estimated for the considered stratigraphic interval, such as in Equation 3-3:

$$D = \frac{TWTT}{2} \times \frac{V}{1000}$$

Equation 3-3

Velocity data for the three case studies in this thesis were obtained using well-log information (Chapters 4 and 6). For Chapter 5, the time conversions were attained using information from DSDP Site 516 (Barker et al., 1983), located in the Santos Basin. Further details are indicated in the section *3.2.2.*

3.3. Datasets used in this thesis

This thesis used three different seismic datasets. The location, acquisition and processing parameters of each of the interpreted seismic surveys will be summarised in this section. This section will also outline additional data used in this research, including 2D lines and wells. The timing(s) of salt dome growth and collapse, and associated fault formation in the Samson Dome area, were analysed using a seismic dataset located in the Barents Sea, offshore Norway, provided by the BG Group. The controls of salt growth in fault reactivation and compartmentalisation in the Espírito Santo Basin, Southeast Brazil, were investigated using a 3D seismic volume provided by CGG. The effect(s) of fault reactivation on the geometry of submarine channels was assessed using a dataset from

the Taranaki Basin, offshore New Zealand, provided by the New Zealand Petroleum Board.

3.3.1. Chapter 4

The interpreted seismic volume covers an area of 1,840 km^2 on the Bjarmeland Platform, at a maximum water depth of approximately 296 m. The seismic data were pre-stack time-migrated with a 12.5 x 25 m line spacing, and were acquired with a 10 x 6,000 m array of streamers, each with 480 geophones. The seismic data are in the time domain, zero-phased, and were processed within a 4 ms vertical sampling window. The seismic profiles in this thesis are displayed using the normal SEG convention for a zero-phase wavelet such that an increase in acoustic impedance with depth is a peak or positive reflection. Peaks are black reflections on seismic profiles, and relative decreases in acoustic impedance are shown as negative or red seismic reflections.

Data processing for the Barents Sea data included resampling, TAU-P linear noise attenuation, TAU-P domain deconvolution and zero-phase conversions undertaken prior to the 120-fold stacking of seismic traces. Three-dimensional pre-stack time migration was completed using the Kirchhoff algorithm. In addition to the 3D seismic survey, regional 2D seismic data (line SG8737-112) was used to tie the observed structures to the geological context of the Bjarmeland Platform and surrounding areas. Wells 7224/7-1 and 7214/3-1 are located along the interpreted 2D seismic line in Figure 3-6.

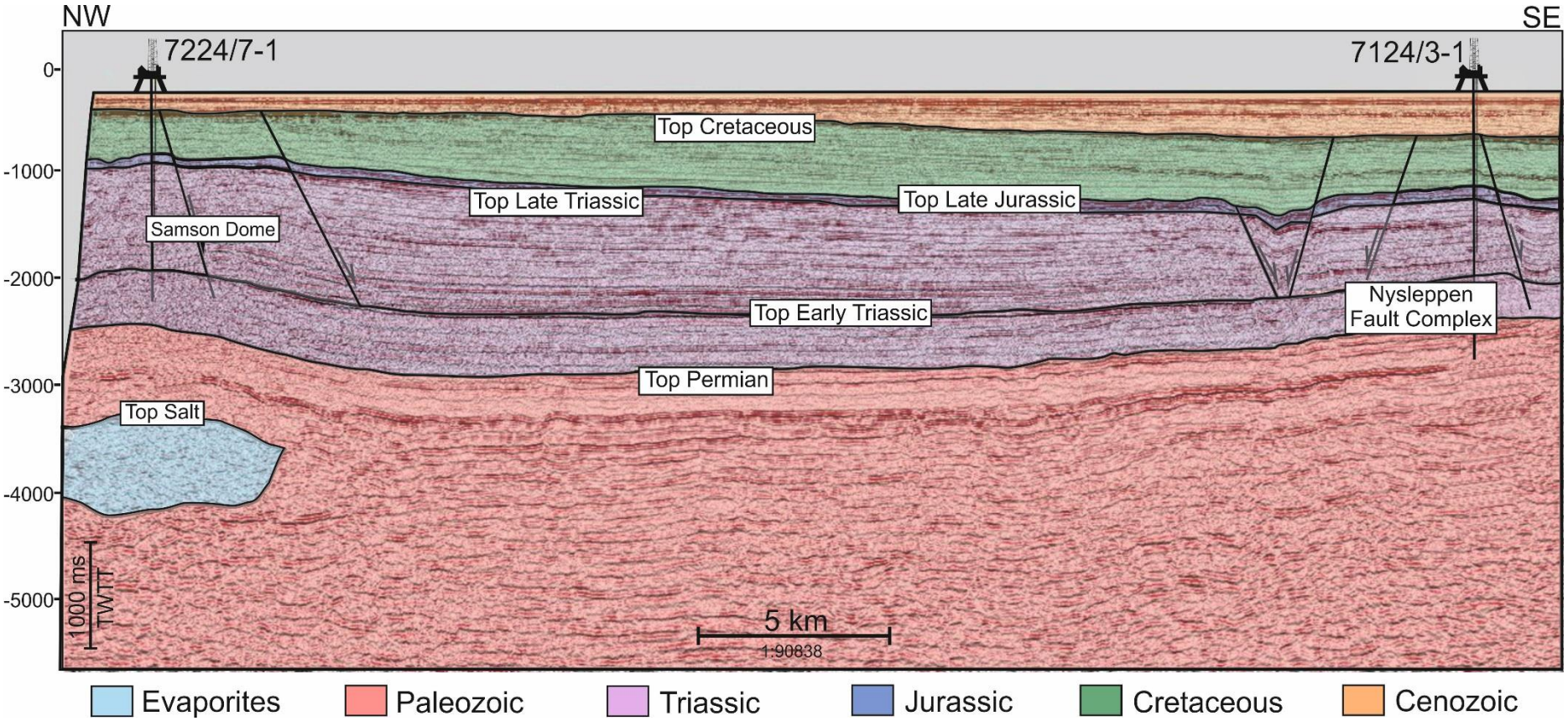

Figure 3-6: Interpreted regional seismic profile of the Bjarmeland Platform indicating the location of the Samson Dome and Nysleppen Fault Complex. Wells 7224/7-1 and 7214/3-1 are located along this seismic profile

Well 7224/7-1, a wildcat drilled by Den Norske Stats Oljeselskap A.S. in 1988, crossed the Samson Dome (Figure 3-6). Well 7224/7-1 aimed at evaluating the reservoir potential of Late Triassic and Early Jurassic sandstones, and tested previous geophysical and structural interpretations (NPD, 2004). The well has a total depth of 3067 m (RKB) and penetrates strata spanning in age from the Early-Middle Triassic (Sassendalen Group) to the Pliocene-Pleistocene (Nordland Group).

Well 7124/3-1 comprises a wildcat drilled by Saga Petroleum ASA in 1987 (Figure 3-6). This well penetrated the Nyslepp Fault Complex, east of the Hammerfest Basin, and reached a total depth of 4730 m. The primary aims of the well were to test the presence of hydrocarbons in Middle Jurassic strata, to investigate the source rock potential of Triassic rocks, and to characterise Upper Carboniferous reservoir rocks. Well 7124/3-1 is the reference well for the Bjarmeland Group and Ørret Formation (Late Carboniferous-Early Permian). Strata penetrated by this well range from the Late Carboniferous (Ørn Formation) to the Plio-Pleistocene (Nordland Group).

An average P-wave velocity of 5500 m/s TWT is recorded in strata crossed by well 7224/7-1 and was used for time-depth conversions. As the well 7224/7-1 was drilled without crossing Permian strata, P-wave velocities of 5800 m/s for Upper Permian strata and 6000 m/s for the Mid Permian were based on the average velocities in well 7124/3-1 (Alves, 2016). These velocities were used to convert the mapped faults and horizons to depth, and to obtain true dip values for faults.

3.3.2. Chapter 5

The interpreted 3D seismic volume covers an area of 1,670 km^2 in the Espírito Santo Basin, at a water depth between 100 m to 1,800 m (Figure 3-7). These seismic data were pre-stacked time migrated with a 12,5 x 12,5 m grid line spacing. They were acquired with a 6 x 5,700 m array of streamers. The seismic data are in the time domain, zero-phased, and were processed within a 2 ms vertical sampling window. Resampling at 4 ms and application of anti-aliasing filter, TAU-P linear noise attenuation, and TAU-P domain deconvolution preceded the stacking of the seismic volume. Three-dimensional pre-stack time migration used the Kirchhoff algorithm.

The interpreted seismic profiles for SE Brazil are displayed in the standard European polarity convention for a zero-phase wavelet, with peaks of acoustic impedance shown as grading red reflections on seismic profiles and relative decreases in acoustic impedance with depth shown as grading blue seismic reflections (Figure 3-8). The vertical extent of the seismic survey is limited to a depth of 4.0 s Two-Way Travel Time (TWTT). Average seismic velocity data from DSDP Site 516 (Barker et al., 1983) include P-wave velocities of 3100 m/s for the Late Cretaceous-Paleocene interval, and P-wave velocities of 2100 m/s and 1800 m/s for Eocene-Oligocene and Miocene-Holocene strata, respectively (Figure 2-8). These velocities were used to convert mapped faults and horizons at depth, and to obtain the true dip of faults.

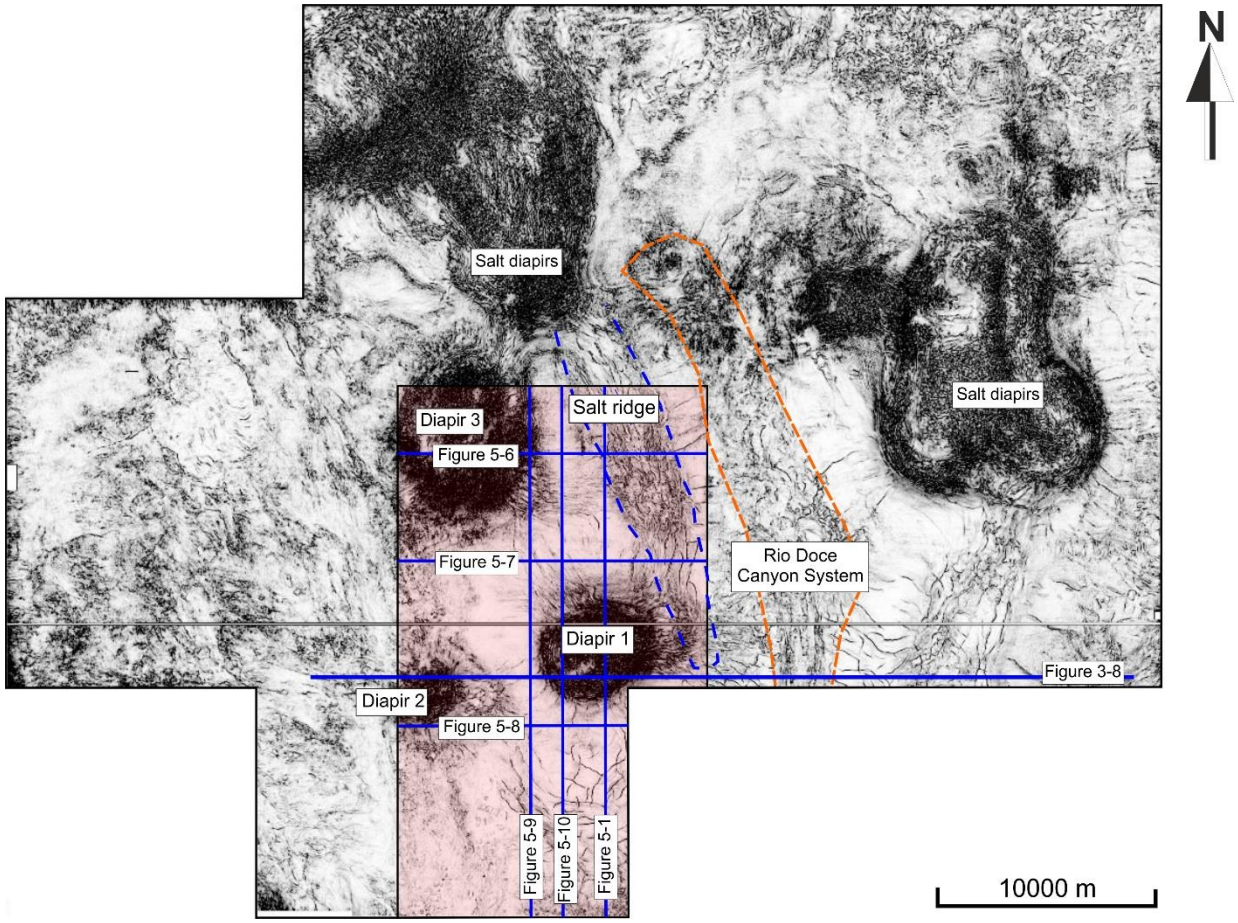

Figure 3-7: Variance time-slice at -3250 ms showing the main geological features in block BES-2. Salt diapirs and ridges are the most distinctive structures in this seismic cube. The Rio Doce Canyon System is delimited by the orange dashed line. The area of interest of this study is delimited by the red polygon. Three radially faulted salt diapirs and a faulted salt ridge are observed within the study area. A large number of faults are observed to the south of the polygon.

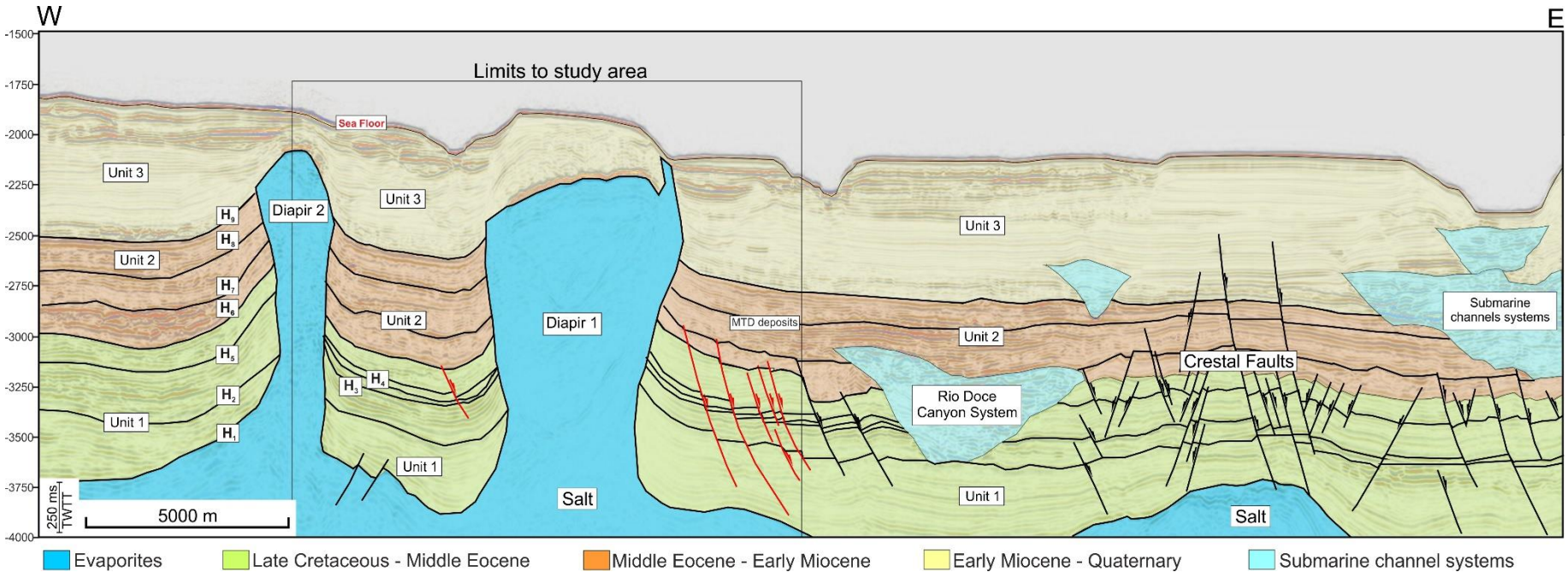

Figure 3-8: Interpreted W-E regional seismic profile of the Espírito Santo Basin showing the main structures of the study area. The black polygon delimits the area of interest, while faults adjacent to Diapir 2 are indicated in red.

3.3.3. Chapter 6

The Parihaka survey covers an area of 1520 km^2 in the NW part of the Taranaki Peninsula, at a maximum water depth of ~ 132 m (Figure 3-9). The survey was acquired using an 8 x 4500 m array of streamers, each with 360 geophones. Data processing included zero-phase conversions, data resampling to a 4 ms vertical sampling window, High-Resolution Radon Transform (XRLIN) linear noise attenuations, TAU-P domain predictive deconvolutions, and NMO corrections to the 60-fold coverage of the seismic trace. A Kirschhoff time migration algorithm was applied to a 1 km grid. The final output interpreted in this thesis consists of stacked data with a line spacing of 12.5 x 12.5 metres. Seismic sections are displayed in normal SEG convention, with increases in acoustic impedance (peaks) displayed as black seismic reflections, and relative decreases in acoustic impedance (troughs) as red seismic reflections. Data from completed time-depth conversions, using check-shot data for well Arawa-1, provided a velocity of ~2000 m/s for the interval studied in this thesis (Giba et al., 2012; Salazar et al., 2015).

The well Arawa-1, is located at the centre of the Parihaka 3D seismic volume, approximately 40 km northwest of New Plymouth. In this well, Arco Petroleum NZ Inc. drilled to a total depth of 3055 m in 1991. The primary goals for the company were to investigate the occurrence of bathyal sandstones in the Miocene Moki Formation, and to test seismic evidence for hydrocarbons in the study area (Arco, 1992). Since only three gas peaks were found in this well, the well Arawa-1 was plugged and abandoned in 1992.

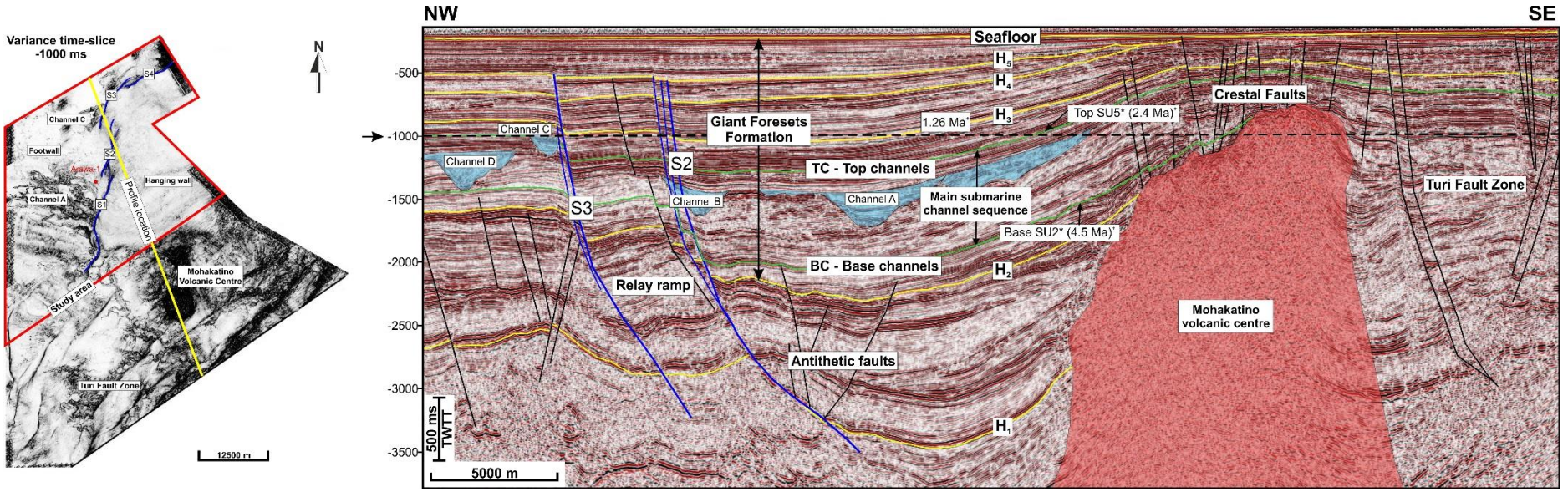

*Figure 3-9: Regional seismic profile of the Parihaka 3D seismic volume showing a relay ramp developed between segments S3 and S2, and the main channel systems occurring in the study area. The Mohakatino Volcanic Centre is observed to the SE of the seismic line. The main submarine-channel sequence is delimited by the horizons marked in green. *Equivalent seismic units from Salazar et al. (2016). +Equivalent ages from Morgans et al. (2006).*

3.4. Seismic interpretation

The interpretation of seismic data in this thesis was entirely undertaken at the 3D Seismic Lab, Cardiff University, and used Schlumberger's Petrel© 2014. This section will provide a description of the methods used to interpret faults and horizons in the study area. It will also summarise the seismic attributes used to reveal key geological features in the interpreted seismic cubes.

3.4.1. Horizon and fault interpretation

A number of seismic reflections were mapped as horizons representing stratigraphic features in the three study areas. Horizon interpretation for 4 *and 6* was assisted by stratigraphic data from industry wells. Once the stratigraphic data from exploration wells were tied to the seismic volumes, key seismic horizons were first manually interpreted along the inline and crossline directions. The line spacing chosen to interpret each seismic horizons varied according to the structural complexity of specific areas. Laterally continuous reflections were mapped using a 30 to 10-line spacing. Smaller intervals, ranging from 2 to 5 lines, were used to map areas of higher structural complexity such as those affected by halokinesis in Chapters 4 *and 5*.

Manually picked seismic reflections were used as seed points for the automatic horizon tracking. The autotracking (or autopicking) option on Petrel 2014 consists of distinct algorithm operations that seek to identify similar features in terms of phase

and amplitude in surrounding seismic traces (Dorn, 1998; Hart, 1999). If the autotracker finds similarities among neighbouring seismic traces, it will pick the trace and move on to the next trace. If the search criteria are not met, the autotracker stops at that trace (Dorn, 1998). In areas with relatively low signal-to-noise ratios, or with geological complexity, the autotracking option may face difficulties. Manual checking and constant edits of the autotracked horizons are thus necessary to establish a locally continuous, reliable stratigraphic framework (Hart, 1999).

Local structural elements were interpreted using the fault interpretation tool. Faults were interpreted along inlines, crosslines and arbitrary lines. The line spacing selected for fault interpretation varied according to the nature and complexity of the investigated structures, but the line spacings most frequently adopted were 3, 5 and 10. A tighter line spacing was preferred for the provision of accurate interpolations between the faults and to provide reliable displacement analyses. The number of fault sticks for each fault varied according to its length. However, each mapped fault had, at least, three fault sticks.

3.4.2. Volume and seismic attributes

Once the mapping of horizons was completed, seismic attribute analyses were carried out in this thesis to reveal the geometry of geological features of interest. Volume attributes used in this thesis include amplitude, root-mean square (RMS) amplitude, dip and coherence (variance) data (Figure 3-10).

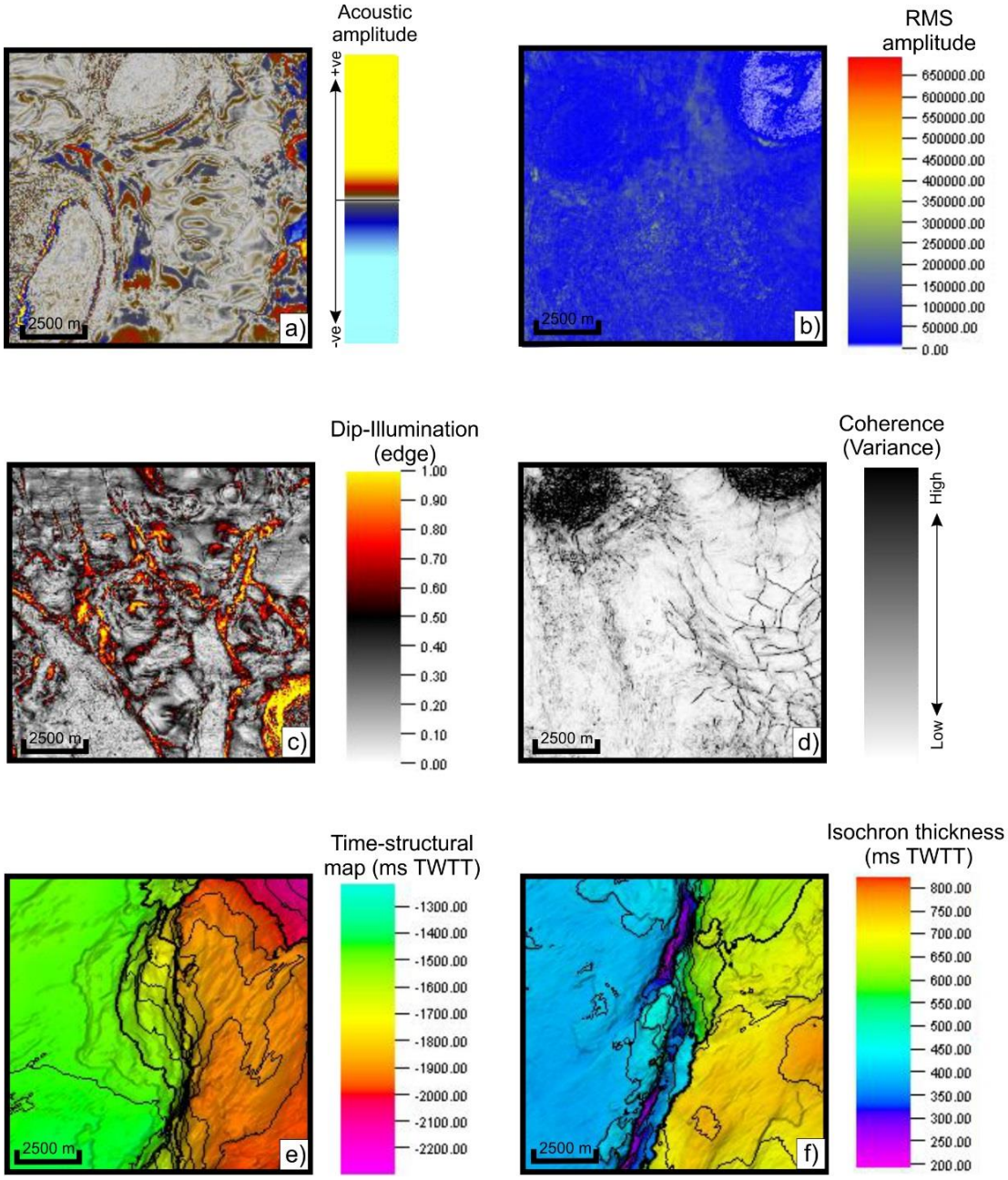

Figure 3-10: Examples of volume attributes used in this thesis. a) Amplitude, b) RMS amplitude, c) Dip (edge), c) Coherence (variance). Time attributes used in this thesis. e) Time-structural map, f) Isochron map.

Amplitude is one of the fundamental attributes of seismic data and is displayed at any point along an interpreted seismic horizon (Brown, 2011). This attribute represents the maximum displacement of the wave at the crest of the reflection wavelet and can be either positive or negative (Figure 3-10a). The amplitude of a seismic reflection varies due to changes in acoustic impedance, which can be caused by variations in subsurface lithological properties (e.g. porosity, thickness and bedding geometries) and fluid content (Brown, 2011). Close to structural heterogeneities such as faults and fractures, it is possible to observe a reduction in the amplitude of seismic reflections, allowing for the mapping of these structures in the seismic profiles.

Root-mean-square (RMS) amplitude is an attribute that shows the average squared amplitude values for individual data samples within a defined interval (Brown, 2011). RMS amplitude maps highlight the occurrence of structures as seismic wavelets are distorted and lose amplitude across faults due to destructive interference of seismic energy (Figure 3-10b). In this thesis, RMS amplitude maps were created to constrain the interpretation of faults and to characterise the geometry of salt diapirs in Chapters 4 and 5.

Dip maps are time-derived and comprise a useful attribute to image faults with small throws (Figure 3-10c). The variations in the horizon gradient are measured through the comparison between the time values of adjacent points of an interpreted seismic reflection (Brown, 2011). Dip maps are useful to the interpretation of seafloor features and to characterise the morphology of deeper seismic horizons.

Coherence (variance) is a geophysical attribute calculated through the application of filters controlling the inline and crossline length and the vertical smoothing of the

data set. It results in the conversion of seismic-amplitude volume into a discontinuity volume (Figure 3-10d). This attribute isolates the edge amplitudes of the seismic volume and is used to highlight its most prominent amplitude discontinuities, such as faults and fractures, salt structures and igneous intrusions (Brown, 2011). Coherence can also be used to detect depositional features such as channels and carbonate reefs (Schlumberger, 2014).

Apart from the use of volume attributes, time attributes comprise an important complement to the analysis of seismic horizons and associated structures. **Time-structural maps** are derived from time attributes, such as dip, and integrates the structural and stratigraphic aspects of the seismic data (Brown, 2011) (Figure 3-10e). Time-structural maps were employed in this thesis to show the morphology of seismic horizons and to image faults with large throws. The use of time-structural maps was complemented by **isochron maps**, which display the time difference between two reference horizons. Isochron maps provide information on the thickness and lateral extent of sedimentary units and their sub-units (Figure 3-10f).

3.5. Structural analyses

Once fault were interpreted on the seismic profiles and coherence time-slices on Petrel®, they were imported into Midland Valley Move® as 3D-mesh surfaces to be later filtered for edge triangles. Key fault attributes, including true dip, strike and azimuth were created on Move® for each fault vertex using the Attribute Analyser

Toolbar. Fault surfaces were then individually imported into 3D Stress® for stress modelling. Fault analyses completed for this thesis include displacement analyses, stress analyses and the creation of juxtaposition diagrams.

3.5.1. Displacement-length (D-x) analyses

The mechanisms of initiation, growth, and evolution of faults through time can be depicted using displacement data (e.g. Baudon and Cartwright, 2008; Cartwright and Mansfield, 1998; Cartwright et al., 2008). In particular, the relationship between maximum displacement (D_{max}) and the length (x) of a fault trace is the basis of displacement-length (D-x) analyses (Chapman and Williams, 1984; Cowie and Scholz, 1992c; Dawers and Anders, 1995; Muraoka and Kamata, 1983; Nicol et al., 2002; Peacock and Sanderson, 1991; Pollard and Segall, 1987). Displacement variations were computed using Microsoft Excel® at a defined cut-off horizon for representative faults in *Chapters 4 and 5*. Displacement and distance data, originally in two-way travel time (ms TWTT), were converted to metres in a second stage. Plots of maximum displacement (D_{max}) against length (x) for the faults interpreted in each case study were then compared to data previously published (e.g. Muraoka and Kamata, 1983; Scholz and Cowie, 1990; Walsh et al., 2002; Walsh and Watterson, 1987) for normal, strike-slip and reverse faults, using the Fault Analysis Module in Midland Valley Move®.

3.5.2. Throw-depth (T-z) analyses

Throw-depth relationships were calculated for representative faults using seismic profiles orthogonal to the fault strikes, and considering the difference between seismic reflections on footwall and hanging-wall cut-offs (Baudon and Cartwright, 2008a; Mansfield and Cartwright, 1996; Omosanya and Alves, 2014). Throw and heave comprise the vertical and the horizontal displacement components on a fault (Figure 3-11).

Throw measurements were displayed for individual fault sections with the throw in the horizontal axis and the depth on the vertical axis. In Chapter 4, throw measurements were undertaken at intervals of 25 m, whereas in Chapter 5 an interval of 10 m was used to document the subtle changes in the throw gradients observed. The resulting T-z profiles were created in Microsoft® Excel, with values displayed in two-way travel time (ms TWTT).

An error of ± 2ms was considered based on the vertical sampling rate, verified on on-screen wiggle displays. Pitfalls in the throw measurements are derived from the occurrence of drag folding adjacent to the fault plane (Baudon and Cartwright, 2008a, 2008b; Mansfield and Cartwright, 1996; Walsh and Watterson, 1987). To provide consistent throw analyses throughout the core chapters of this thesis, drag folds with large wavelengths (> 100 m) were considered part of fault deformation and were included in the throw measurements. Drag folds with smaller wavelength were not considered part of the fault, and the measurements took place at the points closest to

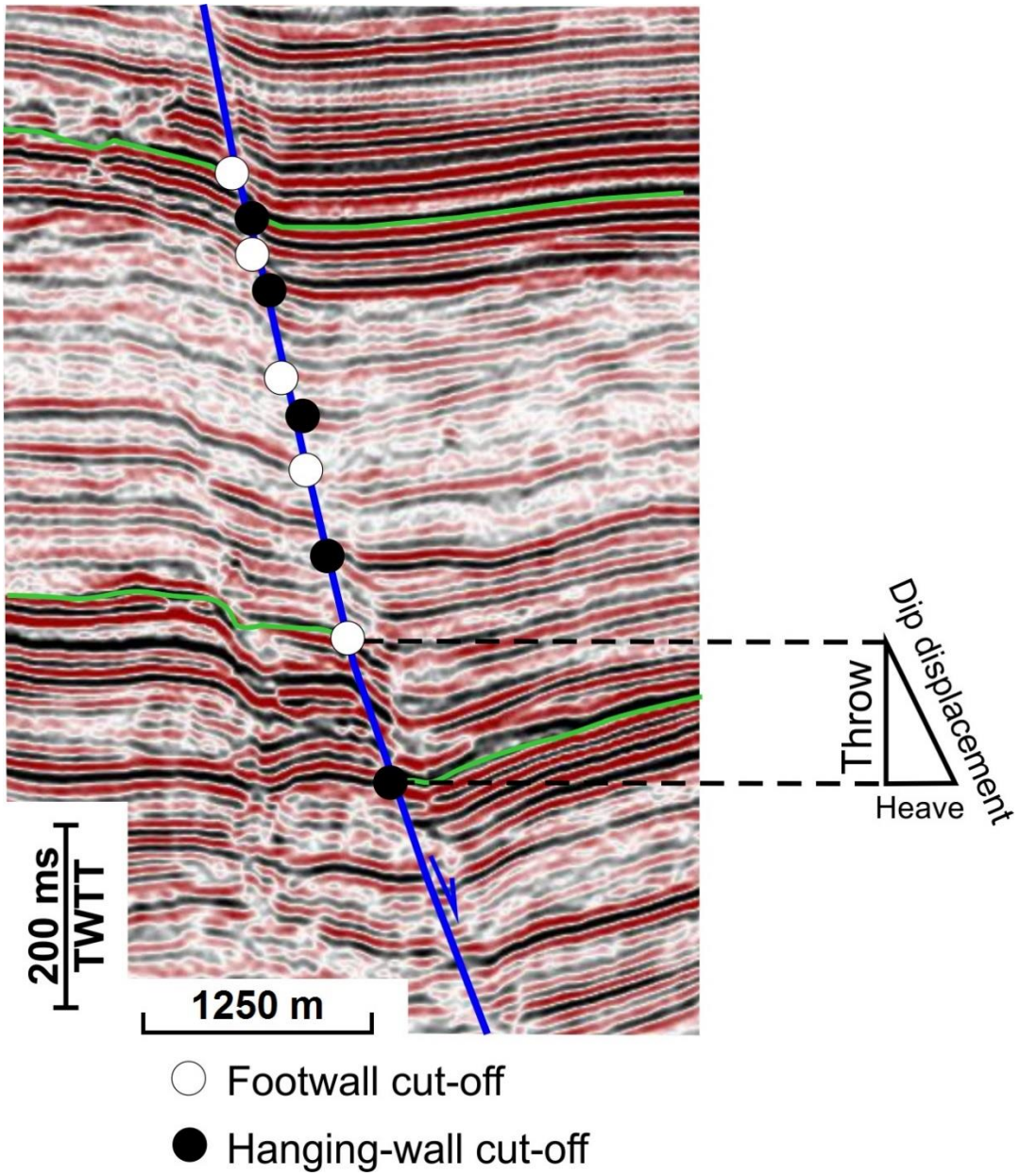

Figure 3-11: Representation of a interpreted fault in the Taranaki Basin (Chapter 6) to illustrate the technique used to estimate the throw from the difference between footwall (represented by the white dots) and hanging-wall cut-offs (represented by the black dots). The heave is the horizontal component of the displacement and the dip displacement is the square root of the sum of the vertical and the horizontal displacement components.

represent the hanging-wall and the footwall cutoffs (Baudon and Cartwright, 2008a, 2008b; Mansfield and Cartwright, 1996).

3.5.3. Stress analyses

Fault analyses were performed to assess the orientation and the distribution of tectonic stresses across the study area (Morris et al., 1996). After mapping the faults in *Chapters 4 and 5,* the stress inversion method of M^{c}Farland et al. (2012) was applied to determine the principal paleostress tensors associated with these same faults.

Stress analyses can include the case-by-case modelling of the tendency of faults to slip and leak fluids. The *Stress Analysis Module* allows the colour-scaled visualisation of the fault planes more likely to reactivate and leak in a 3D view window. The workflow followed to obtain the 3D model for slip tendency and leakage factors in *Chapter 4* utilised the magnitudes and azimuths of present-day stresses for the Finnmark Platform, obtained from the World Stress Map (Heidbach et al., 2008). Data from the World Stress Map indicate compressional regimes at shallow depths, giving σ_1 as σ_{Hmax}, σ_2 as σ_{hmin}, and σ_3 as σ_v for present-day stress conditions. Stress data are not available for the study area in *Chapter 5* and slip tendency and leakage factor for faults in the Espírito Santo Basin were modelled using only the azimuths and magnitudes of the principal paleostress tensors via fault inversion.

The workflow used to obtain leakage factor values is similar to that for slip tendency. The magnitudes and azimuths from the paleostress analysis or present stress

data were used together considering the fluid pressure (P_f) for the studied areas. The fluid pressure values were obtained considering the depth of the unit of interest, or borehole breakouts, if available, and the depth of the water column above the seafloor.

4. Crestal fault geometries reveal late halokinesis and collapse of the Samson Dome, Northern Norway: Implications for petroleum systems in the Barents Sea

Abstract

This chapter uses 2D and high-quality 3D seismic reflection data to assess the geometry and kinematics of the Samson Dome, offshore Norway, stressing the implications of the new data to hydrocarbon exploration in the Barents Sea. The study area was divided into three (3) zones in terms of fault geometries and predominant strikes. Displacement-length (D-x) and Throw-depth (T-z) plots showed faults to consist of several segments that were later dip-linked. Interpreted faults were categorised into three families, with Type A comprising crestal faults, Type B representing large E-W faults found in the northwest of the study area, and Type C consisting of polygonal faults. The Samson Dome developed in three major stages: a) a first stage recording buckling of the post-salt overburden and formation of radial faults; b) a second stage involving dissolution and collapse of the dome, causing subsidence of the overburden and linkage of initially isolated fault segments; and c) a final stage in which large fault segments were developed. Faults formed during the Late Cretaceous strike predominantly to the NW, whereas NE-trending faults comprise Triassic structures that were reactivated in a later stage. The results obtained in this chapter provide scarce evidence for the escape of hydrocarbons in the Samson Dome, in contrast to previous work. In addition, fault analyses based on present-day stress distributions indicate a tendency for 'locking' of faults at depth, with the largest leakage factors occurring close to the surface. The Samson Dome is an analogue to salt structures in the Barents Sea where oil and gas exploration has occurred with varied degrees of success.

4.1. Introduction

The Barents Sea is a region where hydrocarbon potential is larger in basins associated with salt tectonics (Bugge et al., 2002; Chand et al., 2008; Henriksen et al., 2011a, 2011b; Koyi et al., 1993; Nilsen et al., 1995; Perez-Garcia et al., 2013; Stoupakova et al., 2011). However, most halokinetic structures in the region are poorly studied due to the sparse availability of high-resolution data. So far, most published studies on the Barents Sea used 2D seismic data of regional extent and limited resolution (Breivik et al., 1998, 1995; Faleide et al., 1993; Gabrielsen et al., 2013, 1990; Gernigon and Brönner, 2012; Glørstad-Clark et al., 2010; Gudlaugsson et al., 1998). This relative absence of high-quality 3D seismic data has led to incomplete structural interpretations in areas where salt tectonics is an important control on Late Palaeozoic and Early Mesozoic reservoir compartmentalisation, as shown in this paper.

The present chapter is focused on the Samson Dome (Figure 2-1), a structural high located in the Ottar Basin (Breivik et al., 1995). The Ottar Basin comprises a Permian depocentre developed on the Bjarmeland Platform (Gabrielsen et al., 1990). The anticlinal structure that forms the Samson Dome is thought to result from the Middle to Late Triassic halokinesis (Breivik et al., 1998, 1995; Gabrielsen et al., 1990). Recently, Vadakkepuliyambatta et al. (2013) found shallow gas and widespread evidence for fluid leakage through faults in the Samson Dome. This leakage zone, at approximately 141 km^2, was considered as one of the largest fluid-flow features in the western Barents Sea (Vadakkepuliyambatta et al., 2013).

This chapter uses 3D and 2D seismic data to reassess the geometry and kinematics of the Samson Dome, Barents Sea, including an evaluation of the timing of salt growth, collapse and associated fault formation. In summary, this work aims at addressing the following research questions:

a) What is the history of fault growth and propagation in the Samson Dome area, and how does halokinesis influence fault styles?
b) Is there a late strike-slip reactivation affecting the Samson Dome area during the Late Mesozoic?
c) How does the current stress regime of the Barents Sea control fluid flow and trapping in the study area?
d) How can the Samson Dome provide insights into the Mesozoic-Cenozoic evolution of the Barents Sea, contributing to the analysis of seal unit competence and fluid migration in regions with similar halokinetic structures?

This study is the first to test previously published 2D structural models for the Samson Dome by using a 3D seismic dataset. Stratigraphic and structural features are enhanced in the interpreted 3D seismic volume, allowing a more detailed evaluation of the dome as a potential fluid-flow and seepage zone. The new data not only provide an insight into the Mesozoic-Cenozoic evolution of the Barents Sea, but also contributes to the analysis of seal unit competence and timings of fluid migration in areas with similar halokinetic structures.

4.2. Database and specific methods

The main data source for this chapter is a 3D seismic volume from the Ottar Basin, located on the Bjarmeland Platform, Barents Sea. For full details of the acquisition and processing parameters of this survey see *Chapter 3 section 3.3.1.* Additional data include the wells 7224/7-1 and 7214/3-1 and the regional 2D seismic line SG8737-112, used to tie the observed structures to the geological context of the Bjarmeland Platform and surrounding areas (Figure 2-2). Details on these wells and the 2D seismic line are also described in *Chapter 3, section 3.3.1*. The general seismic interpretation methods employed in this chapter are described in *Chapter 3, section 3.5*. Displacement analysis methods and the distribution of the tectonic stress across the study area are also detailed in *Chapter 3, section 3.5*.

Seismic interpretation included fault and horizon mapping, seismic attributes and time-depth conversions on Petrel®. Eight (8) key seismic reflections and one hundred and thirty-three (133) faults were mapped on seismic profiles and coherence data. Eight representative faults (F1 to F8) were selected to the displacement-length (D-x) and throw-depth (T-z) analyses.

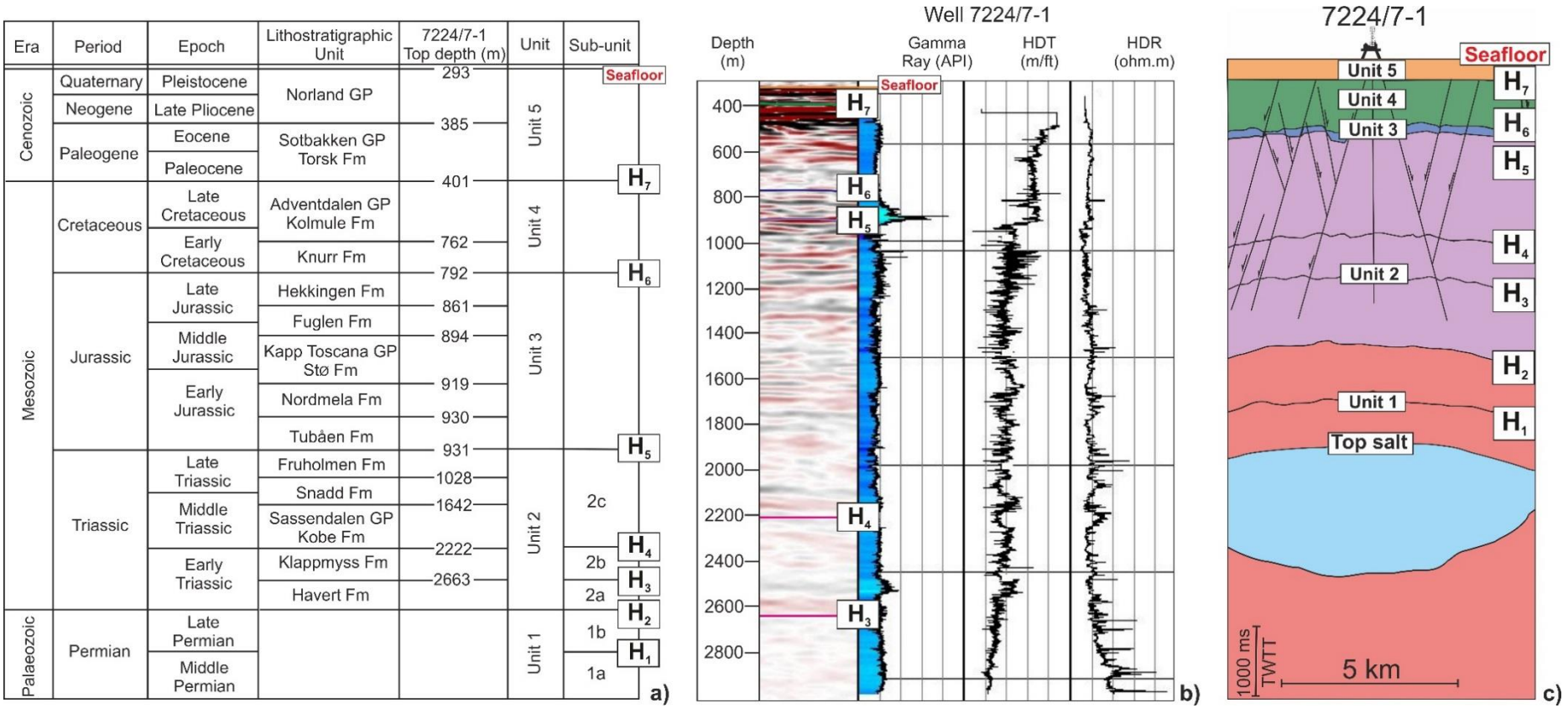

Figure 4-1: a) Simplified stratigraphic column of the Ottar Basin showing the top depth for lithostratigraphic units crossed by well 7224/7-1. The interpreted horizons and respective seismic units are located to the right of this same column. Seismic horizons interpreted below the well 7224/7-1 reach are also indicated. b) Interpreted seismic line and Gamma Ray, Density (HDT) and Resistivity (HDR) logs for the interval of interest in well 7224/7-1. c) Interpreted seismic profile highlighting interpreted horizons, seismic units and faults

*Table 4-1: Seismic characteristics and lithologies of main seismic units interpreted in the study area. Correlation between the seismic units in this work and seismic sequences in the literature: *(Glørstad-Clark et al., 2010); #(Ehrenberg et al., 1998); +(Nilsen et al., 1993).*

Epoch	Seismic Unit	Seismic Sub-unit	Horizon	Thickness (m)	Internal character, geometry and terminations	Lithology (Larssen et al., 2002; Dalland et al., 1988)	Seismic sequences in the literature
Pleistocene	5		Seafloor	108	Discontinuous reflections close to the seafloor. No mapped faults in this unit. Occurrence of bright spots is frequent	Sands and clays grading into sandstones and claystones	
			H_7				
Late Cretaceous	4			391	Strong amplitude and high-frequency positive reflections. Horizon H_7 is truncated on the crest of the Samson Dome. Large and shallow amplitude anomaly cut by faults	Brownish grey to dark grey shales and claystones interbedded with occasional limestone, siltstone and sandstone	
			H_6				
Late Jurassic	3			139	Strong amplitude and high-frequency negative seismic reflections. Offset by faults. Discontinuous reflections on the Samson Dome	Basal and top shales interbedded with siltstones and sandstones	
			H_5				
Late Triassic	2	2c		1291	Strong to moderate and high to medium frequency negative reflections. Offset by faults. Discontinuous reflections on the Samson Dome	Basal grey to dark shales grading upwards into interbedded sandstones, shales and coals	S5*
			H_4				
Early Triassic		2b		441	High amplitude and positive reflections. Constant thickness throughout the study area. Offset by faults on the Samson Dome and away from this structure	Dark grey shales grading upwards into interbedded shales, sandstones and siltstones	S2*
			H_3				
		2a		1537	High amplitude negative reflection. Loss of seismic resolution close to the dome. Seismic reflections offset by faults on the Samson Dome	Medium to dark grey shales with minor intervals of siltstones and sandstones	S1*
			H_2				
Late Permian	1	1b		4200	Low- to moderate-amplitude internal and positive reflections. Continuous over the study area. Not intersected by faults	Calcareous silty shales, calcareous spiculites with clay matrix and shale lenses (Ehrenberg et al., 1998)	L9# Unit IV+
			H_1				
Middle Permian		1a		5500	Strong amplitude and positive reflections. Wavy towards the top of the unit. Loss of seismic resolution close to the dome. Not intersected by faults	Carbonates interbedded with the evaporitic (lenticular) body	L7-L8# Unit II-Unit III+

4.3. Seismic interpretation

The eight (8) seismic horizons interpreted in this study are shown in Figure 4-1 and Table 4-1. These horizons correspond to the tops of the Lower Triassic Havert and Klappmyss Formations, the Upper Triassic Fruholmen Formation, the Upper Jurassic Hekkingen Formation, the Upper Cretaceous Kolmule Formation and the Pleistocene Nordland Group in well 7224/7-1 (Figure 4-1). Furthermore, the eight horizons were grouped into five sedimentary units from the Permian (Unit 1) to the Paleogene-Quaternary (Unit 5), according to their internal character and the geometry of the seismic reflections.

The Middle and Late Permian horizons H_1 and H_2 were not intersected by well 7224/7-1. Hence, they were picked based on their acoustic impedance contrast and data from previous workers in the area such as Alves (2016), Breivik et al. (1995), Ehrenberg et al. (1998), Glørstad-Clark et al. (2010), Larssen et al. (2002), and Nilsen et al. (1993). Younger Permian strata were correlated with regional unconformities crossed by well 7124/3-1 (Figure 3-6).

4.3.1. Unit 1 (Permian)

Unit 1 comprises two sub-units (1a and 1b) bounded by Mid Permian (H_1) and Late Permian (H_2) unconformities (Table 4-1). The Mid Permian horizon (H_1) is marked by a high-amplitude, positive reflection at a depth of approximately 4230 m (Figure 4-2). Strata in sub-unit 1a consist of grainstones and packstones rich in foraminifera and algae

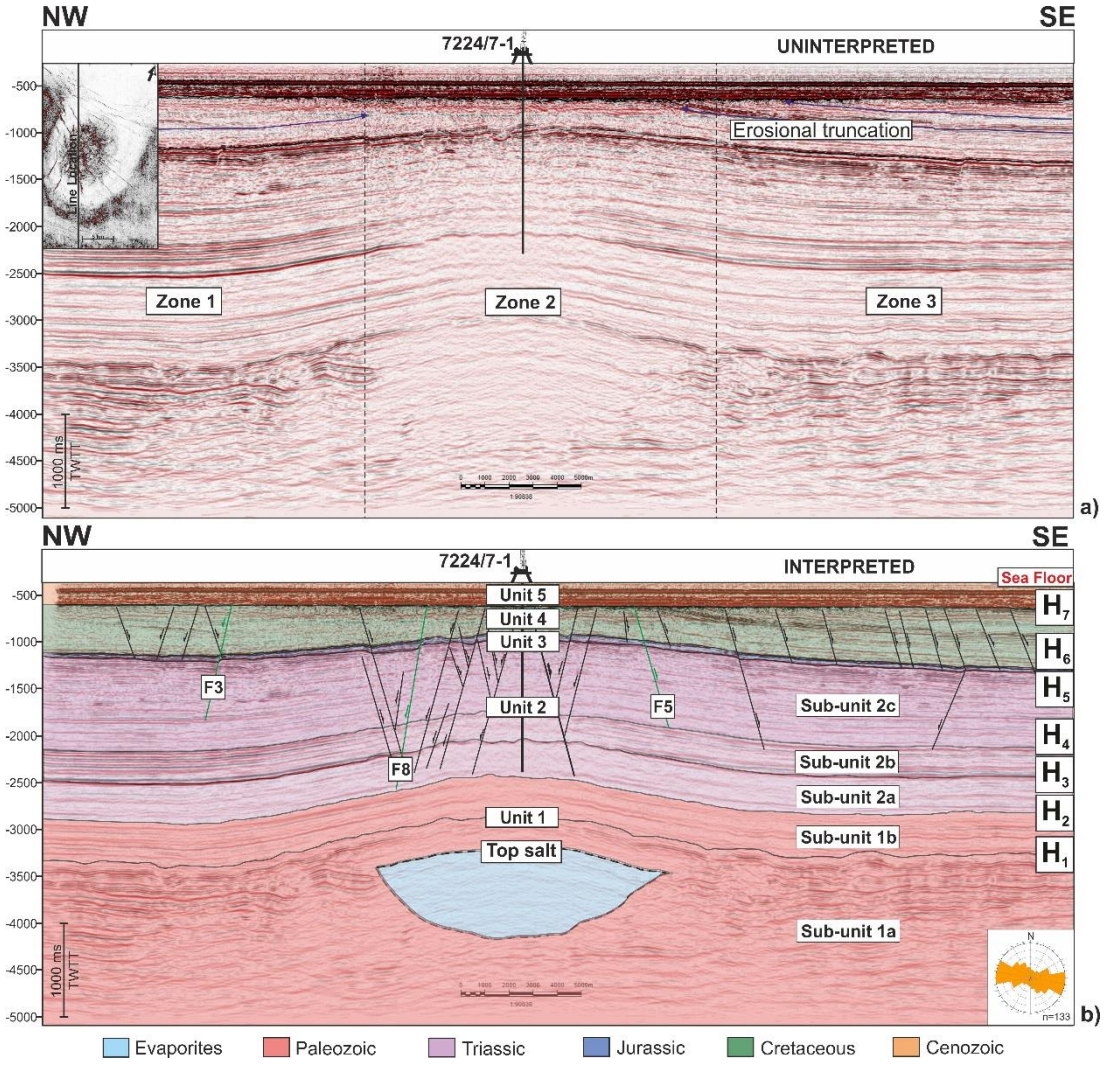

Figure 4-2: a) Uninterpreted SE-NW seismic inline across the Samson Dome. The dashed lines indicate the subdivision of the study area into three distinct zones. b) Interpreted section showing the interpreted seismic units and horizons and some of the faults observed in the study area. Representative faults F3, F5 and F8, used in the D-x and T-z analyses, are identified in the figure. This section comprises an anticline with seismic units of relatively constant thickness, with exception of the Late Cretaceous unit (Unit 4) which is truncated over the crest of the Samson Dome. The location of well 7224/7-1 is also indicated in this section. The rose diagram indicates the strike orientation of all 133 faults mapped in the study area. The location of the seismic profile is shown at the bottom of the figure.

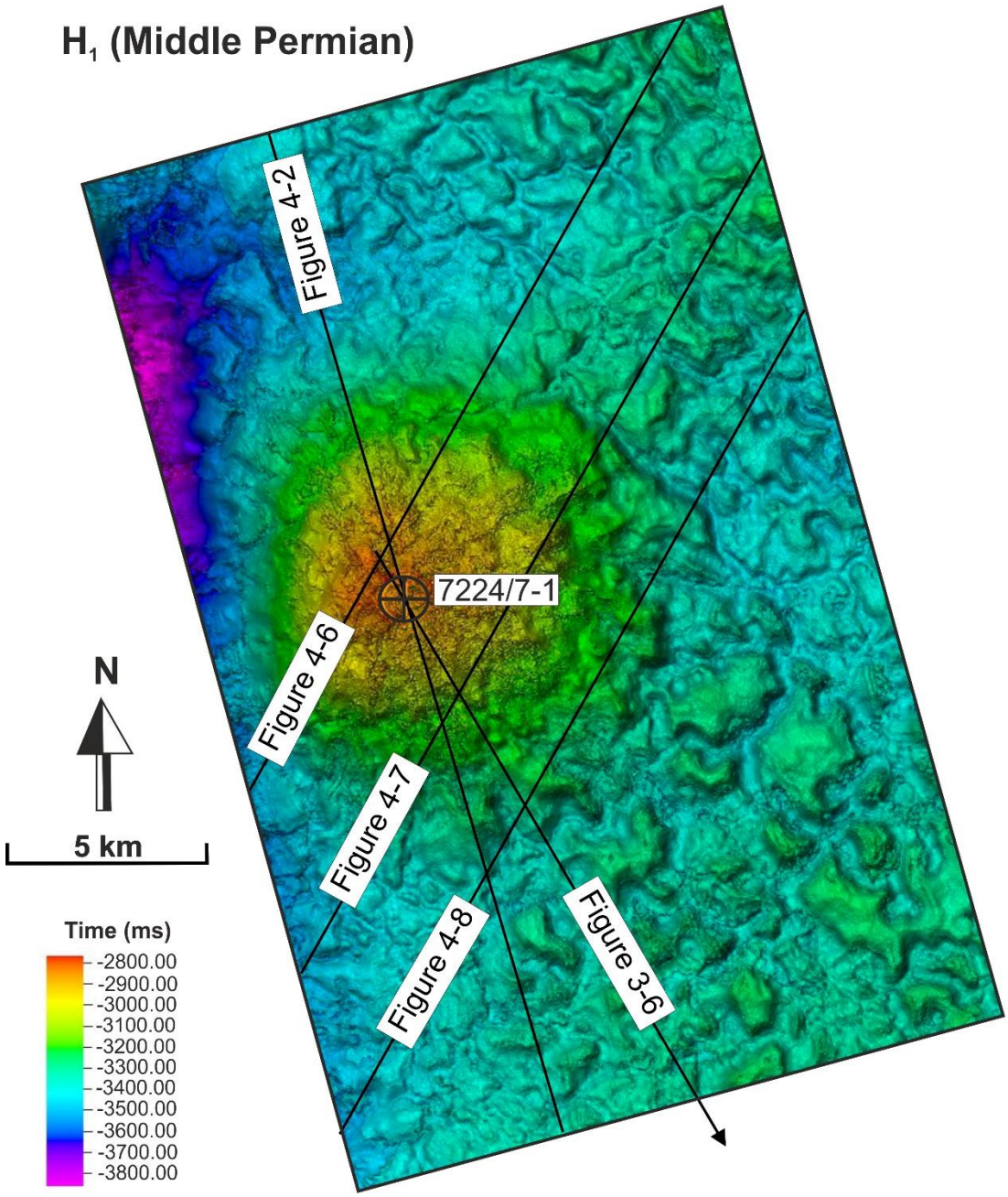

Figure 4-3: Time-structural map for the Middle Permian horizon H_1 highlighting the occurrence of carbonate buildups at this stratigraphic level. The location of the seismic profiles interpreted in this chapter are displayed on the map.

(Ehrenberg et al., 1998). Carbonate buildups occur in sub-unit 1a and are shown as high-amplitude wavy reflections. These structures are also observed on the thickness map in Figure 4-3. Carbonate build-ups were deposited in relatively shallow basinal environments together with variable amounts of anhydrite (Nilsen et al., 1993). Below it is possible to observe a loss of continuity, probably resulting from a lower resolution, as a small number of faults offsets horizon H_3 (Figure 4-2). The 865 m-thick sub-unit 2a shows no major thickness variations throughout the study area, and consists of medium to dark-grey shales with minor intervals of pale-grey siltstones and sandstones (Dalland et al., 1988; Larssen et al., 2002). Sub-unit 2a corresponds to seismic sequence S1 in Glørstad-Clark et al. (2010).

Horizon H_4 correlates with the top of the Klappmyss Formation, and occurs at a depth of 2222 m in well 7224/7-1 (Figure 4-2). This horizon shows low amplitude and negative positive polarity and, as with horizon H_3, loses its continuity in areas close to the Samson Dome (Figure 4-2). Below H_4, sub-unit 2b comprises a 441 m-thick stratigraphic interval with regular thickness, offset by faults around the Samson Dome (Figure 4-2). However, faults are also observed away from this structure. Sub-unit 2b consists of dark-grey shales grading upwards into interbedded shales, sandstones and siltstones (Dalland et al., 1988). This sub-unit correlates with the Olenekian seismic sequence S2 of Glørstad-Clark et al. (2010) (Table 4-1).

One of the strongest negative reflections in Unit 2 is horizon H_5, which marks the top of Upper Triassic strata (Figures 4-1 and 4-2). In well 7224/7-1, this reflection correlates with the top of the Fruholmen Formation, and occurs at a depth of 931 m (Figure 4-2). Horizon H_5 marks the top of the 1291 m-thick sub-unit 2c, which includes the Fruholmen

(97 m thick), the Snadd (614 m thick) and the Kobe Formations (580 m thick) (Figure 4-1). The lithology of these three formations is similar, comprising grey to dark shales grading upwards into interbedded sandstones, shales, siltstones and coal (Dalland et al., 1988; Larssen et al., 2002). The Fruholmen Formation shows no discernible thickness variations (Figure 4-2). Sub-unit 2c is mainly faulted over the salt dome, but faults are also observed away from this structure. This sub-unit is equivalent to the top of the Upper Triassic S5 unit of Glørstad-Clark et al. (2010) (Table 4-1).

4.3.2. Unit 3 (Jurassic)

Unit 3 has its upper boundary at the top of the Late Jurassic horizon H_6, which is characterised by a strong amplitude and high-frequency negative reflection (Figures 4-1 and 4-2). In well 7224/7-1, this reflection corresponds to the top of the Hekkingen Formation and occurs at a depth of 792 m (Figure 4-1). Unit 3 is an interval comprising brownish grey to dark grey shales and claystones with minor thin amounts of limestone, dolomite, siltstone and sandstone (Dalland et al., 1988). This thin (139 m) interval has a regular thickness and is markedly faulted. Faulting causes this horizon to be discontinuous around the Samson Dome (Figure 4-2).

4.3.3. Unit 4 (Cretaceous)

Unit 4 is bounded at its base by horizon H_6 and at its top by horizon H_7, a Late Cretaceous unconformity occurring at a depth of 401 m below the sea floor in well 7224/7-1 (Figure 4-1). Horizon H_7 is a positive and high-amplitude reflection, which coincides with the top of the Kolmule Formation. The horizon is truncated over the crest of the Samson Dome (Figure 4-2) and, at the same time, comprises the most faulted seismic-stratigraphic marker in the study area, as observed in the time-structural map for this horizon (Figure 4-4).

In well 7224/7-1, the Unit 4 thickness reaches 391 m and includes the Knurr and Kolmule Formations (Figure 4-1). The Lower Cretaceous Knurr Formation, 30 m thick, comprises dark-grey shales and red to yellow-brown claystones at its top (Larssen et al., 2002). In parallel, the Kolmule Formation is about 361 m-thick and is composed of brownish grey to dark grey shales, interbedded with occasional intervals of siltstone and sandstone (Dalland et al., 1988; Larssen et al., 2002). The Kolmule Formation is Early to Late Cretaceous in age.

4.3.4. Unit 5 (Paleogene – Quaternary)

On the interpreted seismic profiles, the top of Unit 5 coincides with the modern sea floor (Figure 4-2). This Paleogene to Quaternary unit is 108 m-thick and shows continuous and high-amplitude reflections at its base and top. Low-amplitude and

discontinuous reflections are observed in Unit 5, hindering the mapping of faults in its interior.

Unit 5 comprises the Nordland and Sotbakken Groups (Figure 4-1). The Nordland Group consists of marine sand and clays grading to sandstones and claystones (Dalland et al., 1988; Glørstad-Clark et al., 2010). Clays are grey to greyish green, blocky, locally silty and non-calcareous. The softness of the clays from the Nordland Group is a distinctive feature when comparing to the claystones from the underlying Sotbakken Group (Dalland et al., 1988) (Table 4-1).

4.4. Fault distribution on the Samson Dome

The structural interpretation of a coherence slice from a depth of -980 ms resulted in the sub-division of the study area into three distinct zones (Figure 4-5). The sub-division is done based on the density, geometry, and orientation of the interpreted faults. Fault density is greater over the Samson Dome (Zone 2) and decreases towards the southeast and northwest in Zones 1 and 3 (Figures 4-6 and 4-7). Most faults developed away from the Samson Dome are restricted to Unit 4 (Cretaceous). However, a considerable number of faults also extend into the Triassic Unit 2 (Figure 4-8).

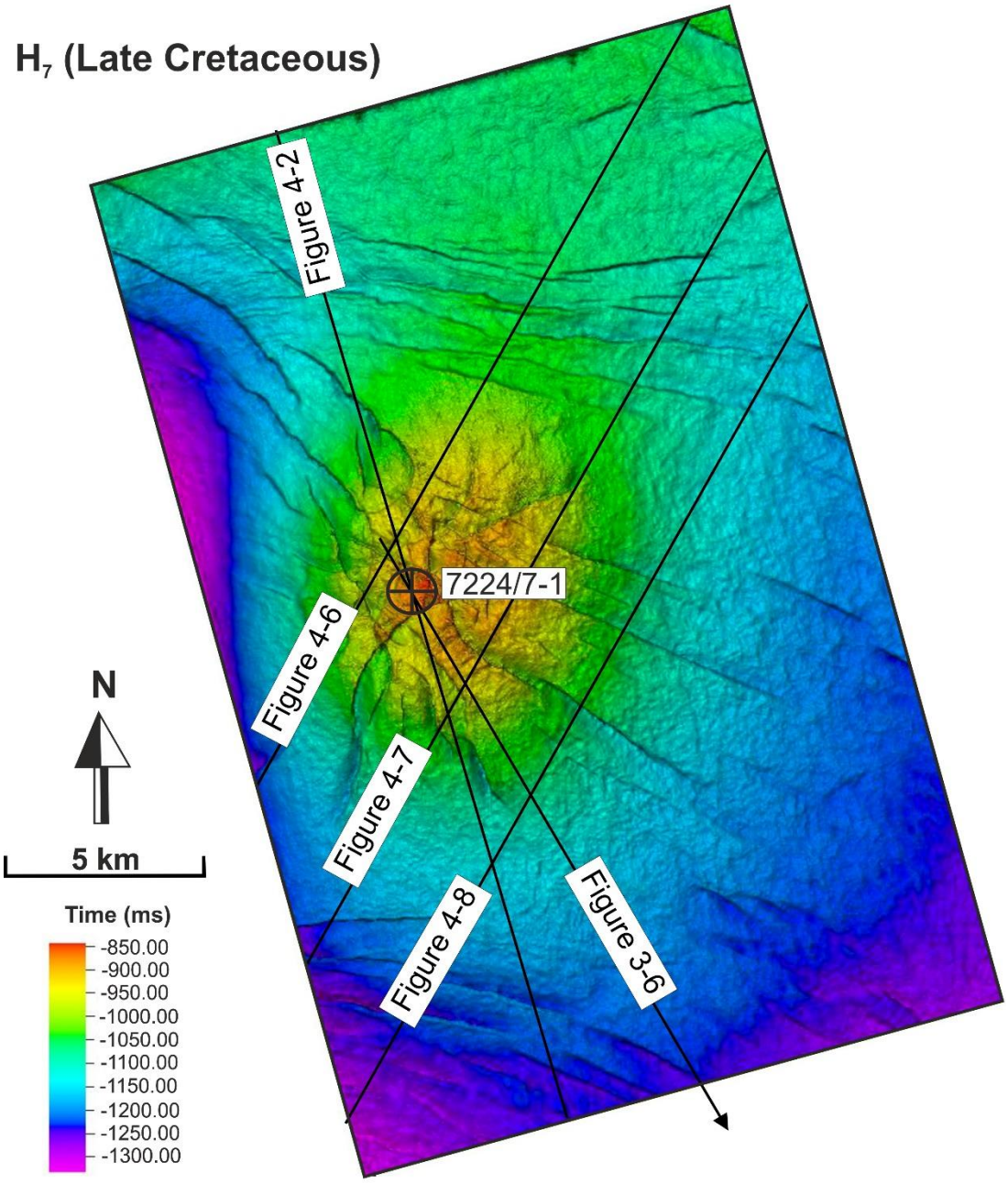

Figure 4-4: Time-structural map for the Late Cretaceous horizon H_7 showing the faults pattern both at the crest of the Samson Dome, and more distally in the study area. The location of the seismic profiles interpreted in this chapter are displayed on this map.

4.4.1. Zone 1

Zone 1 occurs to the northwest of the Samson Dome (Figures 5-6 to 5-8). The mean strike direction for the 21 faults mapped in this zone is ENE, with the largest faults striking E (see rose diagram in Figure 4-8). Zone 1 is not located on the Samson Dome, but this broad anticline still influences its structural configuration (Figure 4-6). Small-scale bright spots were also identified within sub-unit 2c (Figures 4-6 and 4-8). With the exception of fault F1 the deepest offsetting faults in Zone 1 dip all to the NE. Faults that occur at Cretaceous level (Unit 4) dip both to the SW and NE (Figures 4-6 and 4-8).

4.4.2. Zone 2

Zone 2 is located in the central part of the study area and comprises faults developed on the crest of the Samson Dome (Figure 4-5). Zone 2 is the most deformed of the three interpreted zones and includes deeply seated faults such as F5, which offsets Upper Permian to Upper Cretaceous strata (Figure 4-7). Significantly, the top of Upper Cretaceous strata shows evidence of erosional truncation (Figures 4-6 to 4-8).

In Zone 2, the predominant strike for faults is NW-SE. However, NE-SW striking faults are also interpreted Figures 4-6 to 4-8). Close to the Samson Dome, sub-units 2b, 2c, Unit 3, and Unit 4 are highly faulted with a succession of tilt-blocks (Figures 4-6 and 4-7). These structures are asymmetric and limited by synthetic and antithetic faults (Figure 4-6). Relatively large tilt-blocks are observed in Figure 4-7. The tilted blocks are delimited by F4 to the NE and by other fault segments to the SW. These fault segments extend from the top of the Lower Triassic to the top of Upper Cretaceous strata (Figures

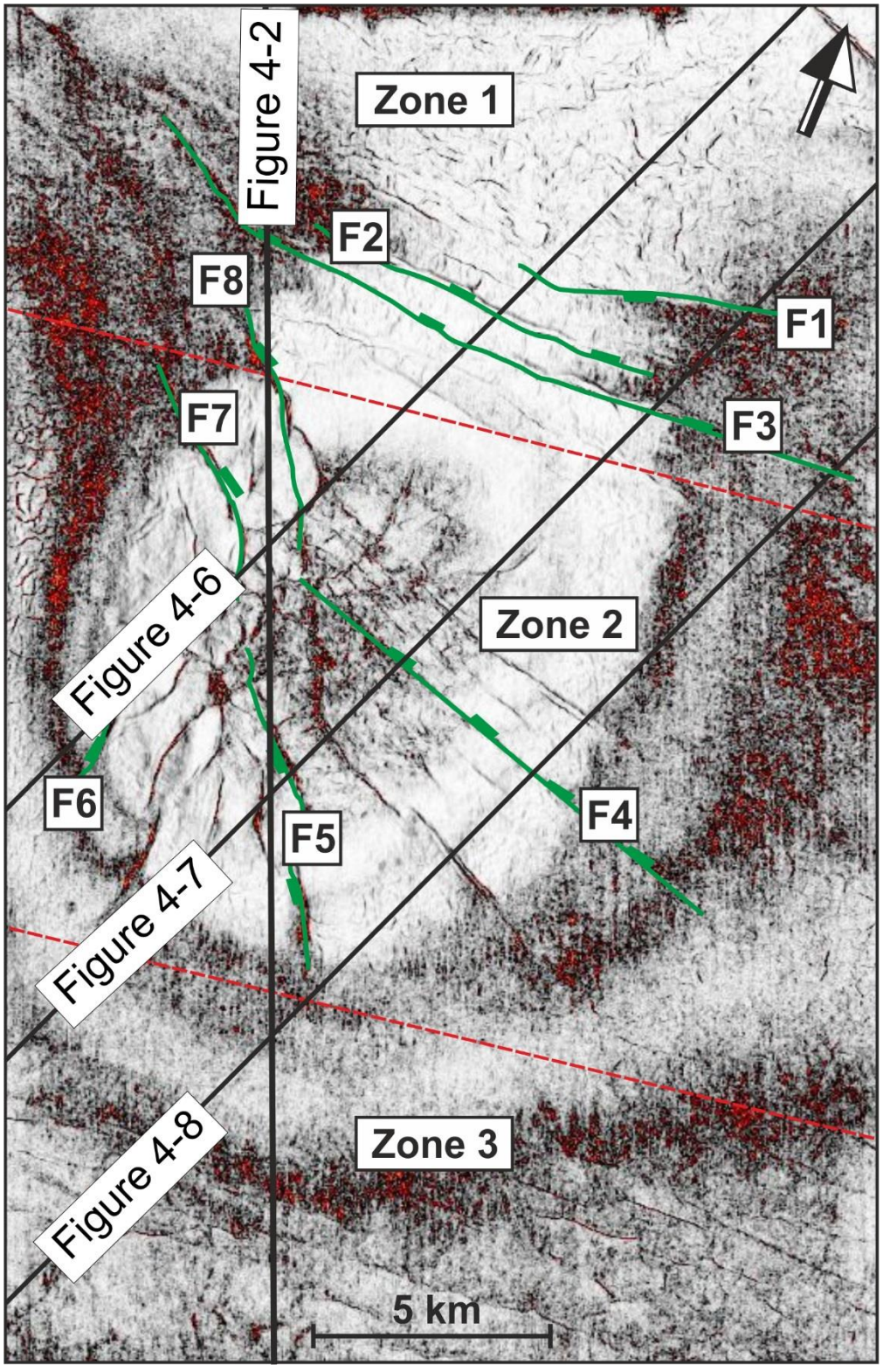

Figure 4-5: Coherence slice at Z = -980 ms of the Samson Dome, which is subdivided into three distinct zones. Green lines represent the location of the eight representative faults interpreted in D-x and T-z plots (see Figures 5-9 and 5-10).

4-6 to 4-8). Away from the Samson Dome, it is possible to see a large tilt-block where all the faults located to the right of the seismic profile dip to NE and the faults located on the left of this section dip to the SW (Figure 4-8). In addition, bright spots were interpreted in Zone 2 below horizon H_5 (Figure 4-6). In Figure 4-7, distinctive high-amplitude anomalies are observed on seismic data and are interpreted as bright spots.

4.4.3. Zone 3

Zone 3 is located in the southernmost part of the study area and comprises large faults that offset sub-unit 2b to Unit 4 (Figure 4-5). Most of the faults in this zone are, however, contained within Upper Cretaceous strata in Unit 4. Faults in Zone 3 strike in an E-W direction (Figures 4-7 and 4-8). As faults predominantly dip to the SW, the main distinctive feature of Zone 3 is the occurrence of a NE-dipping segment between horizons H_4 and H_7 (Figure 4-8). Two faults within Unit 4 crosscut this latter fault segment. Relative to the other two zones, Zone 3 show little connection to the Samson Dome. Several bright spots are also observed below horizon H_5 and close to the seafloor in this zone (Figures 4-7 and 4-8).

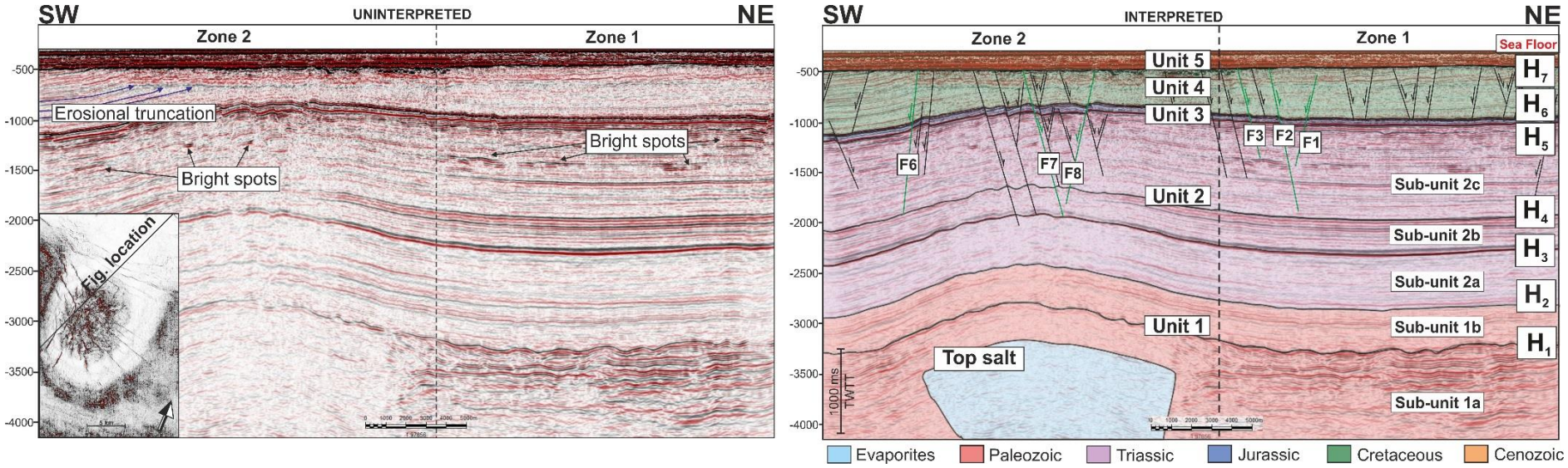

Figure 4-6: Uninterpreted SW-NE seismic lines and corresponding interpreted sections for each of the three fault zones in the study area. Brightspots are indicated in the uninterpreted seismic profiles. The eight representative faults (F1 to F8) used for the D-x and T-z plots in Figures 4-9 and 4-10 are highlighted. Seismic line displaying zones 2 and 1. This line is the most affected by the growth of the Samson Dome and exhibit a succession of asymmetric tilted blocks in Zone 2. In Zone 1, large faults offset strata between horizons H_5 and H_7. Faults confined to the horizon H7 are also observed in Zone 1. Representative faults F6, F7 and F8 occur in Zone 2, while faults F1, F2 and F3 are found in Zone 1. The location of the seismic profile is indicated at the bottom of the figure.

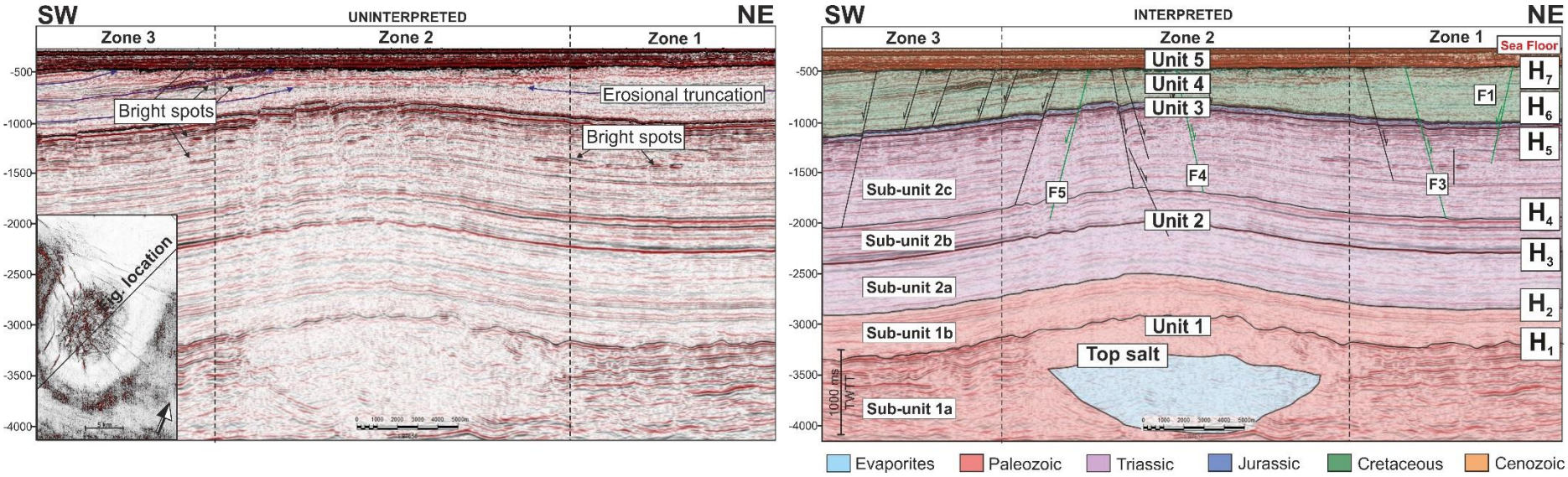

Figure 4-7: Uninterpreted SW-NE seismic lines and corresponding interpreted sections for each of the three fault zones in the study area. Brightspots are indicated in the uninterpreted seismic profiles. The eight representative faults (F1 to F8) used for the D-x and T-z plots in Figures 4-9 and 4-10 are highlighted. Seismic line showing the three (3) zones defined for the study area and the location of faults F5 and F4 (Zone 2) and F1 and F3 (Zone 1). The location of the seismic profile is indicated at the bottom of the figure.

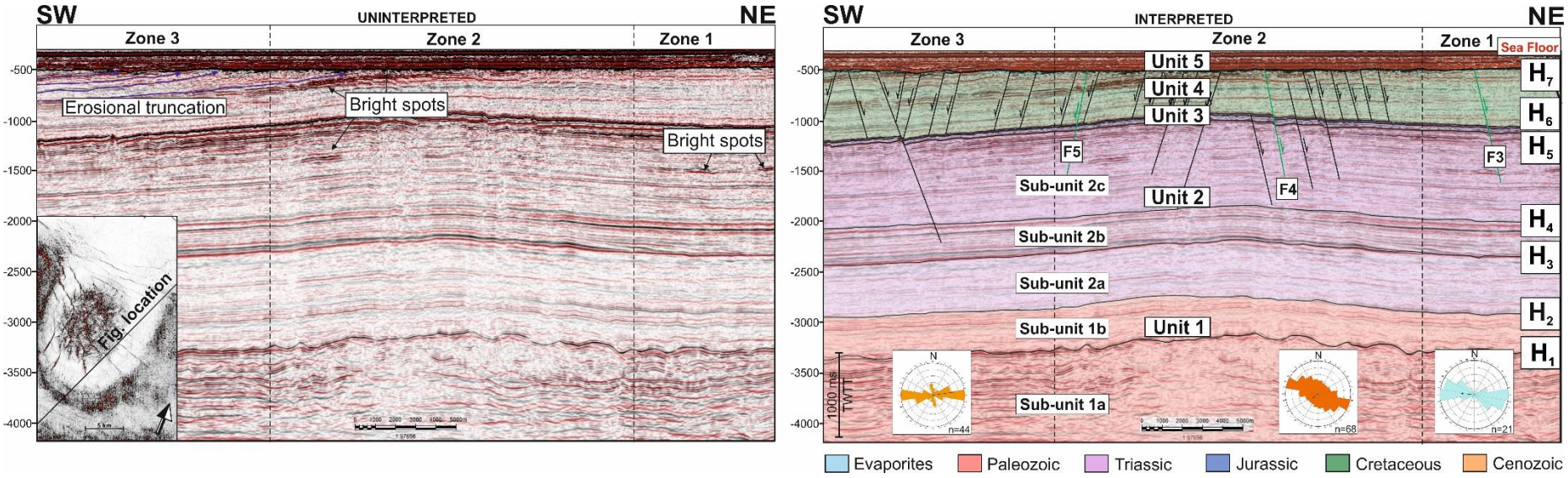

Figure 4-8: Uninterpreted SW-NE seismic lines and corresponding interpreted sections for each of the three fault zones in the study area. Brightspots are indicated in the uninterpreted seismic profiles. The eight representative faults (F1 to F8) used for the D-x and T-z plots in Figures 5-9 and 5-10 are highlighted. Seismic line showing the three (3) structural zones in an area less affected by the Samson Dome. An NE-dipping fault segment offsetting horizons H_4 and H_7 are observed in Zone 3. Faults F5 and F4 occur in Zone 2. Fault F3 is interpreted in Zone 1. The rose diagram indicates the strike orientation of all faults mapped in each zone. The location of the seismic profile is indicated at the bottom of the figure.

4.5. Fault displacement analyses

4.5.1. Main fault families

The interpreted faults are divided into distinct families; named types A to C. Type A faults are crestal faults located on the crest of the Samson Dome (Figure 4-6). They form small-scale graben, half-graben and horst structures, and show predominant NW to ENE strikes and an average dip of 39º. Faults F4 to F8 are examples of faults in this category. Type A faults chiefly occur in Zone 2 where the Samson Dome is located, but they may also extend to Zone 1, e.g. faults F7 and F8 (Figure 4-5). These faults are among the deepest in the study area, occurring from Lower Triassic to Upper Cretaceous strata (Figures 4-6 to 4-8).

Type B faults are located away from the Samson Dome and consist of near-parallel faults with predominant E-W strikes and dips ranging from 33º to 48º. Type B faults show no evidence for strike-slip movement. Faults F1 to F3 are examples of Type B faults (Figures 4-5 to 4-7). Fault F3 is the largest fault in the study area, with a length of around 20000 m (Figure 4-5). This fault offsets Upper Triassic to Upper Cretaceous strata i.e. from horizons H_4 to H_7 (Figure 4-7). F3 also delimits a bright spot in Zone 1 (Figures 4-6 and 4-7).

Coherence data in Figure 4-5 show that Type C faults follow a pattern that resembles polygonal fault systems (Cartwright, 1996; Lonergan et al., 1998). Type C faults are observed within Cretaceous strata (Unit 4) and have a predominant strike direction to the

NW (Figures 4-2 and 4-8). Faults striking NE are also found. The dips for these faults are variable, ranging from 29º to 52º.

4.5.2. Interpretation of displacement-length (D-x) plots

Figure 4-9 shows displacement-length (D-x) plots for the eight representative faults. The shapes of D-x plots relate to the observed displacement variations. For a single and isolated fault, D-x profiles will exhibit triangular or flat-topped shapes, representing a near-symmetric slope with gentle variations in displacement (Childs et al., 1995; Muraoka and Kamata, 1983; Nicol et al., 1996; Peacock and Sanderson, 1991). These are the C-type faults of Muraoka and Kamata (1983) and represent deformation in soft, homogeneous layers. Faults with abrupt variations in displacement indicate linkage of individual fault segments at displacement minima (Nicol et al., 1996; Walsh et al., 2003). Their corresponding profiles show a broad central section with no significant slope variations, and flanking portions with an abrupt displacement change, thus resulting in a marked asymmetric character. These structures are classified as M-type faults, reflecting deformation in rigid units (Muraoka and Kamata, 1983).

Displacement-length (D-x) plots for Type A and Type B faults are provided in Figure 4-9. Overall, the geometry of the D-x profiles vary from asymmetric (F1, F3, F4, F5, and F6) to symmetric (F2, F7, and F8). Faults F7 and F8 have distinctive M-type profiles. The other faults have more complicated displacement profiles. For example, profiles for faults

F1 and F6 are skewed to the right (Figure 4-9). Fault F5 is a combination of two distinct C-type profiles. Fault F4 include an M-type profile to the left and a C-type to the right (Figure 4-9). Fault F2 displays the most complicated D-x profile with combination of several types of C-, M- and skewed-type profiles. The complex D-x profile points to lateral segmentation of the faults (Muraoka and Kamata, 1983; Nicol et al., 1996). This is evidence that these faults were not isolated during their propagation and growth. For example, Faults F5 developed by combination or linkage of two disparate and initially isolated faults (*cf.* Childs et al., 1995; Peacock and Sanderson, 1991). Hence, the most laterally segmented fault is F3, with twelve (12) segments, followed by F2 with ten (10) segments. Fault F8 and F4 have six (6) segments each, whereas faults F6 and F7 have five (5) segments. Fault F1 consists of four (4) segments and the least segmented fault is F5, with two (2) segments (Figure 4-9).

Apart from fault segmentation, the eight representative faults also have variable maximum displacement (d_{max}) and fault length (Figure 4-9). D_{max} ranges from 81 m (F5) to 23 m (F2), while fault length varies from about 2.8 km (F6) to 20 km (F3). The point of maximum displacement for the fault may coincides with their point of nucleation (*cf.* Barnett et al., 1987; Nicol et al., 1996; Walsh and Watterson, 1987). This assertion will only be true for isolated blind faults or faults that show less segmentation. In terms of their connection to the Samson Dome, the Type A faults (crestal) have length that are lesser than those of Type B. The longest faults are located on the margin of the Samson Dome. However, Type A faults have higher D_{max} relative to the type B faults.

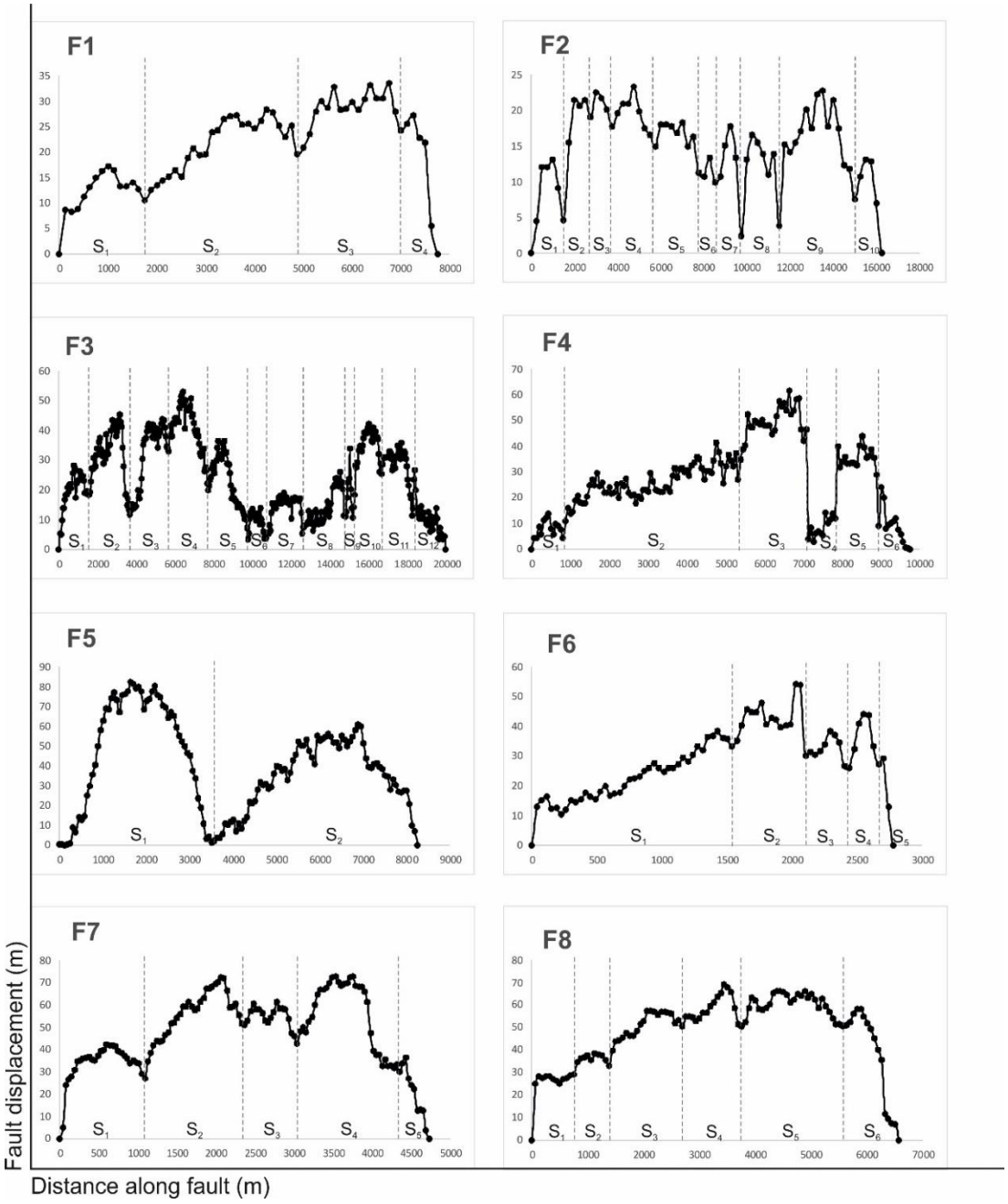

Figure 4-9: Displacement-length (D-x) plots for the eight representative faults in the study area. Faults are classified as C-type and M-type profiles from Muraoka and Kamata (1983), as described in this work. Displacement curves were created along horizon H_5 (Late Triassic). The grey lines indicate minimum displacements and segment linkage. Fault displacement and distance along the fault length are displayed in metres. Dotted lines and S_1 to S_n denote distinct fault segments later linked to form a continuous fault plane.

4.5.3. Interpretation of throw-depth (T-z) plots

The throw-depth (T-z) plots for the eight representative faults are shown in Figure 4-10. Time-structure data for horizon H_7 (Figure 4-4) and the profiles in Figure 4-10 show that interpreted faults can display average throw values ranging from 12 to 33 ms on the Samson Dome. The greatest throw values occur for fault F5, where a throw maximum of 68 ms is observed (Figure 4-10). Throw-depth profiles include C-type (F1, F6 and F7), skewed M-type (F3 and F4), M-type (F2 and F8) and skewed C-type (F5). Although the profiles can also be grouped into simpler types e.g., the profile for fault F1 being classified as an M-type, F1 is interpreted here as a combination of two C-types profile (Figure 4-10).

Throw values generally increase with depth for faults F1, F3 and F4 (Figure 4-10). A different geometry is observed for faults F2, F5 and F7, whose throws increase from their upper tips to a depth of about 700 ms. Displacement minima are recorded at 800 ms for faults F2 and F5, and at 900 ms for fault F5. The maximum throw occurs at ~ 1200 ms towards the lower tip in faults F5 and F7, and at ~1400 ms in fault F2 (Figure 4-10). Throw-depth plots for all the faults show that the maximum displacement occurs within Upper Triassic strata (Figure 4-10). The T-z plots signify the complex vertical segmentation of the faults and likelihood of fault reactivation through dip linkage. This aspect is discussed further in *Section 4.7.2.*

4.6. Stress distribution, slip tendency and leakage factors for faults in the Samson Dome area

The styles of deformation in the Samson Dome area reflect a complex stress distribution. Stress inversions for all the faults indicate paleostress conditions that are similar to those initially expected, considering the high standard deviation for stress azimuths gathered from the literature (Table 4-2). Paleostress analysis, following the method of McFarland et al. (2012), for the faults in the study area estimated a sub-horizontally oriented σ_1, plunging 12° along a N130° azimuth. The orientation of σ_3 is sub-vertical, plunging 77.5° along an N298.4° azimuth. Earthquake focal mechanisms from the Finnmark Platform, located 339 km from the Samson Dome, as described in *Section 2.2.2*, also favour a compressional stress regime with a σ_3 plunging 70° along an N25° azimuth. The orientation of σ_1 is, therefore, sub-horizontal, plunging 5° along a N281° azimuth (Figure 2-4).

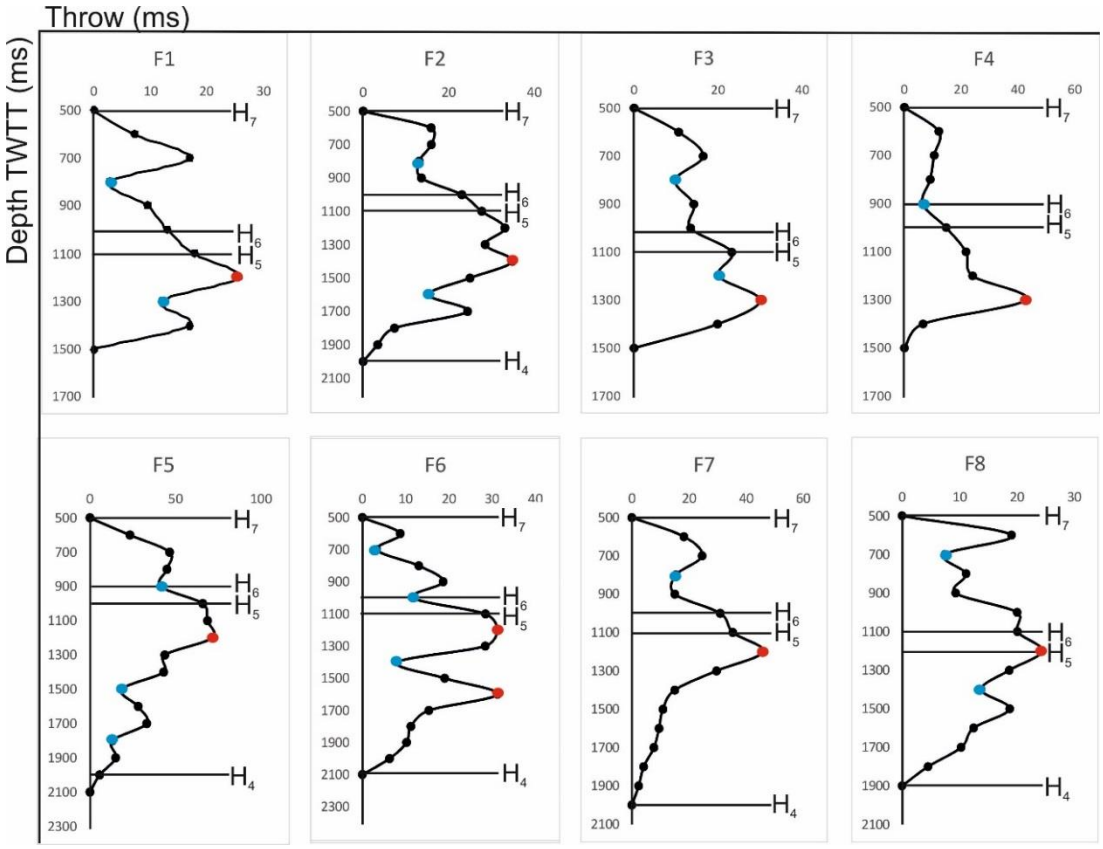

Figure 4-10: Throw-depth profiles for eight representative faults with both depth and throw measured in ms. Three throw profiles were identified: asymmetric, M-type and skewed M-type. Black lines indicate the horizons cut by the faults. The maximum throw for the majority of the faults occurs at horizon H_5 (Late Triassic). Throw maxima are indicated by red dots and the blue dots highlight the minimum throw values.

Table 4-2: Stress inversion values obtained considering the total number of faults and each distinct zones of the study area. Results from paleostress inversions indicate that a sub-vertical σ_1 and sub-horizontal σ_3 predominate in the study area.

Area	Number of faults	σ_1		σ_2		σ_3	
		Plunge	Azimuth	Plunge	Azimuth	Plunge	Azimuth
Total study area	133	12˚	N130˚	2.4˚	N39.1˚	75º	N298.4º
Zone 1 (North)	21	1.6º	N235.9º	0.2º	N145.9º	88.4º	N48.8º
Zone 2 (Diapir)	68	14º	N102.7º	10.9º	N15.4º	72.1º	N322.1º
Zone 3 (South)	44	0.3º	N82.5º	3.9º	N352.5º	86.1º	N167.5º

Slip tendency values for faults in the study area vary from 0.0 to 0.6 (Figure 4-11). Most faults in Zones 1 and 3 (Type B and C faults) show slip tendency values between 0.3 and 0.5. Faults in Zone 2 (Type A faults) have the highest slip tendency values. In Figure 4-11, one can note that some faults on the Samson Dome show a decrease in slip tendency from their lower to upper tips.

Leakage factor was also calculated considering present-day stress states for Finnmark and a fluid pressure of 11 MPa, obtained based on vertical stress measurements. In this case, the leakage factor values obtained for the study area range from 0.20 to 0.85, with the most faults in the southern and northern parts of the study area showing leakage factors varying from 0.50 to 0.70 (Figure 4-12). An interesting pattern is observed in Zone 2; some of the NW-SE trending faults show larger leakage factors close to their upper tips (Figure 4-12). These values diminish along the fault with depth. The faults most prone to leak are the faults offsetting the shallowest strata on the crest of the Samson Dome (Figure 4-12).

4.7. Discussion

4.7.1. Structural evolution of the Samson Dome and timing of faults

A conceptual model for the evolution of the Samson Dome is presented in Figures 4-13 to 4-16. At a regional scale, the first halokinetic movements in the Ottar Basin took place from Middle

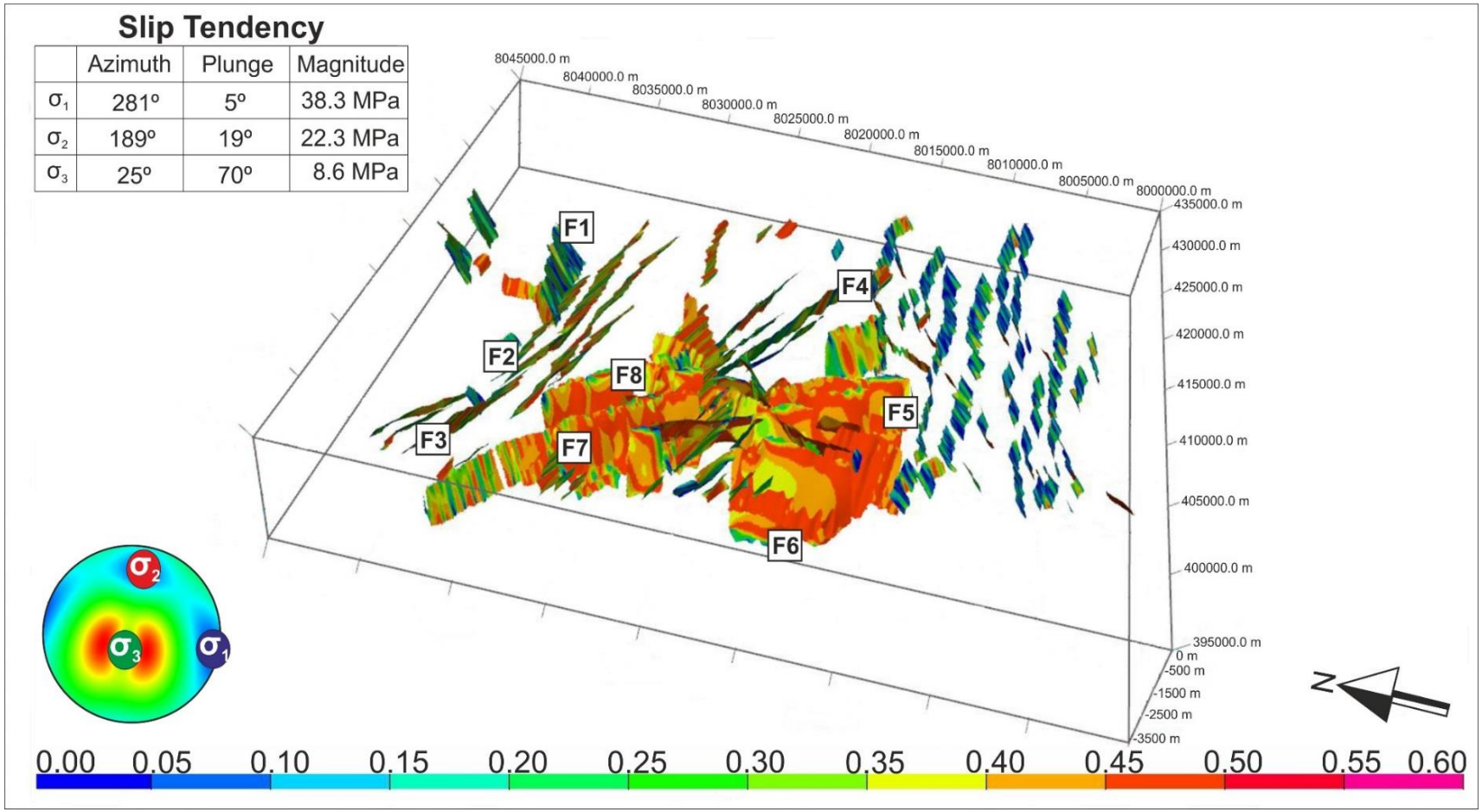

Figure 4-11: Slip Tendency model for faults in the study area, considering present-day stress data from Finnmark. Slip tendency values range from 0 to 0.6, with faults in Zone 2 showing the highest values and a decrease in the slip tendency towards their upper tips. In Zones 1 and 3, slip tendency varies between 0.3 and 0.5.

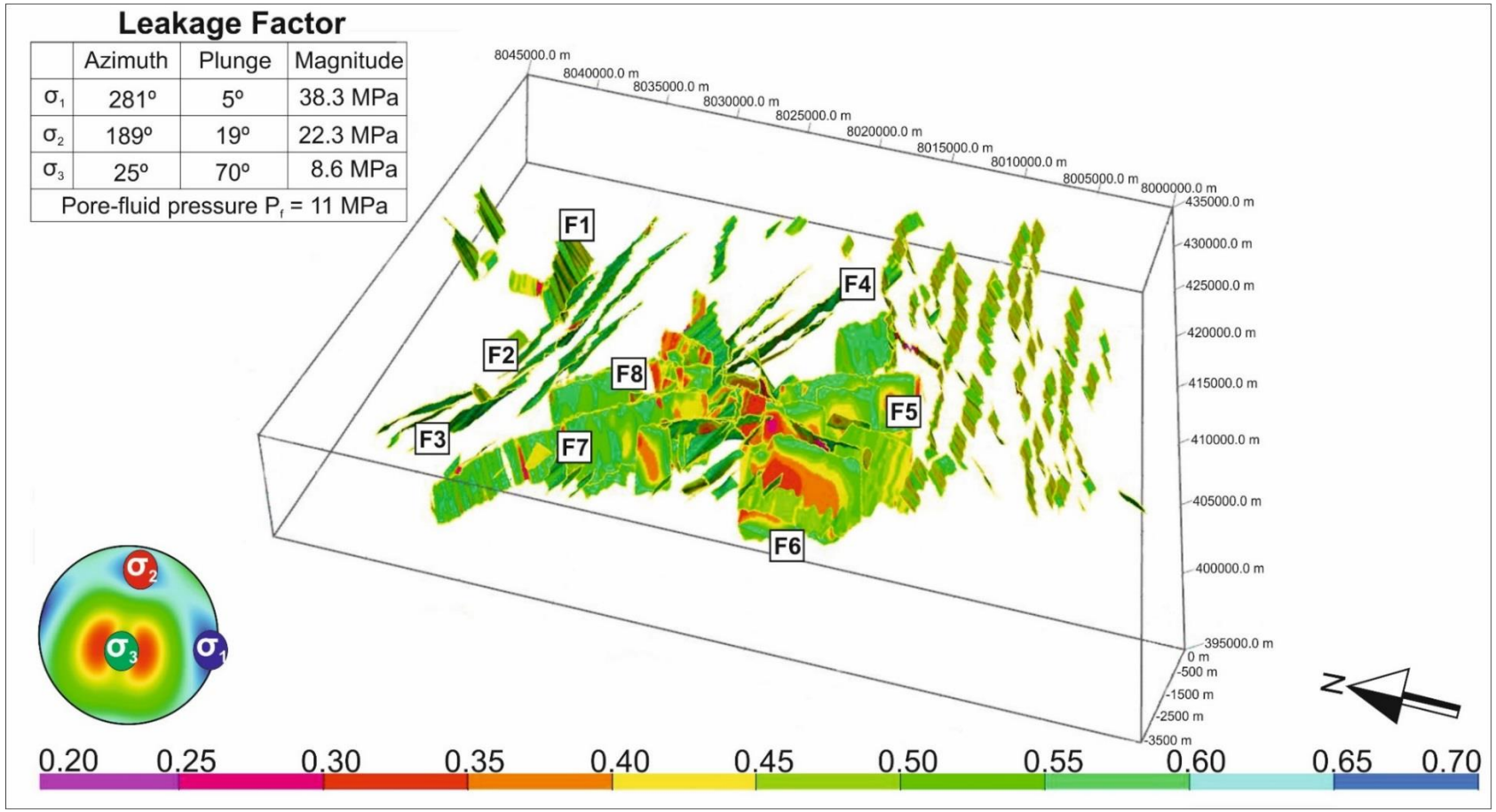

Figure 4-12: Leakage Factor model for faults in the study area considering present-day stress data from Finnmark. Leakage factors for the study area range from 0.2 to 0.85. For Zone 2 these values are greater towards the upper tip of the faults, decreasing with depth.

to Late Triassic, resulting from differential loading imposed by NW-prograding shelf deposits and by the reactivation of basement faults (Breivik et al., 1995; Klausen and Mørk, 2014). However, considering that equivalent NW-prograding strata arrived to the Samson Dome area relatively late in the Triassic, and that thick carbonates cover the Upper Palaeozoic evaporites in the study area, it is suggested that Middle to Late Triassic halokinesis barely deformed the post-salt overburden around the Samson Dome. The only evidence for important Middle to Late Triassic tectonics is the occurrence of a few NE-trending faults at the level of H_4 and H_5 (Figures 4-2 and 4-13). Examples of these NE-trending faults that reach the Triassic horizons are faults F5, F6 and F8 (Type A faults). These representative faults comprise maximum and minimum throw displacements between the Triassic Horizons H_4 and H_5, indicating these fault segments have been reactivated.

Furthermore, the interpreted 3D seismic cube indicates that the bulk of halokinetic movements occurred in the Late Mesozoic-Early Cenozoic. Faults formed during the Late Cretaceous in the Ottar Basin trend preferentially to the NW, whereas Middle to Late Triassic NE-trending faults were reactivated later. Extension in the Barents Sea, associated with the opening of the North Atlantic Ocean, is likely to have caused the mobilisation of salt in the Ottar Basin and the subsequent reactivation of NE-trending faults (Faleide et al., 1993; Gudlaugsson et al., 1998; Safronova et al., 2014). Evidence for this salt mobilisation includes the generation of a broad anticline deforming the Late Cretaceous strata (Figures 4-13 to 4-16). Faults surrounding the dome area offset Upper Triassic, Jurassic and Cretaceous strata. Conversely, faults are scarce in Lower Triassic and Permian strata imaged over the Palaeozoic evaporites (Figures 4-2 and 4-6 to 4-8).

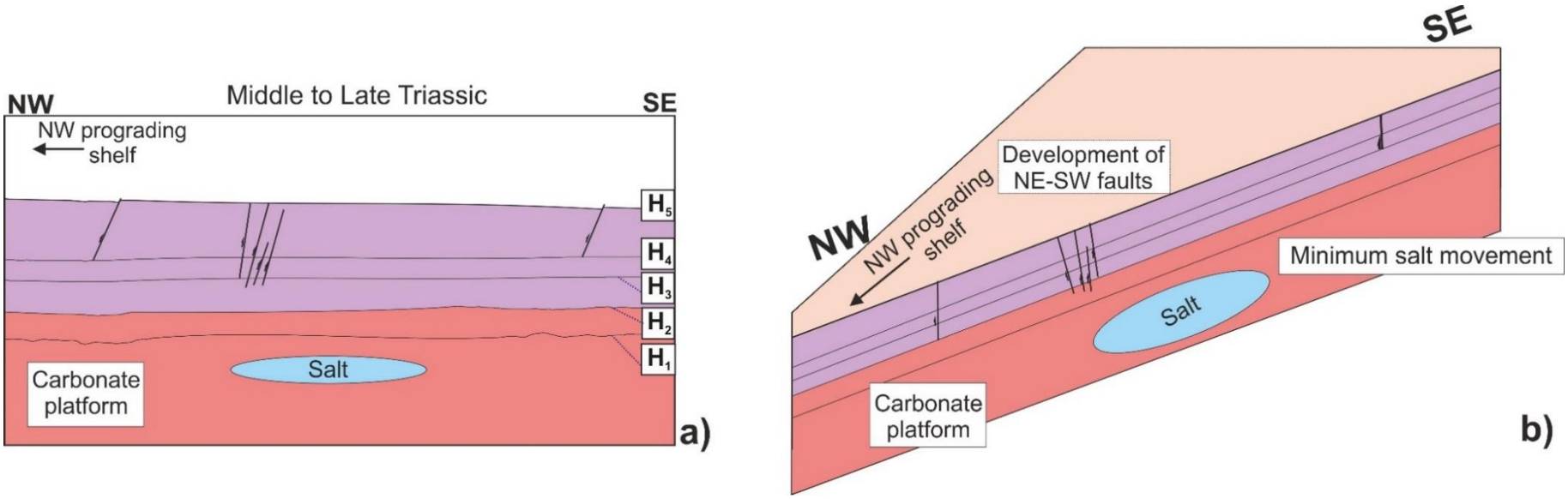

Figure 4-13: Proposed evolution model for the Samson Dome area, with a 2D and 3D representation for each of the evolution stages considered in this chapter. a) and b) During the Middle and Late Triassic a NW-prograding shelf reached the study area. However, the post-salt overburden was barely mobilised and the only structures developed at this period comprised a few NE-SW faults.

The first stage occurred during the Late Mesozoic (Figure 4-14). The growth of the Samson Dome resulted in the formation of an arched roof above Upper Palaeozoic evaporites, with associated radial faults and graben structures - including an apical block at the dome crests. The limits of the dome, as well as of radial faults, are indicated in Figure 4-5. Faults crossing Upper Triassic to Upper Cretaceous strata follow the NW-SE trend of the Ottar Basin, whereas older Middle to Late Triassic (NE-trending) faults in the study area were formed at early in the evolution of the Samson Dome and were reactivated later, as indicated by cross-cut relationships between the faults and the throw-depth profiles (Figure 4-10). In a second stage, the cessation of salt growth resulted in local dissolution of the dome (Figure 4-15). Dissolution was most likely initiated at the crest of the Samson Dome, evidenced by the lenticular geometry of the salt body (Figures 4-2 and 4-6 to 4-8). The removal of the buried salt initiates and tends to be greater at the top and in more elevated parts of the diapir where the salt rises faster (*cf.* Ge and Jackson, 1998; Seni and Jackson, 1984). The third stage is associated with the collapse of the dome (Figure 4-16). Salt dissolution and loading imposed by post-salt overburden units is one of the main mechanisms to form collapse structures such as the one observed in the Samson Dome area (e.g., Clark et al., 1999; Ge and Jackson, 1998; McDonnell et al., 2007). Most of the faults in the study area are located at Samson Dome and underlain by the salt diapir suggesting these structures are related to the salt removal and crestal collapse, with the uppermost Mesozoic layers being particularly affected by the development of Types B and C faults.

The model proposed bears some similarity to data in Walter and Troll (2001) addressing the formation of volcanic calderas by doming and collapse. Walter and Troll

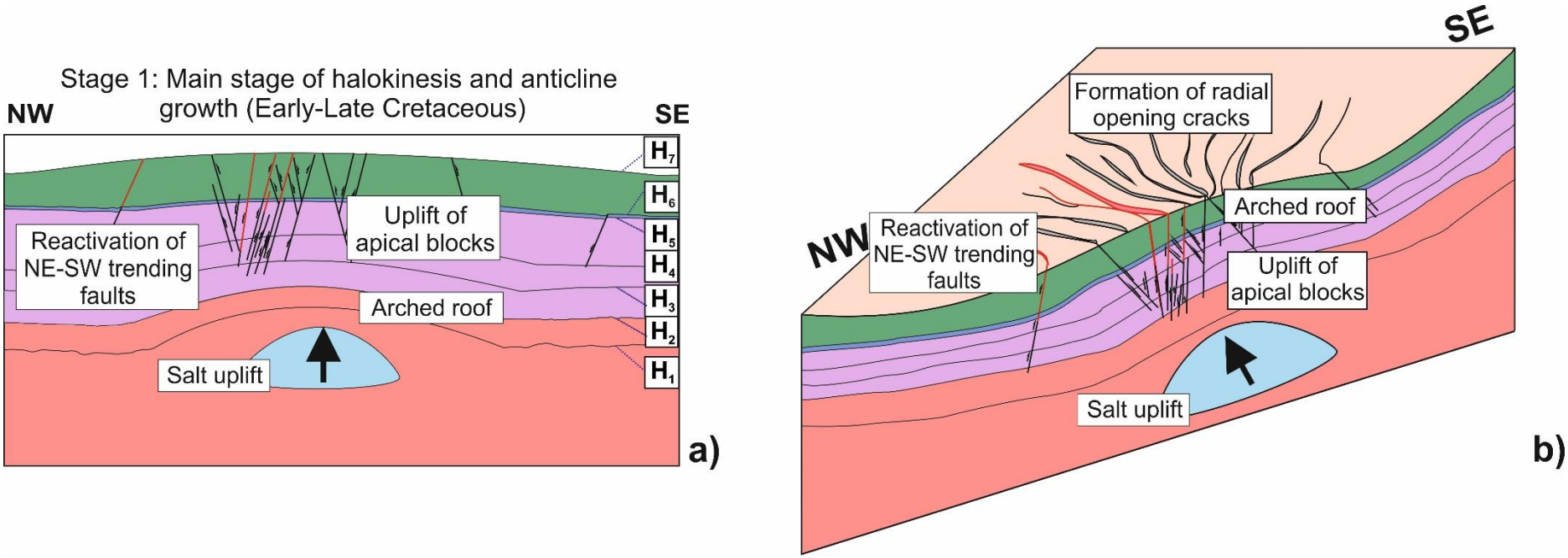

Figure 4-14: Proposed evolution model for the Samson Dome area, with an a) 2D and b) 3D representation for each of the evolution stages considered in this chapter. Stage 1: main stage of halokinesis and anticline growth (Early-Late Cretaceous). At this stage salt pierced the overburden causing the opening of radial faults and the reactivation of the NE-SW faults.

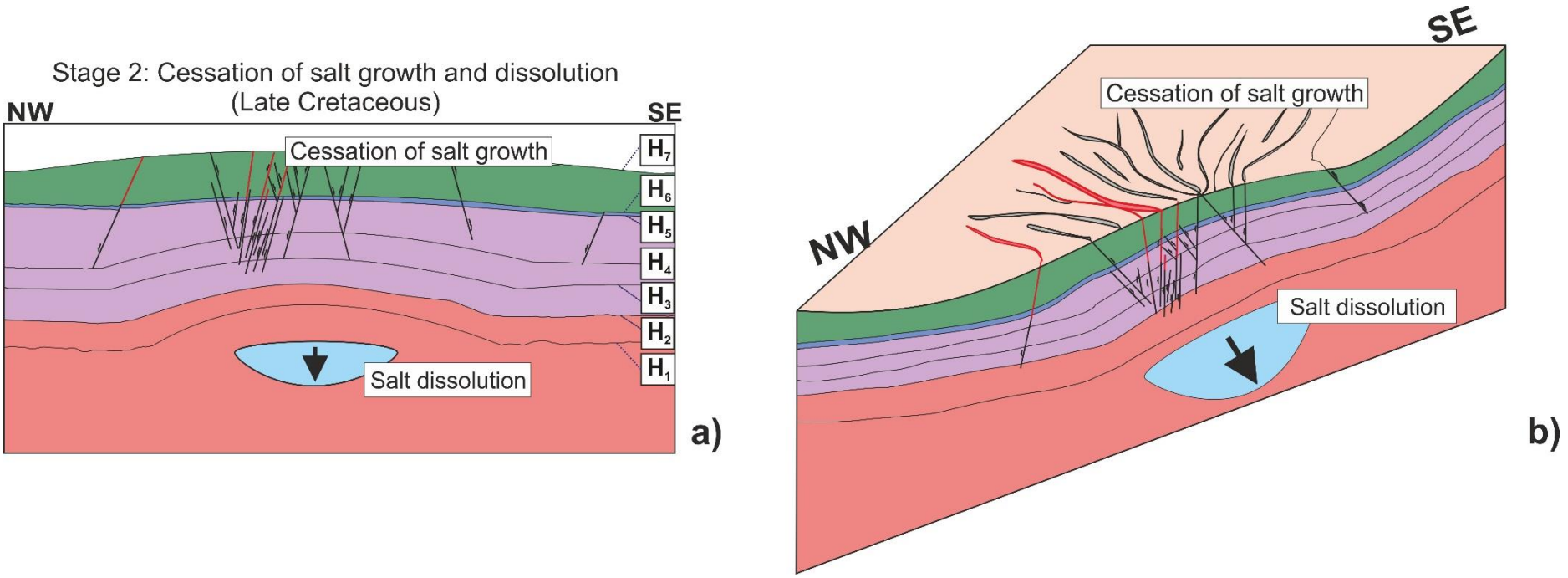

Figure 4-15: Proposed evolution model for the Samson Dome area, with an a) 2D and b) 3D representation for each of the evolution stages considered in this chapter. Stage 2: the second stage is characterised by the ceasing of the salt uplift in the Ottar Basin and caused the dissolution of the crest of the dome.

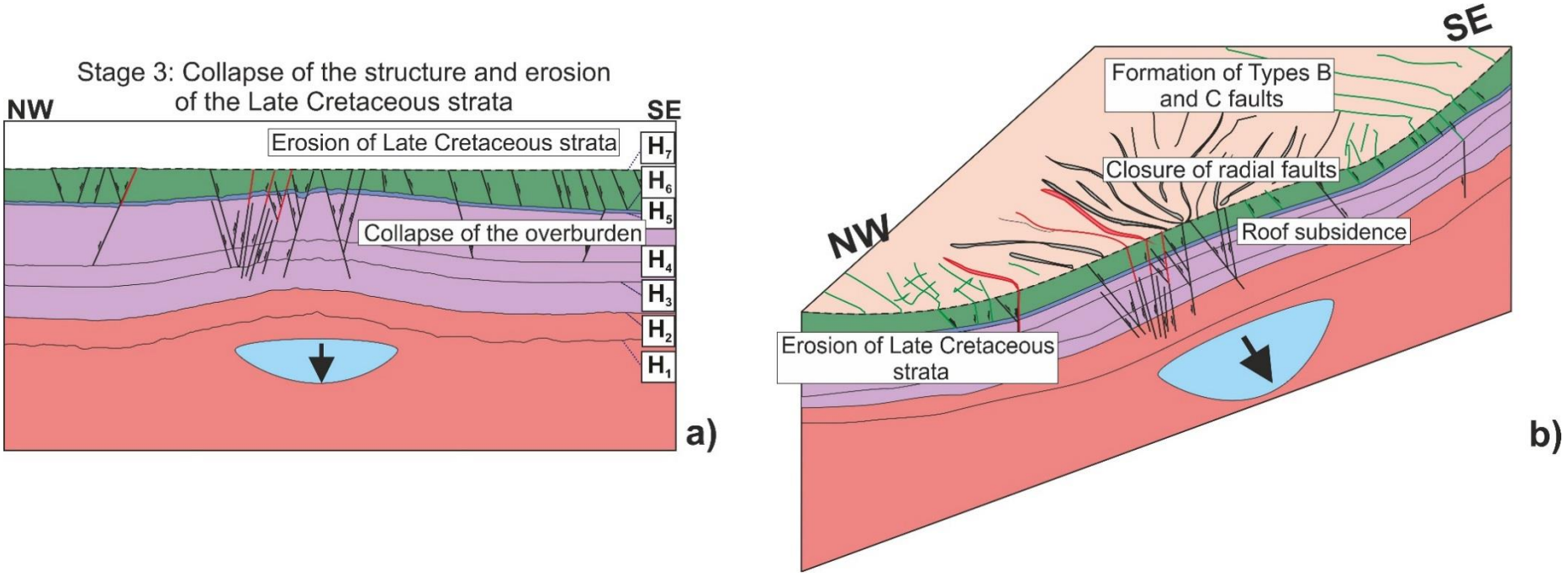

Figure 4-16: Proposed evolution model for the Samson Dome area, with an a) 2D and b) 3D representation for each of the evolution stages considered in this chapter. Stage 3: late dissolution of the salt dome caused the structure to collapse over its weight resulting in the formation of Types B and C faults, and the closure of radial faults. An intensive erosional episode removed part of the overburden during the Late Cretaceous-Paleogene transition.

(2001) consider the inflation of volcanic chambers as capable of generating radial opening cracks that lead to their subsequent collapse - usually caused by later magma withdrawal from an underlying chamber. The collapse of calderas results in roof subsidence and closure of previously formed radial faults, a phenomenon accompanied by the formation of periphery en-echelon fractures with variable dips. Evidence for collapse of faults similar to those found on volcanic calderas are found in the interpreted seismic volume, where no substantial height differences between the tilted blocks at the crest of the Samson Dome are observed. The greatest fault displacements occur for fault segments located close or above the salt dome (Figure 4-9). Moreover, as with volcanic calderas, dome collapse has resulted in a maximum displacement of 81 m in fault segments located on the crest of the Samson Dome. Displacement maxima tend to be of smaller magnitude in faults located distally from the dome. The rise and collapse of the anticlinal structure caused initially isolated segments to link, forming the radial fault pattern observed in the study area (Figures 4-13 to 4-16).

Away from the Samson Dome, the seismic horizons seem to be flat and undisturbed by halokinesis. Nevertheless, the occurrence of Type C faults (Figures 4-2 and 4-6 to 4-8) and small-scale fractures offsetting Cretaceous strata highlight the importance of the Late Cretaceous tectonics in the study area. From key seismic lines and well 7224/7-1, it is clear that horizon H_7 is the only surface denoting significant erosion, being thinner at the top of the Samson Dome (Figures 4-6 and 4-8). Away from the Samson Dome, thickness variations are not observed. These thickness variations are probably associated with Late Cretaceous-Paleogene erosion, which removed part of the Upper Cretaceous overburden that was uplifted and folded on top of the Samson Dome (Figure 4-16).

4.7.2. Mechanisms of fault linkage and reactivation

Displacement plots in *sections 4.5.2. and 4.5.3.* provide insights into the mode of propagation and linkage of faults around the Samson Dome. The observed fault geometries and cross-cutting relationships are also important clues to understand the evolution of the study area. For most representative Types A and B faults, throw-depth (T-z) data show maximum displacement close to horizon H_5 (Middle Triassic). Type A faults generally consist of either two or three segments and, in map view, radiate out from the Samson Dome (Figure 4-5). The collapse of the salt dome is likely to have caused the individual fault segments to link, following a geometry akin to caldera-collapse structures, as discussed in *section 4.7.1.* (Figures 4-6 to 4-8). Lateral segmentation and linkage in Type A faults is presumably associated with the growth and collapse of the Samson Dome. For Type B faults, dome uplift is considered an important factor influencing their lateral and vertical propagation.

As for fault reactivation, a large number of segments in F2 and F3, as shown by the multiple displacement minima, indicate that Type B faults consist of multiple overlapping fault segments (Figures 4-9 and 4-10). For the majority of Type A and B faults, throw minima occur in Unit 3 (Late Jurassic) and in Unit 4 (Cretaceous). Decreases in fault throw observed for individual fault segments suggest reactivation along dip or dip linkage (Baudon and Cartwright, 2008b; Omosanya et al., 2015). It is therefore proposed that important fault reactivation took place in the Samson Dome area during the Cretaceous (e.g. Faleide et al., 1993). A supporting evidence for reactivation in the Cretaceous is the generation of a third fault family, Type C, at this time.

4.7.3. Implications for petroleum systems in the Samson Dome

The interpreted seismic data provide little evidence for the presence of large-scale dim-spots previously interpreted in the area. Vadakkepuliyambata et al. (2013) considered the Samson Dome to form a large fluid-seepage structure based on the presence of an extensive area of dimmed strata on 2D seismic data. However, the interpreted 3D seismic volume, which denotes a dramatic improvement in the quality of the seismic signal, does not image the interpreted dimmed zone. In the interpreted seismic cube, it possible to delineate horizons and interpret faults with a great level of certainty, and bright reflections were only found at shallow depths above the Samson Dome. The largest bright spots are observed in Zone 2, which is located farther from the Samson Dome. Bright spots occur close to faults formed below horizons H_5 and H_7 in Zones 1 to 3, respectively. Some of these faults have their upper tips close to the seafloor (Figures 4-6 to 4-8). A plausible argument is that the associated hydrocarbons or fluids migrated or leaked through the faults from deeper source rocks into shallow stratigraphic units.

The area where Zone 2 faults occur records a major erosional event at the transition between the Mesozoic to Cenozoic. The erosion of Upper Cretaceous strata in Unit 4 resulted in a reduction in the overburden stresses and, consequently, in migration and leakage of fluids towards the surface. This assumption for the Samson Dome area is in agreement with previous data from other parts of the Barents Sea such as the Loppa High and Hammerfest Basin (Chand et al., 2012, 2008; Doré, 1995; Faleide et al., 1996; Ohm et al., 2008; Ostanin et al., 2012; Rajan et al., 2013). A similar fluid migration pattern is observed in the Loppa High, where shallow gas escapes to the water column through open

faults (Chand et al., 2012). Fluid also migrates into shallow sediments and escapes at the seafloor through polygonal faults in the Hammerfest Basin (Ostanin et al., 2012), as shown by amplitude anomalies in the hanging-wall of the faults and shallow bright spots. It is important to notice, however, that the evidence for sub-surface migration and fluid leakage in the Samson Dome area occurs only locally, in the form of a few bright spots observed on the 3D seismic volume, and not through a large area as suggested by regional 2D data.

Leakage factor calculations indicate values ranging from 0.5 to 0.7 as the average for all the faults in the Zones 1 and 3, a character suggesting the likelihood of failure of seal units across the Samson Dome, and consequently a greater potential to leak fluids (Figure 4-12). It must be noted that Zones 1 and 3 comprise large faults, offsetting horizons H_4 (Early Triassic) to H_7 (Late Cretaceous), but they also show small-scale faults within Unit 4. Fault F3 cuts a bright spot in section view, and could constitute a possible pathway for fluid migration in Zone 1 (Figures 4-6 to 4-8). In Zone 3, bright spots in Unit 4 are intersected by Type-C faults, indicating the possibility of fluid migration to the surface. Zone 2, corresponding to the Samson Dome *per se*, shows NW-striking faults with high leakage factors towards the surface, above the Late Cretaceous horizon (H_7). In contrast, they present relatively low leakage factors at depth.

Based on the results obtained in this chapter, it is proposed that the lower leakage factor values at depth to relate to the geometry of collapse of this structure under its own weight. Despite consisting of multiple segments, faults in Zone 2 occur in a continuous plane, a character increasing the seal competence of these faults (Leveille et al., 1997). Considering that faults in Zone 2 show relatively larger values of slip tendency and lower

leakage factors at depth relative to Zones 1 and 3, it is proposed that the stresses to which these faults are subjected at depth result in a tendency to 'lock' or close the faults, with subsequent generation of structural compartments capable of retaining fluids below the depth of Cretaceous-Jurassic strata.

An important implication of this work to the remainder of the Barents Sea is that the seal competence of faults on salt anticlines such as the Samson Dome increases with depth. Therefore, the trapping styles of hydrocarbons in salt structures across the Barents Sea exhibit greater variability than previously assumed. This is particularly noted in the largest branches of faults cross-cutting the Samson Dome, where stress analyses show leakage factor to be very high towards the surface, but decreasing significantly at depth below a neutral surface in which extension changes to compressional stresses at depth (e.g. Cosgrove and Ameen, 1999; Yeats, 1986) (Figure 4-12). In such a setting, the stress modelling results not only provide evidence for decreasing leakage 'risk' with depth but also show that unravelling the evolution of structures such as the Samson Dome is key to understanding if Upper Palaeozoic strata are capable of accumulating economical volumes of hydrocarbons in the whole of the Barents and Arctic Seas.

4.8. Conclusions

The difficulty in dating halokinetic structures in the Barents Sea motivated the analysis of the Samson Dome as a case study that can be extrapolated to other areas of the Arctic Sea, where salt tectonics exerts an important control on fault geometry and fluid flow. In parallel, this work aimed at evaluating the possibility of a late strike-slip

reactivation affecting the Samson Dome area. However, no structural evidence to corroborate this event was found. This area was most likely subjected to extensional events, as revealed by the paleostress analyses. The main conclusions of this work can be summarised as follows:

a) The study area was divided into three different zones with respect to the Samson Dome and the predominant strike of the faults. Type A faults are crestal faults that predominate in Zone 2; Type B are E-trending faults abundant to the northwest of the Samson Dome; Type C are small-scale faults generated at shallow levels around the Samson Dome.
b) Zone 1 is located to the north of the Samson Dome and comprises major E-trending and minor NW and NE-trending faults. Faults of types B and C predominate in Zone 1. The slip tendency values for these faults are relatively low but leakage factors are high, indicating a low seal competence. A feature of interest is the occurrence of bright spots within Upper Triassic strata. These anomalies are intersected by Fault F3, which acted as a focused conduit for fluids in Zone 1.
c) Zone 2 is located over the Samson Dome. Acoustic anomalies in this zone are found below horizon H_5 (Middle Triassic) and between horizon H_7 (Late Cretaceous) and the seafloor. This zone is the most faulted, with Type A and C faults predominating with a prominent NW strike. Leakage factor values denote higher values towards the upper tip of faults. The leakage factor of these faults reduces significantly with depth, indicating these faults may act as a barrier to fluids in clayey Triassic successions.

d) Zone 3 occurs to the south of the Samson Dome and is characterised by the occurrence of Type C faults, although in a smaller number than in Zones 1 and 2. The mean strike direction is NW and E. Reactivated NE-SW faults are also found in Zone 3. This zone shows small slip tendency values and relatively high leakage factor. Acoustic anomalies around faults (bright spots) are found below horizon H_5 and near the seafloor.

e) The evolution of the Samson Dome as a salt anticline started during the Middle-Late Triassic, as recorded by deep-seated faults striking NE-SW at this same stratigraphic level. Pre-existing faults were reactivated during the Late Cretaceous, a period commonly regarded as reflecting tectonic quiescence in the Barents Sea. Locally, however, this was a tectonically active period associated with extension in the North Atlantic Ocean.

f) The study area was uplifted during a regional phase of Late Cretaceous extension; this event resulted in halokinesis in the Samson Dome region. Salt dissolution led to the collapse of the dome under its own weight.

g) Slip tendency and leakage factor analyses indicate that the Samson Dome is a smaller seepage structure than previously proposed. The variable stresses to which faults in the Samson Dome are subjected at depth result in a tendency to 'lock' and close the faults, with the subsequent generation of structural compartments capable of retaining fluids below Jurassic and Cretaceous strata.

5. Corridors of crestal and radial faults linking salt diapirs in SE Brazil

Abstract

This chapter uses high-quality 3D seismic data to access the geometry of fault families developed around distinct salt structures in the Espírito Santo Basin. It aims at evaluating the timing of the fault growth around the investigated salt structures, and suggests the generation of corridors for fluid migration linking discrete salt diapirs. The study area comprises three salt diapirs and one salt ridge, and faults were divided into five families according to their locations relative to the salt structures. Displacement-length (D-x) and Throw-depth (T-z) plots and maps indicate that faults consist of several segments that were reactivated during salt movement by dip-linkage following a preferential NE-SW direction; i.e. distinct from the eastern part of the Espírito Santo Basin, where the preferential mode of reactivation is by upwards vertical propagation. Reactivation of units above the Mid Eocene discontinuity is scarce in the study area. Importantly, halokinesis occurred at different timings for distinct salt structures and formed corridors connecting distinct diapirs and anticlines. The controls of the halokinesis on the local stress variations and on the juxtaposition of permeable strata through faults were also assessed. This chapter postulates the presence of fault corridors likely to leak fluids adjacently to salt structures, and that the fluids will migrate towards the shallower salt structures as a result of fluid focusing and updip migration along the fault corridors.

5.1. Introduction

The Espírito Santo Basin has a geological evolution similar to the Campos and Santos Basins, two of the most prolific hydrocarbon-bearing basins in SE Brazil (Bruhn et al., 2003; Chang et al., 1992; Cobbold et al., 2001; Demercian et al., 1993; Guardado et al., 2000; Guerra and Underhill, 2012; Meisling et al., 2001; Milani et al., 2001). Although relatively less known than its counterparts to the south, the Espírito Santo Basin hosts significant hydrocarbon accumulations in Cretaceous, Eocene-Oligocene and Miocene strata (Bruhn and Walker, 1997; Estrella et al., 1984; Fiduk et al., 2004; Katz and Mello, 2000). The Espírito Santo Basin also contains volumes of evaporites deemed to have controlled its tectono-stratigraphic evolution, in similarity to sedimentary basins in the Gulf of Mexico (Diegel et al., 1995; Rowan et al., 1999; Talbot, 1993), West Africa (Duval et al., 1992; Hudec and Jackson, 2002; Morley and Guerin, 1996) and Norway (Chand et al., 2008; Henriksen et al., 2011b; Kane et al., 2010; Koyi et al., 1993). Halokinesis in the Espírito Santo Basin started in the Late Aptian–Early Albian and continued through the Cenozoic, leading to the development of salt structures and associated fault families that controlled the distribution and continuity of reservoir intervals within the Urucutuca Formation (Demercian et al., 1993; Fiduk et al., 2004). Hence, the structural framework of the Espírito Santo Basin comprises horsts, grabens, and salt-related structures such as salt diapirs, salt rollers and rollovers, turtle anticlines, rafts and salt walls (Alves, 2012; Fiduk et al., 2004; Varela and Mohriak, 2013).

The main aim of this chapter is to describe and assess the geometry and character of faults located radially to three developed salt diapirs and at the crest of one salt ridge. The timing of formation of the interpreted faults is investigated to test the hypothesis that they

form structural corridors connecting different salt structures. The controls on fluid flow and strata compartmentalisation exerted by fault corridors under different local stress regime(s) are also assessed in this work. In summary, this work aims at addressing the following research questions:

a) How does halokinesis influence fault families developed adjacent to distinct salt structures?
b) Is there any preferred directions for the reactivation of faults in the study area?
c) Is there a relationship between fault reactivation and the migration (or trapping) of fluids around salt structures?
d) How can the studied diapir systems provide insights into the evolution of the Espírito Santo Basin, and contribute to the analysis of seal competence and fluid migration in areas where halokinesis plays a central role.

This chapter is the first to determine a paleostress tensor in the Espirito Santo Basin to model slip tendency and leakage factors for the interpreted faults and to create juxtaposition diagrams to assess where fluids were more likely to migrate laterally along or across faults. In the discussion section, an evolution model is presented for the interpreted salt structures and related faults, providing the timing and the relationship between different fault families. The reasons why only some faults reactivate, but others do not, are investigated and discussed considering previously published works on different parts of the Espírito Santo Basin. The results obtained in this chapter and the

integrated effects of halokinesis on trapping and migration of fluids, can be extrapolated to areas with similar halokinetic structures.

5.2. Database and specific methods

The main data source for this chapter is the 3D seismic volume BES-2, located on the Espírito Santo Basin, SE Brazil. For full details of the acquisition and processing parameters of this survey see *Chapter 3, section 3.3.2*. The general seismic interpretation methods employed in this chapter are described in *Chapter 3, section 3.4.* Displacement analysis methods and the distribution of the tectonic stress across the study area are also detailed in *Chapter 3, section 3.5*.

Seismic interpretation included horizon and fault mapping, seismic attributes and time-depth conversions on Petrel®. Ten (10) key seismic reflections, including the seafloor, were mapped every ten lines (125 m). Smaller line intervals of 1-5 lines (12.5 to 62.5 m) were used to map the observed salt diapirs as discrete structures. Structural maps of horizons H_1, representing the top salt horizon in the study area, and H_6 (corresponding to an Eocene unconformity that bounds Unit 1 at the top), complemented the interpretation of distinct horizons on seismic data.

Two hundred and fifteen (215) fault planes were mapped on seismic profiles and coherence time-slices. Twelve representative faults (F1 to F12) were selected to the displacement-length (D-x) and throw-depth (T-z) analyses. Throw contour plots complement the displacement analyses for the faults in the Espírito Santo Basin. Further analyses performed for this chapter include the creation of juxtaposition diagrams and stress analyses.

Stratigraphic juxtaposition is a widely applied method to predict the potential of fluid retention and migration through faults (Allan, 1989; Knipe, 1997; Reilly et al., 2016). The juxtaposition of impermeable strata, such as shales, against permeable units (sandstones), potentially creates an effective seal, whereas the juxtaposition of permeable units is more likely to promote cross-fault lateral migration. The Fault Analysis Module in Move® was used to create hanging-wall and footwall cut-off lines for stratigraphically-assigned seismic horizon using a trim distance of 15 m. The 3D juxtaposition diagrams (Allan diagrams) were created for the 12 representative faults. The diagrams present a colour code chart to indicate the juxtaposition of the units. Superimposed shale units are indicated in brown along the fault trace, whereas sand juxtaposition is defined in yellow. Unavailable data to perform the juxtaposition analysis are displayed in white.

5.3. Seismic stratigraphy of the Espírito Santo Basin

Based on the character and geometry of the interpreted seismic reflections, and on the relative chronostratigraphic dates of seismic stratigraphic units (Alves et al., 2009; Fiduk et al., 2004; Gamboa et al., 2012; Gamboa and Alves, 2015; Viana et al., 2003), the imaged strata were divided into three principal units: Late Cretaceous – Paleocene (Unit 1), Eocene – Oligocene (Unit 2), and Miocene – Quaternary (Unit 3). (Table 5-1).

*Table 5-1: Seismic characteristics and lithologies of main seismic units interpreted in the study area. Correlation between the seismic units in this work and seismic sequences in the literature: *(Alves et al., 2009); #(Baudon and Cartwright, 2008); +(Gamboa and Alves, 2015); °(Viana et al., 2003).*

Epoch	Seismic Unit	Seismic Sub-unit	Horizon	Thickness (ms)	Internal character, geometry and terminations	Lithology	Seismic sequences in the literature
Quaternary - Miocene	3		Seafloor	500 - 800	Transparent to low amplitude reflections. Scarce mapped faults in this unit. Frequent bright-spots	Interbedded sand to clay-rich turbidites and hemipelagic sediments (Viana et al., 2003; Fiduk et al., 2004)	Units C3 and C4* Unit 3#,+
			H_9				
Early Miocene - Middle Eocene	2	2c		50 - 225	Moderate amplitude chaotic seismic reflections. Frequent bright-spots. Separated from sub-unit 2a by an unconformity	Increase of sand contents. Mass-transport deposits (MTDs) blocks (Gamboa and Alves, 2015)	Unit IIº
			H_8				
		2b		50 - 150	Moderate amplitude chaotic seismic reflections. Frequent bright-spots. Separated from sub-unit 2b by an unconformity	Increase of sand contents. Mass-transport deposits (MTDs) blocks (Gamboa and Alves, 2015)	Unit C2*
			H_7				
		2a		20 - 120	Chaotic low amplitude to transparent reflections intercalated to moderate to high-amplitude internal reflections. Frequent bright-spots	Mass-transport deposits (MTDs) blocks (Gamboa and Alves, 2015)	Unit 2#,+
			H_6				
Middle Eocene - Early Cretaceous	1	1e		75 - 175	Transparent to low amplitude internal reflections. Chaotic reflections close to diapirs. Delimited by an unconformity. Concentrates the majority of faults in the study area	Fine-grained sediments, including clayey turbidites. Interbedded with sand-rich units (Alves et al., 2009; Viana et al., 2003)	Unit Iº
			H_5				
		1d		40	Moderate amplitude positive seismic reflection. Amplitude increases adjacent to salt structures. Offset by radial and crestal faults	Increase in sand contents	
			H_4				
		1c		25	Moderate amplitude negative reflection. Offset by radial and crestal faults	Increase in the shale content in the turbidite package	Unit K5/C1*
			H_3				
		1b		75 - 175	Increase in amplitude of the seismic reflections. Offset by radial and crestal faults	Increase in sand content in distal turbidites	Unit 1#,+
			H_2				
		1a		200 - 500	Predominance of low amplitude to transparent reflections. Offset by radial and crestal faults	Distal turbidites and clay-rich carbonates (Alves et al., 2009; Fiduk et al., 2004; Viana et al., 2003)	
			H_1				
					Chaotic low amplitude to transparent reflections	Evaporites	

5.3.1. Unit 1 (Early Albian – Middle Eocene)

Unit 1 is the primary unit of interest in this chapter (Figure 5-1). Unit 1 comprises five sub-units (1a to 1e), being bounded at its base by horizon H_1 and at its top by horizon H_6 (Figure 5-1). Sub-unit 1a is bounded at its base by horizon H_1 (Figure 5-2), a moderate- to high-amplitude, negative reflection, and at its top by a moderate and nearly continuous seismic reflection (horizon H_2). Low-amplitude to transparent seismic reflections predominate in this sub-unit. Its thickness ranges between 200 – 500 ms, decreasing close to the flanks of salt structures. The probable lithology of sub-unit 1a consists of distal turbidites and clay-rich carbonates (Alves et al., 2009; Fiduk et al., 2004; Viana et al., 2003).

Horizon H_2 delimits the base of sub-unit 1b, where it is possible to observe an increase in the amplitude of seismic reflections. This sub-unit is offset by faults that are radial to the smaller salt diapirs, and by faults developed at the salt ridge crest (Figure 5-1). In the eastern part of this area, the internal character of sub-unit 1b becomes chaotic in the proximity of the Rio Doce Canyon System (Figure 3-8). Within the area of interest in this study, sub-unit 1b is characterised by moderate-amplitude, sub-parallel reflections that likely represent an increase in sand content relative to sub-unit 1a. The upper boundary of this 75 ms- to 175 ms-thick sub-unit is defined by the moderate- to high-amplitude horizon H_3.

Sub-unit 1c is defined at the base by horizon H_3 and at its top by horizon H_4 (Figure 5-1). This sub-unit consists of a 25 ms-thick, moderate amplitude package interpreted as a shale interval. Horizon H_4 delimits the base of Sub-unit 1d, and is characterised

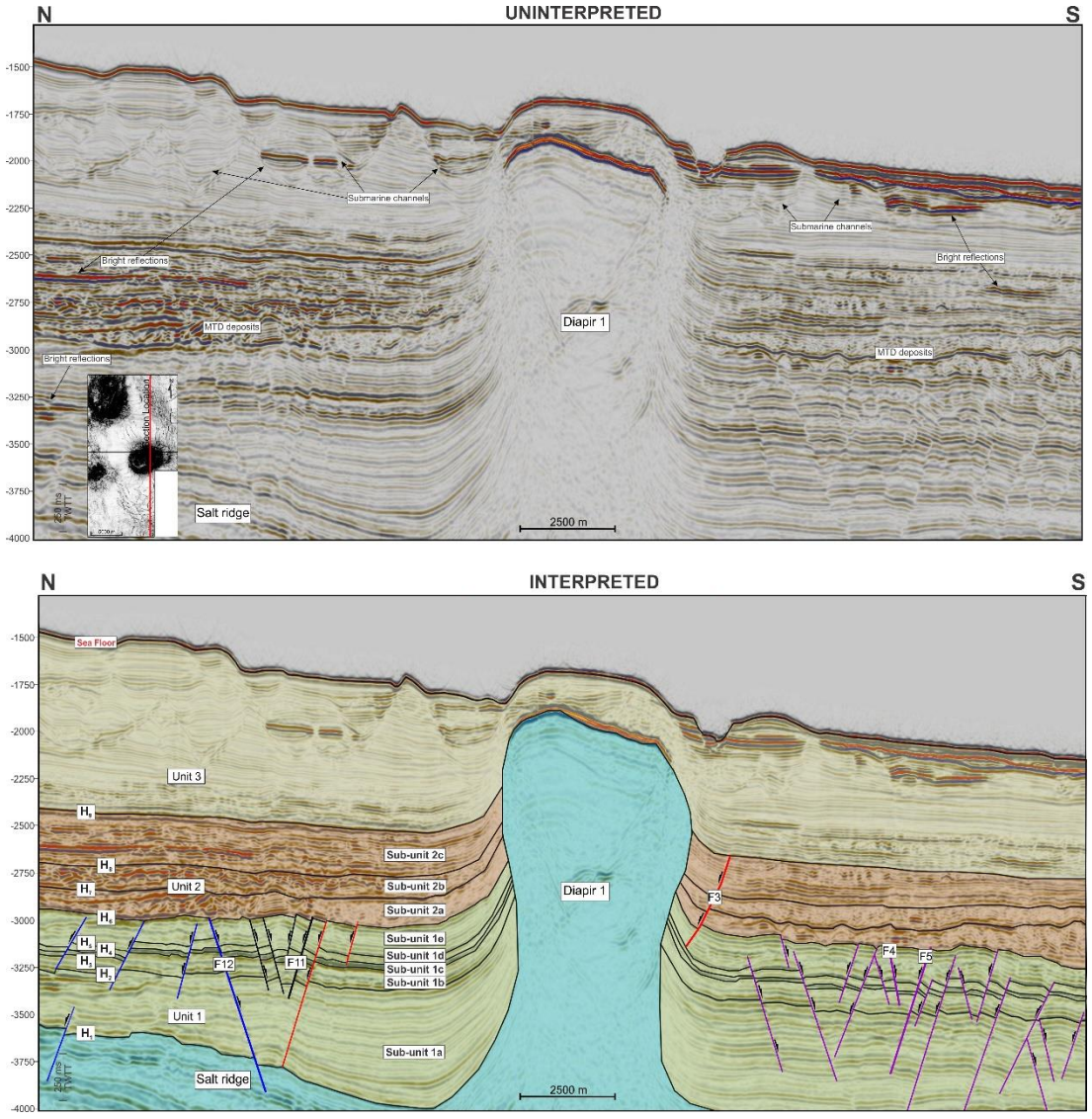

Figure 5-1: Uninterpreted and interpreted N-S section exhibiting the internal geometry and seismic character of Units 1, 2 and 3 and its respective sub-units in the proximities of the Salt ridge and Diapir 1. Unit 1 concentrates the majority of faults in the study area is sub-divided into sub-units 1a to 1e. Sub-unit 1a is characterised by low amplitude to transparent seismic reflections. A bright-spot is observed at the top of this unit to the north of this section. Sub-unit 1b shows an increase in amplitude, related to an increase in the sand contents. Sub-unit 1c comprises a 25 m-thick moderate amplitude reflection that was interpreted an interval rich in shales. An increase in the sand content is interpreted to occur in Sub-unit 1d. Sub-unit 1e shows transparent to low amplitude reflections and is delimited to the top by an unconformity. Unit 2 was sub-divided into sub-units 2a to 2c and is characterised by mass-transport deposits (MTDs) and sand-rich turbidite lobes. Distinctive bright-reflections are observed in this unit. Unit 3 is characterised by low amplitude reflections often incised by submarine channels. Bright-reflections are observed adjacent to these submarine channels and close to the seafloor.

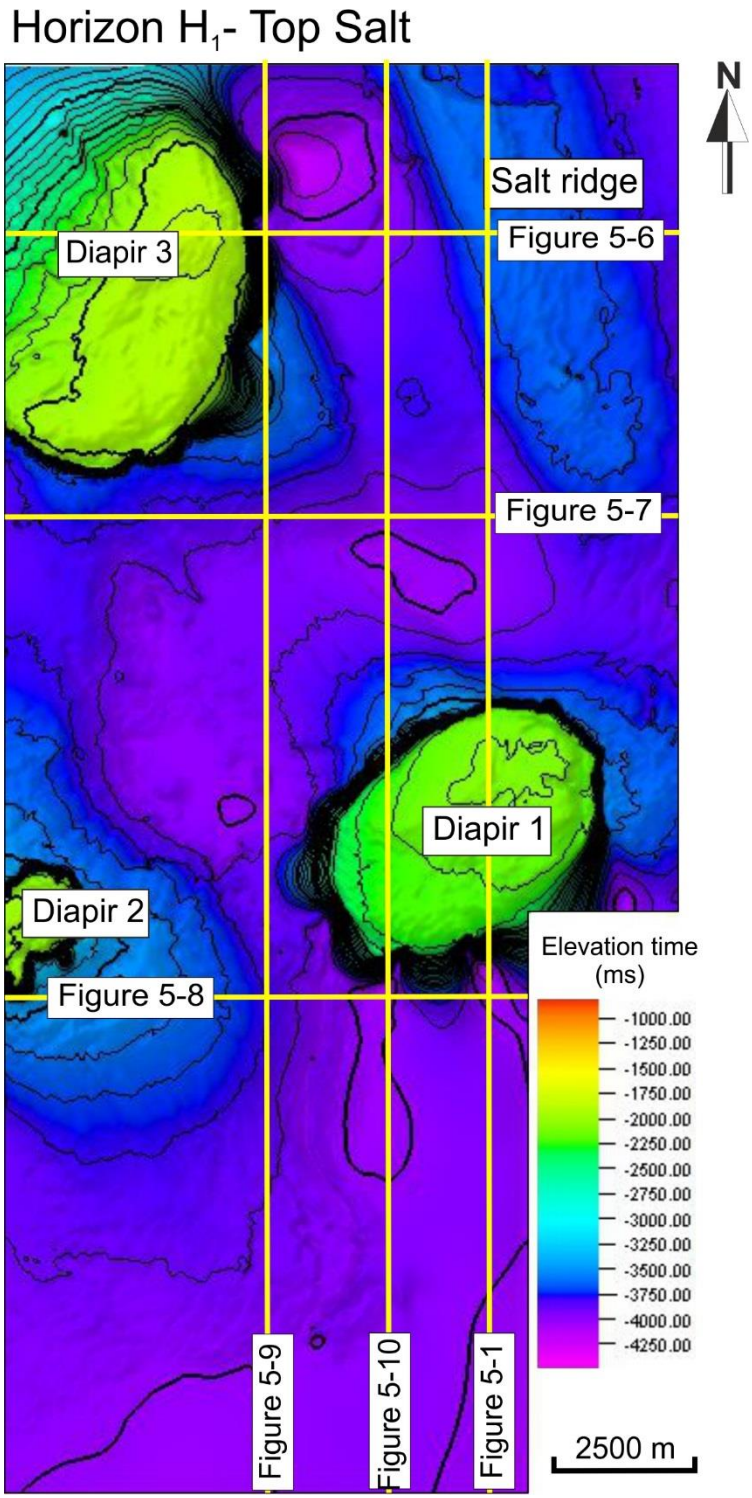

Figure 5-2: Time-structural map of horizon H_1 highlighting the occurrence of salt structures such as diapirs and ridges in the study area.

by a 40 ms-thick moderate amplitude package. The amplitude of this sub-unit increases particularly close to diapirs and salt-ridge crests, and was interpreted as reflecting an increase in sand content.

Horizon H_5 delimits the top of Sub-unit 1d and the base of Sub-unit 1e, a 75 ms- to 175 ms-thick sub-unit is delimited at its base by a regional unconformity; horizon H_6 (Figure 5-1). Sub-unit 1e exhibits transparent to low-amplitude internal reflections that become chaotic close to diapirs and the Rio Doce Canyon System. It is likely composed of fine-grained (clayey) turbidites. In the proximities of the Rio Doce Canyon System, these fine-grained units alternate with sand-rich turbidites (Alves et al., 2009; Viana et al., 2003). The majority of faults in the study area occur radially to the three salt diapirs and at the crest of the salt ridge. These faults are truncated at their upper tips by horizon H_6 (Figure 5-1).

5.3.2. Unit 2 (Middle Eocene – Early Miocene)

Unit 2 is delimited at its base by horizon H_6 (Figure 5-3), and corresponds to a regional Mid-Eocene unconformity. Faulting is ubiquitous at this level, but rarely propagates into the upper part of Unit 2 (Figure 5-1). Unit 2 consists of chaotic low-amplitude to transparent reflections that are intercalated with moderate amplitude strata. The base of Unit 2 (sub-unit 2a) is characterised by the occurrence of blocky mass-transport deposits (MTDs) around the buried salt ridge formed between diapirs 1 and 2 (Gamboa and Alves, 2015). Blocks are shown as moderate amplitude reflection features with sharp to smooth edges, distributed between low-amplitude reflections reflecting fine-grained sediments

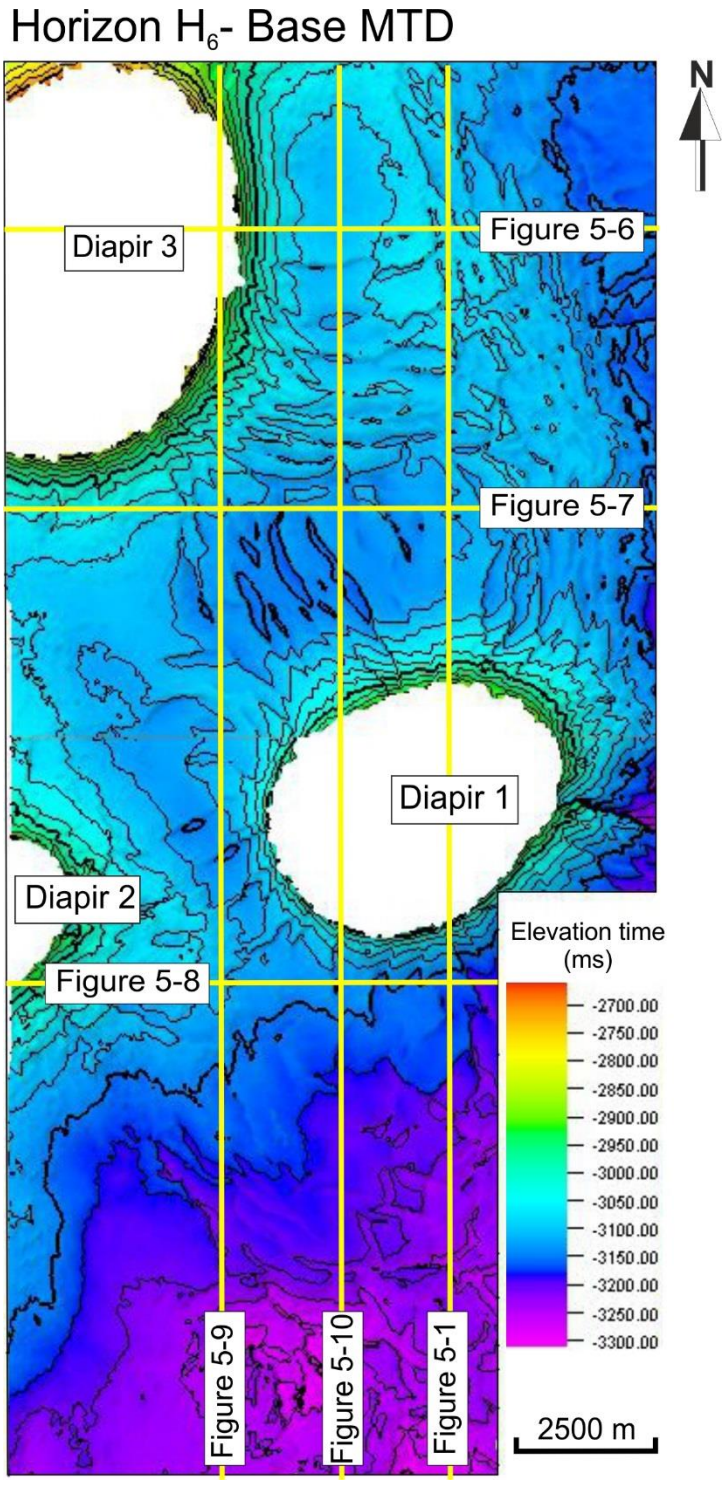

Figure 5-3: Time-structural map of the regional Mid-Eocene unconformity represented by horizon H_6. Radial faults are observed adjacently to diapirs 2 and 3. However, these faults rarely propagate into the upper part of Unit 2, which is delimited by horizon H_6 at its base.

(Figure 5-1). The middle and upper parts (sub-units 2b and 2c) of Unit 2 are characterised by the occurrence of high-amplitude reflections (horizons H_7 and H_8), which have been previously interpreted as sand-rich turbidite lobes (Alves et al., 2009; Gamboa and Alves, 2015). These two sub-units are separated by an unconformity (Figure 5-1). Unit 2 is offset by diapirs throughout the study area. The upper boundary of Unit 2 is defined by the Early Miocene horizon horizon H_9 (Figure 5-1).

5.3.3. Unit 3 (Miocene – Quaternary)

The base of Unit 3 coincides with Horizon H_9, whereas the seafloor delimits its top. Unit 3 is characterised by low-amplitude, sub-parallel internal reflections that are incised by submarine channels filled with moderate to high-amplitude reflections (Figure 5-1). Submarine channels may be deformed at the proximities of salt diapirs. The interpreted lithologies for this unit includes interbedded sand, clay-rich turbidites and hemipelagic sediment (Fiduk et al., 2004; Viana et al., 2003).

5.4. Fault distribution around salt structures

Structural interpretation based on the analysis of coherence time-slices (Figure 5-4) and seismic profiles (Figure 5-6 to 5-10) resulted in the subdivision of imaged faults into five (5) families, depending on their position relative to the principal salt ridge and adjacent diapirs.

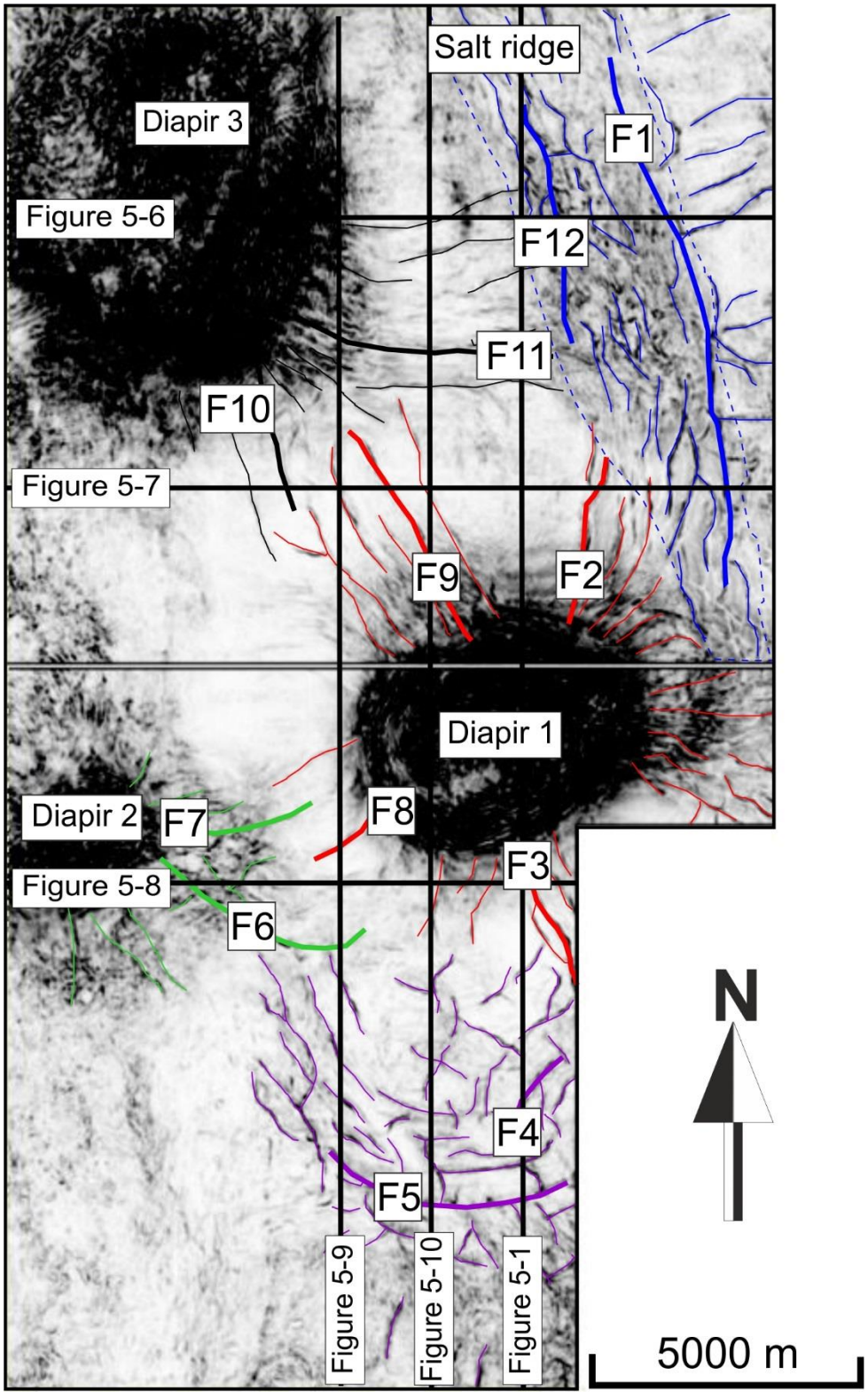

Figure 5-4: Coherence time-slice at -3500 ms showing the locations of the main fault families in the study area. Salt Ridge faults are represented by the colour blue, whereas faults adjacent to Diapir 1 are in red. Faults in the Southern Area, Diapir 2 and Diapir 3 are represented respectively by purple, green and black faults.

5.4.1. Salt ridge faults

A NW-SE-trending salt ridge occurs to the NE of the interpreted volume, with a maximum width of ~ 2.7 km and a length of 10 km, and terminates in the proximity of diapir 1. On seismic data, the salt ridge forms an anticlinal structure with a lenticular shape (Figure 5-6). In contrast to the adjacent salt diapirs, Units 1 to 3 bury the salt ridge in its whole extent.

The main strike for the 55 faults mapped at the salt ridge is NW-SE, denoting an average strike of 332.65º (Figure 5-5) for the largest faults in the study area, including F1. The predominant strike for the (comparatively) smaller faults is NE-SW. Faults occurring in this area dip both to NE and SW. Representative faults include F1 and F12, two NW-SE striking faults developed at the crest of salt diapirs and with fault traces spaced ~ 2.95 km at their upper tips (horizon H_6) and ~ 1 km at their lower tips (horizon H_1).

The average length of the faults in the salt ridge is 1.2 km. However, one of the most distinctive features of this group of faults is the occurrence of fault F1, the largest fault mapped in the study area, with a length of 9.5 km. Fault F1 occurs parallel to the salt ridge and terminates ~ 1.3 km away from diapir D2 in the southeastern part of the study area. Fault 12 occurs ~ 4.9 km away from Diapir 1. The faults follow the same direction of the salt ridge and are confined within Unit 1, with no evidence of faults reaching the MTDs in Unit 2 (Figure 5-6). Tilt blocks formed at the crest of the salt ridge do not show any growth strata on the seismic profiles (Figure 5-6). Distinctive bright reflections occur between -3280 and -3420 ms, at Sub-Unit 1c (Figure 5-6).

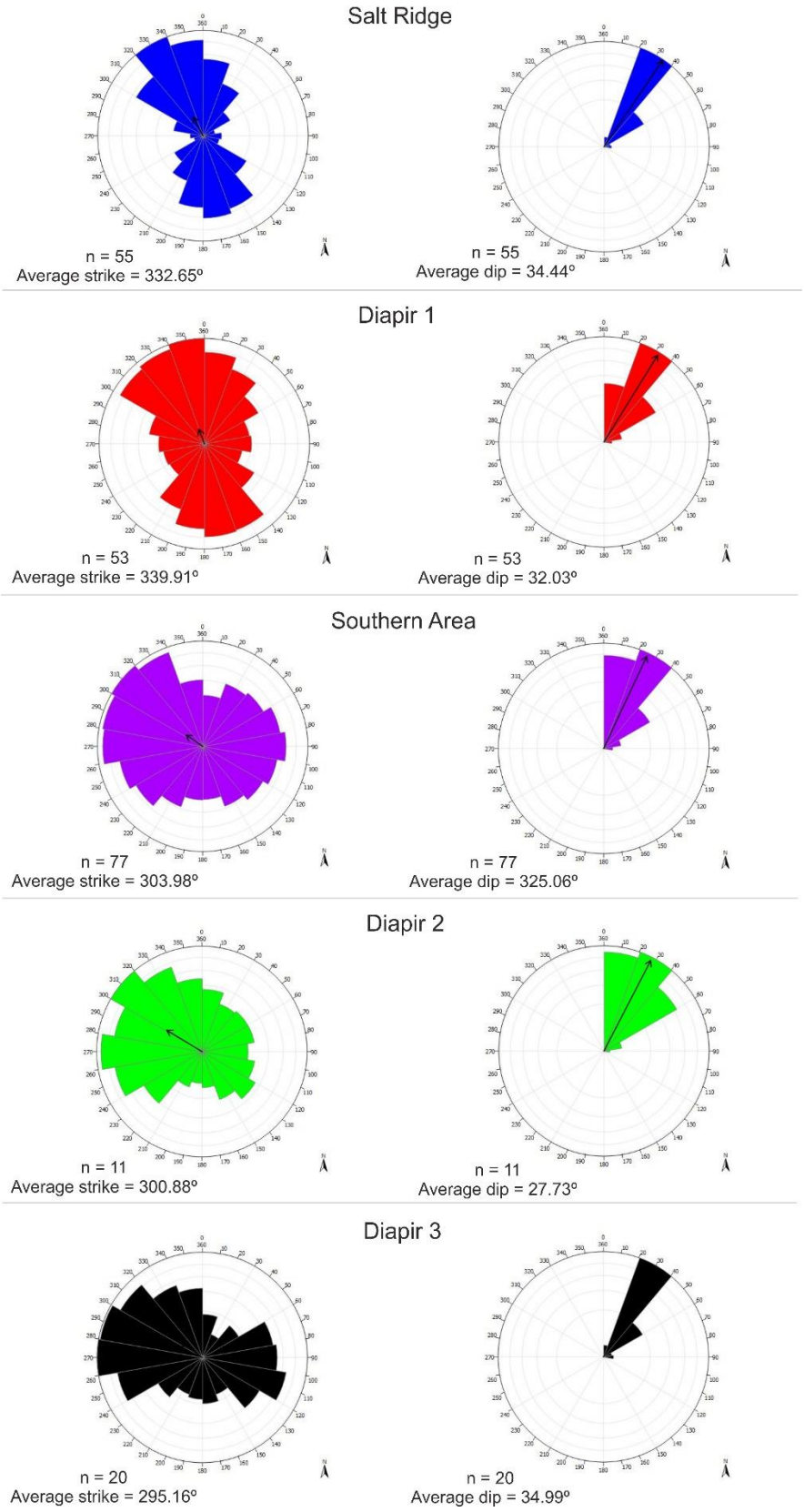

Figure 5-5: Rose diagrams showing the strike and dip for the faults in the study area.

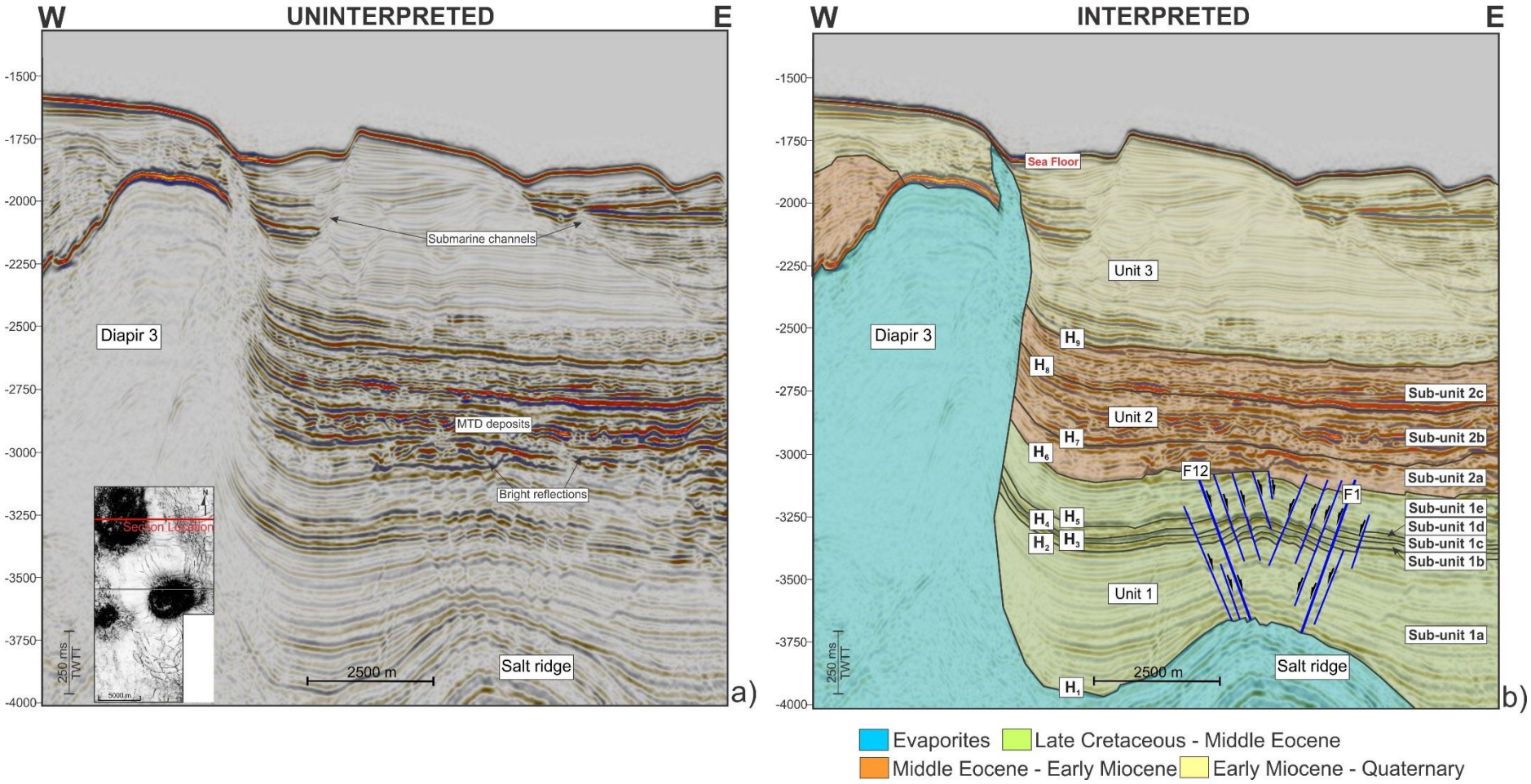

Figure 5-6: W-E seismic profile crossing Diapir 3 and the Salt Ridge. Submarine channels are observed close to the seafloor and characterised by bright reflections. The interpreted seismic profile highlights the presence of faults F1 and F12. Faults at the crest of the salt ridge comprise tilt blocks and terminate at horizon H6, where bright reflections are also observed. The strata from Units 1 to 3 are deformed adjacent to Diapir 3.

5.4.2. Diapir 1

Diapir 1 occurs to the East of the study area, showing a diameter of ~5.4 km. Fifty-three (53) faults were mapped with a main strike to NW-SE and an average strike direction of 339.91º (Figure 5-5). The second most common group of radial faults to Diapir 1 strikes NNE-SSW. In contrast, E-W striking faults are less common around Diapir 1 than close to Diapir 3. Faults located adjacent to Diapir 1 dip preferentially to NE, showing an average dip of 32.03º. Representative faults located radially to Diapir 1 include F2, F3, F8 and F9. Most faults occur between horizons H_2 and H_6. However, an important number of faults also offset the top salt horizon H_1, including F2 and F9 (Figure 5-7).

Radially to Diapir 1, one of the most striking features of this area is the occurrence of fault F3, a NW-SE fault with an average dip of 40.81º that offsets horizons H_2 to H_9 along its length (Figures 5-1 and 5-8). Approximately 2.7 km separate faults F2 and F9 at the depth of horizon H_2, whereas faults F3 and F9 are separated by ~ 4.2 km. Fault F2 is NNE-striking terminating against the salt ridge. Fault F9 is NW-striking and intersects with the trace of fault F10, radial to Diapir 3 (Figure 5-8). The trace of fault F8 overlaps with the trace of faults F7 and F6, both developed at the crests of Diapir 2. Faults F7 and F6 are spaced ~ 1.2 km and ~ 1.45 km from F8, respectively (Figure 5-8). The interpretation of the seismic profiles indicates the presence of pop-up structures around Diapir 1 and close to Diapir 3 (Figure 5-8). Next to Diapir 1, seismic profiles mainly show NW-striking faults. Bright reflections are observed in strata offset by fault F8.

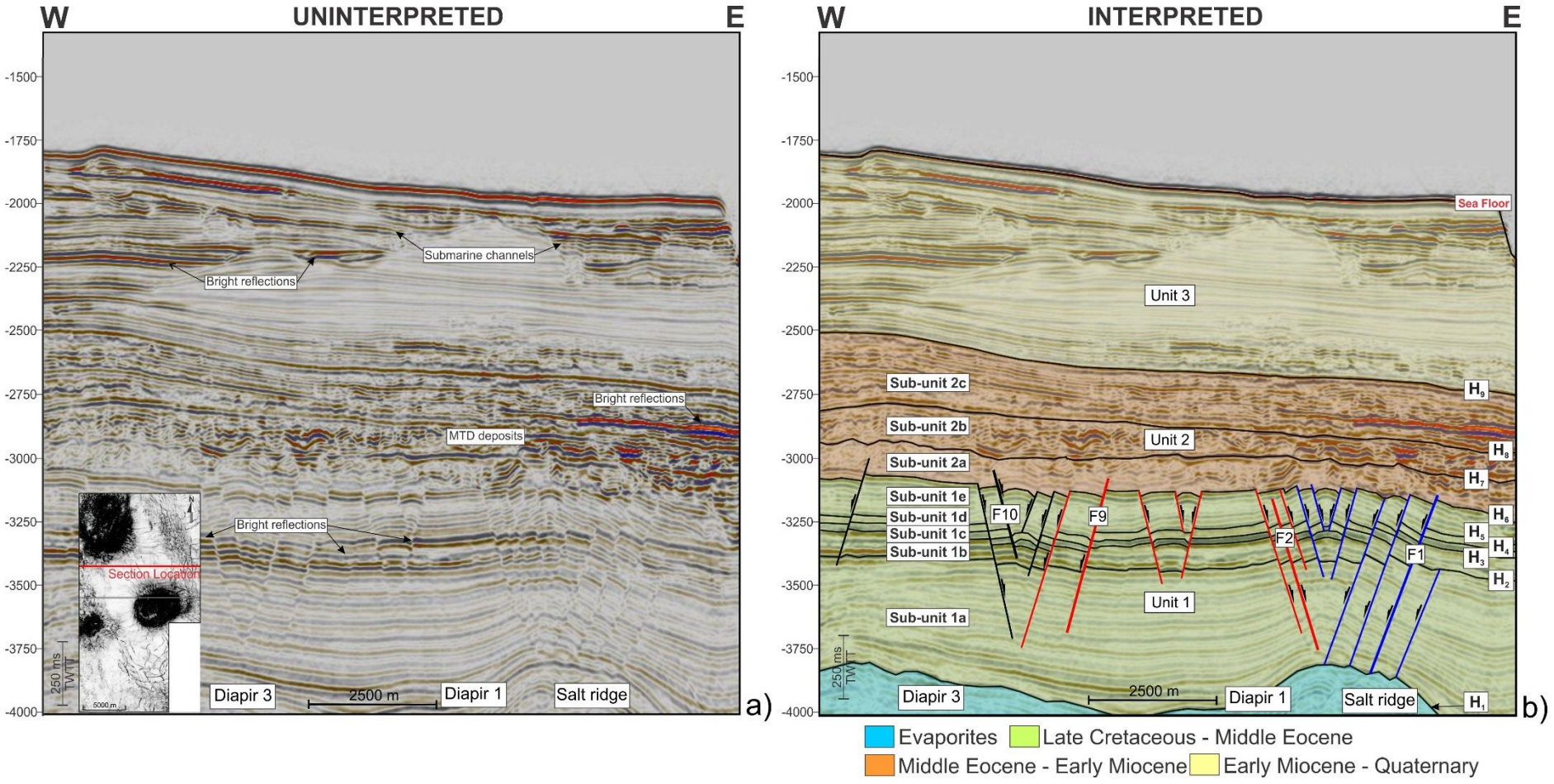

Figure 5-7: W-E seismic profile located between the salt structures highlighting the occurrence of bright reflections adjacent to Diapirs 1 and 3 and the Salt Ridge. The interpreted seismic profile shows that faults adjacent to Diapir 1 form tilt blocks with faults from the Salt Ridge and Diapir 3. Faults from Diapirs 1 and 3 propagates to Sub-unit 2a, whereas faults from the Salt Ridge terminates at horizon H6. Representative faults observed in this section include F1, F2, F9 and F10.

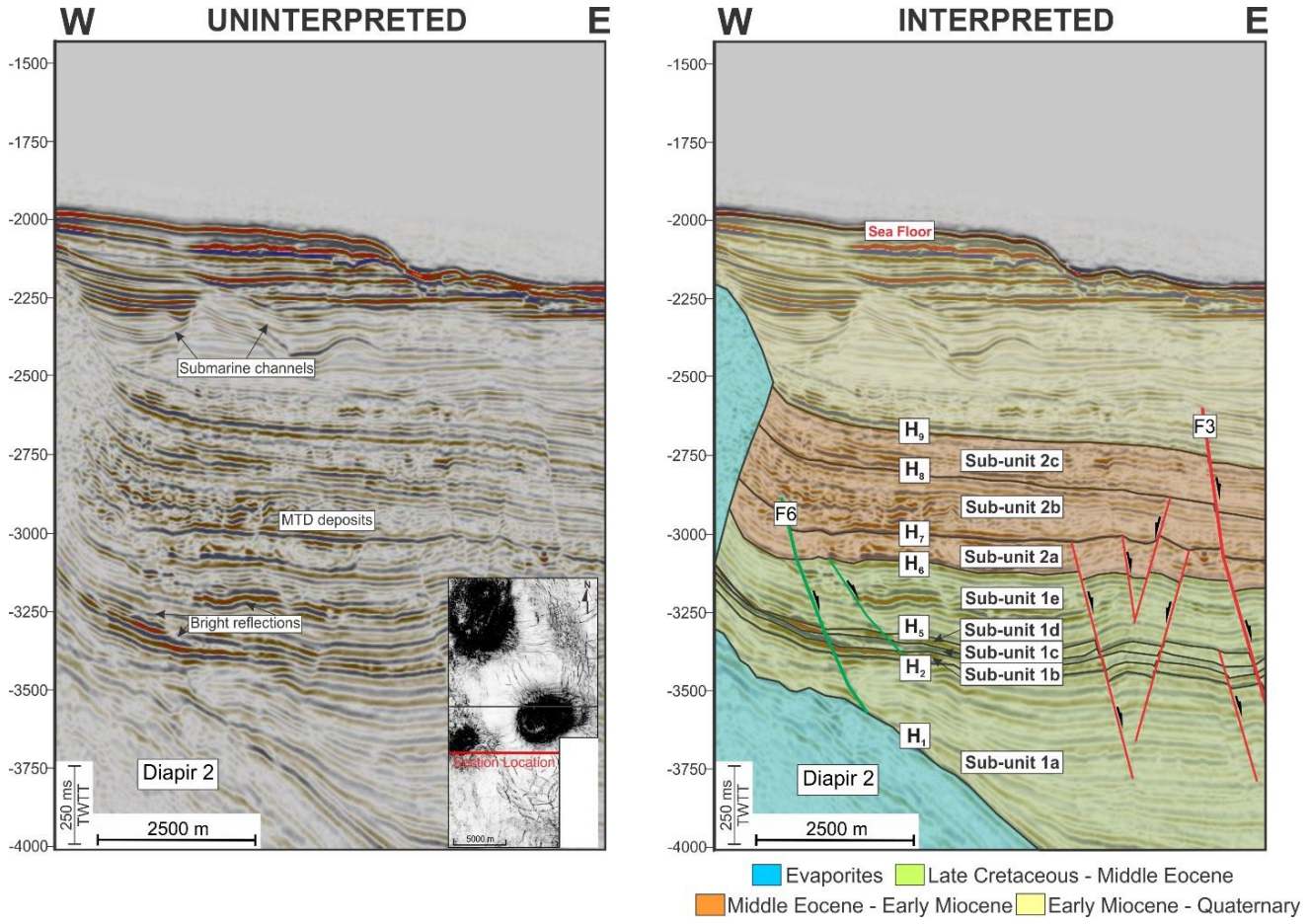

Figure 5-8: Uninterpreted and interpreted W-E seismic profile in the Espírito Santo Bain highlighting the occurrence of bright reflections adjacent to Diapir 2. Submarine channels are observed at a depth of -2500 ms below the seafloor. Diapir 2 deforms the three stratigraphic units. Representative faults in this seismic line include faults F3 and F6. Fault F3 offsets units 1 to 3, whereas fault F6 offsets units 1 and 2.

5.4.3. Southern Area

The southern part of the study area shows a relatively small influence of halokinesis (Figure 5-4). However, this is the most faulted part of the study area, with 77 faults interpreted. The average strike for the faults in the Southern Area is 303.98º. Comparing the faults mapped in the southern area with the faults associated with the salt diapirs it is possible to observe that the former are smaller in length (average length 0.8 km) and are confined within Unit 1. Some of the faults mapped in the South are deep-seated, reaching depths of -3880 ms. However, none of the faults mapped in this area offset horizon H_6 or extend vertically to Unit 2. On the coherence data, faults mapped in the southern part have a pattern resembling polygonal faults (Figures 5-9 and 5-10). Two faults are representative of this area, the NNE-SSW striking F4 and the NE-SW striking F5. Compared to other areas, the southern part of the study area shows a greater concentration of bright reflections along fault blocks (Figures 5-9 and 5-10).

5.4.4. Diapir 2

Diapir 2 is located to the west of the block BES-2, showing a diameter of 2.6 km and consisting of the smallest diapir in the study area (Figure 5-4). Eleven (11) faults were mapped around Diapir 2, showing an average strike of 300.88º (NW-SE) and an average dip of 27.73º (Figure 5-5). The longest faults radial to Diapir 2 have a predominant NW strike, whereas small faults around Diapir 2 strike to NE. However, E-W-striking faults,

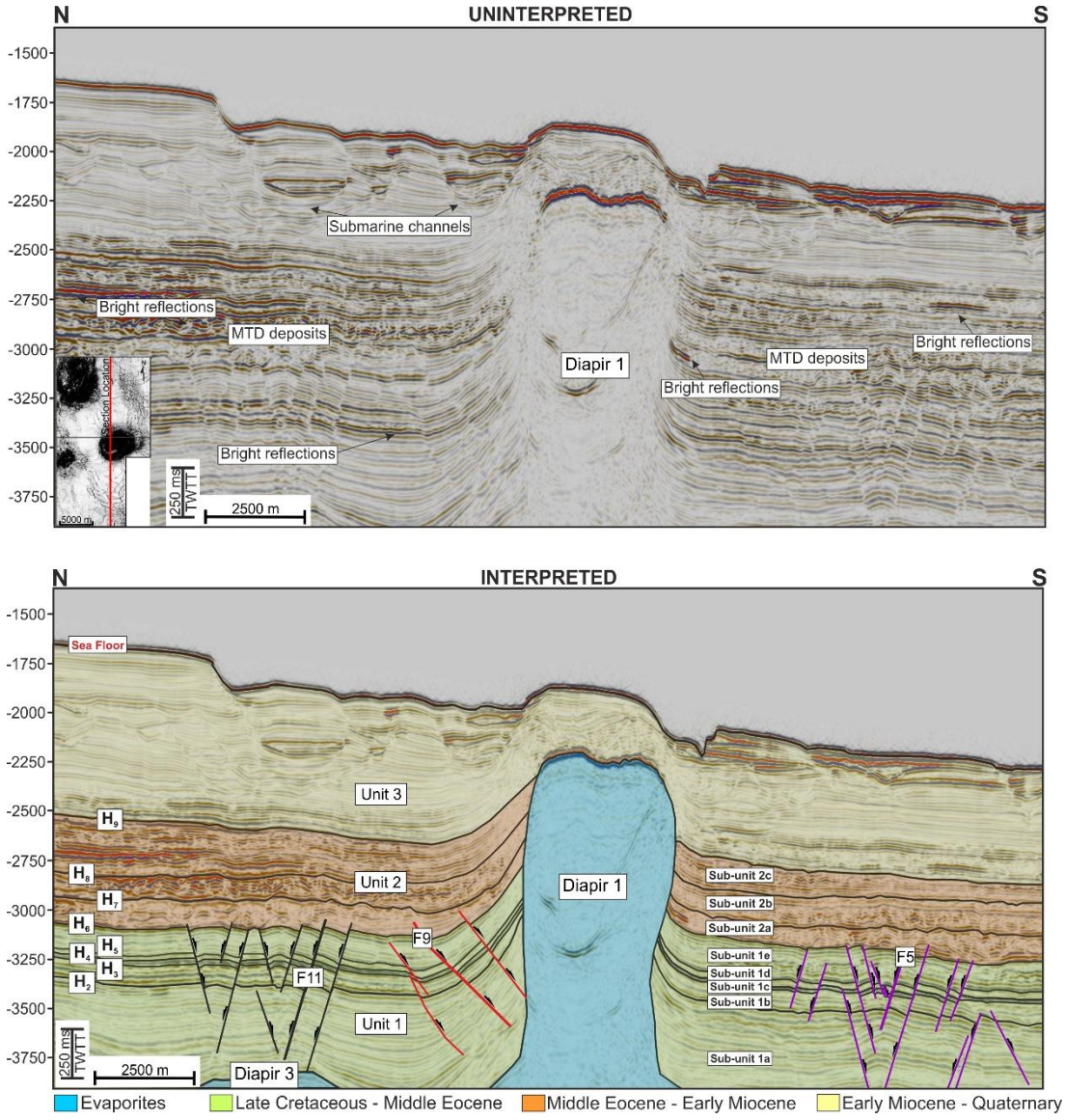

Figure 5-9: N-S seismic profile showing that strata is deformed in the proximities of Diapir 1 and the radial character of the faults adjacent to this salt structure. Faults related to Diapir 3 and faults in the Southern Area form tilt blocks to the north and the south of this section, respectively. Representative faults observed in this section include F5, F9 and F11.

including fault F6, also occur in this part of the study area. Although most of the faults are contained within Unit 1, some structures close to this diapir (including fault F7) offset the top of the salt horizon (H_1) and terminate in the Sub-unit 2b (Figure 5-8). Away from the salt diapir, the NE-striking F7 offsets horizons H_2 to H_5. Faults F6 and F7 are separated by ~ 1.8 km. The interpretation of the seismic profile shows a bright reflection occurring close to Diapir 2, on the footwall of fault F6.

5.4.5. Diapir 3

Diapir 3 occurs in the NW part of the study area, with a diameter of ~ 7.1 km (Figure 5-4). Nineteen (19) faults were mapped around Diapir 3, showing a main strike of 295.16º (NW-SE) (Figure 5-5). Faults striking to E-W are also common. A large number of faults occur between horizons H_2 and H_6, on the crest of Diapir 3, with observed faults rarely offsetting the top salt horizon (H_1). A distinctive feature is the occurrence of faults offsetting MTDs in Unit 2, including fault F11 (Figures 5-7, 5-9 and 5-10). The average length for this group of faults is 1.6 km, with representative faults F10 and F11, striking NW. These two faults show a spacing of ~ 1.1 km at the bottom of Unit 1, and ~ 2.9 km at the top of this unit. Bright reflections are observed adjacent to the faults developed radially to Diapir 3 (Figure 5-9). A large number of bright reflections are also found in Unit 2, immediately above these faults (Figure 5-10).

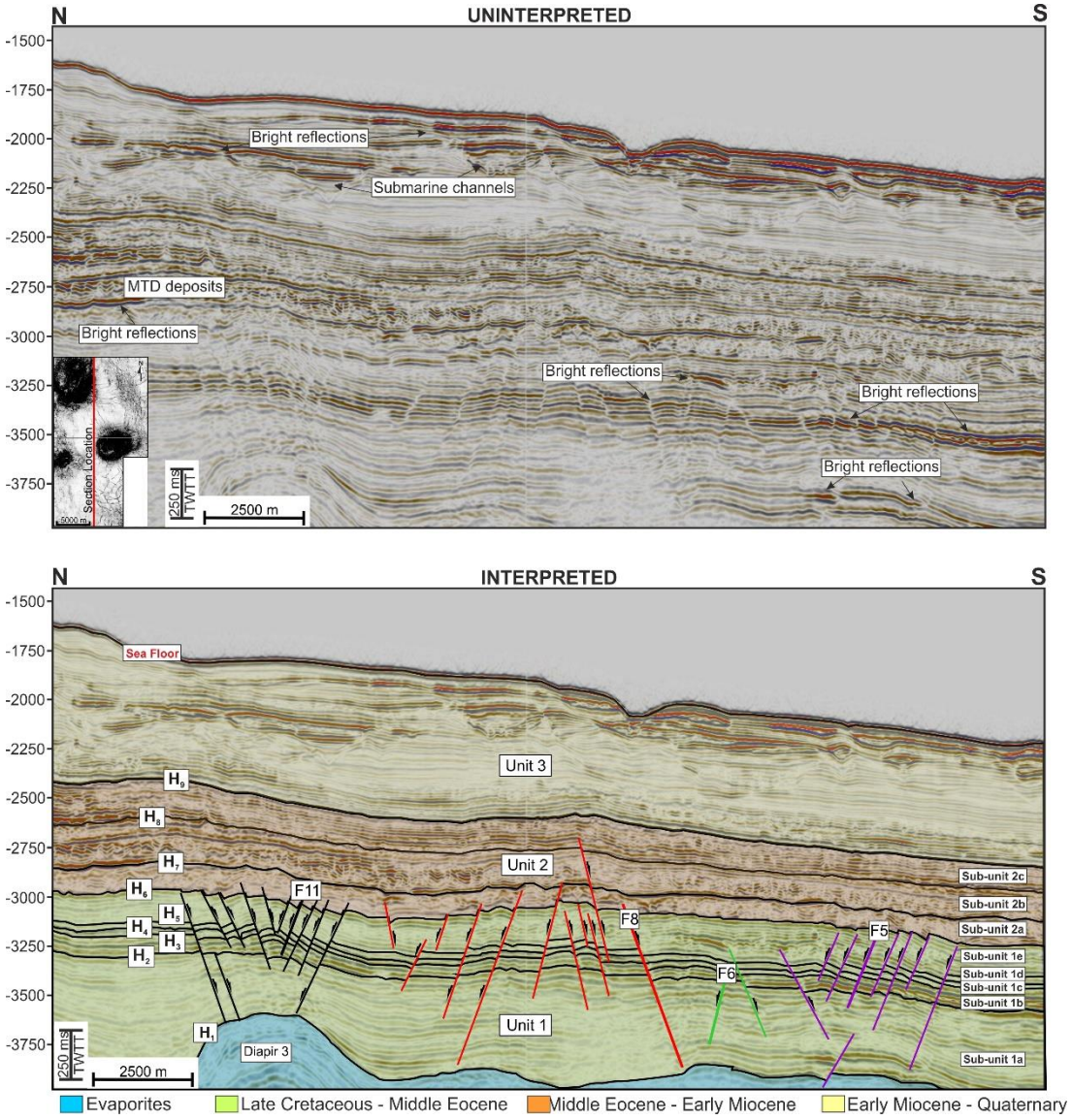

Figure 5-10: N-S seismic profile showing faults adjacent to diapirs 1, 2 and 3, and faults in the Southern Area. Bright reflections occur close to the seafloor and at Unit 2 to the north and in sub-units 1a to 1c for faults adjacent to diapirs 1 and 2 and in the Southern Area. Faults adjacent to diapirs 1 and 3 offset Unit 2, whereas faults in the Southern Area are restricted to Unit 1. Representative faults observed in this section include F5, F6, F8 and F11.

5.5. Fault displacement analyses

5.5.1. Interpretation of distance-length (D-x) plots

Displacement-length (D-x) plots were computed for the twelve (12) representative faults using horizon H_5 as a reference (Figure 5-11). The geometry of the profiles relates to the observed displacement variations along the fault length. For a single and isolated fault, D-x profiles represent a near-symmetric slope with gentle variations in displacement and flat-topped curves, characteristic of a C-type fault (Childs et al., 1995; Muraoka and Kamata, 1983; Nicol et al., 1996; Peacock and Sanderson, 1991). Complex D-x profiles derive from the presence of abrupt variations in displacement along the fault length, indicating linkage of individual fault segments through their displacement minima during the fault growth (Walsh et al., 2003). These structures are classified as M-Type faults (Muraoka and Kamata, 1983), and their characteristic profiles show a broad central section with no significant slope variations. Their flanking portions show abrupt displacement variations, resulting in their marked asymmetric character. Displacement maxima relate with the nucleation point for individual fault segments (Barnett et al., 1987; Nicol et al., 1996; Walsh and Watterson, 1987). This assertion, however, is only true for unsegmented or isolated blind faults.

Displacement-length (D-x) plots for the faults located around the salt diapirs and ridges are provided in Figure 5-11. Overall, the geometry of the D-x profiles varies from asymmetric (F1, F5, F6, F7, F9, F10 and F11) to symmetric (F2, F3, F4, F8, and F12). Faults F3 and F4 have distinctive M-type profiles. F5 is skewed to the left, whereas F6 is skewed to the right. The remaining faults have more complicated displacement profiles.

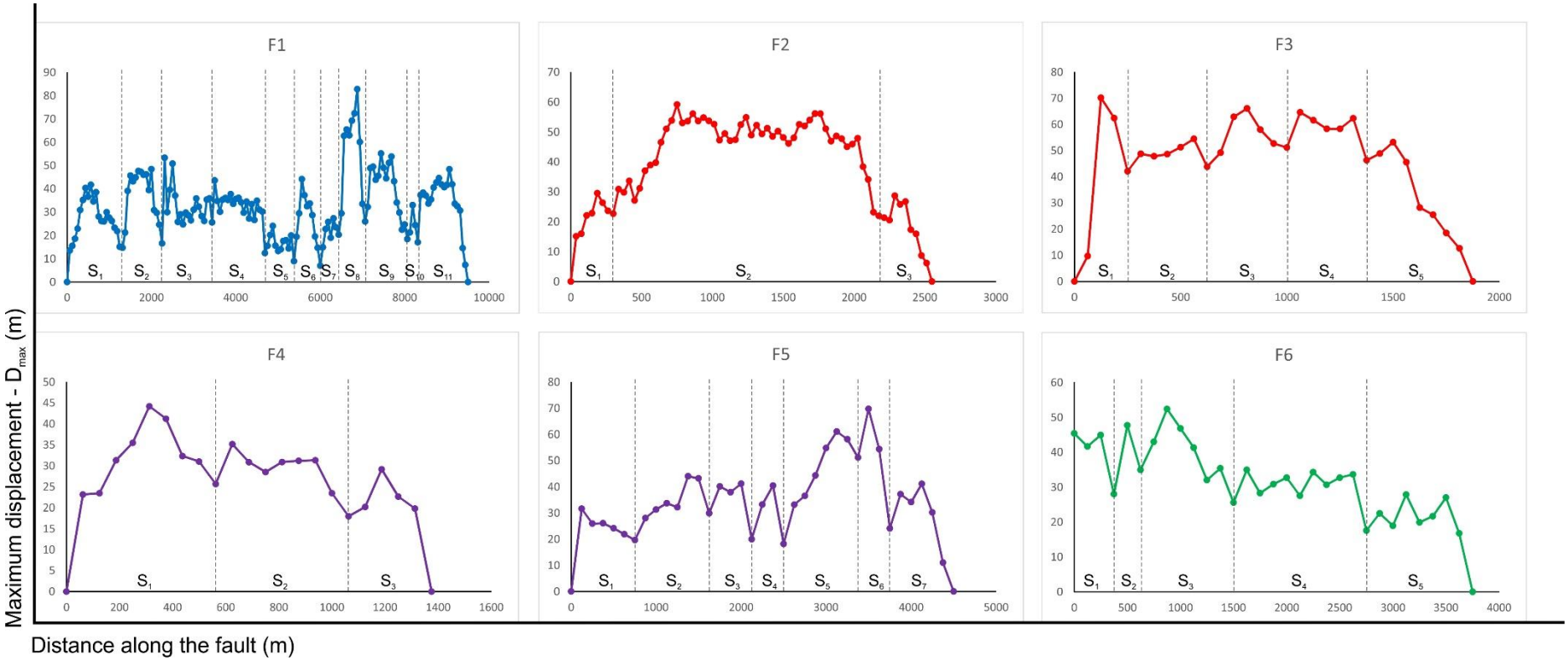

Figure 5-11: Displacement-length (D-x) plots for eight representative faults in the study area. Faults are classified as C-type and M-type profiles from Muraoka and Kamata (1983). Displacement curves were created along horizon H_5. Fault displacement and distance along the fault length are displayed in metres. Dotted lines and S1 to Sn denote distinct fault segments later linked to form a continuous fault plane.

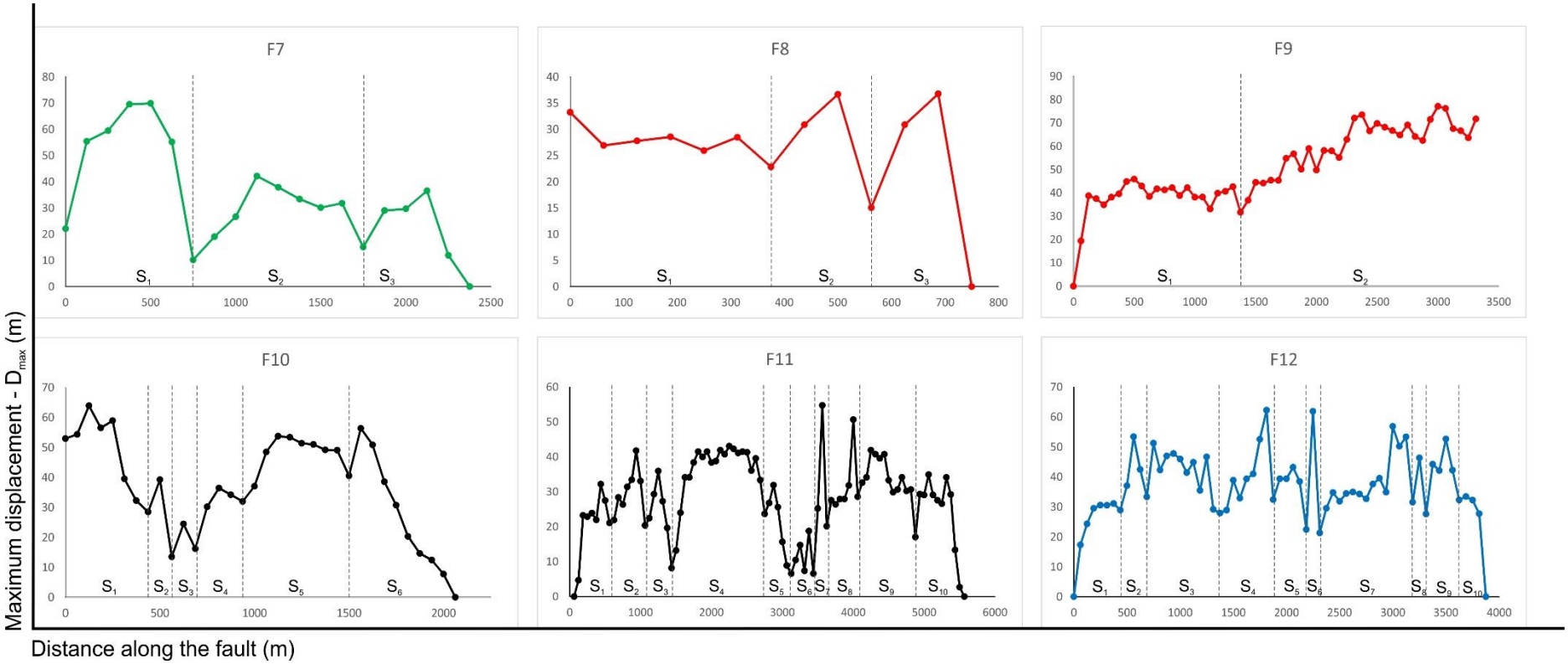

Figure 5-11 (cont.): Displacement-length (D-x) plots for eight representative faults in the study area. Faults are classified as C-type and M-type profiles from Muraoka and Kamata (1983). Displacement curves were created along horizon H_5. Fault displacement and distance along the fault length are displayed in metres. Dotted lines and S1 to Sn denote distinct fault segments later linked to form a continuous fault plane.

Faults F4 and F7, for example, are a combination of a C-type profile on the left and an M-type profile on the right. Faults F6, F7, F8 and F10 show one of their terminations coinciding with the salt diapir, and no zero displacements were observed at such point (Figure 5-11). Fault F9 extends beyond the seismic cube. However, the two nearly flat-shaped profiles seem to be the preferential D-x profile for this fault. Faults F1, F11 and F12 have the most complex displacement profile, with a succession of several C-, M-, and skewed-type profiles. The complexity of these D-x profiles indicates the faults formed around the salt structures were not isolated during their propagation and growth. Fault F2 is the only fault in the study area with an overall shape resembling the C-type profile of Muraoka and Kamata (1983). However, it is possible to observe the occurrence of two displacement minima areas, indicating this fault developed as a combination of three initially isolated fault segments (*cf.* Childs et al., 1995; Peacock and Sanderson, 1991).

Faults associated with the salt ridge are among the most segmented in the study area. Fault F1 consists of eleven (11) segments, whereas F12 has ten (10) segments. The faults developed around Diapir 1, in contrast, are the least segmented, with fault F5 comprising five (5) segments, faults F2 and F8 with three (3) segments and F9 with only two (2) segments. In the southern part of the study area, F4 consists of three (3) segments and F5 of seven (7) initially isolated segments. Close to Diapir 2, fault F6 has five (5) segments, and fault F7 consists of three (3) segments. The fault complexity increases close to Diapir 3, with F10 comprising six (6) segments and F11 consisting of the lateral linkage of ten (10) initially isolated fault segments.

In addition to fault segmentation, representative faults also have variable maximum displacement (d_{max}) and fault length (Figure 5-11). Values of D_{max} range from 82.83 m (F1) to 36.75 m (F8), while fault length varies from about 750 m (F8) to 9.5 km (F1). A relationship between the number of segments and the fault length can be delineated considering that large faults such as F1 (9.5 km), F11 (5.5 km) and F12 (3.8 km) have up to eleven segments, and small faults such as F4 (1.4 km) and F8 (750 m) have three segments each. For the remaining faults, the number of segments varies with the fault length at different scales. A diagram relating the maximum displacement and the fault length was created for all the 12 representative faults in the study area and compared to data for faults from different settings from the literature (Figure 5-12). The scale relationships for the faults in the Espírito Santo Basin coincide with the field where normal faults predominate.

5.5.2. Interpretation of throw-depth (T-z) plots

The throw-depth (T-z) plots for the twelve representative faults are shown in Figure 5-13. Throw profiles include M-types (F1, F2, F6, F9) and C-types (F4, F5) *cf.* Muraoka and Kamata (1983). Fault F3 is an example of a skewed M-type profile. The profiles of some of the faults show a hybrid character that results in the combination of two or more throw profiles. Fault F7 consists of a combination of M- and C-types in Unit 1, whereas an M-type profile is observed in Units 2 and 3. The throw profiles for faults F10 and F12 show a combination of M- and C-types profiles. Faults F8 and F11 consist of two M-type profiles (Figure 5-13).

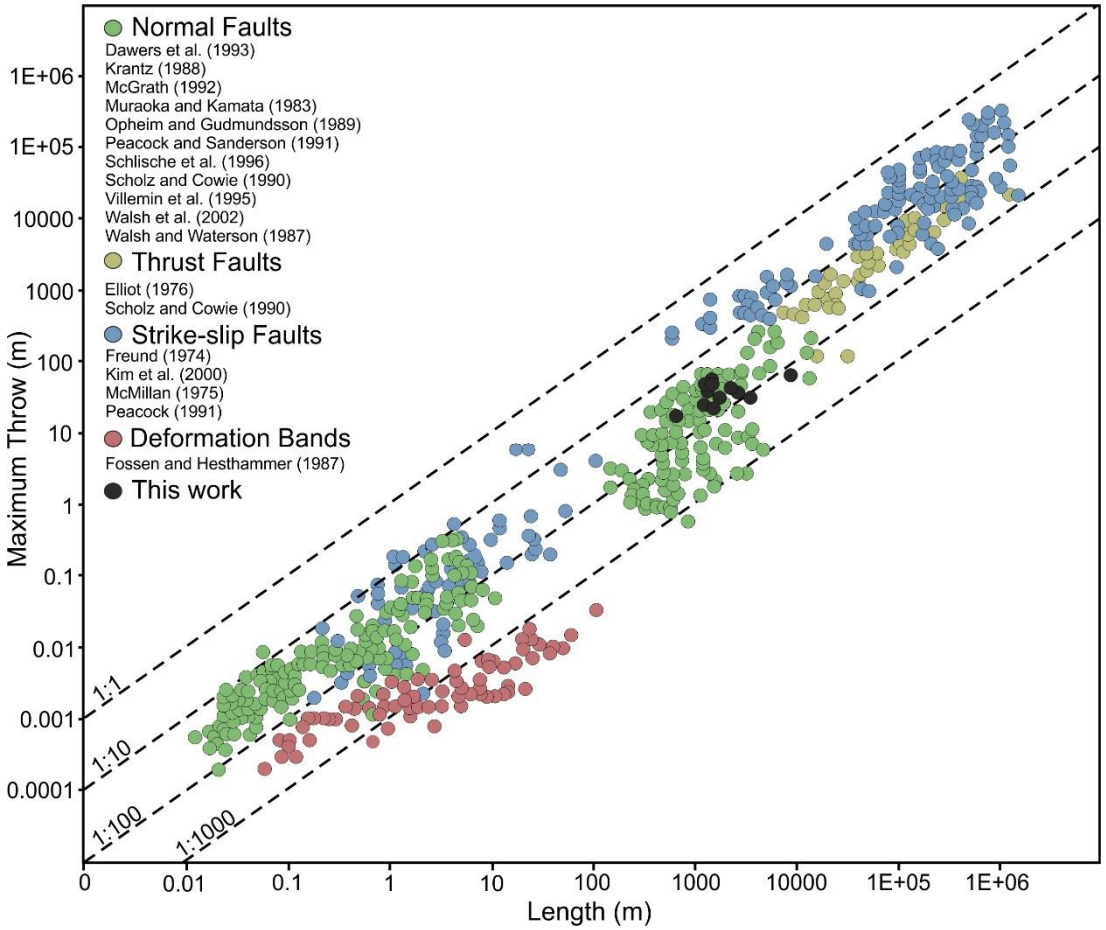

Figure 5-12: Maximum throw (m) vs. length of faults in the study area compared to different types of fault collected from the literature. The 12 representative faults are indicated by the light blue dots and coincide with the field where normal faults predominate.

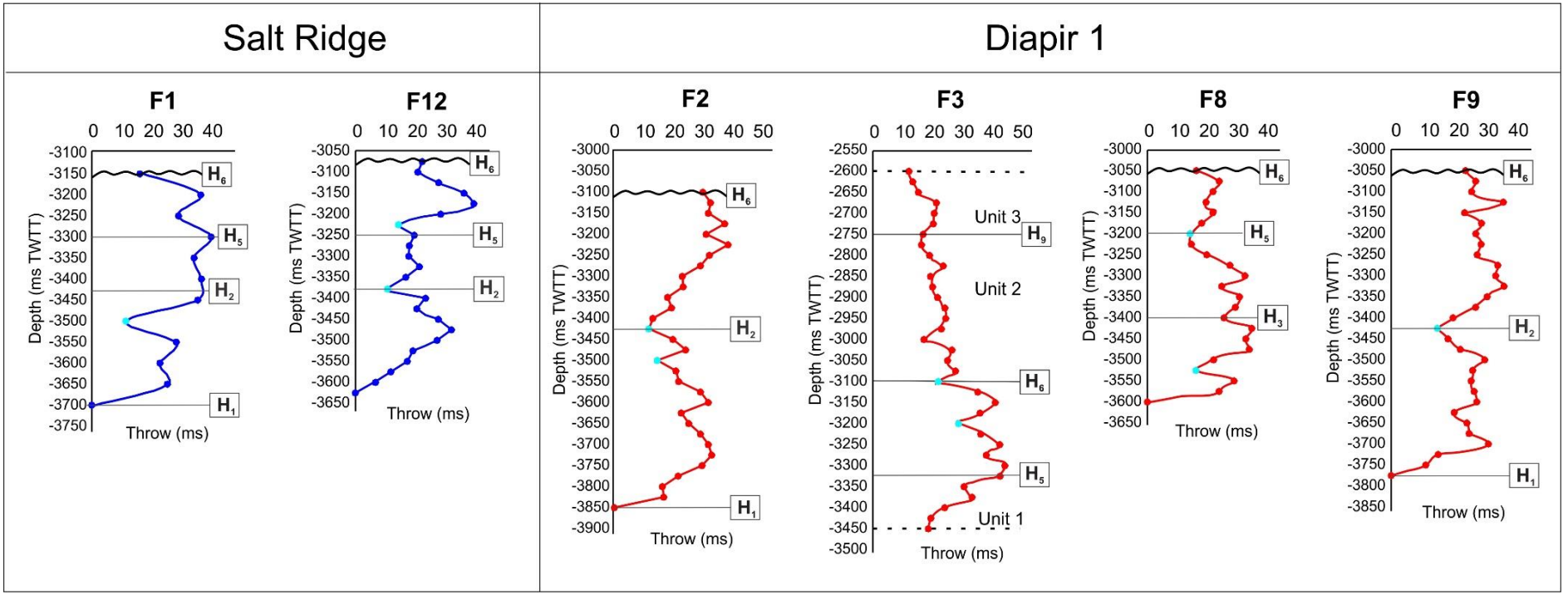

Figure 5-13: Throw-depth profiles for twelve representative faults in the study area with both depth and throw measured in ms TWTT. Three throw profiles were identified: asymmetric, M-type and skewed M-type. Grey lines indicate the horizons cut by the faults. The maximum throw for the majority of the faults occurs at horizon H5. Throw minima are indicated by blue dots.

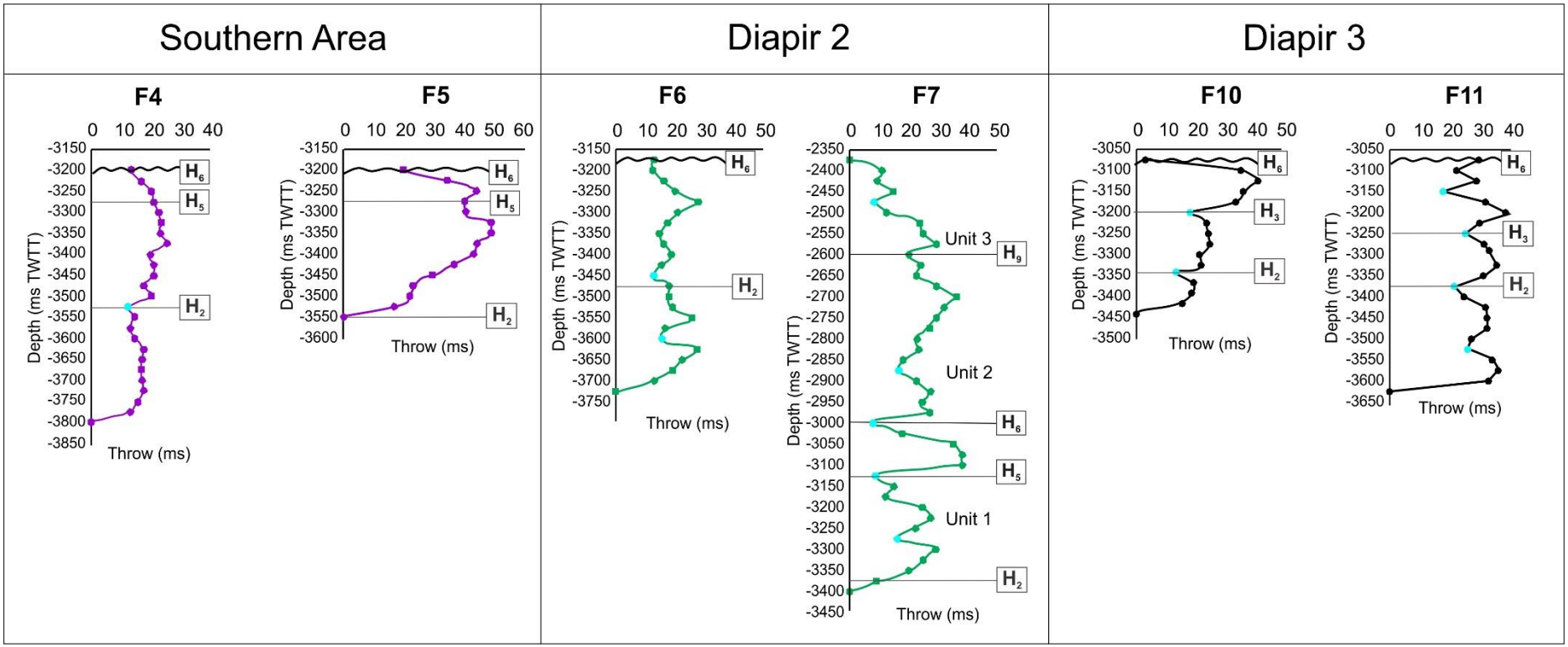

Figure 5-13 (cont.): Throw-depth profiles for twelve representative faults in the study area with both depth and throw measured in ms TWTT. Three throw profiles were identified: asymmetric, M-type and skewed M-type. Grey lines indicate the horizons cut by the faults. The maximum throw for the majority of the faults occurs at horizon H5. Throw minima are indicated by blue dots.

Throw minima and maxima vary across horizons and with depth. The variation of the position of the throw minima and maxima across stratigraphic levels relate to fault segmentation and reactivation by dip-linkage (Baudon and Cartwright, 2008a, 2008b; Omosanya and Alves, 2014; Walsh and Watterson, 1989). For faults F2, F4, F9, F10, F11 and F12, a significant reduction in the throw values occur at horizon H_2. Faults F1, F6, F7 and F8 show distinct throw minimum located within the Sub-unit 1a. A second negative displacement is recorded close or at horizon H_5 for faults F1, F3, F5, F7, F8, F11 and F12. Throw maxima occur at Sub-unit 1e, delimited by horizons H_5 and H_6 for faults F2, F3, F6, F7, F9, F10 and F12, while for fault F1 the maximum throw occurs at horizon H_5. The position of the throw maxima may imply nucleation of the faults in sub-unit 1e. The maximum displacement recorded for the faults in the study area is 49.94 for fault F5. Compared to the other faults, F8 show a distinct throw profile, characterised by small throw values close to the upper tips of the fault and increase with depth, whereas the majority of the faults seem to show a throw decrease pattern with depth. Excluding faults F3 and F7, no other representative faults in the study area show zero displacements at their upper tips, a character reflecting erosional truncation by horizon H_6. These two faults propagate upwards and reach Unit 3. Throw minima for faults F3 and F7 occur at horizon H_6. For fault F7, the upper tip is truncated by a submarine channel in Unit 3 (Figure 5-13). The throw position indicates the reactivation of faults F3 and F7, located respectively in diapirs 2 and 3, and a restriction of the upwards propagation of the remainder faults by the MTDs overlying horizon H_6 (Figure 5-13).

5.5.3. Interpretation of throw contour plots

Throw measurements were taken from the upper to the lower tips of the 12 representative faults in cross-sections orthogonal to the fault plane, and spaced 62.5 m to 125 m (Figure 5-14). The throw distribution along the faults is represented on a throw-contour plot for the main fault plane, with the contours representing lines of equal throw values spaced every 5 ms TWTT. The throw contour plots show zones of small throw values are represented by blue to green colours, with a maximum of 20 ms TWTT and of large throw represented by yellow to orange colours, starting at 25 ms TWTT.

For fault F1, four zones with large throws were identified (Figure 5-14a). The first zone occurs along segment 2, at 1800 m from N to S with a maximum throw of 25 ms. The second zone of throw maxima occurs at 6800 m, along with segment 8, with a maximum throw of 41.8 ms TWTT. The main throw maxima zone (up to 45 ms TWTT) is located along segment 9, between 7200 and 7900 m. The fourth throw maxima zone (throw up to 27 ms TWTT) occurs along segment 11, between 8600 and 9000 m. Zones of smaller throws occur throughout the fault length, with areas of distinctive throw minima representing the linkage of segments (Peacock and Sanderson, 1991; Walsh and Watterson, 1991; Cartwright et al., 1995). Fault F2 is characterised by the occurrence of two elliptical zones of large throws along the fault length (Figure 5-14b). The first zone occurs from 250 to 2100 m, at depths ranging from 3450 to 3850 ms. The second zone occurs from 250 m to 1900 m. The upper part of this zone coincides with the fault truncation by horizon H6 and the lower part terminates at 3450 ms. Two zones with small throws occur between 0 and 250 m and between 2100 to 2500 ms. Fault F2 is, therefore, interpreted as an isolated segment, as shown on Figure 5-11. However, the two zones of

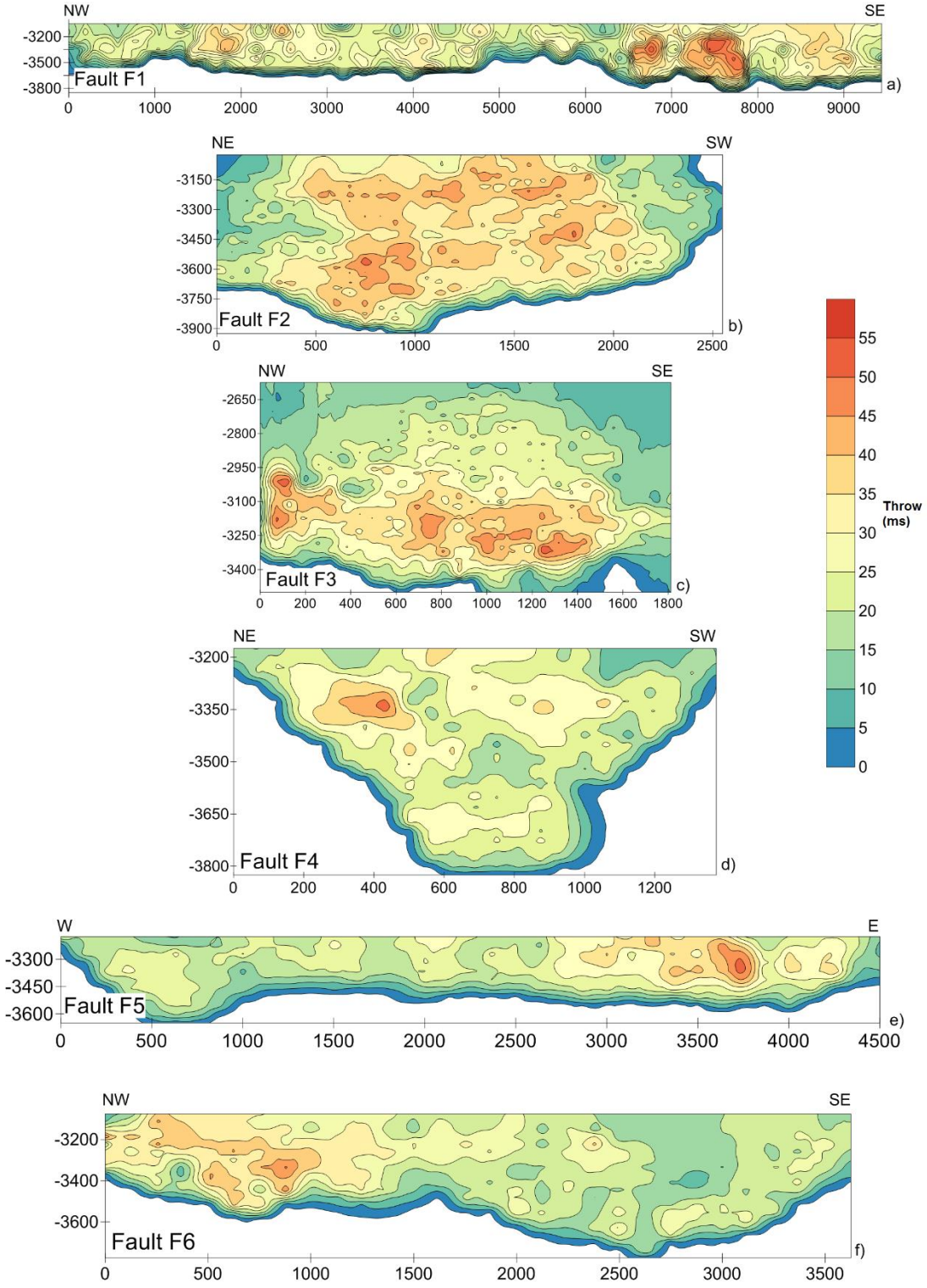

Figure 5-14: Throw contour plots for the 12 representative faults in the study area. Large throw values along the fault length are represented by the red to yellow contours whereas small throws are indicated by the green to blue contours. Areas characterised by a throw minima represent the linkage of initially isolated fault segments, whereas the throw maxima indicate areas of fault nucleation.

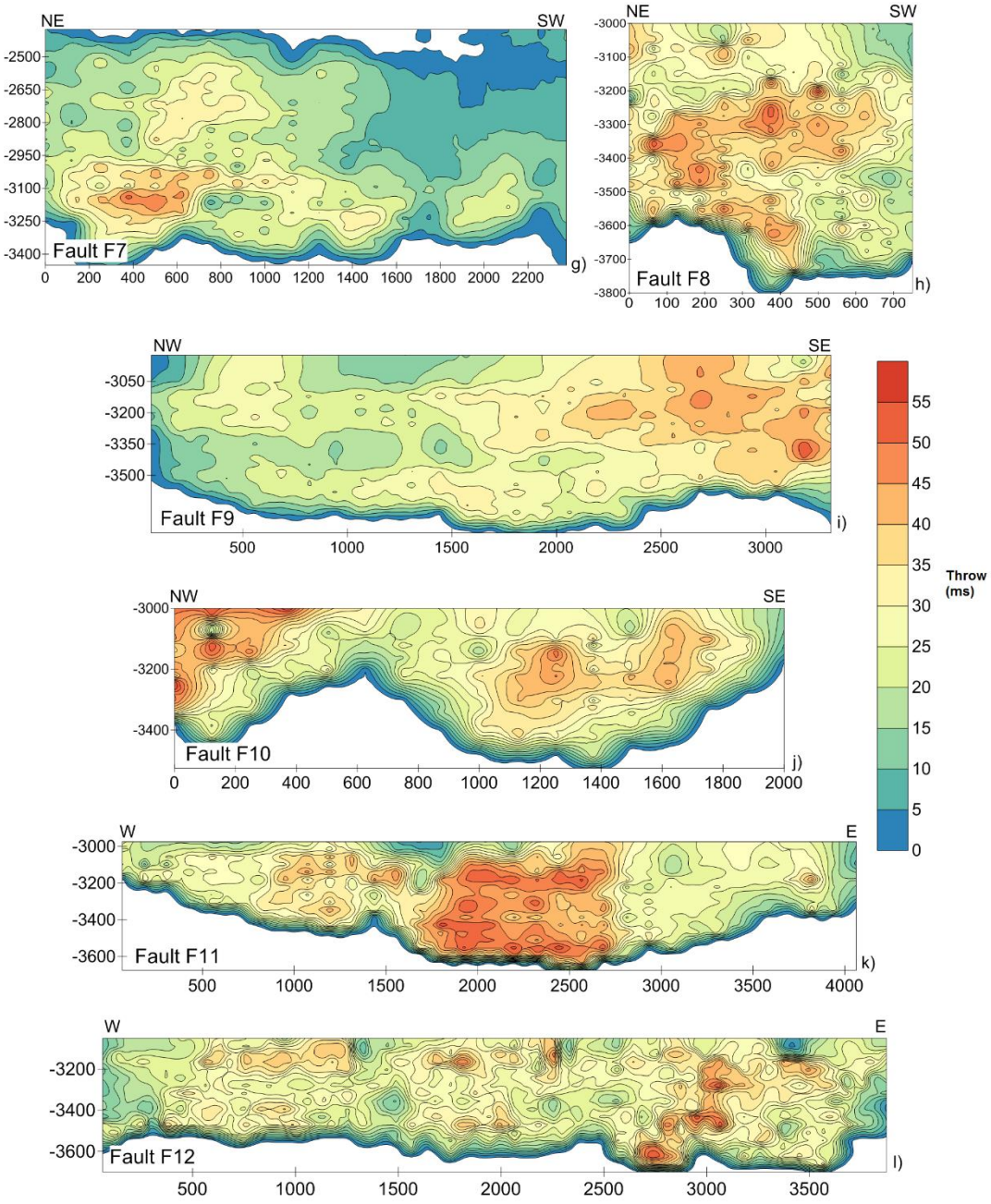

Figure 5-14 (cont.): Throw contour plots for the 12 representative faults in the study area. Large throw values along the fault length are represented by the red to yellow contours whereas small throws are indicated by the green to blue contours. Areas characterised by a throw minima represent the linkage of initially isolated fault segments, whereas the throw maxima indicate areas of fault nucleation.

larger throws suggest this fault has undergone an important reactivation phase. Fault F3 shows four vertical zones of throw maxima (Figure 5-14c). The first zone occurs at 100 m, with a maximum throw of 40 ms. The second and third zones show a maximum throw of 35 ms and occur at 700 m and between 300 and 1100 m, respectively. These four throw maxima are contained within an elliptical zone with a minimum throw of 25 ms TWTT, at depths ranging between 2995 and 3460 ms TWTT. From depths between 2600 to 2995 ms TWTT this fault is characterised by throws ranging from 20 to 0 ms TWTT. Fault F4 is characterised by one zone of throw maxima (up to 35 ms TWTT) between 250 and 400 m (Figure 5-14d). This fault shows two elliptical throw zones. The first zone, at depths between 3200 and 3400 ms TWTT, shows the largest throws for this fault. A second zone occurs between 500 and 1000 m, in the central part of the fault, at depths between 3600 and 3800 ms TWTT, with a throw maxima of 20 ms TWTT. Fault F5 show three zones of small throw, with a maximum throw of 10 ms TWTT (Figure 5-14e). An elliptical zone with large throws occurs between 2900 and 4250 m, with a throw maxima of up to 40 ms TWTT occurring at 3750 m. Fault F6 has a large throw zone located next to Diapir 3 that extends to 1000 m, reaching a maximum throw of up to 35 ms TWTT at 800 m (Figure 5-14f). A vertical small throw zone occurs at 2500 m. The contour plot for fault F7 is complex, consisting of two elliptical zones with throws over 20 ms TWTT (Figure 5-14g). The first elliptical zone occurs at depths ranging from 2600 to 2900 ms TWTT, and at 500 to 1000 m of the fault length. The second small throw zone occurs between 1600 to 1800 m. From 1800 m to the fault termination, a zone with a maximum throw of 20 ms TWTT occurs at depths between 3100 to 3250 ms TWTT. Fault F7 is interpreted as a result of the linkage of two initially isolated segments and the reactivation of the upper tips.

Fault F8 is characterised by a large throw zone at its centre, with a maximum throw of up to 45 ms TWTT occurring at 350 m along its length, and at depths between 3250 and 3300 ms TWTT (Figure 5-14h). The throw values for this fault decrease towards the fault tips. In the first 200 m of this fault, the maximum throw is 25 ms TWTT. An elliptical zone with small throws occurs from 0 to 1250 m, at depths between 3250 and 3500 ms TWTT. The maximum throw for fault F9 increases towards the southern termination coinciding with Diapir 1, where the throw maxima is up to 50 ms TWTT at 3150 m (Figure 5-14i). Fault F10 is characterised by two distinctive segments separated by a zone with small throws occurring at 630 m (Figure 5-14j). The northern part of this fault is related to Diapir 3, with throws of up to 38 ms TWTT. From 600 m to 2000 m the contour plot is elliptical, with large throws in the fault centre and small throws towards the fault tips. The throw maxima for fault F11 (up to 40 ms TWTT) occurs between 1750 and 2750 m, where the fault reaches it maximum depth (~3600 ms TWTT) (Figure 5-14k). Three zones with small throws occur along the fault length, representing areas of segment linkage. Fault F12 is characterised by the occurrence of up to five zones with small throws, indicating this fault consists of seven initially isolated segments (Figure 5-14l). The throw maxima (up to 45 ms TWTT) area occurs between 2750 and 3250 m.

5.6. Stratigraphic juxtaposition

The displacement of permeable and impermeable units across fault planes can be graphically represented in the form of Allan Diagrams (Allan, 1989). For the faults in the study area, juxtaposition (Allan) diagrams were created by assigning stratigraphic intervals as salt, limestone, shale, silt and sand (Figures 5-15 to 5-20). In the salt ridge,

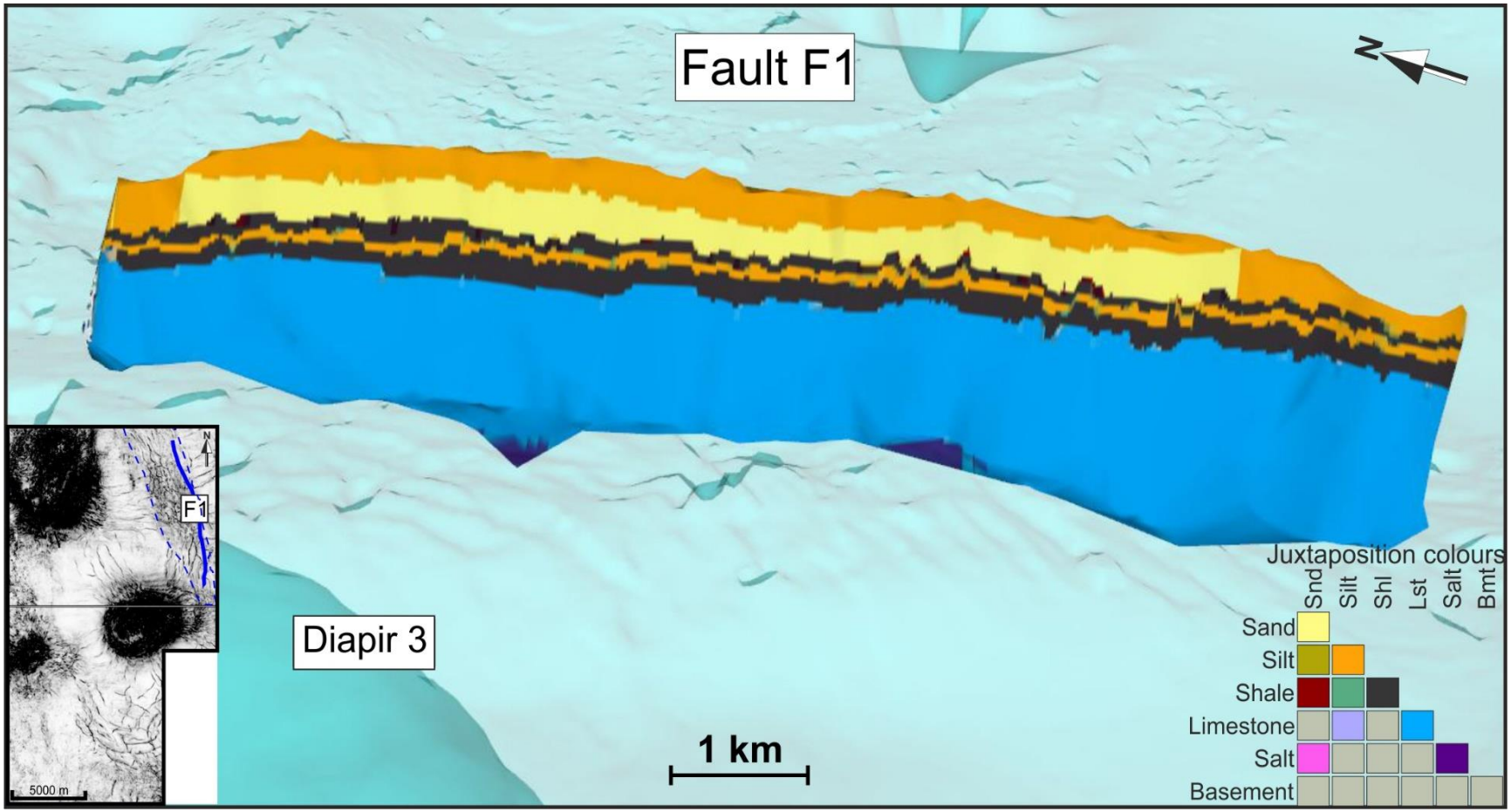

Figure 5-15: Juxtaposition map for Fault F1 showing juxtaposed sand units in its central part and a im,permeable interval defined by a shale interval. Close to the fault terminations juxtaposed limestone and sand-shale and sand-silt contacts are observed.

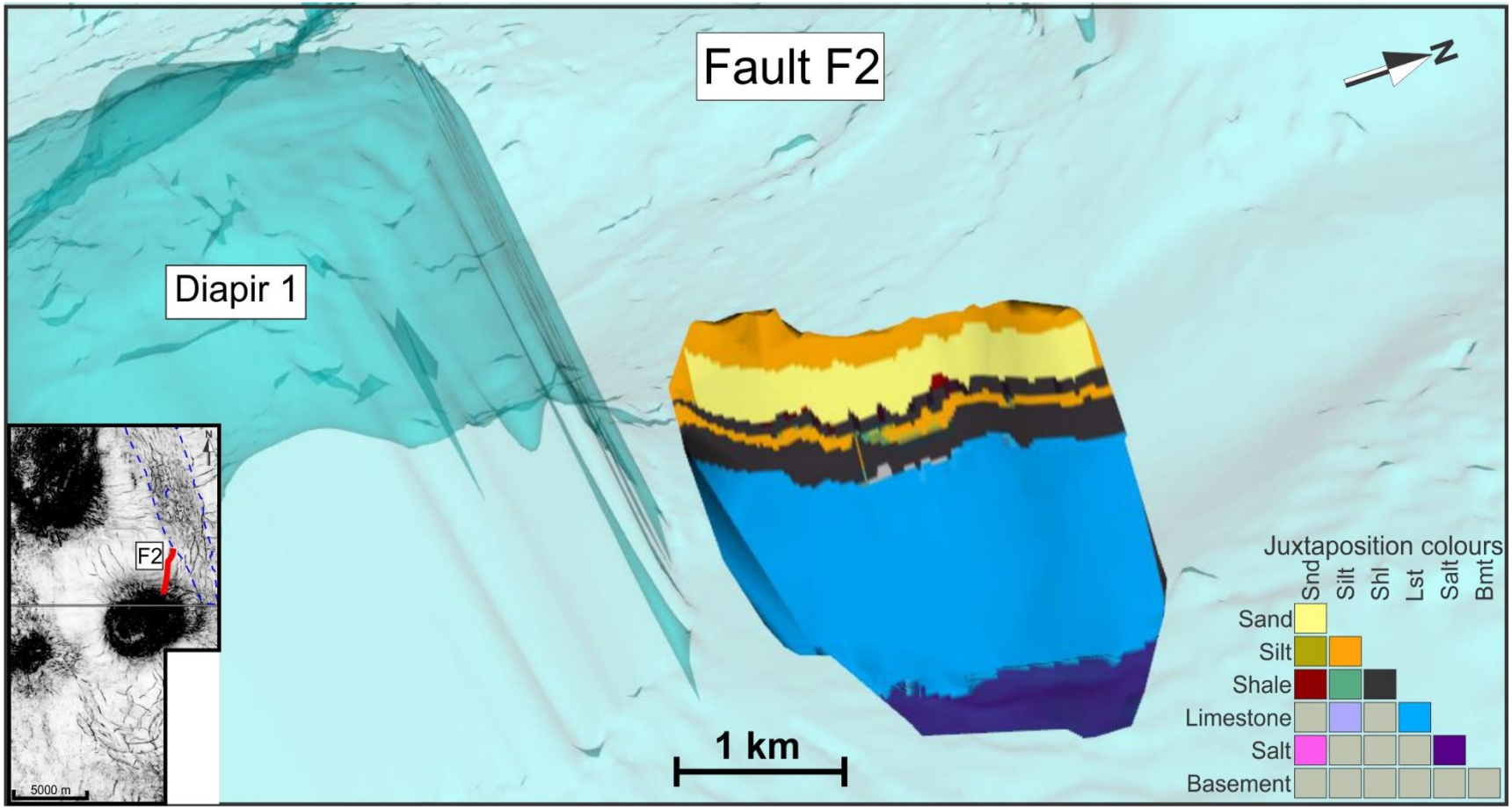

Figure 5-16: Juxtaposition map for Fault F2 showing sand units delimited vertically and laterally by impermeable units.

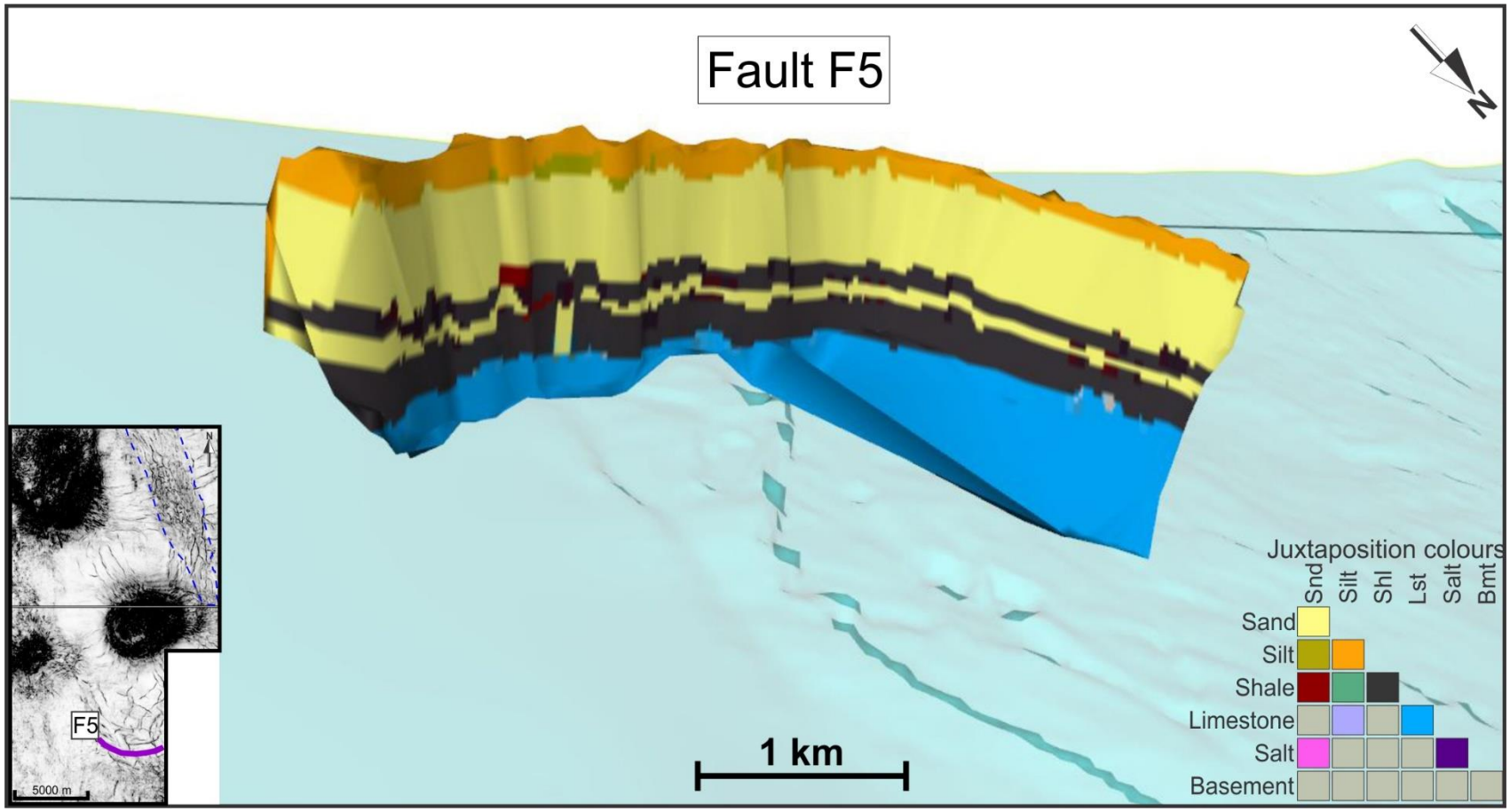

Figure 5-17: Juxtaposition map for Fault F5 showing an upper sand body laterally delimited by contacting silt units to W.

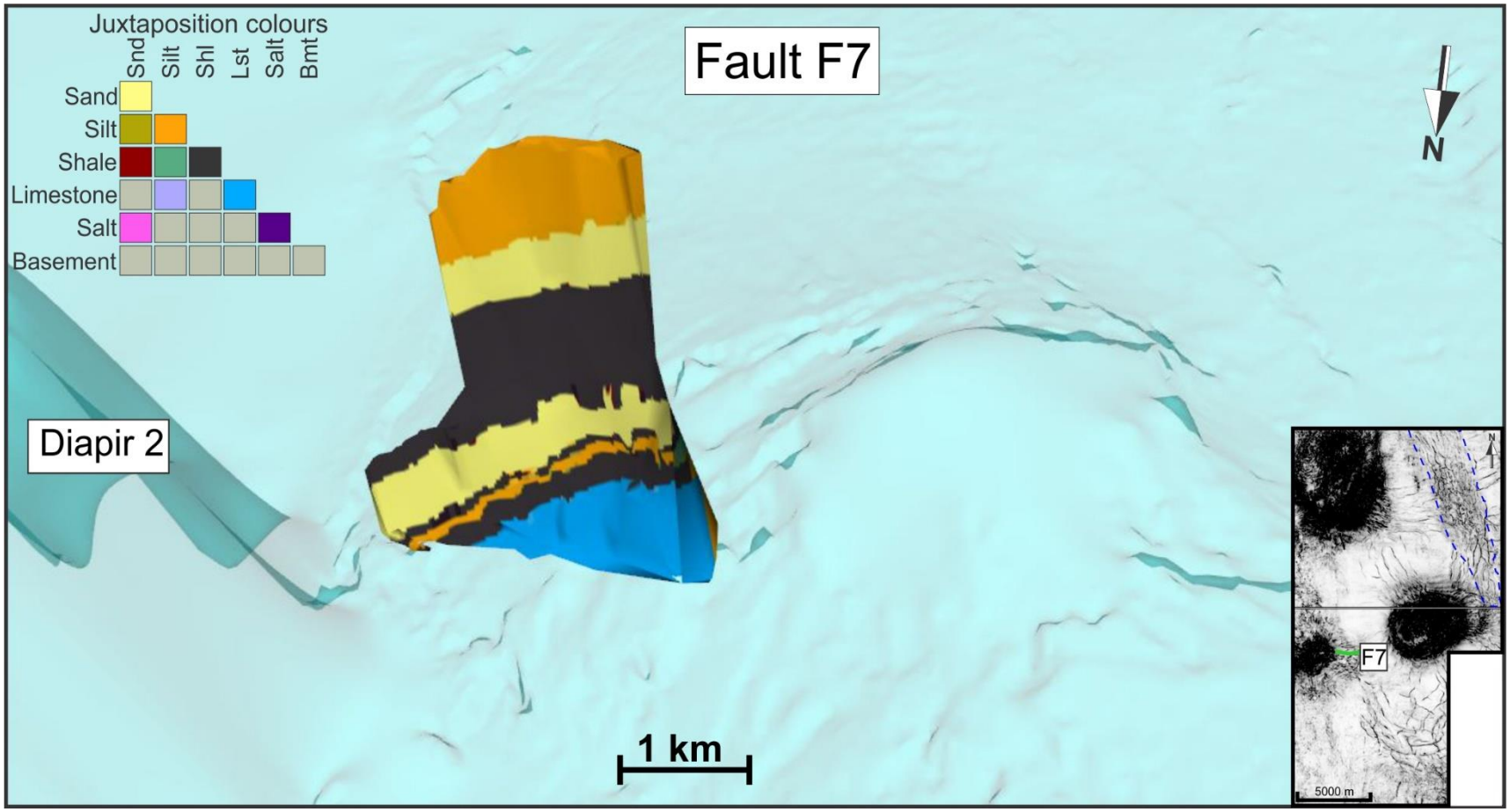

Figure 5-18: Juxtaposition map for fault F7 showing that juxtaposed sand bodies are delimited vertically by a thin shale layer close to Diapir 2.

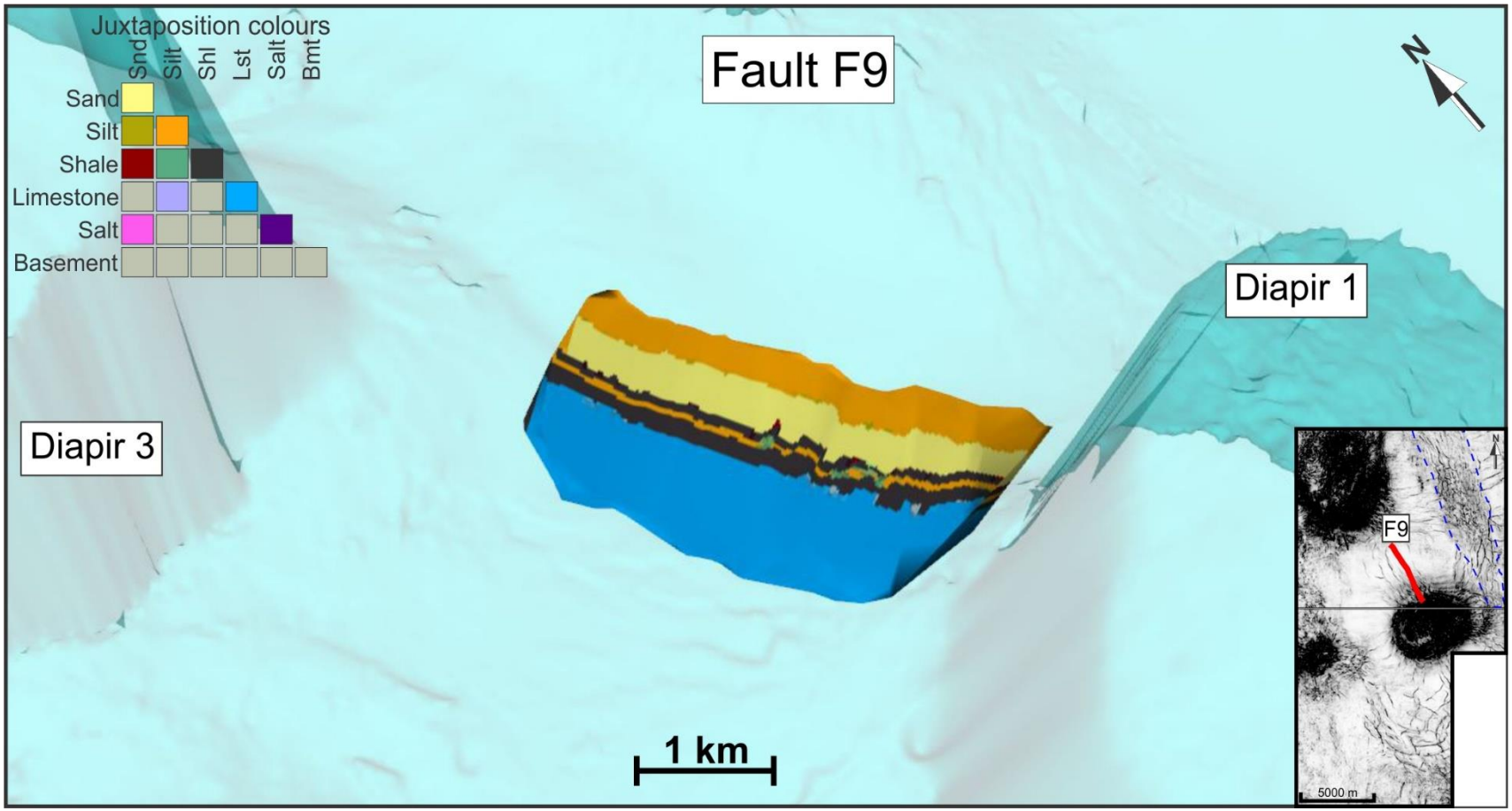

Figure 5-19: Juxtaposition map for fault F9 showing a sand body isolated by a sit-silt juxtaposition at the NW and SE terminations.

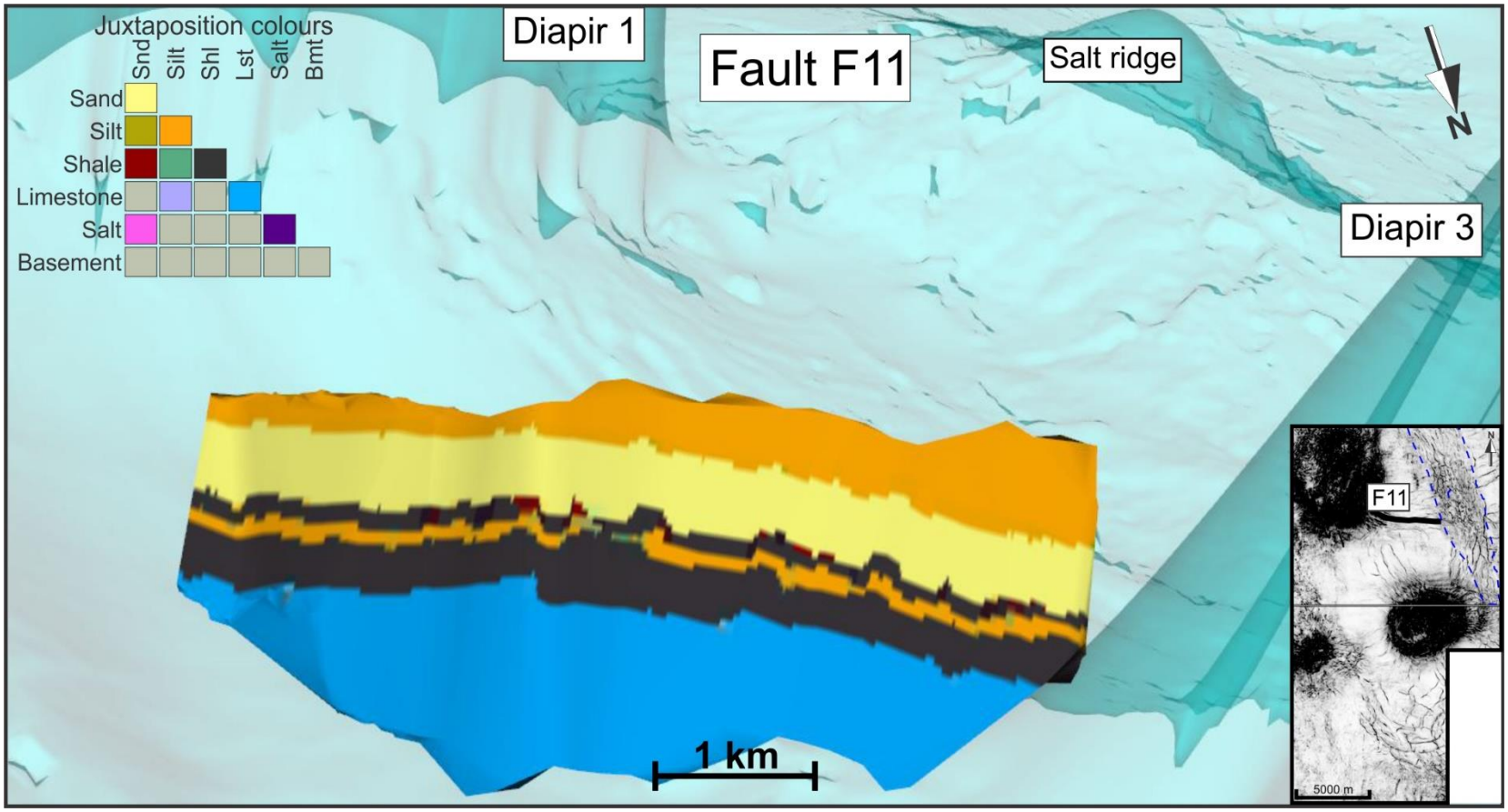

Figure 5-20: Juxtaposition map for fault F11 showing the sand-sand contact delimited vertically by a silt-silt juxtaposition that increases in thickness towards the Diapir 3.

juxtaposed sand units were estimated in the central part of fault F1 (Figure 5-15). This permeable interval is delimited laterally and at the top by a relatively thin shale interval. For this fault, apart from the thin salt juxtaposition close to the lower fault tip, it is also possible to observe juxtaposed limestone and sand-shale and sand-silt contacts. Fault F2, around Diapir 1, has a juxtaposition diagram similar to F1, with sand units delimited vertically and laterally by impermeable units (Figure 5-16). Distinctive shale-silt and shale-sand juxtapositions are also observed at the centre of this fault. In the Southern Area, the Allan diagram for fault F5 shows the upper sand body laterally delimited by contacting silt units to W (Figure 5-17).

The complex geometries of faults located adjacent to Diapir 2 are reflected on the juxtaposition diagram for fault F7 (Figure 5-18). Fault F7 shows a sand-silt juxtaposition at the upper fault tip towards the west. This fault reactivates towards the east and the juxtaposed sand bodies are not delimited laterally by impermeable units. The lowermost sand unit is delimited by a sand-silt contact to the west and by a shale-silt juxtaposition to the east. Fault F9, adjacent to Diapir 1 displays distinct juxtaposition relations. The Allan diagram for fault F9 shows a silt-silt juxtaposition at the NW and SE fault terminations that isolate the sand body. Shale-sand and shale-silt contacts are also observed (Figure 5-19). No impermeable lateral juxtapositions are observed for faults located adjacent to Diapir 3 (Figure 5-20). Fault F11 shows the sand-sand contact delimited vertically by silt-silt juxtaposition that increases in thickness towards the Diapir 3. Shale-shale, shale-sand and shale-silt contacts are observed underlying this thick sand interval (Figure 5-20).

5.7. Stress analyses

The faulting styles and known evolution of the Espírito Santo Basin point towards an extensional character of the study area (Chang et al., 1992). Stress inversions for all the 215 faults in the area of interest confirm this proposition with a sub-vertical σ_1 plunging 57.89º along an N237.63º azimuth (Table 5-2). A sub-horizontal σ_3 plunging 17.34º along an N177.46º azimuth was also estimated to the study area. Assuming the differences in the fault geometry observed in the seismic profiles, the position of the faults in relation to the salt diapirs and ridges, and all displacement analyses, the paleostress conditions were estimated for the faults located in the five areas described in this study (Table 5-2). Results from paleostress inversions obtained for each family of faults adjacent to the salt structures also points towards a sub-vertical σ_1 and sub-horizontal σ_3. Thus, the results from stress inversions for all faults were used to perform slip tendency and leakage factor analyses for the faults in the study area.

Slip tendency values for all the interpreted faults vary from 0 to 0.56, with an average of 0.27 (Figure 5-21). Most of the faults located in the salt ridge area show slip tendency values ranging from 0.10 to 0.50. Faults striking NE-SW show smaller slip tendency values than the NW-SE striking faults, as observed in the 3D fault model for the study area (Figure 5-21). For the faults located close to Diapir 1, slip tendency varies from 0.01 to 0.56. Slip tendency for the faults on the Southern Area varies from 0.02 to 0.54, with faults striking to SE and SW showing slip tendency values between 0.01 to 0.34 and the NE and NW-striking faults having slip tendencies from 0.34 to 0.54. For the faults in the Diapir 2, slip tendency ranges from 0.02 to 0.50, with the majority of the faults showing slip tendencies ranging from 0.20 to 0.40. Faults located

close to Diapir 3 have slip tendency values ranging from 0.00 to 0.54, with faults striking NE-SW showing larger slip tendency values than the NW-SE striking faults.

Normalised leakage factors were also estimated considering the paleostresses for the faults in the Espírito Santo Basin and a fluid pressure of 9 MPa, based on vertical stress measurements (Figure 5-22). For all the faults in the study area, the leakage factor varies from 0.1 to 1.0, with the largest leakage factors related to large slip tendency values. The largest leakage factor occurs for faults located close to Diapir 3 and in the Southern Area, as observed in Figure 5-22. Importantly, leakage factor varies along the fault length, as observed for the faults located in the salt ridge and Diapir 3 (Figure 5-22).

Table 5-2: Stress inversion values obtained considering the total number of faults and each fault family. Results from paleostress inversions indicate that a sub-vertical σ_1 and sub-horizontal σ_3 predominate in the study area.

Area	**Number of faults**	**σ_1**		**σ_2**		**σ_3**	
		Plunge	**Azimuth**	**Plunge**	**Azimuth**	**Plunge**	**Azimuth**
Total study area	215	57.89˚	N237.63˚	26.11˚	N276.26˚	17.34º	N177.46º
Salt ridge	55	52.7º	N187.1º	15.4º	N118.3º	33º	N218.6º
Diapir 1	53	39.7º	N6.3º	50.2º	N4º	1.2º	N95.4º
Southern area	77	60.3º	N73º	8.6º	N358.3º	28.2º	N92.9º
Diapir 2	11	44.6º	N96º	42.5º	N121.4º	13º	N199.2º
Diapir 3	19	66.3º	N74.9º	20.6º	N43.6º	11.3º	N137.9º

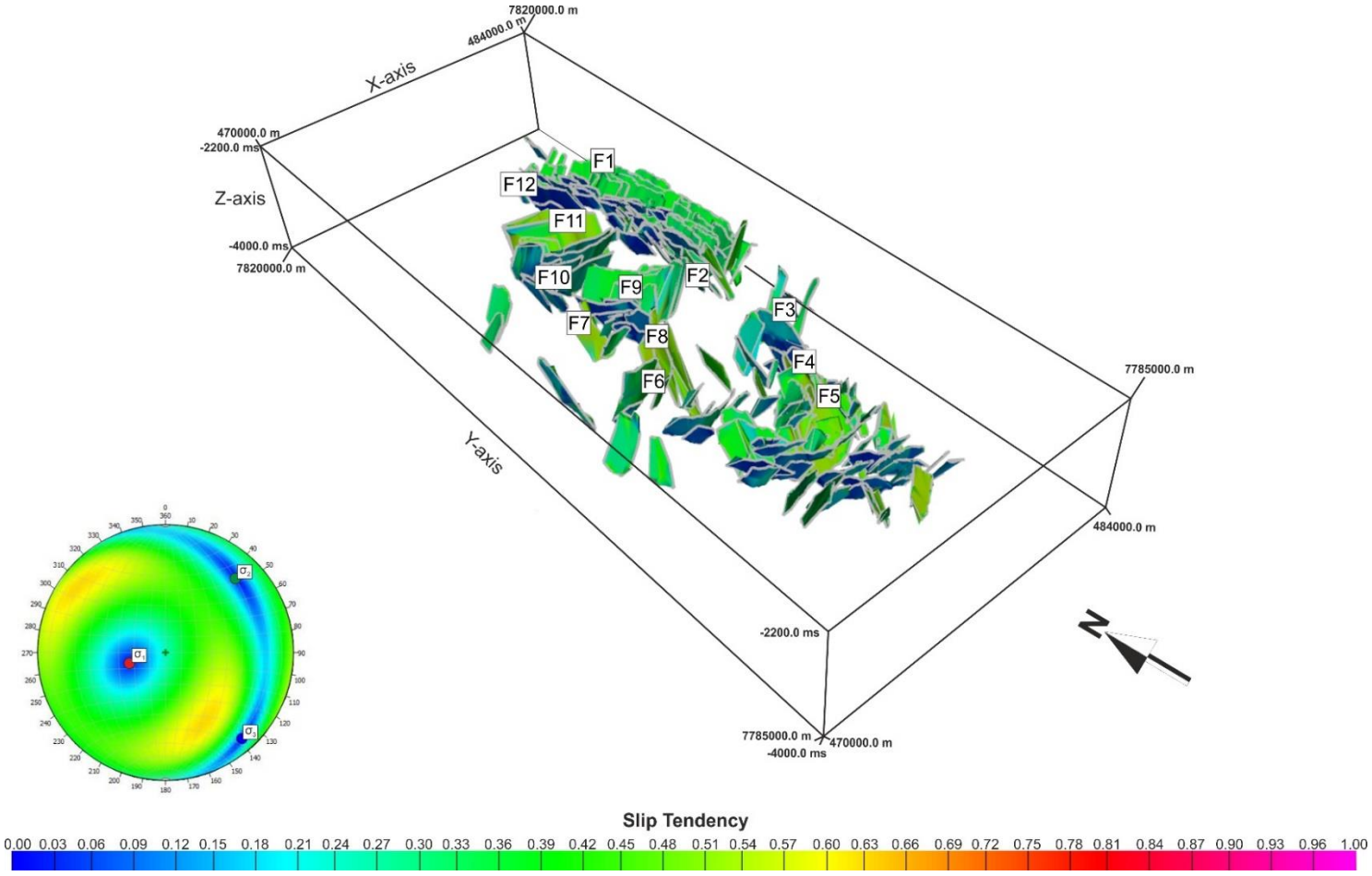

Figure 5-21: Slip Tendency model for faults in the study area, considering the paleostress tensor. Slip tendency values range from 0 to 0.56, with an average of 0.27. Faults striking NE-SW show smaller slip tendency values than NW-SE striking faults.

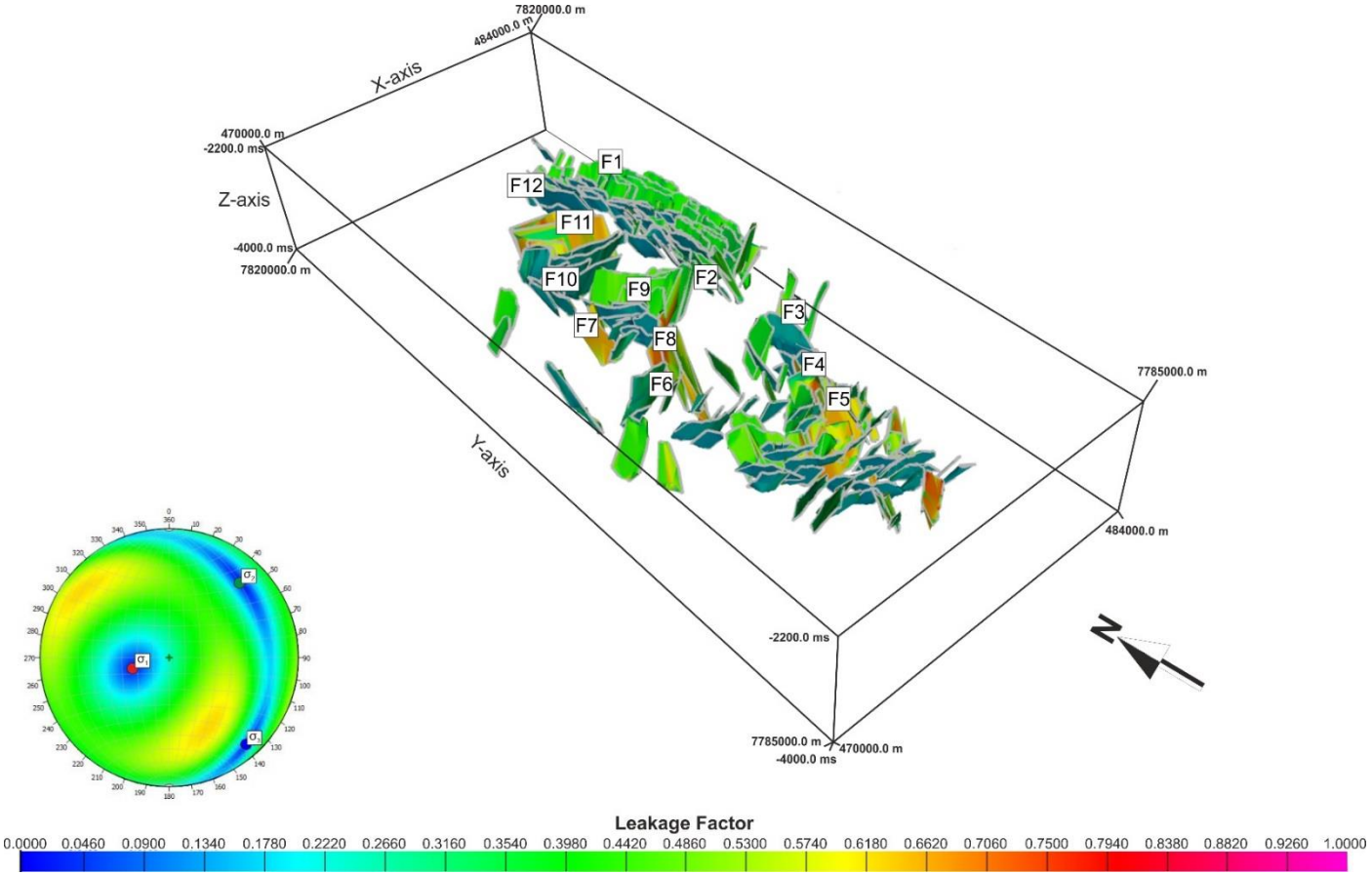

Figure 5-22: Leakage Factor model for faults in the study area considering the paleostress tensor and a fluid pressure of 9 MPa. Leakage factors for the study area range from 0.1 to 1.0.

5.8. Discussion

5.8.1. Structural evolution of the salt structures in the Espírito Santo Basin and timing of faulting

A conceptual model for faults associated to halokinesis is shown in Figure 5-23. In the study area it is necessary to consider that horizon H_6 corresponds to a regional early- to mid-Eocene unconformity developed during a period of tectonic activity on the Brazilian Margin (Baudon and Cartwright, 2008b; Fiduk et al., 2004). Uplifted strata, as well as the faults cutting these units, were later removed by erosion (Moraes et al., 2007). In throw-depth data for the 12 representative faults (Figure 5-13), horizon H_6 corresponds to the point of minimum fault displacement. However, it is always greater than zero, as it does not represent the cessation of vertical propagation (Baudon and Cartwright, 2008b; Omosanya and Alves, 2014). An important observation is the absence of marked thickness variations on the hanging-wall and footwall blocks of the faults, suggesting faults developed after the deposition of Unit 1. At a regional scale, the first halokinetic movements in the Espírito Santo Basin took place during the Late Aptian – Early Albian, resulting from the combination of differential sediment loading, gravity spreading and downslope thin-skinned gravitational gliding above Aptian evaporites (Demercian et al., 1993; Fiduk et al., 2004). Considering the geometry of the interpreted seismic profiles (Figures 5-1 and 5-6 to 5-10), it is possible to agree that halokinesis from the Late Aptian – Early Albian deformed the post-salt overburden deposited in the Espírito Santo Basin. However, this deformation was not continuous, and at least three phases of faulting were identified in this study for

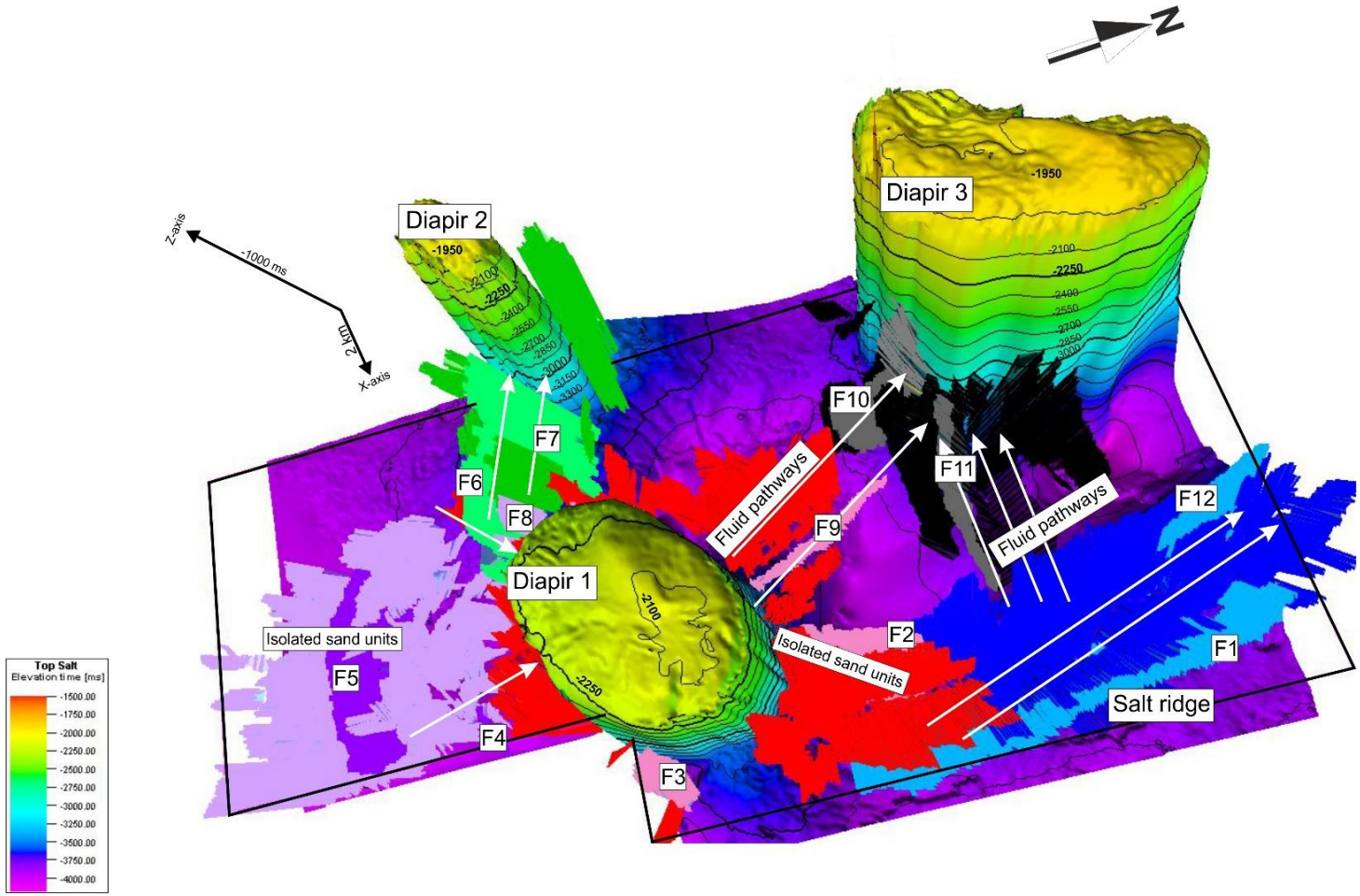

Figure 5-23: Conceptual model for the faults associated with halokinesis in the study area. The white arrows indicate a preferential fluid flow direction based on the leakage factor and juxtaposition analysis from south to north-northwest, in direction to Diapir 3. Isolated sand units were found in the vicinities of fault F2, adjacent to Diapir 1, and fault F5, in the Southern Area.

different salt structures. This observation agrees with discrete (and localised) salt deformation phases taking place in the Espírito Santo Basin during the Albian, Campanian, Paleogene and Neogene (Cobbold et al., 2001).

The interpreted seismic cube reveals the occurrence of deep-seated faults terminating at the crest of salt structures (Figures 5-1 and 5-6 to 5-10). Deep-seated faults, reaching the level of the top salt (horizon H_1) include F1, F2, F9 and F11 located in the northern part of the survey area on the crests of the salt ridge and Diapir 1 (Figures 5-6, 5-9 and 5-10). Except for fault F2, all the other interpreted faults strike to NW-SE. These faults have lower tips on the top of the salt horizon, and were initiated in the middle portions of sub-unit 1a (F6, F10 and F12). T-z data indicates that the first episode of reactivation affected the whole of the study area. However, the vertical extent in which faults propagated vertically above sub-unit 1a is limited. Away from salt structures, seismic reflections seem to be less disturbed by halokinesis towards the Southern Area (Figures 5-9 and 5-10). Nevertheless, the occurrence of deep-seated faults to the south, such as fault F4 (with a throw minimum at horizon H_2) highlights the importance of Late Albian – Early Eocene salt tectonics in the study area.

The occurrence of a throw minimum at horizon H_3 for faults F10 and F11 suggests a second reactivation event for faults close to Diapir 3, likely resulting from local growth of this salt structure. Local halokinesis also occurred at this time over the salt ridge and Diapirs 1 and 2, as reflected by the T-z data for sub-unit 1e. This episode of salt movement is interpreted here as the last halokinetic event recorded on the salt ridge, as this structure is buried by a non-deformed post-salt overburden, represented

by Units 2 and 3. Cessation of salt growth resulted in local dissolution at the crest of the salt ridge, evidenced by the lenticular shape of this salt body on the seismic profiles (Figures 5-6 and 5-7). The removal of salt occurred preferentially on the crest of salt structures where the salt rises faster, and then continues to the diapir flanks (Ge and Jackson, 1998; Seni and Jackson, 1984). Salt dissolution and the pressure exerted by the overburden units eventually led to the collapse of the salt ridge, (e.g. Frumkin et al., 2011; Ge and Jackson, 1998; Mattos et al., 2016; Ze and Alves, 2016).

The interpretation shows that the bulk of the halokinetic movements occurred during the Middle Eocene – Early Miocene, as reflected by the local growth of salt diapirs 1, 2 and 3. The thinning and folding of strata in units 1 and 2 on the flanks of salt diapirs reflect post-depositional halokinesis (Figures 5-1 and 5-6 to 5-10). However, this halokinetic episode had little influence on the fault reactivation in the study area. No faults were found on the crest of the salt structures, and only a few faults were reactivated above horizon H_6 in the western part of the study area. Reactivated faults include F3, adjacent to Diapir 1, and F7 adjacent to Diapir 3. Throw profiles for these two faults are similar, evidencing a decrease in the throw values for Units 2 and 3 towards their upper tips.

5.8.2. Mechanisms of fault linkage and reactivation

Displacement profiles in *Sections 5.5.1 and 5.5.2* provide insights into the mode of propagation and linkage of faults in the western part of the Espírito Santo Basin.

The fault geometries and their relations with the sedimentary packages are also taken into account when proposing an evolutionary model to the study area. For the majority of the representative faults, throw-depth (T-z) data show a maximum throw close to horizon H_5 (Figure 5-13). Faults developed radially to Diapirs 2 and 3 consist of either three or five segments (Figure 5-11), and in the map view radiate out from the diapirs in the direction to other salt structures, where these faults overlap (Figure 5-4). Faults developed radially to Diapir 1, and the crestal faults in the salt ridge are more segmented than the diapirs 2 and 3 counterparts, exhibiting six to eleven segments (Figure 5-11). The uplift and collapse of the salt ridge were likely to have caused the individual fault segments to link, whereas the successive halokinetic movements of Diapir 3 were likely to be responsible for the lateral and vertical propagation of faults radial to this structure. The local growth of Diapirs 1 and 2 are also responsible for the lateral segmentation of faults adjacent to these structures.

Multiple displacement minima for the faults radial to diapirs (e.g. F3, F7, F10 and F11) indicate that these faults consist of multiple vertically overlapping segments (Figure 5-13). For the majority of the representative faults, throw minima occur in sub-unit 1a. The throw-depth profiles indicate larger throw for the faults in the western portion of the Espírito Santo Basin than for the faults found in the eastern part of this basin (e.g. Baudon and Cartwright, 2008a). As displacements are greater in the western part of the study area, distinctive throw minima are also observed. The occurrence of successive throw minimum on the T-z plots suggests dip-linkage reactivation (Baudon and Cartwright, 2008b; Mansfield and Cartwright, 1996; Omosanya et al., 2015). Dip-linkage reactivation is less common for the faults in the eastern part of the study area, as the majority of faults were reactivated by upward propagation (Baudon and Cartwright, 2008b). In the western

part of the study area, dip-linkage seems to be the preferential reactivation mode with upward propagation being more restricted.

A possible explanation for the different modes of reactivation found within the same sedimentary basin relies on the relationship between the fault strike and the stress state. The orientation of the principal stress obtained considering the all the faults in the study area is NE-SW (Table 5-2), coinciding with the overall NNE extension direction for the South Atlantic continental margin (Chang et al., 1992) and agreeing with maximum throw vs. length diagram for normal faults (Figure 5-12). A coinciding orientation of the principal stress and the strike direction of the faults result in a greater tendency of the faults to reactivate vertically along their length (Baudon and Cartwright, 2008b; Ze and Alves, 2016). The predominant strike direction for the faults in the western part of the Espírito Santo Basin is NW-SE. However, an important group of faults striking to NE-SW and E-W are also found in the study area. In general, the representative faults striking NNE-SSW display a variable number of throw minima on their throw profiles, whereas NW-SE and E-W striking faults show only two negative displacements on their profiles (Figure 5-13). An opposite strike and principal stress orientation can pose implications into the preferential fault reactivation mode, favouring the nucleation of segments with similar dip and strikes.

Faults F3 and F7 are the only representative faults that after a negative break on the throw gradient at horizon H_6 propagates vertically to Units 2 and 3, where a reduction in the throw values is observed. These faults followed a weakness path along the MTD units overlying horizon H_6. F3 and F7 strike to opposite directions, NW-SE and NE-SW, respectively. While the fault profile for fault F3 indicates a gradual reduction in the throw

gradient from horizon H_6 upwards, F7 has at least six abrupt throw minima along its throw profile (Figure 5-13). The observations for these two faults are an exception to the general pattern of fault growth and evolution observed to the faults in the study area. This indicates that not only the stress orientations must be considered when assessing the fault reactivation and other factors including the presence of overlapping faults (Childs et al., 1995; Kelly et al., 1999) and fault size (Peacock and Sanderson, 1996, 1991) should be taken into account.

5.8.3. Implications for petroleum systems in the Espírito Santo Basin

A dense and connected fault network can either constitute a preferential conduit to fluids (Cox et al., 2001; Gartrell et al., 2004) or form barriers to fluid flow resulting from shear processes or post-deformation cementation (Gartrell et al., 2003; Sibson, 1996). The crestal and radial faults in the study area comprise corridors connecting different salt structures that discretely evolved through time during the extension of the Espírito Santo Basin (Figure 5-23). The Juxtaposition (Allan) Diagrams for the study area evidence that faults located radially to Diapirs 2 and 3, and located in the Southern Area, display thicker juxtaposed sands in comparison with faults formed adjacently to Diapir 1 and the salt ridge (Figures 5-15 to 5-20). This observation coincides with the preferential location of bright-spots in the seismic profiles. The largest and most continuous bright-spots were found adjacent to faults developed radially to diapirs 2 and 3 at sub-unit 1e (Figures 5-1 and 5-6 to 5-10). Faults F9 and F10, located respectively adjacent to diapirs 1 and 3, cut

a bright-spot in section view and could constitute a possible pathway for fluids (Figure 5-9). Bright-spots were also identified at Unit 2, above the faults radial to Diapir 3, whereas in the salt ridge, the occurrence of bright reflections predominates above the faults in sub-units 2b and 2c (Figure 5-8).

Leakage factor calculations indicate two different trends for faults in the study area. The majority of faults have a leakage factor ranging from 0.2 to 0.3, suggesting that seal units were juxtaposed during faulting and implying on a smaller potential to leak fluids (Figure 5-22). Juxtaposition diagrams reveal that for some faults (e.g. F2 and F5) seal units are isolating the sand units and potentially retarding fluid migration (Figures 5-15 to 5-20). A second leakage factor trend for the study area ranges from 0.5 to 1.0, a character that suggests the likelihood of the seal units fail across the study area, and consequently, a greater potential to leak fluids. The parts of the fault where leakage seems to be occurring coincides with the parts of the fault that are most likely to slip. This constitutes evidence that fault slip is the main mechanism responsible for fluid leakage parallel to faults (Barton et al., 1995; Wiprut and Zoback, 2000). The location of the high leakage factors for faults adjacent to the three salt diapirs in the study area coincides with the fault terminations close to the diapir. This is the area where the fault segments are uplifted, indicating the fault will leak vertically through the salt diapir. The faults with higher leakage factors include the NE-striking crestal faults, faults adjacent to diapirs 2 and 3 and a small number of faults in the Southern Area (Figure 5-22).

Based on the findings of this chapter, it is proposed that the corridor of faults developed around the interpreted salt structures constitute a preferential pathway for fluids in the study area. Fluid tends to flow vertically parallel to the fault trace and reach

the most uplifted areas. The preferential fluid route in this system of salt structures is from south to north-northwest, where the densest accumulation of bright reflections occurs, either cut by faults or over the faults developed radially to Diapir 3, and above the faults from the salt ridge (Figure 5-23). In such a setting, the stress analysis altogether with the juxtaposition diagrams show that reservoir units within the Espírito Santo Basin are connected through corridors of faults that were developed through consecutive reactivation episodes.

5.9. Conclusions

The difficulty in dating the timing of development of faults related to halokinesis episodes motivated the analysis of a system of diapirs in the Espírito Santo Basin as a case study that can be applicable to other South Atlantic-type passive continental margins, where the salt tectonics is of paramount importance in controlling the fault geometry and the fluid flow. In parallel, the evaluation of the occurrence of a main reactivation direction for the faults in the study area and how this reactivation does affect the fluid flow was also an objective of this chapter. The main conclusions of this work can be summarised as follows:

a) The faults in the study area were divided into five fault families, according to their location relative to the salt structures. Radial faults occur adjacent to the three salt diapirs, and the crestal faults were developed over the NW-SE-trending salt ridge. The fifth family of faults occurs in the Southern Area, an area less affected by halokinesis. The largest faults in the study

area, including F1 strikes to NW-SE, whereas the predominant strike direction for the smaller faults is NE-SW and E-W.

b) The evolution of the salt structures occurred at discrete timings from the Late Aptian through the Early Miocene. The observations indicate that the uplift for salt ridge was the first to cease in the study area, followed by dissolution of the salt at the top of this structure and collapse. Halokinesis in Diapirs 1 to 3 resulted in the formation of radial faults that overlap in map and section view.

c) A preferential NE-SW reactivation took place in the study area, coinciding with the paleostress inversion that revealed this area was most likely subjected to an NNE extension. Dip-linked reactivation seems to be the preferential reactivation mode for the faults in the western area of the Espírito Santo Basin, in opposition to the eastern part where reactivation by upwards propagation predominates. The overburden deposited above the unconformity is barely affected by the reactivation of the faults in the study area, except in areas where weakness zones were reached by faults F3 and F7.

d) Slip tendency and leakage factor analysis in combination with juxtaposition diagrams for the faults in the study area indicate that the areas most prone to leak fluids occur adjacent to the salt structures, indicating that the fluids are most likely to leak vertically through the salt structures.

e) The evolutionary model for the faults in the study area demonstrates that the faults are mainly extensional and comprise corridors that connect different salt structures and can provide a preferential path for fluid flow from the

South to North-Northwest. This model suggests that Diapir 3 was the most active diapir in the study area, influencing the configuration of the different fault families and the fluid-flow in the study area.

6. Fault evolution as a control on Plio-Pleistocene submarine-channel geometry in the Northern Graben, Taranaki Basin, New Zealand

Abstract

This chapter uses high-quality 3D seismic data to investigate the geometry of submarine channels as a function of the structural evolution of the Northern Graben of the Taranaki Basin during the Plio-Pleistocene. The Parihaka Fault is one of the most distinctive structures of the Cape Egmont Fault Zone, and comprises four segments with variable vertical displacements. The structural controls of the Parihaka Fault on the geometry of four representative channel systems incising the Giant Foresets Formation are investigated based on representative seismic profiles, time-structural maps of the base of the channels, and variance time-slices. Sinuosity values in submarine channels reflect the reactivation of pre-existing fault segments to the south, with the channels evolving from meandering to straight on the footwall block while becoming meandering on the hanging-wall block. The formation of new segments to the north controlled the deposition of sinuous channels both on footwall and hanging-wall blocks. Channel deflections also reflect structural controls on channel configuration, combined with significant sediment inputs. Three drainage types were identified in the study area: oblique, transverse and parallel to the Parihaka Fault trace. To assess channel distribution throughout the study area, a channel density plot was created based on the identification of Channel Points (CP) and later compared to an isochron thickness map of channel-fill deposits. A discrepancy between channel density and the thickness map was found, as the areas of maximum sediment supply are positioned at the footwall block, while two depocentres are located in the NE of the study area. The control of relay zones developed between the Parihaka Fault segments on channel geometry was assessed in this study. Channels

developed close to the transfer zone diverted from their original courses close to the Parihaka Fault segments and flowed transversally to the fault trace, instead of running through the relay ramps.

6.1. Introduction

Submarine channels are key features on deep-water continental margins, extending from the shelf edge to distal lower-slope areas (Babonneau et al., 2002; Galloway, 1998; Jegou et al., 2008; Normark et al., 1979; Prather, 2003). The rates of deposition and sediment supply in submarine channels, as well as their geometry, are dependent on local tectonic activity and the influence of climate and relative sea-level changes (Bouma, 2004; Kolla, 2007; Shepard and Emery, 1973; Wood, 2007). Tectonic activity on continental margins may result in the development of structures such as faults, folds, and diapirs. These structures can largely influence channel sinuosity, in combination with other factors such as flow density and velocity, seafloor topography and sediment volume and thickness (Kane et al., 2008; Kolla et al., 2001; Kolla et al., 2007; Peakall et al., 2007).

The development and evolution of faults close to submarine channels can change their course either by obstructing the flow downslope or guiding the sediment supply into alternative paths (Clark and Cartwright, 2009; Gee et al., 2007). For instance, the evolution of initially isolated fault segments within a sedimentary basin results in the formation of transfer zones that control the development and distribution of accommodation space, sediment influx from the footwall to the hanging-wall

depocentres, and basin architecture (Athmer and Luthi, 2011; Gawthorpe and Hurst, 1993; Gupta et al., 1999; Larsen, 1988; Leeder and Gawthorpe, 1987). As such, relay ramps are a type of transfer zone developed between two overlapping reoriented fault segments that dip in the same direction (Gawthorpe and Hurst, 1993; Larsen, 1988; Peacock et al., 2000; Peacock and Sanderson, 1991).

One key example of a developed relay ramp system is found in the Taranaki Basin, offshore New Zealand (Figure 6-1a and b). The Parihaka Fault (Giba et al., 2012) is a structure developed in association with the Cape Egmont Fault Zone (CEFZ), consisting of four initially isolated fault segments with lengths varying from 8 to 15 km (Figure 6-1a and b). Relay ramps were formed between different segments of the Parihaka Fault in response to oblique reactivation of a pre-existing basement fault during the Plio-Pleistocene back-arc extension (Giba et al., 2012, 2010; Hansen and Kamp, 2004a; King, 2000; King and Thrasher, 1996). High sedimentation rates accompanied the reactivation of the Parihaka Fault and the opening of the Northern Graben, as marked by the deposition of the Giant Foresets Formation, a thick syn-rift sequence comprising clinoforms incised by Pleistocene submarine channels (King and Thrasher, 1996; Salazar et al., 2015) (Figure 6-1c).

The controls the Parihaka Fault exerted on submarine channel evolution and geometry in the North Taranaki Graben are investigated in this chapter. In summary, this chapter aims at addressing the following questions:

a) What are the drainage types in the study area and how do they relate to the growth of the Parihaka Fault?

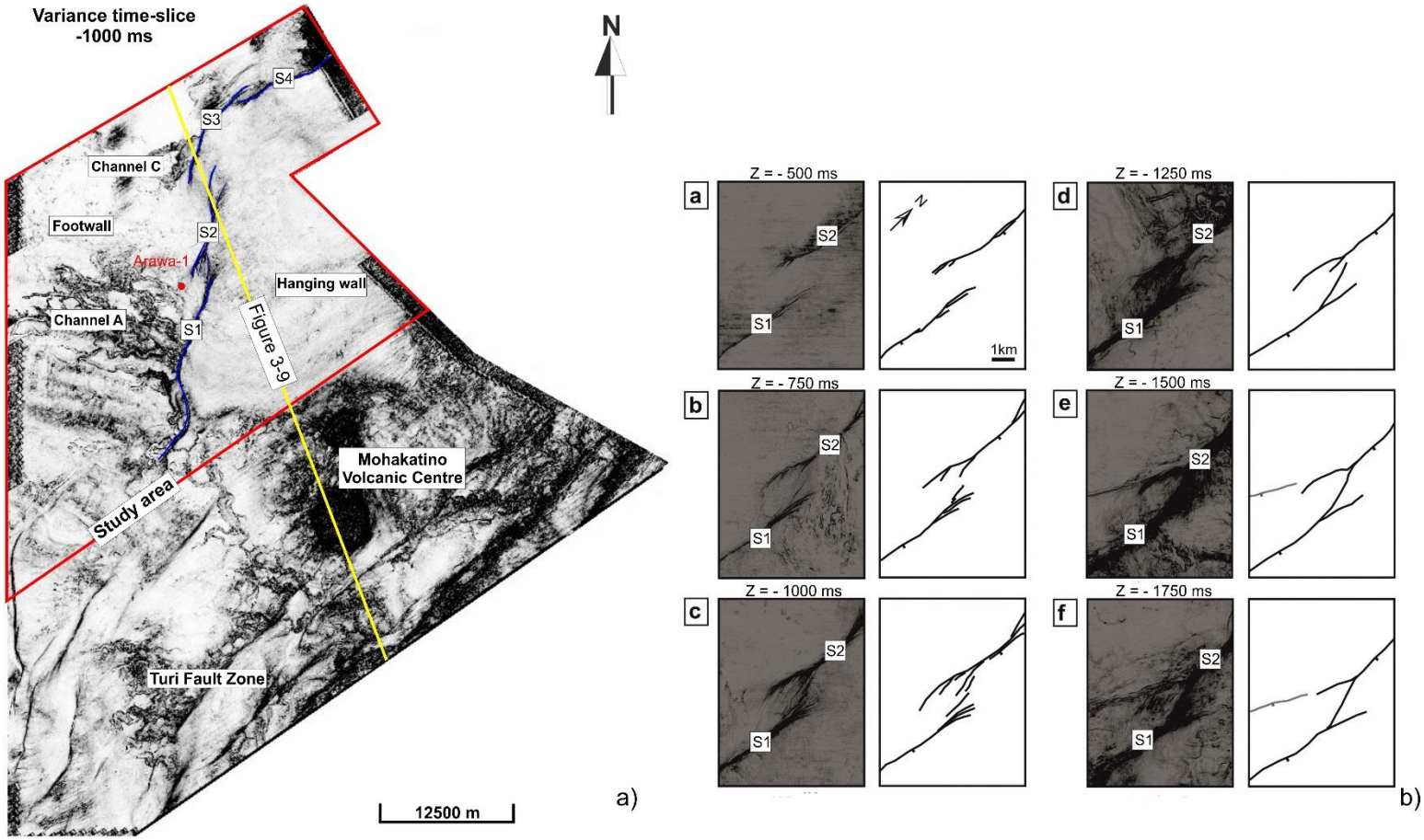

Figure 6-1: The geometry of the Parihaka Fault. a) Variance slice at -1000 ms showing the main features of the 3D seismic volume. The red polygon delimits the study area. b) Evolution of the relay ramp in the Parihaka Fault at each -250 ms showing the the unbreached relay ramp at shallow levels (Z = -500 ms), and the soft linkage of segments (Z = -1000ms), followed by the hard linkage of faults (Z = -1250 ms), and the breaching of the relay ramp (Z = -1750 ms). Modified after Giba et al. (2012).

b) How did the relay ramps, developed between the Parihaka Fault segments, controlled channel deposition?

c) What is the reason for the thickness variations observed within the channelised units deposited next to the Parihaka Fault?

d) How can channel geometry relate to the evolution of the Taranaki Basin documented in the literature?

In this chapter, different drainage types were documented using the Density Point Plot model of Gamboa et al. (2012), and assessing the relationship between drainage networks and the Parihaka Fault segments. The results obtained in this chapter will contribute to the understanding of areas where submarine-channel geometry and migration are controlled by faulting, such those as offshore West Africa (Anderson et al., 2000; Deptuck et al., 2007; Gee and Gawthorpe, 2006), Levant Basin (Clark and Cartwright, 2009), and Gulf of Corinth (Charalampakis et al., 2007; Ferentinos et al., 1988).

6.2. Database and specific methods

The main data source for this chapter is a 3D seismic volume from the Northern Graben, New Zealand. For full details of the acquisition and processing parameters of this survey see *Chapter 3, section 3.3.3*. The general seismic interpretation methods employed in this chapter are described in *Chapter 3, section 3.4*. Specific methods for this chapter include the mapping of individual channel forms and the analysis of the channel morphology.

Seismic sections were interpreted along the Parihaka Fault trace to highlight any relationships between interpreted channels and imaged fault segments (Figure 6-1c). Individual V- and U-shaped channels were identified on seismic data, based on amplitude contrasts between the channel-fill and its surroundings. The base of distinct channels was defined by the occurrence of the lowermost channel incision surface (Deptuck et al., 2003). Four submarine channel systems, Channel A to Channel D, were analysed in detail in this chapter. Isochron maps of the base of these channels were created to show the areal extent and the minimum (and maximum) depths for each channel system.

The relationship between the interpreted channels and the growth of the Parihaka Fault was highlighted by flattening the seismic and associated variance cubes to remove minor discontinuities, such as fractures, from the seismic cube (cf. Lee, 2001; Lomask, 2003). Flattening the seismic data reveals periods of syndepositional fault growth and can be applied to constrain their influence on basin evolution (Lomask, 2003). To flatten the seismic and variance cubes a grid surface generated for Horizon TC was used as reference. As this horizon, with an attributed age of 2.45 Ma (Morgans, 2006), post-dates the onset of reactivation in the Parihaka Fault reactivation, it is possible to discuss the influence of this fault on channel behaviour and geometry. To evaluate the relationships of Channel C, which initiates above the horizon TC, with the Parihaka Fault segments, the seismic and the variance cubes were flattened using the top prograding horizon H_3 (1.26 Ma) as reference.

Analyses of channel morphology included measuring the channel length distance along its thalweg (Figure 6-2), and the straight line distance between final points at each side of the channel (valley length; Flood and Damuth, 1987). Channel sinuosity was

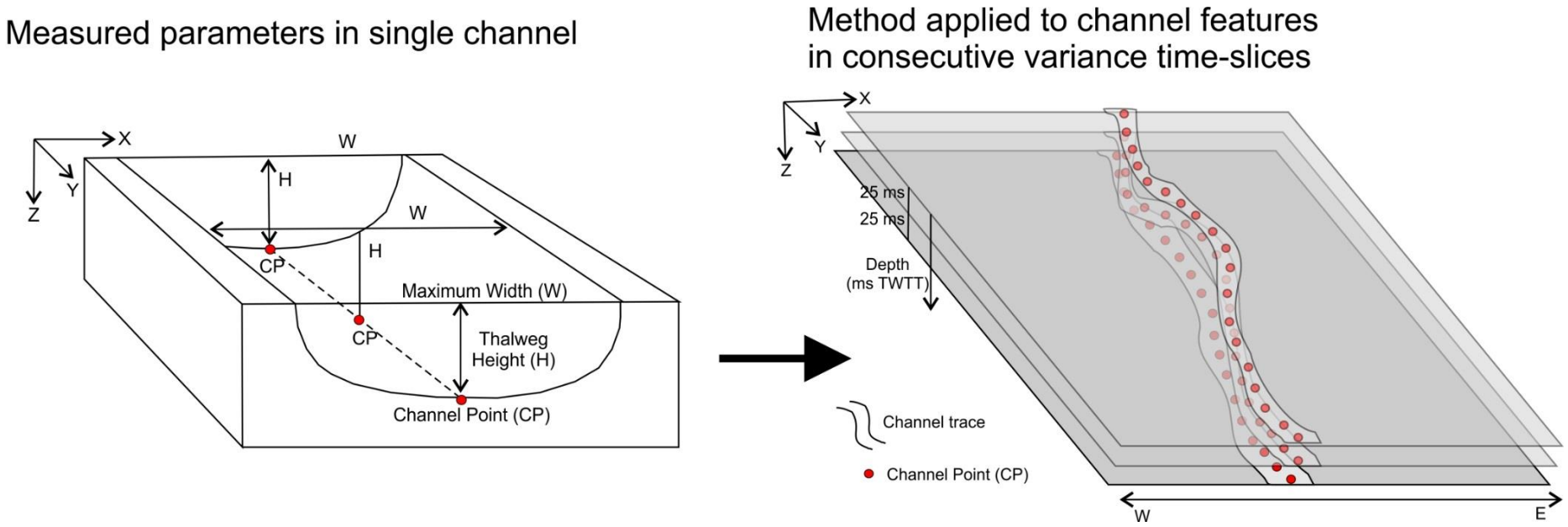

Figure 6-2: Schematic representation of the morphometric analysis of the channels. The thalweg height and width were measured from a reference Channel Point (CP) at the base of the variance time-slices. Modified from Gamboa et al. (2012).

determined as the ratio between the channel and valley lengths, and was plotted on a distribution map.

Morphometric parameters such as channel width, height, and sinuosity along the X and Y coordinates are usually measured from individual (seismically resolved) channel forms (Deptuck et al., 2007; Gamboa et al., 2012; Gee et al., 2007; Wood, 2007). However, using a low-quality seismic dataset can reduce the accuracy of the measurements with the inclusion of the levees, for instance, in the determination of the width of a single channel body (Kolla et al., 2001). The Channel Point (CP) method (Gamboa et al., 2012) was applied to reveal the three-dimensional geometry of the channels in depth (Figure 6-2). The CPs were plotted at the base of channel thalweg on variance time-slices spaced 25 ms, covering the depths between -864 ms and -2616 ms, respectively the shallowest and the deepest record of submarine channels on variance data. The maximum channel width and depth, and channel height, were generated for each CP. The locations of the points on the slope (X, Y and Z), for nearly 80,000 Channel Points obtained for the study area, were exported into ArcMap and gridded using the kriging method with a polygon delimiting the study area. The Channel Point density map was created to highlight the degree of variability in channel clustering and distribution in the study area.

6.3. Seismic interpretation

6.3.1. Seismic interpretation of the main units

The main unit of interest in this work is bounded at the base and at top by horizons BC and TC, respectively (Figures 6-1c, 6-3 and 6-4). Horizon BC is a medium- to high-amplitude positive reflection, generally continuous on the footwall block, and offset by faults on the hanging-wall block of the Parihaka Fault (Figures 6-1c and 6-3). While on the footwall block the depths of Horizon BC range between -1250 ms to -1500 ms, the hanging-wall blocks denote a dramatic increase in depth from south to north, reaching a maximum depth of -2250 ms. Two depocentres are observed in the E and NE parts of the time-structure map of horizon BC (Figure 6-3). Depocentre 1 comprises a broad area to the east, with a width of up to 9 km, and a maximum depth of -2150 ms. Depocentre 2 is a depocentre developed adjacent to segment S4 of the Parihaka Fault with a maximum depth of -2550 ms and width of 7.5 km.

Horizon TC is equivalent to the base of seismic unit SU2 of Salazar et al. (2015), and dated as 4.5 Ma old. The top of the interval with channels is defined by horizon TC, a medium- to high-amplitude positive reflection with good continuity on the footwall block, affected by the incision of small-scale channel tributaries and by the Parihaka Fault segments (Figures 6-1 and 6-4). Horizon TC occurs at depths ranging between -900 and -1050 ms on the footwall block and -950 to -1450 ms on the hanging-wall block (Figure 6-4). This horizon is equivalent to the top of the seismic unit SU5 of Salazar et al. (2016), with an assigned age of ~ 2.45 Ma (Morgans, 2006).

The isochron thickness map for the interval between horizons BC and TC shows the thickness of the footwall block to range from 350 to 400 ms (Figure 6-5). Along

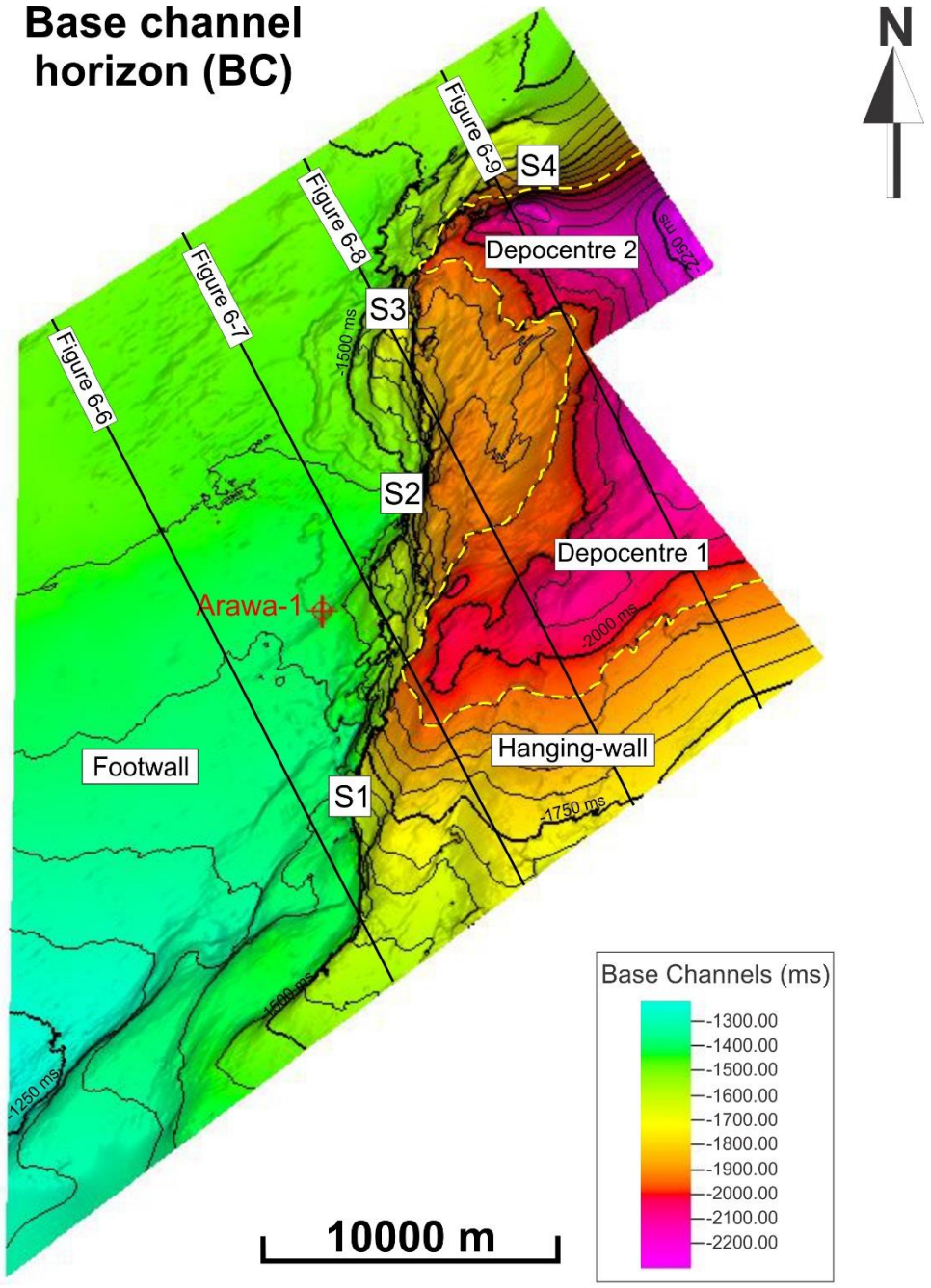

Figure 6-3: Time structural map for the Base Channel horizon BC, highlighting the depth difference between the footwall (-1250 to -1500 ms) and hanging-wall blocks (-1500 to 2250 ms) of the Parihaka Fault. Two depocentres occur in the East (Depocentre 1) and in the North (Depocentre 2) of the study area. The interval of the contour lines is 50 ms. The dashed yellow lines delimit the main depocentres in the study area. A vertical exaggeration 1:5 was applied to the map.

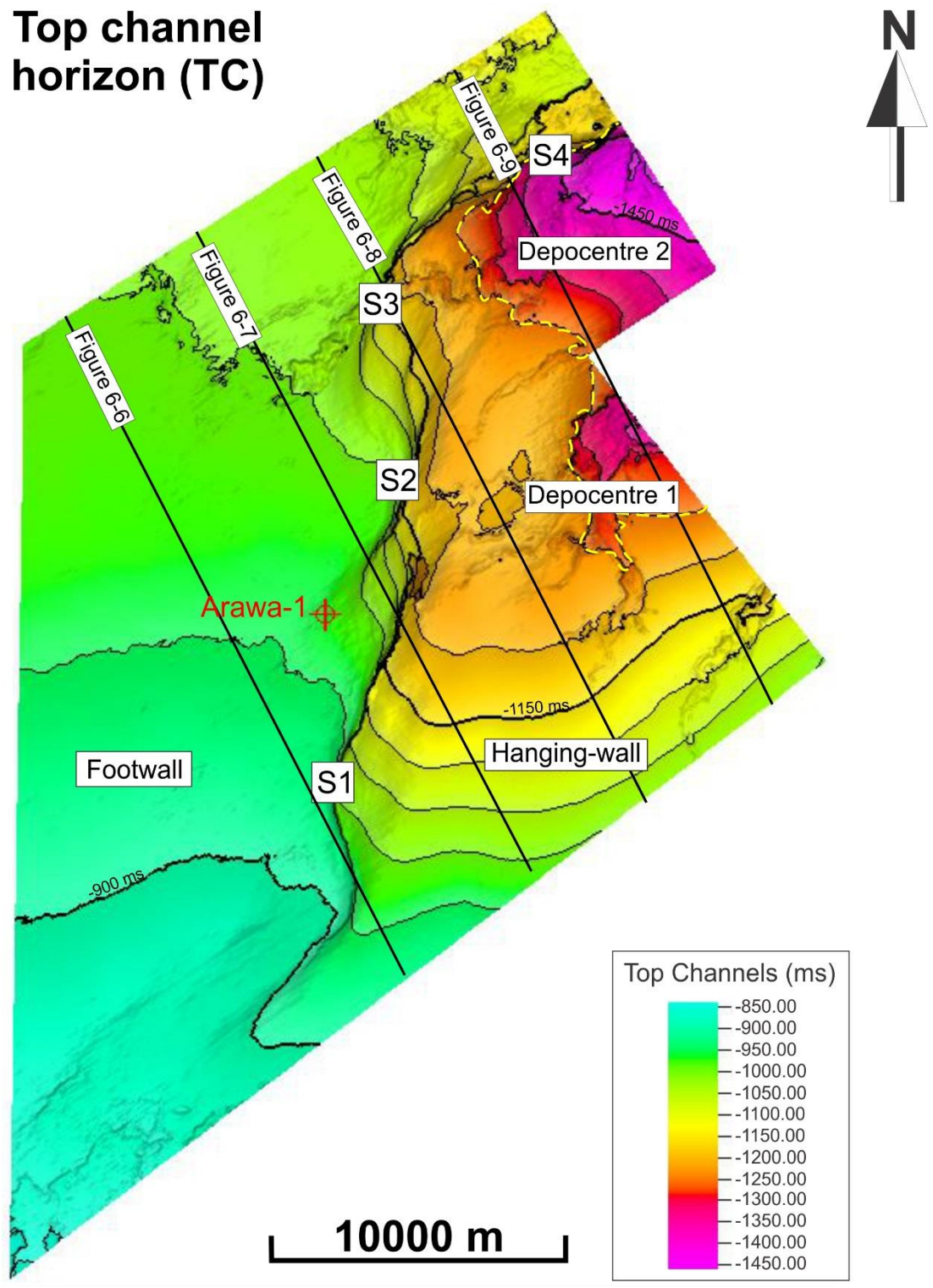

Figure 6-4: Time structural map for the Top Channel horizon TC, indicating the depth difference (in ms TWTT) between the footwall (-900 to -1050 ms) and the hanging-wall (-950 to -1450 ms). Depth differences at TC level are smaller than for the Bottom Channel horizon. Depocentres 1 and 2 are significantly smaller at the TC horizon. The interval of the contour lines is 50 ms. The dashed yellow lines delimit the main depocentres in the study area. A vertical exaggeration 1:5 was applied to the map.

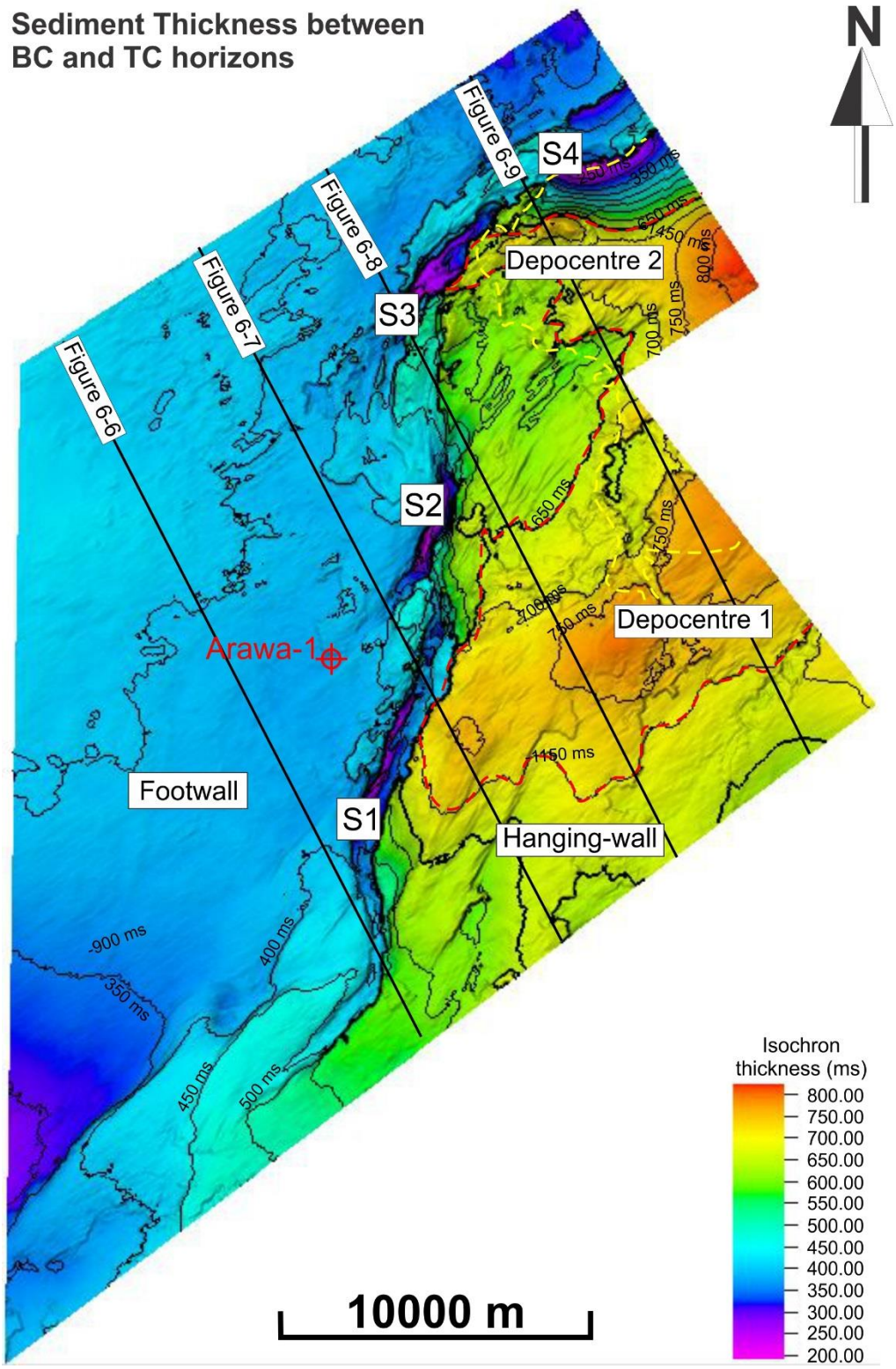

Figure 6-5: Isochron sediment thickness map for the study area based on the horizons BC and TC. The predominant thickness for the footwall block is 400 ms, whereas strata thickness for the hanging-wall block ranges from 500 to 800 ms. The interval for the contour lines is 50 ms. Depocentres 1 and 2 are delimited by the red dashed line and comprise the thickest deposits in the study area. A vertical exaggeration 1:5 was applied to this map.

the Parihaka Fault segments, the thickness between horizons BC and TC reaches its lowest values (200-250 ms). In the hanging-wall block, the same thickness varies from 500 to 800 ms, and is greater toward the E and NE of the study area, where the two depocentres are observed (Figure 6-5).

6.3.2. Seismic character of the submarine channel deposits

Variance slices reveal submarine channels with a variety of scales and shapes adjacently to the footwall block of the Parihaka Fault (Figure 6-1a). Channels in the study area can occur either as single channel bodies with a large erosional base, or as multiple small-scale channel tributaries that converge to form a large submarine channel system at depth (Figures 6-6 to 6-9).

The main channel sequence shows high-amplitude prograding reflections in the footwall block, whose continuity is interrupted by faults and channel-incision surfaces (Figures 6-6 to 6-9). Submarine channels can be identified on the seismic profiles as high-amplitude erosional features with predominantly concave geometries (Figures 6-6 to 6-9). Their channel-fill deposits consist of low- to medium-amplitude chaotic and discontinuous reflections. Evidence of vertical and lateral stacking of the channel bodies is found throughout the study area (Figures 6-6 to 6-9). Wedge-shaped channels, defined by the occurrence of levees that form continuous seismic reflections with variable lateral extent and thinning away from the channel axis, are less common in the study area (Figures 6-6 to 6-9).

Four seismic profiles through the Parihaka Fault segments reveal the configuration of submarine channels both on the footwall and hanging-wall blocks (Figures 6-6 to 6-9). In profile A-B (Figure 6-6), channel-fill deposits occur at a maximum depth of -1100 ms below the seafloor. The footwall block is characterised by the occurrence of V- and U-shaped erosive surfaces incising the prograding foresets. Small-scale channels are recognised as tributaries of the large channel system, herein denominated Channel A (Figure 6-6). The predominant geometry for the channels in profile A-B is concave. However, wedge-shaped channels with small-scale levees are also observed. The main channel body of Channel A system is cut by segment S1 of the Parihaka Fault (Figure 6-6). A high amplitude positive reflection delimits a vertically-stacked channel deposit within Channel A (Figure 6-6).

Profile C-D shows the position, from NW to SE, of three important channel systems in the study area. On the footwall block, Channel D incises the prograding sequence of the Giant Foresets Formation (Figure 6-7). Five channels are vertically stacked within Channel D, whereas two lateral stacks are observed towards the NW. In the central part of this profile, Channel B is characterised by a concave erosional surface filled by low amplitude reflections (Figure 6-7). A small channel is observed incising the SE margin of Channel B. Segment S1 shows a horse-tail geometry in the seismic profile, comprising faults first generated below the horizon BC that propagate to a depth of -1250 ms below the seafloor. On the hanging-wall block, Channel A shows lateral migration at its base, indicating a deflection on its course. Up to nine

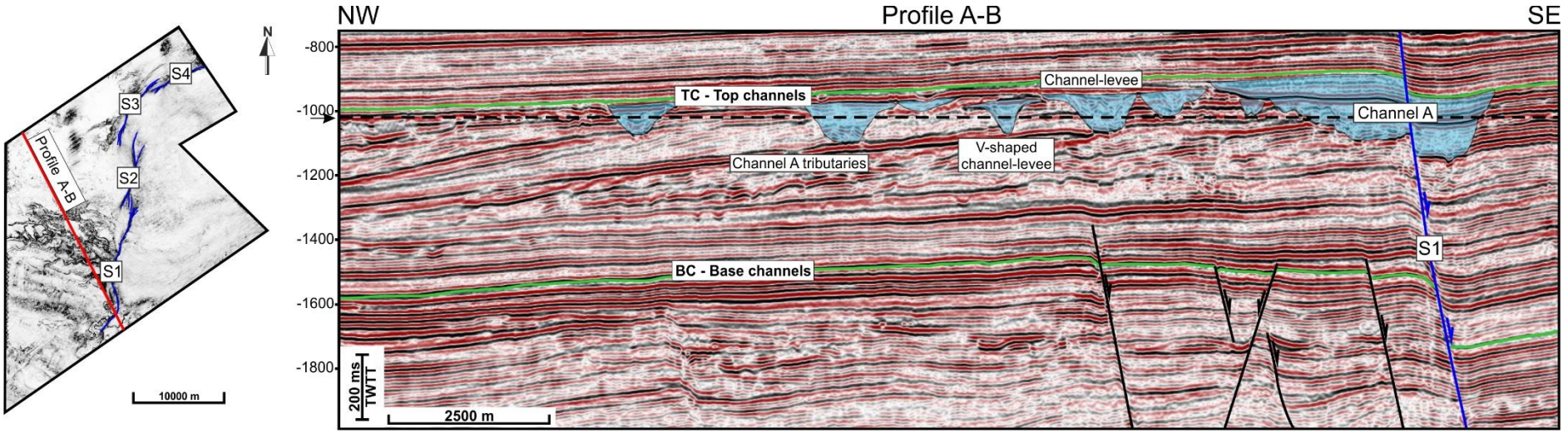

Figure 6-6: NW-SE seismic profile A-B showing the tributaries of Channel A to the NW, which show U- and V-shaped erosional bases. A small channel-levee system is observed on the footwall block. The main Channel A occurs to the SE of the seismic profile and is offset by segment S1. The depth of the time-slice shown as inset is indicated by an arrow and a dashed line on the seismic profiles.

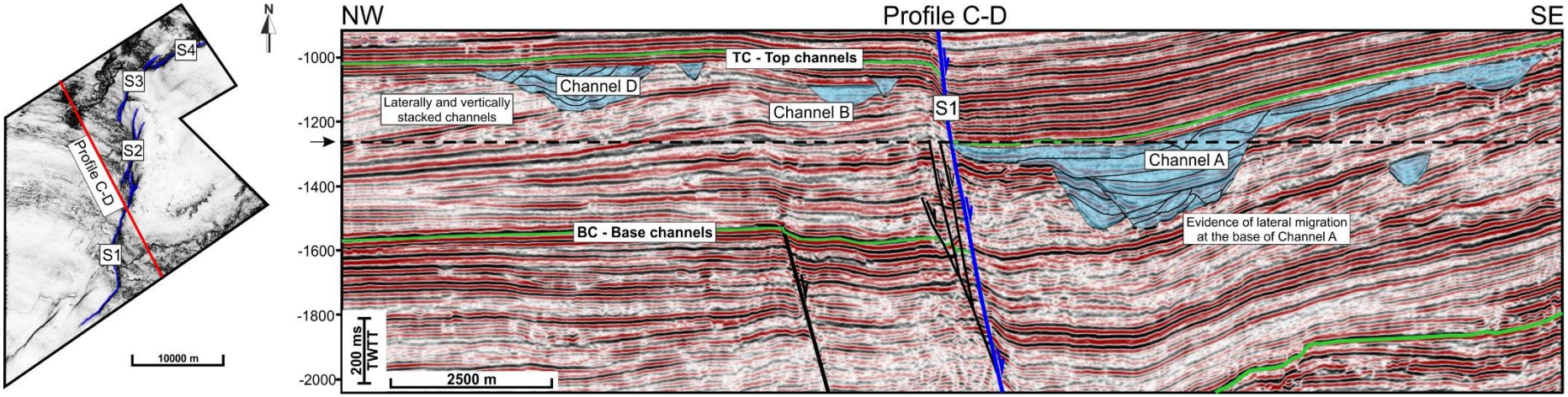

Figure 6-7: NW-SE seismic profile C-D showing three of the four main channel systems in the study area. Channel D occurs to the NW on the footwall block and shows laterally and vertically stacked channels within this system. Channel B occurs close to the trace of S1 and comprises two tributaries. Channel A occurs entirely on the hanging-wall block in this profile. The interpretation of the seismic lines highlights the lateral and vertical stacking within this channel system. The depth of the time-slice shown as inset is indicated by an arrow and a dashed line on the seismic profiles.

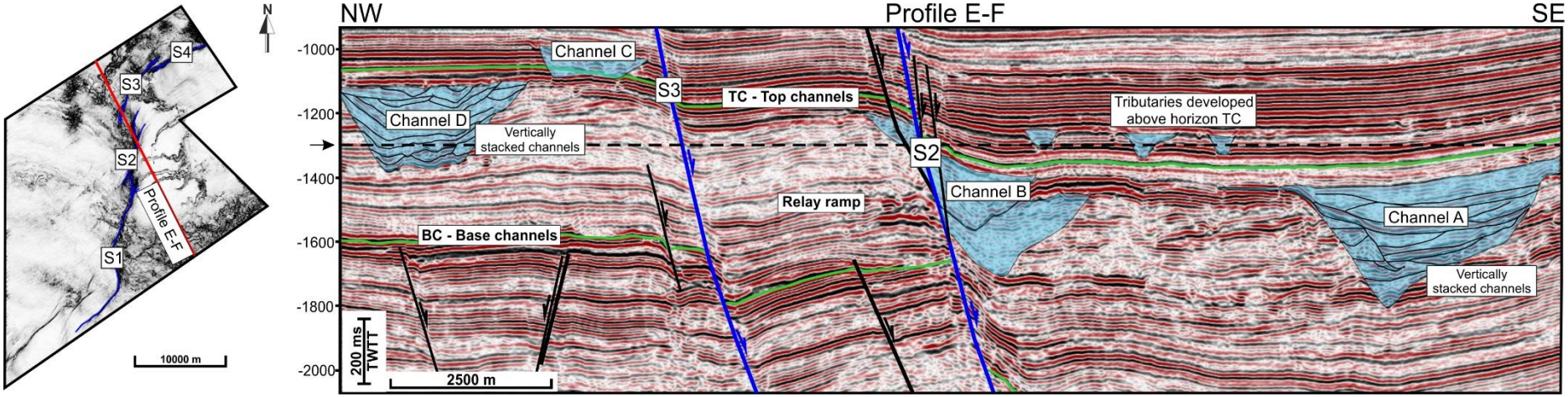

Figure 6-8: NW-SE seismic profile E-F showing Channel D system comprising many vertically stacked channels on the footwall block. Channel C also occurs on the footwall block above Horizon TC and close to S3. A rotated relay ramp developed between S3 and S2 is observed. Channel B is offset by S2 at the SE termination of this relay ramp. Channel A occur at depths between -1600 and -1800 ms to the southeast. The depth of the time-slice shown as inset is indicated by an arrow and a dashed line on the seismic profiles.

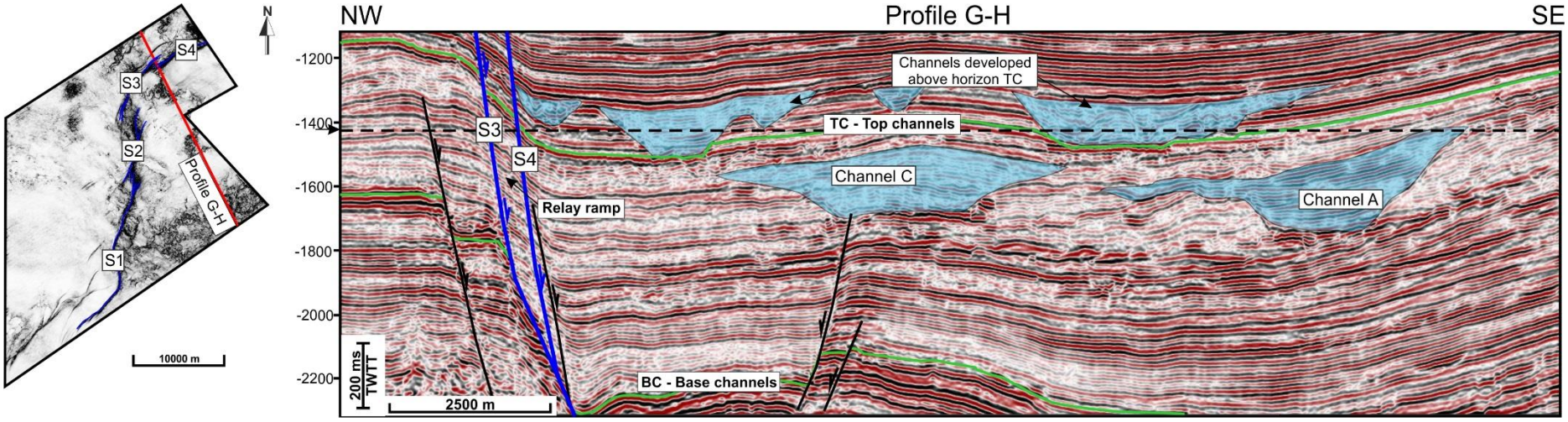

Figure 6-9: NW-SE seismic profile G-H showing a relay ramp developed between S3 and S4 to the NE of the study area. The hanging-wall block is characterised by the occurrence of Channel C incising horizon TC and the termination of Channel A. Channels developed above horizon TC are also observed on the hanging-wall block. The depth of the time-slice shown as inset is indicated by an arrow and a dashed line on the seismic profiles.

channels are vertically stacked within the principal Channel A (Figure 6-7). This channel system becomes broader and shallower close to horizon TC towards the SE (Figure 6-7).

Profile E-F is characterised by a ~ 4 km relay ramp comprising segments S2 and S3 of the Parihaka Fault (Figure 6-8). The base of Channel D occurs at a depth of about -1380 ms below the seafloor, whereas this channel system shows up to 16 channels vertically-stacked. Channel C is observed on the footwall incising horizon TC close to the trace of segment S3. This profile shows Channel B cut by S2 and horsetail splays developed at the upper tips of the fault segment within the SE part of the relay ramp. Here, relay-ramp geometry indicates rotation in relation to the footwall and the hanging-wall blocks (Figure 6-8).

On the hanging-wall block, Channel B incises a large channel body, whereas Channel A occurs to the SE of this profile comprising vertically stacked channels. Above horizon TC it is possible to observe three channel tributaries. The inset map for this profiles at a depth of -1250 ms shows that these channels initiated on the hanging-wall block (Figure 6-8).

Profile G-H is characterised by the occurrence of a small-scale (~ 500 m) relay ramp between segments S3 and S4 (Figure 6-9). Within the main channel sequence, it is possible to observe the occurrence of channel systems C and A on the hanging-wall block. A graben delimited by Segment 4 of the Parihaka Fault at NW and by an antithetic fault dipping to NE is observed on the hanging-wall and appears to influence the sigmoidal shape of Channel C, as this NE-dipping segment terminates at the base of Channel C (Figure 6-9). Channel A shows less stacked channels within its erosive

surface in comparison with the three previous seismic profiles. In the profile in Figure 6-9, it is observed a large number of channels developed above horizon TC, at depths between -1300 ms and -1450 ms below the seafloor (Figure 6-9).

6.4. Interactions between the submarine channels and the Parihaka Fault

The influence of the Parihaka Fault on four large-scale submarine channel systems was investigated using unflattened and flattened seismic profiles, complemented with variance time-slices (Figures 6-10 to 6-13). Channel A is a 27 km-long channel system located southwest of the study area (Figure 6-10). The main direction of the base this channel system is SW-NE, with its main tributary occurring at an angle of 44º to S1. A second SW-NE channel A branch trend to 65º to the fault trace. One of the Channel tributaries flows perpendicular to the trace of the N-striking S1, whereas the northernmost tributary of this channel system forms an angle of 71º to segment S1 (Figure 6-10a). These branches migrate towards S1 to form a large channel base on the hanging-wall block with widths ranging from 900 m to 3.3 km. The minimum depth observed for the base of Channel A is -950 ms and the maximum depth is -1600 ms (Figure 6-10b), coinciding with the location of Depocentre 1 (Figures 6-3 and 6-4). In the unflattened seismic profile, Channel A is offset by segment S1, and a similar channel geometry is observed both on the footwall and hanging-wall blocks (Figure 6-10c). In the flattened seismic profile, using horizon TC as a reference, the removal

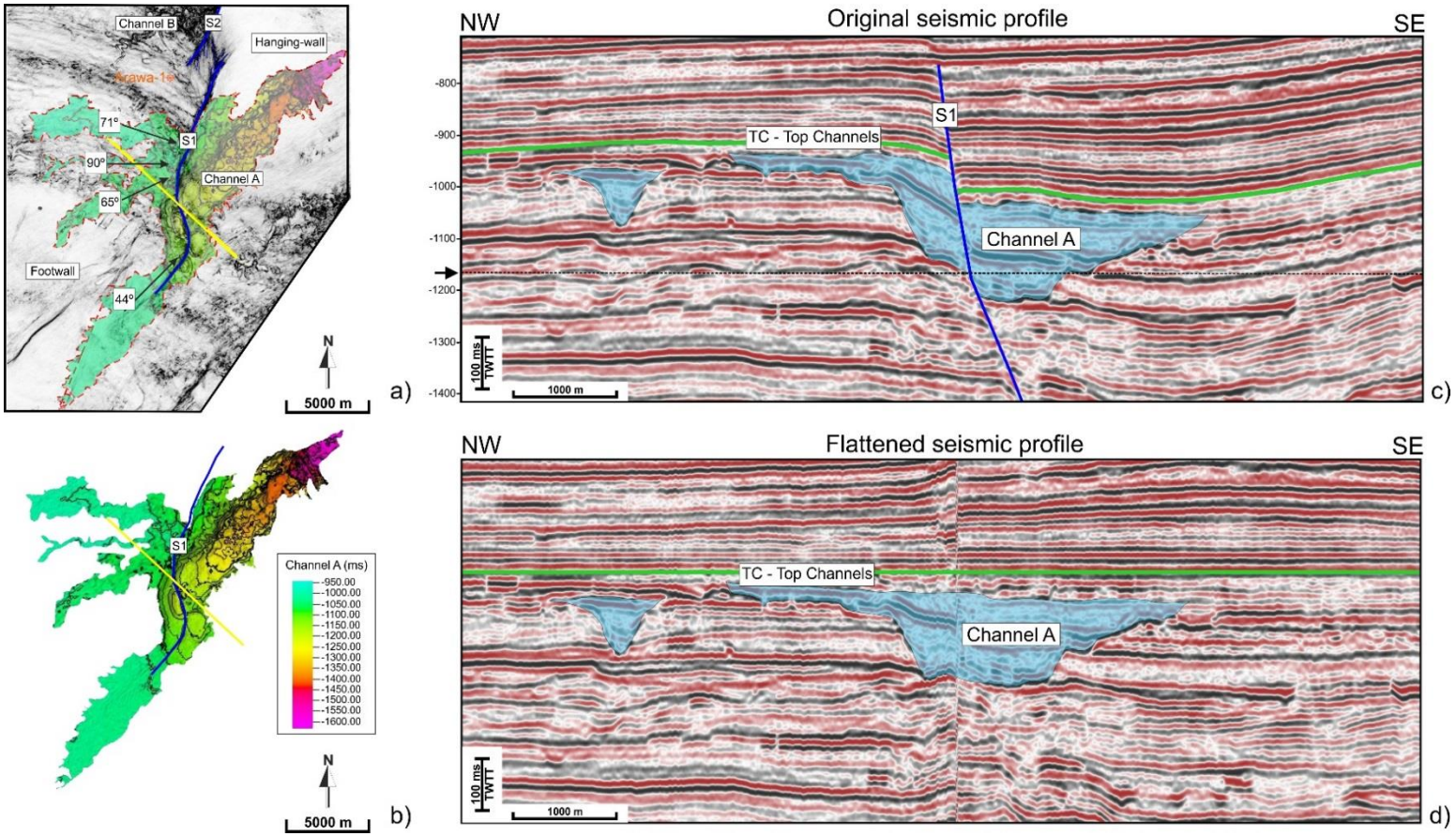

Figure 6-10: Detailed seismic interpretation of Channel A. a) Variance time-slice at -1180 ms indicating the base of the Channel A on the footwall block, the segments of Parihaka Fault, the position of the seismic profile, and the angles this channel system make to S1. b) Time-structural map for Channel A showing the channel tributaries flowing obliquely to S1. c) Original seismic profile highlighting the channel relationships with the fault trace. The depth of the variance time-slice is indicated by an arrow and a dashed line on the seismic profile. d) Flattened seismic profile stressing the minor influence of faulting in channel configuration

of segment S1 allows the reconstruction of the original position of Channel A, indicating this channel was formed prior to the reactivation of S1 at 3.7 Ma (Figure 6-10d).

Channel B is a 15 km-long channel system located in the central part of the study area (Figure 6-11). On the footwall block, the base of Channel B system forms an angle of 61º to S2. Close to the NNE-striking segment S2, this channel is deflected to form a perpendicular angle to this segment. On the hanging-wall block, the flow of Channel B varies from W-E adjacently to S2, to SW-NE towards the channel termination. Small channels flow downslope through the hanging-wall block to form an extensive channel system (Figure 6-11a). The base of Channel B on the seismic lines occurs at a minimum depth of -1000 ms and maximum depth of -1650 ms (Figure 6-11b), coinciding with the location of Depocentre 1 (Figures 6-3 and 6-4). On the time-structure map of the base of Channel B, it is possible to observe that the initially confined flow on the footwall block splays out on the hanging-wall block (Figure 6-11b). Interpretation of unflattened (Figure 6-11c) and flattened (Figure 6-11d) seismic profiles indicate the reactivation of S2 affected the deposition of this channel system, as segment S2 is not removed by flattening using horizon TC as a reference and the channel systems becomes thicker on the hanging-wall block.

The base of Channel C incises horizon BC above the main channel unit on the footwall block (Figure 6-12). With a total length of 12 km, this channel system is characterised by two tributaries that form the base of this channel initially trending 71º and 60º to the NNE-striking segment S3. These tributaries merge into a single thalweg perpendicular to segment S3 of the Parihaka Fault (Figure 6-12a). This channel occurs oblique to the fault

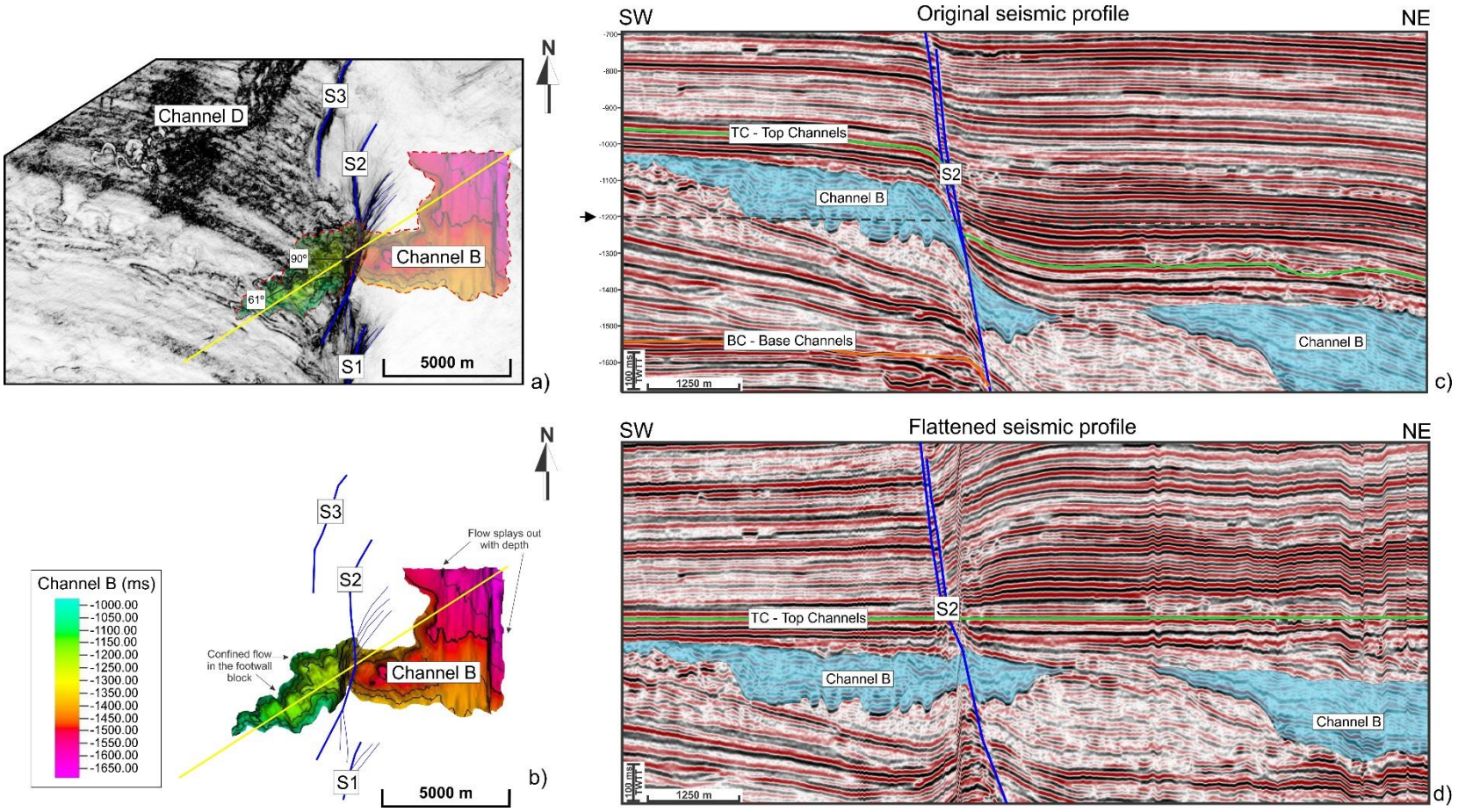

Figure 6-11: Detailed seismic interpretation of Channel B. a) Variance time-slice at a depth of -1200 ms indicating the base of Channel B on the footwall block, the segments of Parihaka Fault, the position of the seismic profile, and the angles this channel system make to S2. b) Time-structural map for Channel B showing the channel initially flowing obliquely to S2 to later divert transversally to the segment trace. c) Original seismic profile highlighting the channel relationships with the fault trace. The depth of the variance time-slice is indicated by an arrow and a dashed line on the seismic profile. d) Flattened seismic profile highlighting the influence of faulting in the Channel B configuration.

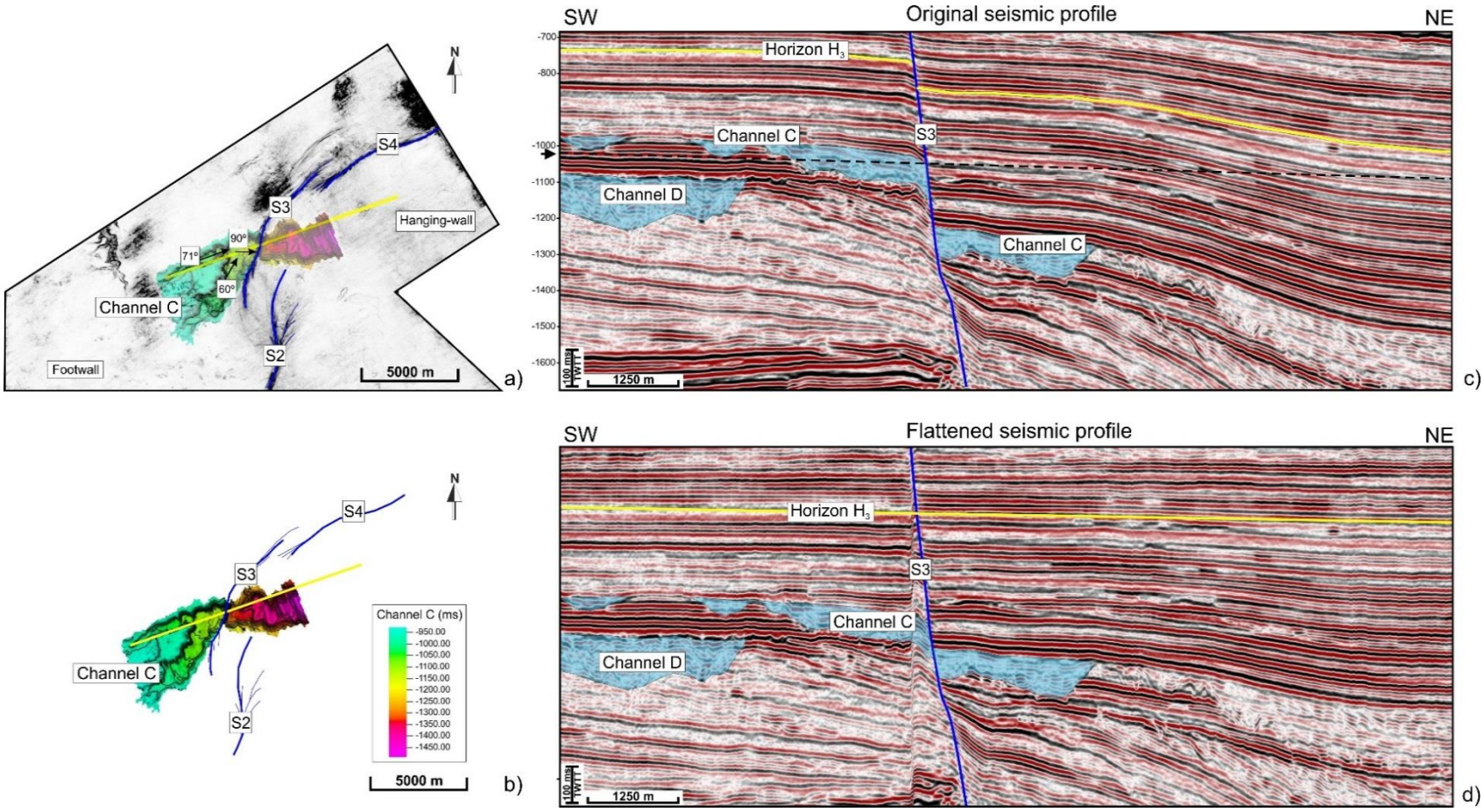

Figure 6-12: Detailed seismic interpretation of Channel C. a) Variance time-slice at -1020 ms indicating the base of Channel C on the footwall block, the segments of Parihaka Fault, the position of the seismic profile, and the angles this channel system make to S3. b) Time-structural map for Channel C showing the two main channel tributaries flowing obliquely to segment 3 of the Parihaka Fault. c) Original seismic profile highlighting the channel relationships with the fault trace. d) Flattened seismic profile using the horizon H3 as reference and highlighting that faulting occurred prior to channel deposition.

segment, with tributaries. On the footwall block, the base of Channel C is observed on the seismic lines at a maximum depth of -1100 ms below the seafloor (Figure 6-12b). On the hanging-wall, the channel initially flows in an E direction, parallel to S3, and is then deflected towards the NE, where the base of this channel is observed at a maximum depth of -1450 m on the time-structural map (Figure 6-12c). To constrain the evolution of this channel relative to the evolution of the Parihaka Fault, the seismic profile was flattened using the top prograding horizon H_3 (1.26 Ma) as a reference. Flattening the seismic profile did not result in the removal of segment S3, indicating that the development and growth of this fault segment had an important role in the evolution of Channel C (Figure 6-12d).

Channel D is an 18 km-long channel system incising a prograding sequence entirely in the footwall block (Figure 6-13a). On the time-structural map, the base of this channel system is observed at a minimum depth of -1050 ms and maximum depth of -1400 ms (Figure 6-13b). This channel follows an initial SW-NE direction. At a distance of 2 km from segment S3 of the Parihaka Fault, the base of this channel is deflected to the NW, following a trace parallel to S3 but with different dips.

6.5. Channel sinuosity

Sinuosity values for 64 channels in the study area vary according to the channel system they are contained and their proximity to the Parihaka Fault segments (Figure 6-14). In general, channels on the footwall block meander away from the fault trace and

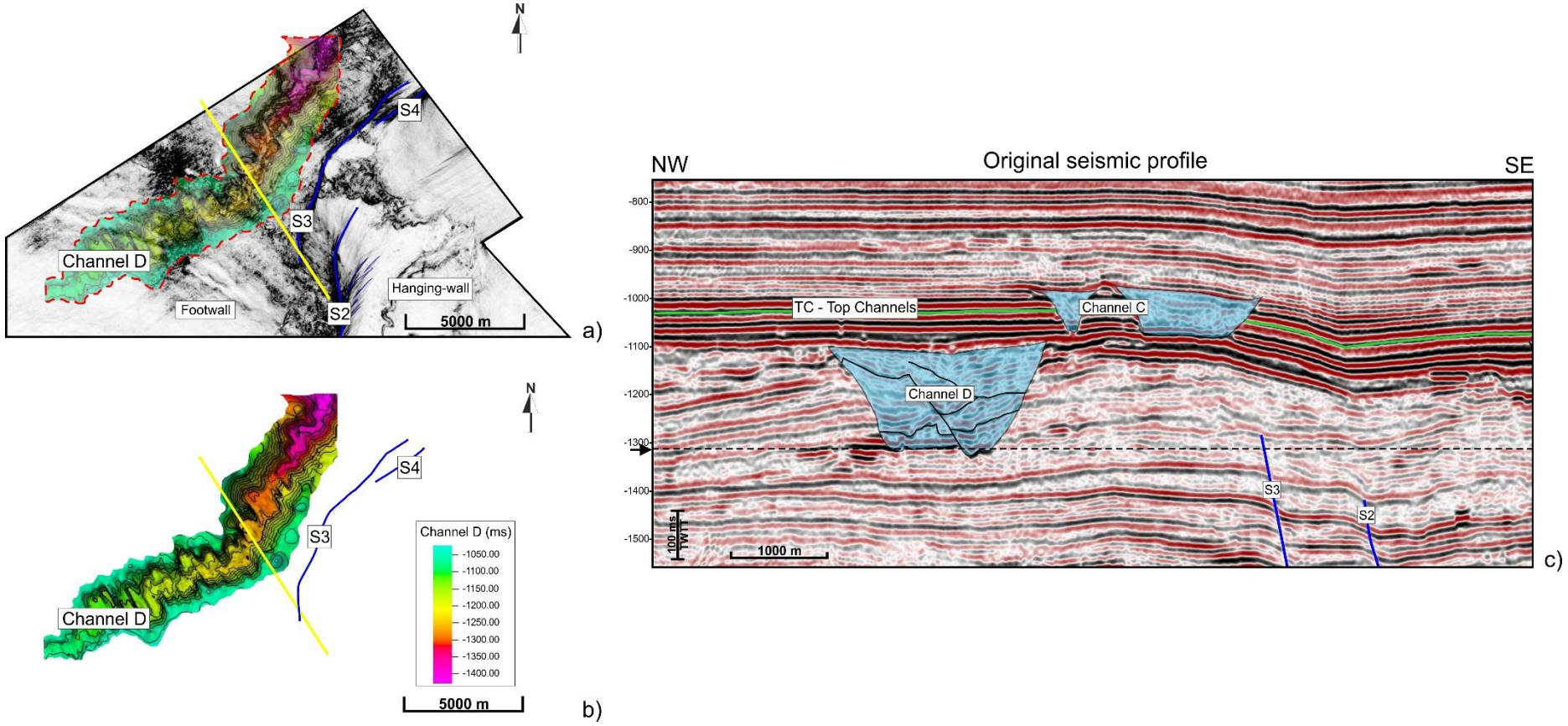

Figure 6-13: Detailed seismic interpretation of Channel D. a) Variance time-slice at -1320 ms showing the base of Channel D on the footwall block. b) Time-structural map for Channel D showing the channel body flowing parallel to the Parihaka Fault trace. c) Original seismic profile highlighting the channel relationship with the fault trace. Channel C is also observed in this seismic profile above horizon TC.

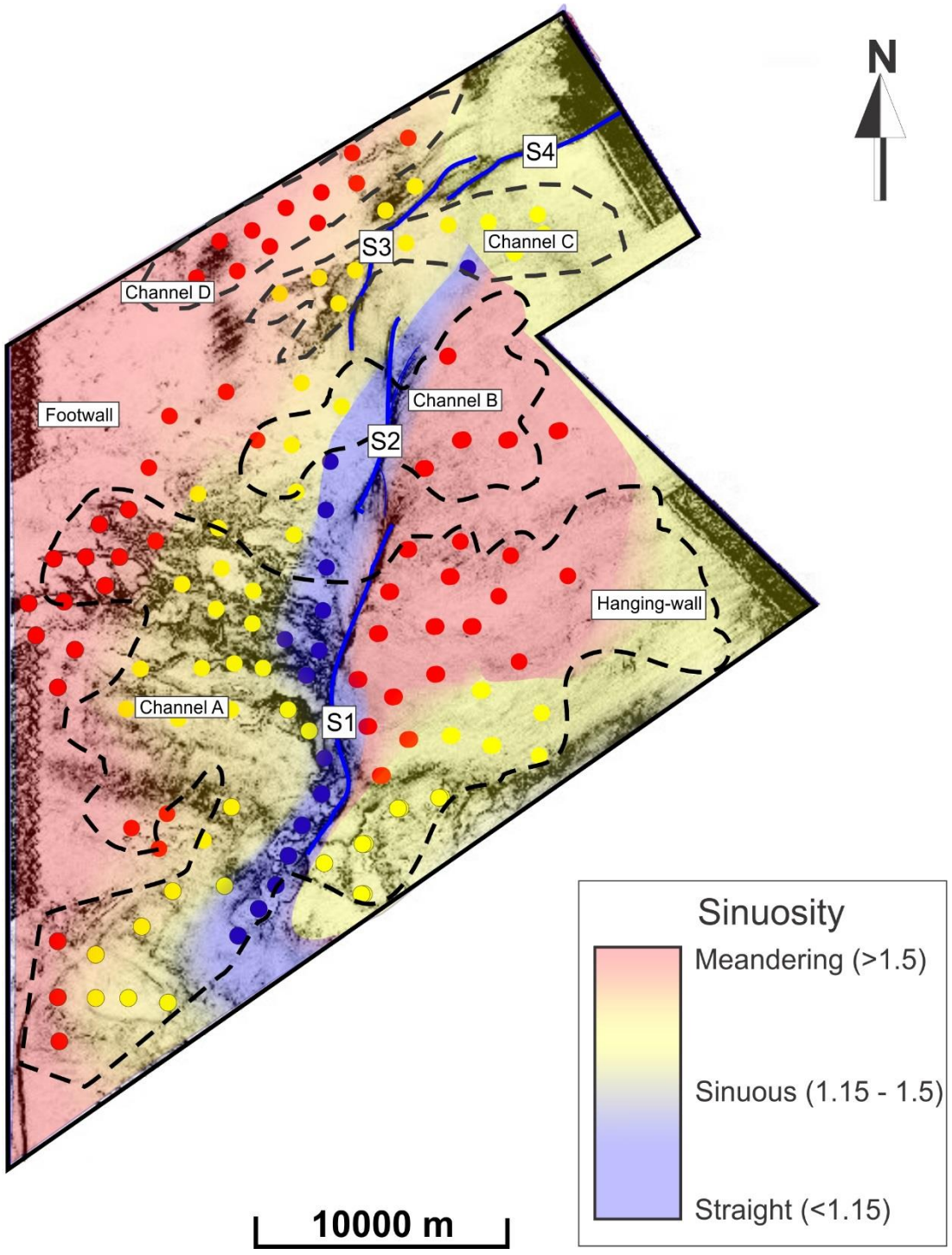

Figure 6-14: Channel sinuosity distribution in the study area. Channels on the footwall block evolve from meandering to straight, according to the proximity of segments S1 and S2. Channels contained within the Channel A system vary from sinuous to meandering on the hanging-wall block. Channel B has a sinuosity distribution similar to Channel A on the footwall block, whereas on the hanging-wall the channels are predominantly meandering. Channel C is mostly meandering both on the footwall and hanging-wall blocks, whereas Channel D, located entirely on the footwall block, is meandering.

tend to become straighter close to segments S1 and S2. On the hanging-wall block, channels are either sinuous or meandering (Figure 6-14). For channels contained within Channel A system, sinuosity decreases from W to E on the footwall block, with meandering channel tributaries showing an average sinuosity of 1.87, decreasing to 1.13 close to segment S1 (Figure 6-14). On the hanging-wall block adjacent to S1, Channel A is more sinuous in the SE of the study area, whereas close to segments S1 and S2 channels are meandering. The sinuosity pattern for Channel B on the footwall block is similar to Channel A. Sinuosity varies from 1.24 to 1.11 towards S2, while channels predominantly meander on the hanging-wall block with sinuosity values varying from 1.5 to 1.7 (Figure 6-14). Channel C is mostly sinuous, both on the footwall and hanging-wall blocks defined by S3, with an average sinuosity of 1.32. Channel D is meandering, with an average sinuosity of 1.9, but no direct interaction is observed between these channels and the trace of segments S3 and S4.

6.6. Channel density in the study area

Channel Point (CP) distribution maps for depths ranging between -864 and -2016 ms are shown in Figure 6-15. The distribution of channels was evaluated with the creation of a CP density plot (Figure 6-16). CP plots reveal a predominant channel distribution between -864 and -1152 ms on the footwall block, including the four representative channel systems in the study area (Figure 6-15a). However, CPs for Channel D are chiefly plotted between -1152 to -1440 ms (Figure 6-15b). One of the most distinctive features

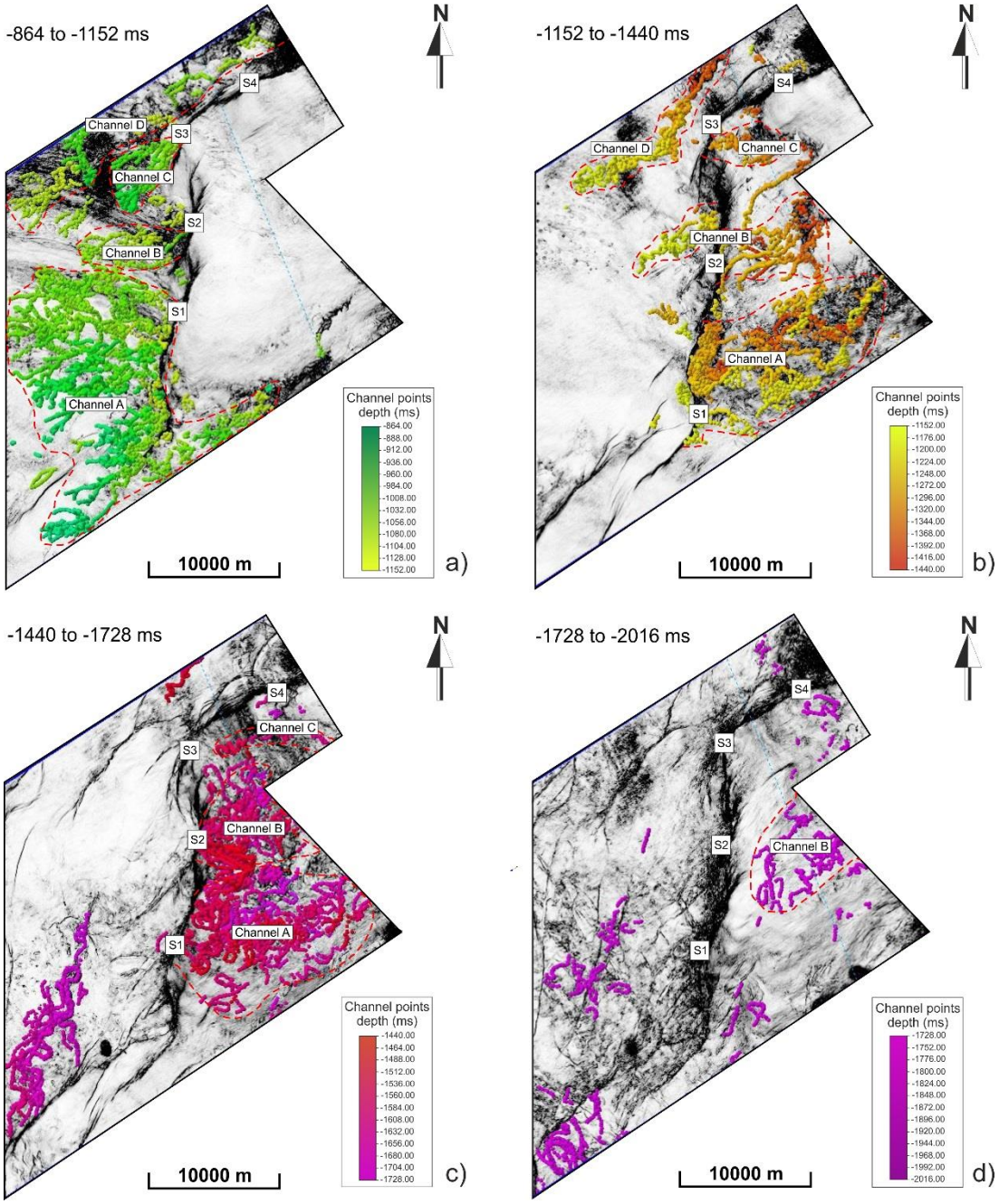

Figure 6-15: Channel point distribution maps at depths from a) -864 to -1152 ms, b) -1152 to -1440 ms, c) -1440 to 1728 ms, and d) -1728 to -2016 ms. These maps evidence that the channel distribution on the footwall block predominates between -864 and -1152 ms. However, channels on the footwall block may occur at greater depths. The channel distribution on the hanging-wall block predominates between -1152 to -1728 ms. Channel density is smaller from -1728 to -2016 ms both on the footwall and hanging-wall blocks of the Parihaka Fault.

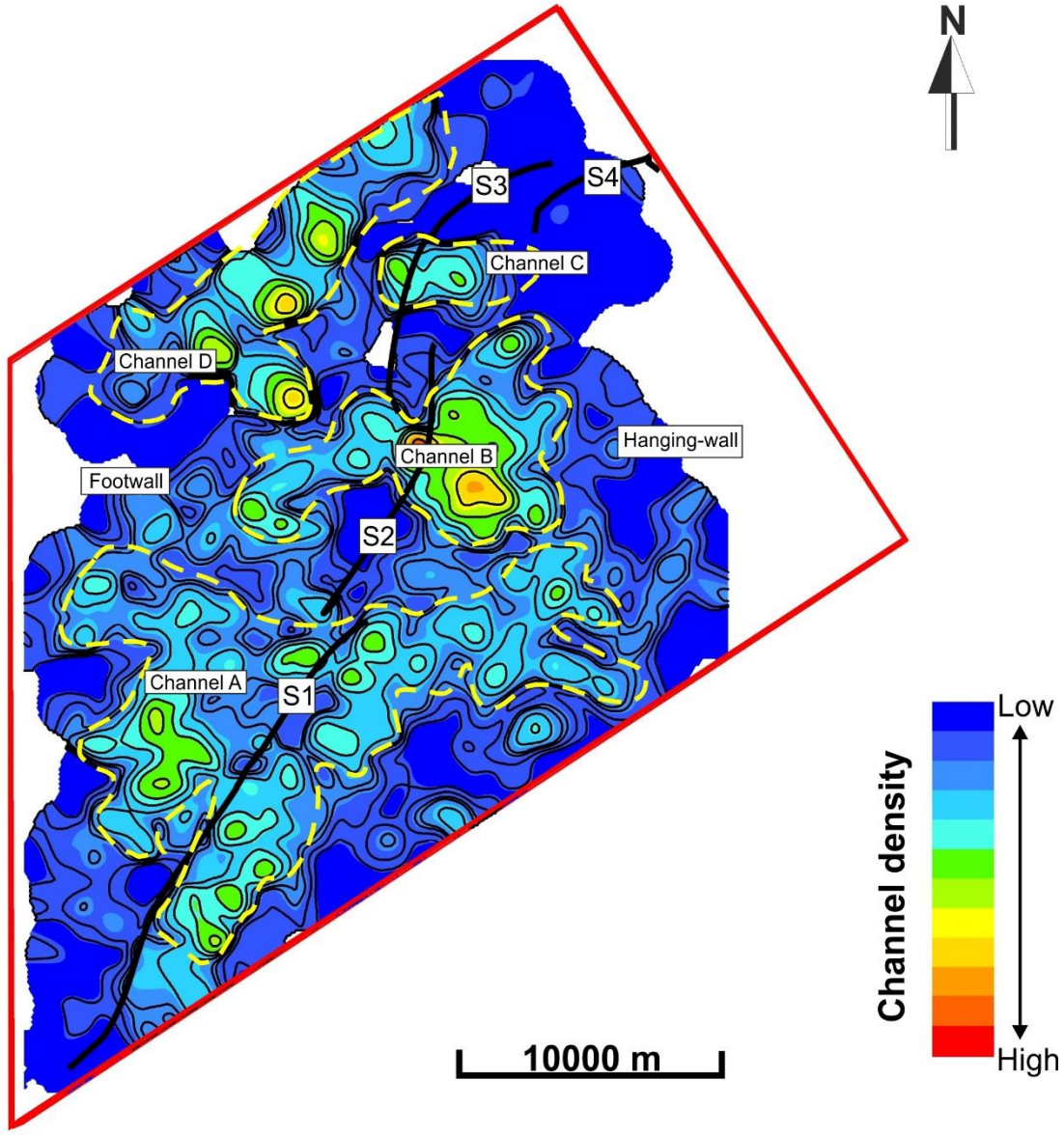

Figure 6-16: Channel density points plot evidencing the lateral and vertical stacking patterns of the submarine channels in the study area. The main channel systems were delimited on this plot to facilitate the interpretation of channel density distribution. The greatest channel density occurs in the areas corresponding to Channel D on the footwall block and Channel B on the hanging-wall block.

on the footwall is the occurrence of a large channel at depths between -1440 and -1728 ms (Figure 6-15c). However, this channel occurs away from the Parihaka Fault trace and relates to a different fault occurring in the Cape Egmont Fault Zone (Figure 6-15c). Channel points on the hanging-wall block predominate at depths ranging between -1152 to -1440 ms and -1440 to -1728 ms. Only a small number of channels were recorded at depths varying from -1728 ms to -2016 ms (Figure 6-15d).

Two areas of high channel concentration were delimited on the density point plot (Figure 6-16). One of the areas coincides with Channel D on the footwall block, while the second area coincides with the location of Channel B adjacent to the hanging-wall of S2. Channel density areas coinciding to Channel A show a medium to low channel density. Channel density is low adjacent to the relay ramps developed between S1 and S2 to the south, and S2 and S3 to the north, indicating a minor influence of the relay ramps on channel configuration. The lack of interpreted CP to the NE of the study area is reflected in the channel density plot (Figure 6-16). Channel density is low in this region, as the channels occur above the interval of interest and are also hard to identify on the variance time-slices (Figure 6-16).

6.7. Discussion

6.7.1. The role of the Parihaka Fault in controlling the configuration of drainage systems

The influence of the Parihaka Fault in channel evolution is observed at different scales for the four studied channels (Figure 6-17). Three main drainage types related to the Parihaka Fault were interpreted in the study area: oblique drainage, transverse drainage and parallel drainage. Channel A is an example of an oblique drainage system that initiates in the southern part of the study area as three of the four main tributaries at the base of this channel system occurs at angles varying from 44º to 71º to S1. On the hanging-wall block, Channel A comprises sinuous to meandering vertically and laterally stacked channels. The flattened seismic cubes (Figures 6-10 to 6-12) reveals that the channels were developed in the southern part of the seismic volume before the reactivation of segment S1 of the Parihaka Fault (Early Pliocene).

Channels B and C are examples of drainage networks that run transverse to the Parihaka Fault trace, indicating a flow deflection from the initial path towards the fault trace. Channel deflections may also indicate a close structural influence in channel configuration, followed by an increase in sedimentary input. The flattened seismic profile using horizon TC as a reference restores the original geometry of Channel B and indicates that S2 was active during the deposition of this channel system. It also suggests that the marked downslope progradation of the Giant Foresets Formation sediments was greater than the vertical propagation of S2 during channel deposition (Figure 6-11). The base of Channel C incises Horizon BC and, in the block-diagram of Figure 6-17, it is possible to

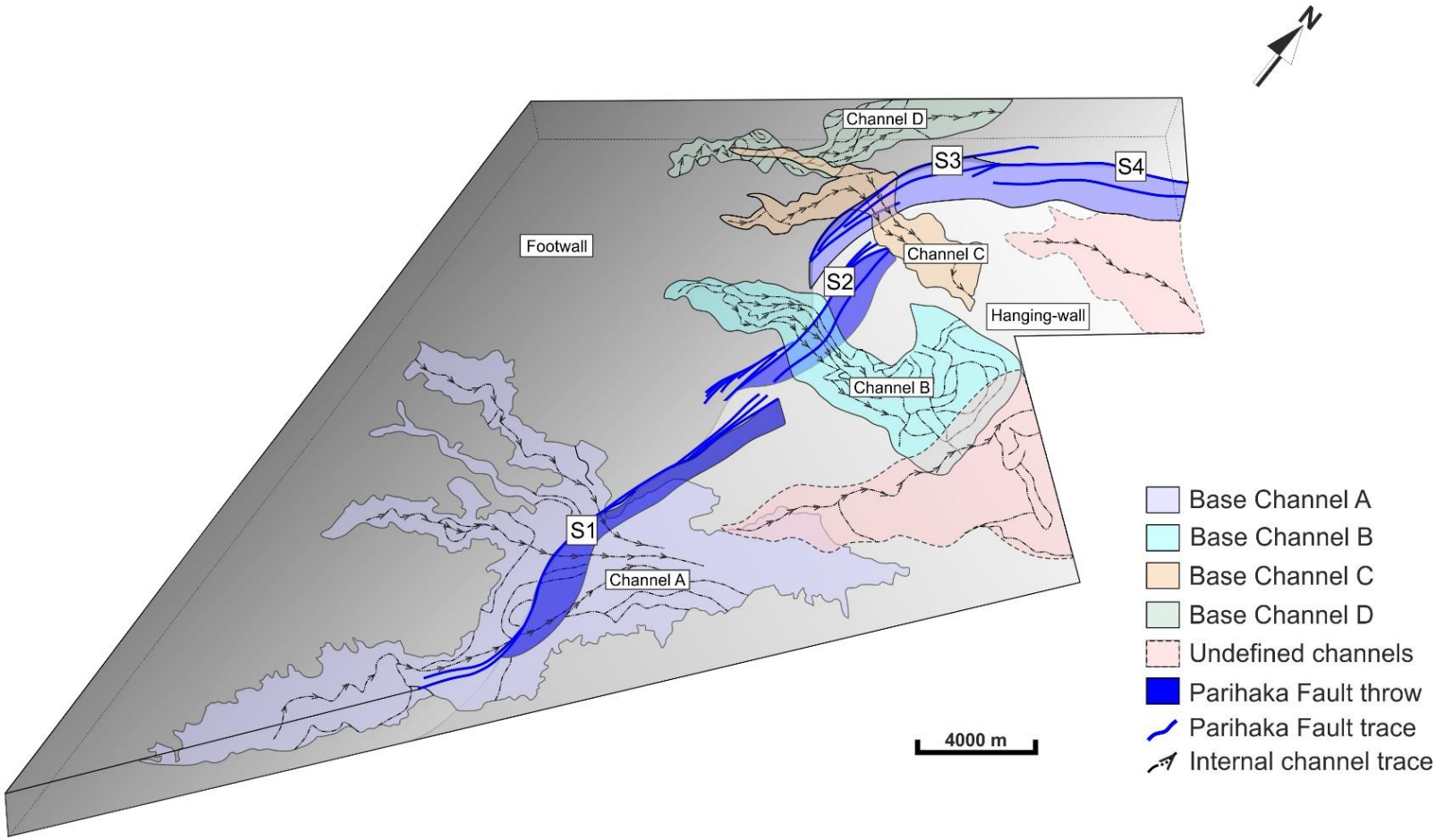

Figure 6-17: Block diagram summarising the channel distribution the study area indicating the three types of drainage related to the Parihaka Fault trace. In the southern part of the study area, Channel A is an example of oblique drainage, while Channels B and C in the central parts of the study area are examples of transverse drainage associated with a greater displacement of Segments S2 and S3 of the Parihaka Fault. Channel D is a channel that changed its course due to the uplift of the footwall block, running parallel to the trace of Segment S3.

observe this channel overlapping Channel B. The geometry of Channel C stresses the active growth of S3 of the Parihaka Fault during its deposition (Figure 6-12).

Oblique-migrating channels are responsible for both lateral migration and vertical stacking of the channels in the study area, as observed on seismic data. The interpretation of Channels B and C along the S2 and S3, respectively, reinforce the implications of the interplay between the structural framework and the channel deflection in the study area, as characteristic of a half-graben system with oblique drainage common in areas of active extensional tectonics. An example that corroborates this postulate is found in the Barents Sea, where half-grabens have controlled the distribution of sand-prone turbidites in the Dønna Terrace (Fugelli and Olsen, 2007).

Channel D is an example of a submarine channel that occurs entirely in the footwall block of the Parihaka Fault, with an initial SW-NE direction (Figure 6-13). It would be expected this channel to follow a pathway oblique to transverse to the fault trace, as it occurs for channels A and B, active during the same period. However, in the proximity of S3, the channel course deflects and becomes parallel to the fault trace. The activation of S3 and S4 in the northern part of the study area resulted in the uplift of the footwall block close to the fault scarp and resulted in the diversion of the channel to an area more easily eroded, and prone to its incision.

Local subsidence along the Parihaka Fault is observed in the time-structural map for horizon BC, where it is possible to observe two depocentres developed in the hanging-wall block towards the NE (Figure 6-3). The time-structural map for the horizon TC (Figure 6-4) indicates a reduction in the depth difference between the

footwall and the hanging-wall blocks. The extent of the accommodation space in Depocentres 1 and 2 and the large volume of sediment accumulation in the hanging-wall block indicates that the Parihaka Fault evolution controlled the basin configuration. The isolation of the footwall block and the growth of strata on the hanging-wall block, observed especially along the Early Pliocene to Recent S3 and S4, are common characteristics observed in passive margin systems (Anderson et al., 2000; Eliet and Gawthorpe, 1995; Gawthorpe et al., 1994; Gawthorpe and Leeder, 2000; Henstra et al., 2016). A well-illustrated example of this concept occurs in the Lower Congo Basin, where the growth of the sediments on the hanging wall is associated with the creation of depocentres filled with turbidite deposits during fault growth (Anderson et al., 2000).

The channel sinuosity map (Figure 6-14) indicates that the closer the channels from Channels A and B are to segments S1 and S2, the lesser is the sinuosity. Channel C is predominantly sinuous close to segments S3 and S4. Channel sinuosity data provides evidence of the footwall titling, also observed in other half-graben systems such as in the Lower Congo Basin (Anderson et al., 2000). On the hanging-wall, channels vary from sinuous to meandering and show a complex geometry, with vertical stacking patterns emulate the evolution model for submarine channel systems of Gee and Gawthorpe (2006). This occurs due to the levelling out of the hanging-wall slope as the sequence thickens, a concept related to the infilling of half-graben structures (Gawthorpe and Leeder, 2000). These growth geometry also support a coherent fault growth model for the reactivation of S1 and S2 and activation of S3 and S4, as proposed by Giba et al. (2012).

6.7.2. Influence of relay ramps on accommodation space for sediments

Displacement between individual fault segments is often increased by the formation of intrabasin transfer zones or relay ramps, especially when fault geometry follows an en-echelon stepping pattern (Leeder and Gawthorpe, 1987). Intrabasin relay ramps may strongly influence sedimentation patterns on a local scale, and may act as pathways for turbidite currents, especially in transverse drainage facies models (Anderson et al., 2000; Athmer et al., 2010; Fugelli and Olsen, 2007; Gawthorpe and Hurst, 1993; Rotevatn et al., 2007; Young et al., 2001). A characteristic elevation decrease towards the ramp is normally associated with intra-basin transfer zones (Gawthorpe and Hurst, 1993; Paul and Mitra, 2013). The morphology of individual transfer zones, however, is poorly constrained in the subsurface, as it depends on the grid spacing and the orientation of the seismic lines (Gawthorpe and Hurst, 1993; Gibbs, 1989).

Two of the three transfer zones occurring within the Parihaka Fault were analysed in this work. The transfer zone developed between S2 and S3 of the Parihaka Fault is fully breached and could act as a conduit for sediment onto the hanging wall. It would be expected Channel C to follow the relay ramp observed between S2 and S3 in the variance slices. However, this channel flows transversally to S3 instead of flowing towards the relay ramp, which resulted in a gentler pathway to sediments flowing towards the hanging-wall block. The geometry of the relay ramps in the study is consistent with the transverse drainage facies models of Leeder and Gawthorpe (1987). However, the transverse nature of the channels towards the fault segments, the absence of interpreted

submarine channels on the seismic profiles, and results of the channel density map do not indicate a great concentration of channels around the transfer zones to support this model.

A small-scale rotated transfer zone located in the north of the study area between S3 and S4 can be identified as an unbreached relay ramp. The channel sinuosity pattern in the northern part of the study area is different when compared to the central and southern parts of the seismic cube (Figure 6-14). It is possible to attribute this character to the fact that the northern section of the fault system underwent large displacement due to the sub-optimal extension angle recorded in this area. The high displacement in the northern part of the study area led to the repeated rotation of beds in the relay ramp and significant hanging-wall deformation (Giba, 2012), which may account for the lower gradient slope and offset in this zone. The submarine channels surrounding the ramp do not show a clear convergence of the footwall drainage flowing through the relay ramp, preferentially feeding into the hanging-wall sub-basin.

6.7.3. Channel-deposit thickness and implication for petroleum reservoirs

While significant subsidence occurred in the Taranaki Basin during Cretaceous-Eocene extension, this study has focused on the syn-rift deposition took place during the Pliocene when submarine channel systems were developed. The thickness map between horizons BC and TC (Figure 6-5) indicate the hanging-wall block as the primary sediment accommodation space, with the formation of two depocentres to the NE of the study area.

However, the great thickness of the hanging-wall block is not reflected in the channel density plots (Figure 6-16), where it is possible to observe that the greater channel density occurs closer to Channels B and D. Channel density was expected to be large towards the E-NE due to the presence of Channel A, as also revealed by the thickness isochron map (Figure 6-5). The presence of channels close to the relay ramps is limited based on the channel density plot (Figure 6-16) and on the isochron map (Figure 6-5). Areas with great channel density in the central part of the study area coincide only partly with the thickness values obtained for the study interval. Observations from this work indicate that the plotting of CP along well-defined channel systems such as Channels B and D lead to a better constraint of the channel density. Large channel systems such as Channel A can be left out this analysis due to the difficulty in delimiting the edges both on the seismic lines and variance time-slices.

Fault activity in the Cape Egmont Fault Zone may have an important role in the petroleum system configuration in the North Taranaki Graben. Considering that the deposition of the Giant Foresets Formation during the Pliocene was influenced by the Parihaka Fault, it is possible to conclude that vertically and laterally stacked channel deposits in Channel B comprise a potential reservoir interval. Although the hanging-wall block presents a larger thickness than the footwall and two major depocentres were formed in the NE, the accumulation of a thick sediment layer may have important implications for the development of petroleum systems at the northern Taranaki Basin (Armstrong et al., 1996; Funnell et al., 1996; Hansen and Kamp, 2004b; Webster et al., 2011). The rapid deposition of sediments of the Giant Foresets Formation can either influence the migration of hydrocarbons or comprise a potential seal unit (Stagpoole and Funnell, 2001). Rapid sediment accumulation rates during basin development may also

contribute to the increasing of thermal gradients and the hydrocarbon maturation and migration through a petroleum system (Armstrong et al., 1996; Pindell, 1995; Spencer, 1987). However, no evidence for fluid accumulations were found in the interpreted seismic volume, probably indicating that a) the influence of subsidence, fast sedimentation, and the presence of the nearby Mohakatino Volcanic Centre have resulted in an incomplete maturation of the source rocks deposited below the channel deposits, or b) the fluids generated migrated upwards along the Parihaka Fault.

6.8. Conclusions

This chapter aimed at evaluating the location of large depocentres in the hanging-wall block of the Parihaka Fault that could constitute a potential reservoir in the northern Taranaki Basin. However, no seismic evidence to corroborate the implications of the study area geometry to petroleum systems were found. The main conclusions of this chapter can be summarised as follows:

a) The reactivation of segments S1 and S2 from Early Pliocene to the Pleistocene, and the formation of segments S3 and S4 until the Recent, generated important sediment accommodation space. This is highlighted by the isolation of the footwall block in the study area and the creation of two depocentres in the hanging-wall block.
b) Sinuosity profiles on the footwall show a channel evolving from meandering to straight towards segments S1 and S2, while channels tend to predominantly

meander on the hanging-wall block. Channel sinuosity on the hanging-wall and channel's vertical stacking, combined with drainage deflection, indicate a depositional style typical of a half-graben system with a transverse through drainage.

c) Three main drainage types related to the Parihaka Fault trace were interpreted in the study area: transverse drainage, oblique drainage and parallel drainage. Channel A, located in the southern part of the study area is an example of oblique drainage system linked to a moderately active fault, while Channels B and C represent channel systems that flow initially oblique and were diverted transversally in the proximity of segments S2 and S3. Channel D is an example of a channel system that flowed parallel to the fault trace in association with footwall uplift along segments 3 and 4 of the Parihaka Fault.

d) Two relay ramps were observed between segments S2 and S3 and segments S3 and S4. Seismic profiles and variance time-slices, however, do not point to submarine channels using the relay ramp as a gentle pathway to reach the hanging-wall block. Channels B and C, developed close to the relay ramps, changed their original courses and flowed transversally in relation to the fault trace, instead of running through the relay ramps.

e) Channels systems are concentrated both on the footwall and hanging-wall blocks, with two depocentres observed in the NE close to the terminations of large submarine channels systems. The vertically (and laterally) stacked Channel D system on the footwall block may comprise an important hydrocarbon reservoir in the study area. Progradational sequences of the Giant Foresets Formation,

rapidly accumulated as vertical and lateral channel systems on the hanging-wall block, can also comprise important hydrocarbons reservoirs in the study area.

7. Discussion

7.1. Introduction and summary of major findings

A diagram summarising the main findings of Chapters 4 to 6 is presented in Figure 7-1. Whereas halokinesis is a key phenomenon controlling the configuration and evolution of the Ottar and Espírito Santo Basins, the Taranaki Basin shows no significant salt accumulations. The present chapter aims at discussing the wider implications of the results in this thesis, outlining the limitations of this research, and suggesting themes for further investigation.

7.1.1. Chapter 4

The key aims of this first results chapter were to reassess the geometry and the kinematics of the Samson Dome, investigating at the same time the importance of fault reactivation to seal-unit competence. The study area in this chapter was divided into three zones relative to their proximity to the Samson Dome, and predominant faults (Figure 4-5). Displacement analyses for observed faults show that reactivation by dip-linkage occurred during the Late Cretaceous (Figure 4-10). Slip tendency (Figure 4-11) and leakage factor (Figure 4-12) data suggest that faults in the Samson Dome area act as competent sealing structures to fluids accumulated at depth. As a result, the Samson Dome is now considered to form a smaller seepage structure than proposed in recent publications. The findings from Chapter 4 show the evolution of the Samson Dome as occurring in three stages, all associated with the doming and collapse of a broad salt structure (Figures 4-13 to 4-16).

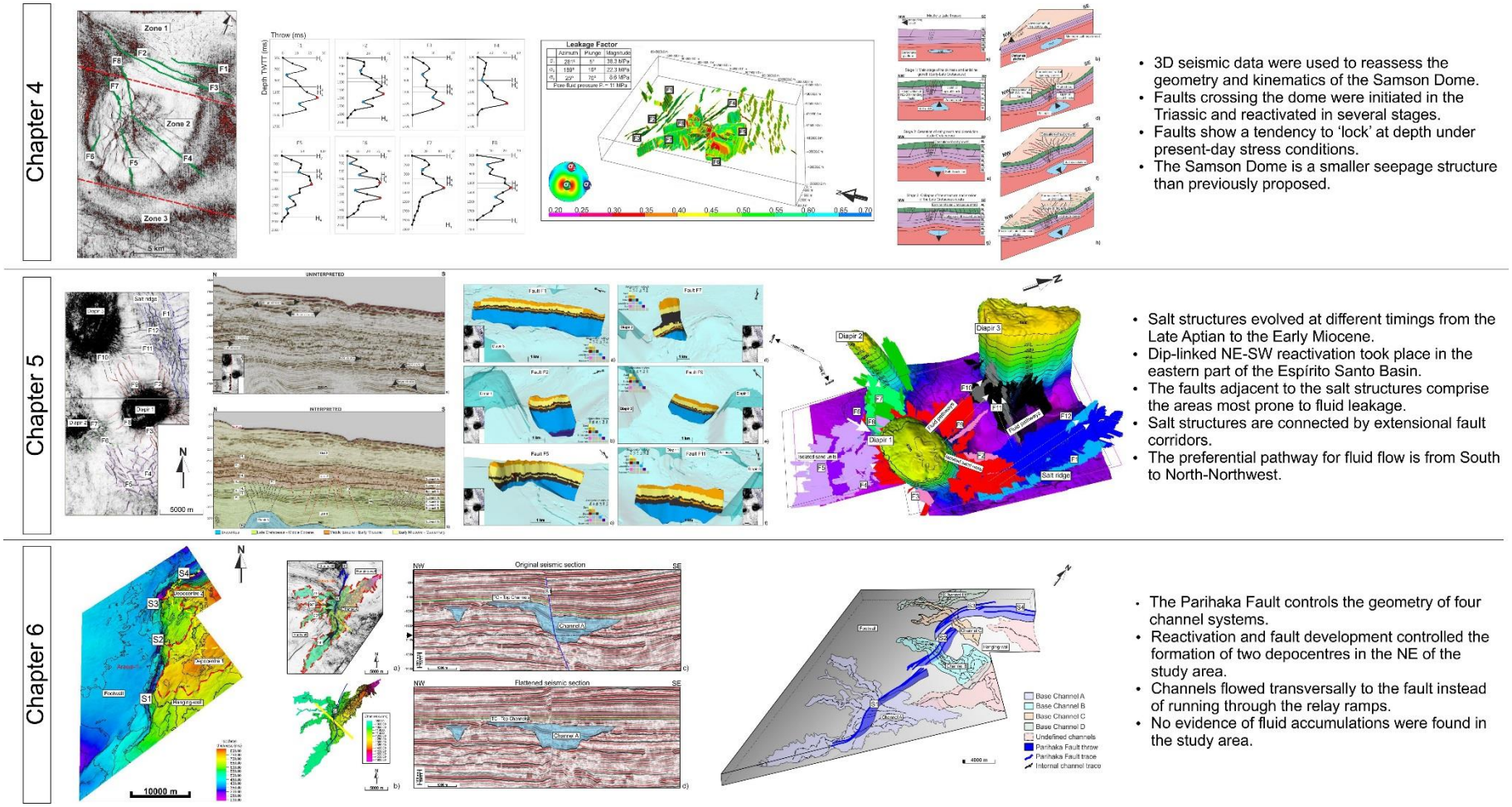

Figure 7-1: Summary of the main findings obtained from the three core chapters of the thesis.

7.1.2. Chapter 5

The main aim of this chapter was to assess the geometry and evolution of faults developed radially, and on the crests of four salt structures in SE Brazil. Interpreted faults were divided in five families taking into account their position relative to three diapirs and one salt ridge (Figure 5-4). Detailed fault analyses revealed that salt structures evolved at different times from Late Aptian to Early Eocene. Displacement analyses indicate preferential NE-SW dip-linked reactivation took place in the eastern part of the Espírito Santo Basin (Figure 5-13), contrasting with analyses previously undertaken in the western part of this basin - where vertical (upwards) propagation is the main reactivation mode. Putative fluid-flow paths were investigated by compiling juxtaposition diagrams (Figures 5-15 to 5-20), and by analysing slip tendency (Figure 5-21) and leakage factors (Figure 5-22) for discrete faults. The data indicate that the areas most prone to fluid leakage occur adjacently to salt structures. The conceptual evolutionary model proposed in this chapter postulates that salt structures are linked by fault corridors providing preferential paths for fluid flow from the South to the North-Northwest (Figure 5-23).

7.1.3. Chapter 6

This case study is based on 3D seismic data from the Taranaki Basin, offshore New Zealand, where back-arc extension resulted in the reactivation of a complex fault structure (Figures 2-10 and 6-1). The main aim of this chapter was to investigate the control(s) of the reactivation and generation of new fault segments on the evolution and geometry of

channel systems. Fault activity from the Early Pliocene to the Recent resulted in the formation of two depocentres in the NE portion of the study area (Figure 6-3). Four channel systems were investigated in the Northern Graben, and three main drainage types were found according to their proximity to fault segments in the larger Parihaka Fault (Figures 6-10 to 6-13). Channel sinuosity also varied in footwall and hanging-wall blocks with distance to fault segments, and relative to the timing(s) of reactivation of these latter (Figure 6-14). The occurrence of relay ramps between discrete fault segments was thought as providing preferential paths to the channel systems. However, detailed analyses of channel density (Figure 6-16) indicated that channels would instead flow transversally from the footwall to the hanging-wall blocks (Figure 6-17). Investigation of the seismic lines revealed no evidence of fluid accumulation in the study area. However, the thick sequences of Giant Foresets Formation could have great importance as reservoirs succession elsewhere in Parihaka area.

7.2. Styles of compartmentalisation in the three study areas

Sedimentary and structural elements observed on seismic data include salt structures (Chapters 4 and 5), stratified turbidites (Chapters 5 and 6), submarine channels (Chapter 6) and faults, the latter of which comprise the common element to the three study areas. The types and degrees of interactions between these elements are expected to vary depending on multiple factors, such as: a) the seismic-stratigraphic units in which elements are included, and b) the scale of structures interpreted in each seismic dataset.

Different architectures of reservoir and seal intervals are also observed at different stratigraphic levels, and show complex interactions with different fault arrays and adjacent salt structures.

In Chapter 4, structural compartmentalisation predominates in Unit 2 (Triassic), in which leakage factors along crestal faults are smaller than for faults offsetting Late Jurassic (Unit 3), Late Cretaceous (Unit 4), or Pleistocene (Unit 5) strata. Leakage factors are also greater for faults that are distant from this salt structure. As shown in *Section 4.7.3.*, relative increases in the seal competence of faults adjacent to the Samson Dome are associated with later uplift and collapse of this structure. The local collapse of the Samson Dome caused the reactivation of faults developed on its crest. In addition, Unit 2 is chiefly composed of shales with minor sandstone intervals, a character increasing the sealing potential of faults crossing it. This contrasts with the overlying units (Jurassic to Pleistocene), which contain more permeable strata (Table 4-1).

A similar approach to investigating structural compartmentalisation relative to halokinesis-induced fault activity was followed in Chapter 5. The results, for SE Brazil, however, were different from those from the Samson Dome. The majority of faults in Chapters 4 and 5 showed evidence for reactivation, as demonstrated in the T-z plots for faults around Samson Dome (Figure 4-10) and from the Espírito Santo Basin (Figure 5-13). Fault reactivation is generally associated with an increase in hydrocarbon entrapment in subsurface units (Wiprut and Zoback, 2000). Hence, it was expected that reactivated faults in both the Samson Dome and the Espírito Santo regions would comprise baffles to fluid leakage. Whereas this is true for reactivated crestal faults on the Samson Dome, a rather different result was found in the Espírito Santo Basin when modelling leakage

factors (Figures 4-12 and 5-22). Throw-depth analyses for the Espírito Santo Basin suggest that the majority of the faults were truncated at their upper tips by a regional Mid-Eocene unconformity, which is also the base of thick mass transport deposits (MTDs) in the study area. Previous work on the Espírito Santo Basin (Gamboa et al., 2010; Gamboa, 2011; Omosanya, 2014; Omosanya and Alves, 2013) discussed the importance of MTDs to the compartmentalisation of reservoir units. Omosanya (2014) postulates that homogeneous MTDs with mud-prone lithologies comprise a competent seal to upward migrating fluid. However, the fault analyses performed in this thesis indicate that non-sealing faults occurring in the proximity of salt domes can comprise a preferential path for fluid leakage.

In Chapter 6, the analysis of channel systems bounded by two distinct horizons (BC and TC) revealed two predominant architectures. On the footwall block of the Parihaka Fault, a submarine channel system parallel to this structure incises prograding turbidite units (Figure 6-6). In contrast, hanging-wall blocks are characterised by the development of two depocentres, which occurred together with the deposition of laterally and vertically stacked submarine channels. Potential reservoir units are stratigraphically compartmentalised, and the distribution of submarine channel systems in the Northern Graben of the Taranaki Basin was controlled by the presence of active faults.

7.3. Fault seal behaviour

It is a fact that this thesis presents valid case-studies highlighting the importance of fault reactivation to reservoir compartmentalisation and fluid flow. However, in this same

thesis the analysis of the seal properties of faults can be limited by the lack of a model explaining why some faults comprise conduits to fluids, whereas other faults constitute barriers or baffles to fluid flow. In other words, more detail should be sought about the heterogeneous nature of strata offset by faults, the geometry of these same faults, and the composition of the fault gouge. The 3D seismic interpretation of stratigraphic units and faults provides a large-scale picture of reservoir units, whereas the fault modelling through the use of the stress data (Chapters 4 and 5) or juxtaposition diagrams (Chapter 5) offers insights into the seal potential of relatively smaller faults. While it has not been an objective of this thesis to discuss all the possible approaches to modelling faults' sealing potential, when assessing the impacts of faults on fluid flow it is necessary to consider three fundamental elements: a) complex juxtapositions of different units (horizons) along faults, b) the occurrence of a fault gouge with different lithologies and structural complexity, and c) the existence of a surrounding damage zone that is lithology-dependent (Allan, 1989; Aydin, 2000; Caine et al., 1996; Scholz and Anders, 1994).

7.3.1. Fault juxtaposition

The juxtaposition of two reservoir units is recognised as one of the main reasons hydrocarbon migration is favoured. In contrast, the juxtaposition of permeable units against non-permeable strata will hinder or impede (baffle) the movement of fluids (Allan, 1989; Fisher and Knipe, 2001; Knipe, 1997). Juxtaposition diagrams are based on the mapping of fault throws across hanging-wall and footwall cut-offs (Allan, 1989), and were used in this thesis as a primary method to assess their seal competence in the Espírito

Santo Basin. However, Allan diagrams only take into account the lithologies and fault throws in two dimensions. The common ways of representing strata juxtaposition do not consider faults as structures with variable thickness, distinct properties and displacements along their total length (Manzocchi et al., 2010).

Fault zone complexity limits the analysis of fault seal behaviour and associated fluid flow paths. In fact, important parameters such as the amount and distribution of smeared shales across a fault, factors that control the porosity and permeability of the fault zones (Manzocchi et al., 2010), can be overlooked due to lack of borehole data (e.g., Caine et al., 1996; Fisher and Knipe, 2001; Koledoye et al., 2003). Apart from variable lithologies and throws, other controls on the transmissibility of fluid in fault zones include their 3D geometry, the conditions that led to their formation, the local stress state, the arrangement of structures within the fault zone, interactions between the fluids and the rock, and how these factors vary in space and time (Caine et al., 1996).

7.3.2. Competence contrasts between sediment layers in the fault zone

Another difficulty when assessing the sealing potential of a fault using seismic data relates to its resolution, which can image a complex structure comprising multiple segments as a single large fault - implying that juxtaposition occurs homogeneously along the fault length (Faulkner et al., 2010). However, in nature it is paramount to consider that the formation and linkage of fault segments are intrinsically associated with the

mechanical properties of fault rocks and the stress states imposed by local structures and faulted basement rocks (Kettermann et al., 2017; Schmatz et al., 2010). Competence contrasts between sediment layers are key controls on deformation, as demonstrated by sandbox analogue models using a ductile representative of clay and dry sand overlying a faulted basement (Kettermann et al., 2017; Schmatz et al., 2010; van der Zee et al., 2003). The reactivation of a fault in a succession comprising dry sand will reflect the brittle behaviour of sands and sandstones (Figure 7-2). The presence of sand and clays results in the formation of multiple small-scale shear zones, whereas deformation in layers where clays predominate can progressively affect the geometry of the fault zone through the rotation of beds (Van der Zee et al., 2003).

In this thesis, a representative example of deformation in ductile layers is found at the Parihaka Fault (Chapter 6), around which was possible to identify the rotation of ductile beds and the development of a fault gouge that probably contains a mix of sandy and clayey strata (Figure 7-3). By comparing New Zealand with the analogues in Van der Zee et al. (2003), it is possible to infer a significant emplacement of clay in segments of the Parihaka Fault, and the development of clayey fault gouges (Figure 7-4). A lenticular structure with a higher degree of deformation than surrounding rocks is also observed in the Parihaka Fault (Figure 7-4). In the Barents Sea (Figures 4-6 to 4-8), and also in SE Brazil (Figures 5-6 to 5-10), the geometry of the interpreted fault zones is less suggestive of the occurrence of thick fault gouges; faults seem to be discretely formed and their geometries ressemble those in Figure 7-2a.

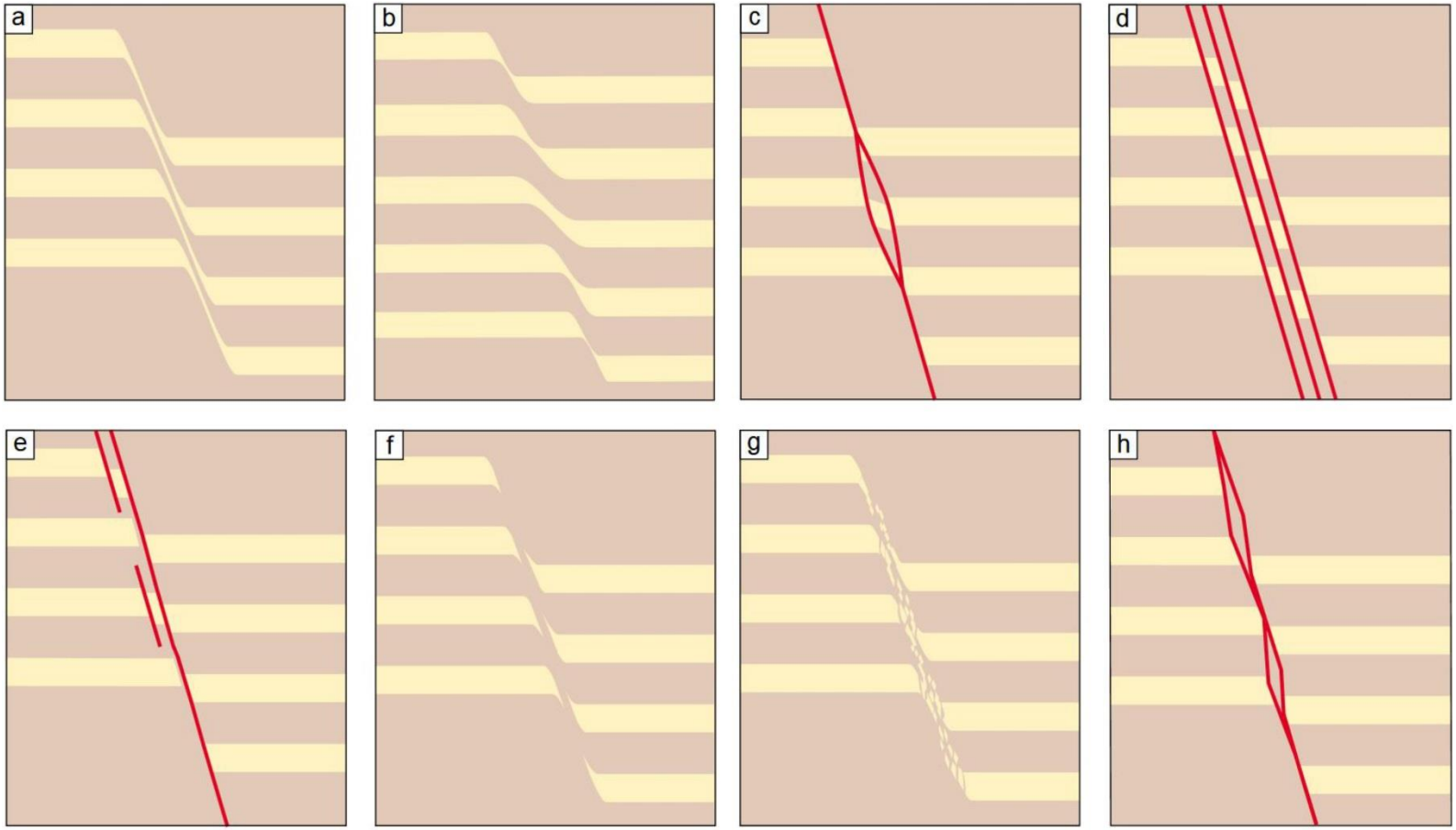

Figure 7-2: Main structural elements found in fault zones offsetting sedimentary layers. a) Heterogeneous simple shear deformation. b) Lateral transition into a localised deformation zone. c) Development of a lenticular structure with a high degree of deformation. d) Fault gouge showing the rotation of individual layers. e) Fault gouge with lateral injection of a brittle layer. f) Fault gouge formed by the smearing of a ductile layer. g) Fault gouge formed by the disruption of a brittle layer, followed by the mixing of brittle- and ductile-layer fragments. h) Development of open fractures in a brittle layer. Modified from Van der Zee et al. (2003).

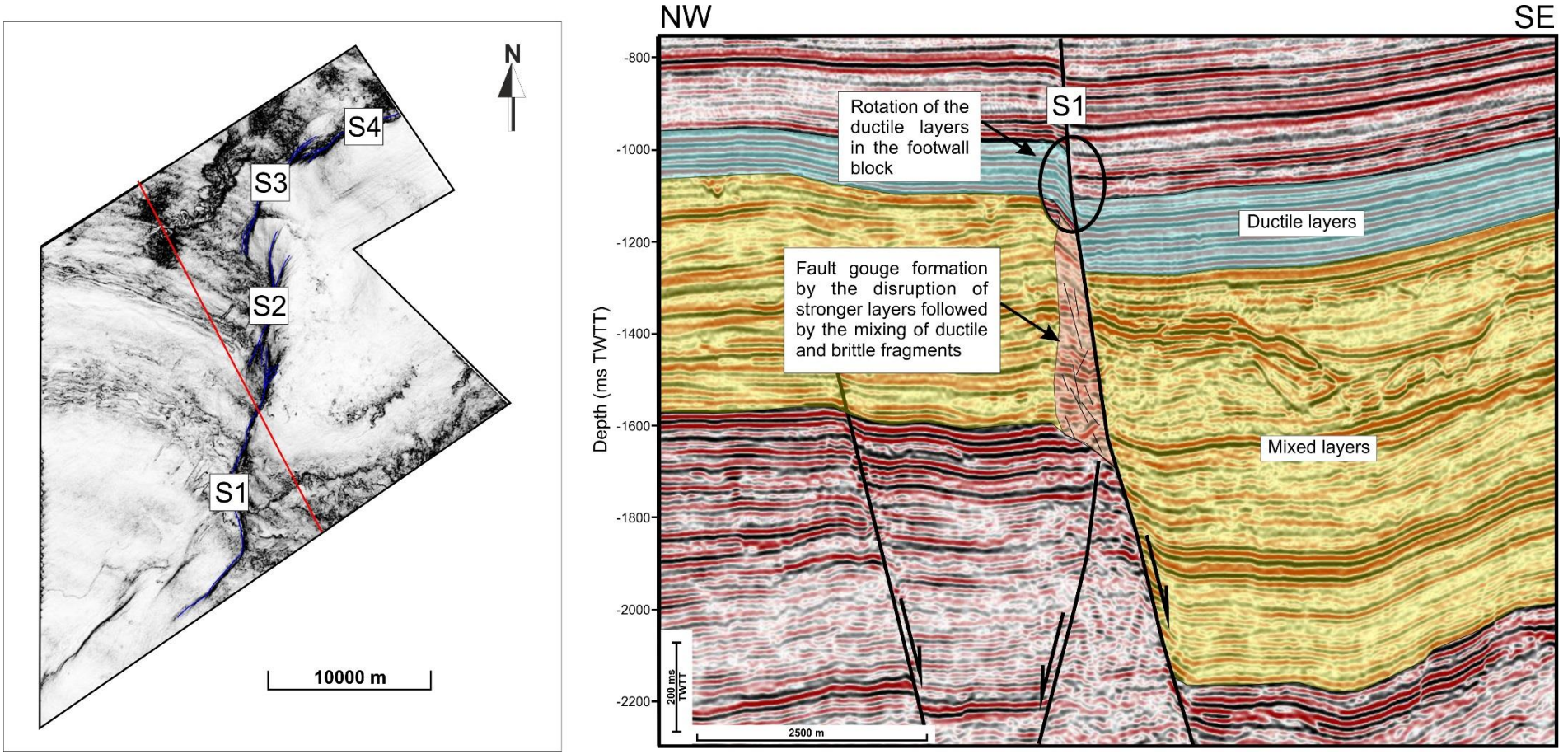

Figure 7-3: Seismic section from the Parihaka survey illustrating the main structural elements observed in the fault zone developed along segment S1, Parihaka Fault. While parts of this section are dominated by ductile layers one can also observe rotations of these same layers. In the area dominated by mixed clay and sand layers a fault gouge develops due to greater disruption of the sandy layers.

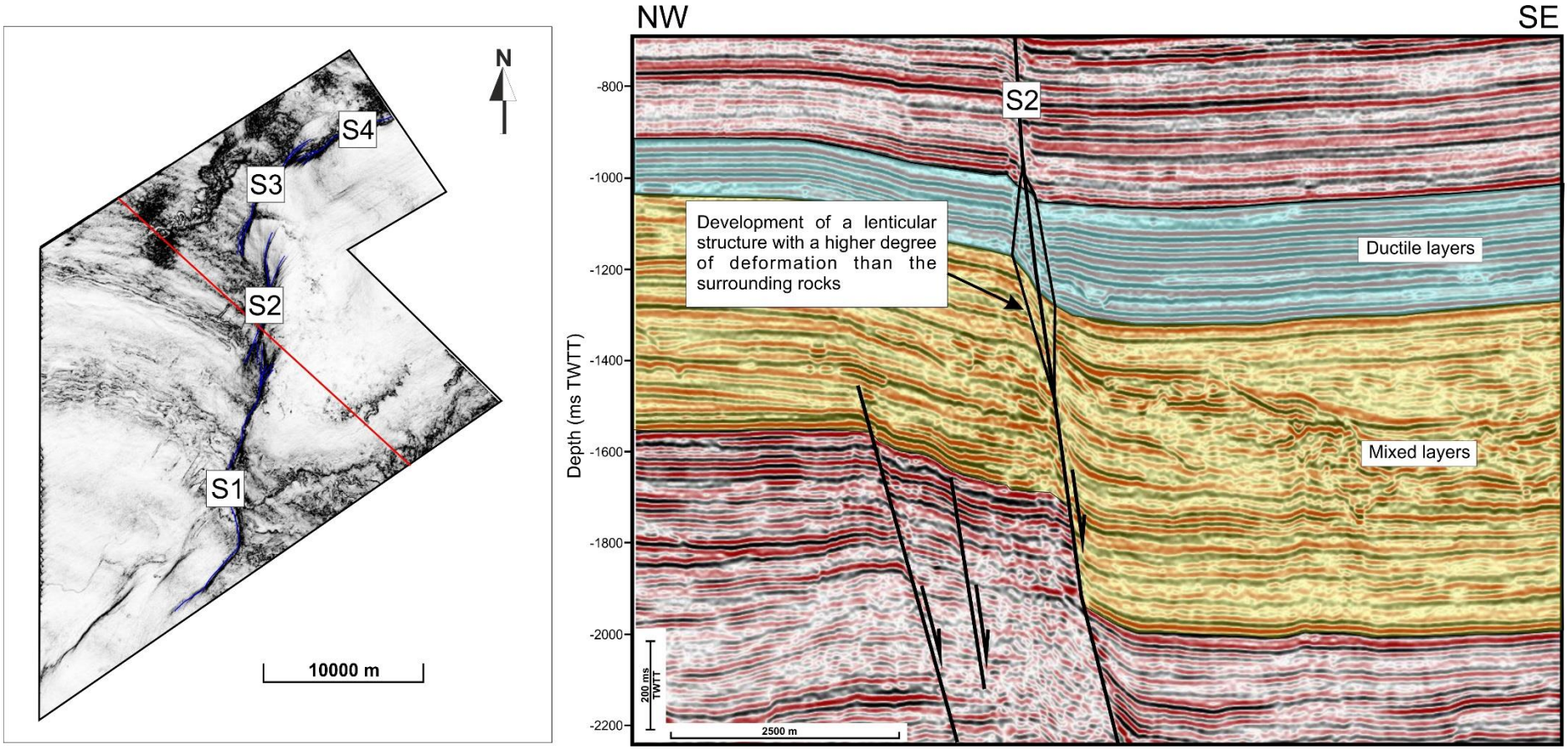

Figure 7-4: Seismic section from the Parihaka survey illustrating the occurrence of a lenticular structure in the fault zone developed along segment S2, Parihaka Fault. This example is similar to the analogue model from Van der Zee et al. (2003) in Figure 7-2c.

7.3.3. Shale gouge ratio as a proxy for compartmentalisation

When the fault gouge is considered in the analysis of fault compartmentalisation, it is necessary to take into account the resulting differences in permeability of the materials forming this same gouge. Heterogeneities in the fault zone can generate points were fluid leakage is enabled, resulting in the establishment of preferential pathways for hydrocarbon leakage (Faulkner et al., 2010; Manzocchi et al., 2010). The permeability of the fault gouge can be estimated using the Shale Gouge Ratio (SGR = [Σ(shale bed thickness)/ throw]* 100%), an equation proposed by Yielding et al. (1997) that quantifies the clay content in percentage of a fault gouge and is used to assess the seal potential of faults. The threshold in SGR required for a fault to seal comprises values above 20% (Yielding, 2002). Calculations of the Shale Gouge Ratio are based on the quantification of fault throws and clay content of faulted successions.

A well-documented example of the use of Shale Gouge Ratios to investigate the leakage potential of a large fault is provided by Reilly et al. (2016). In this paper, the authors performed Shale Gouge Ratio calculations for the Cape Egmont Fault (CEF), Southern Taranaki Basin, using Vshale curves obtained from Gamma Ray logs for well Maui-2, located on the footwall of the CEF. In addition, the authors completed backstripping analyses to constrain fluid-migration history in the Maui Field. The study area in Reilly et al. (2016) is located to the south of the region investigated in Chapter 6 (Figure 6-7a).

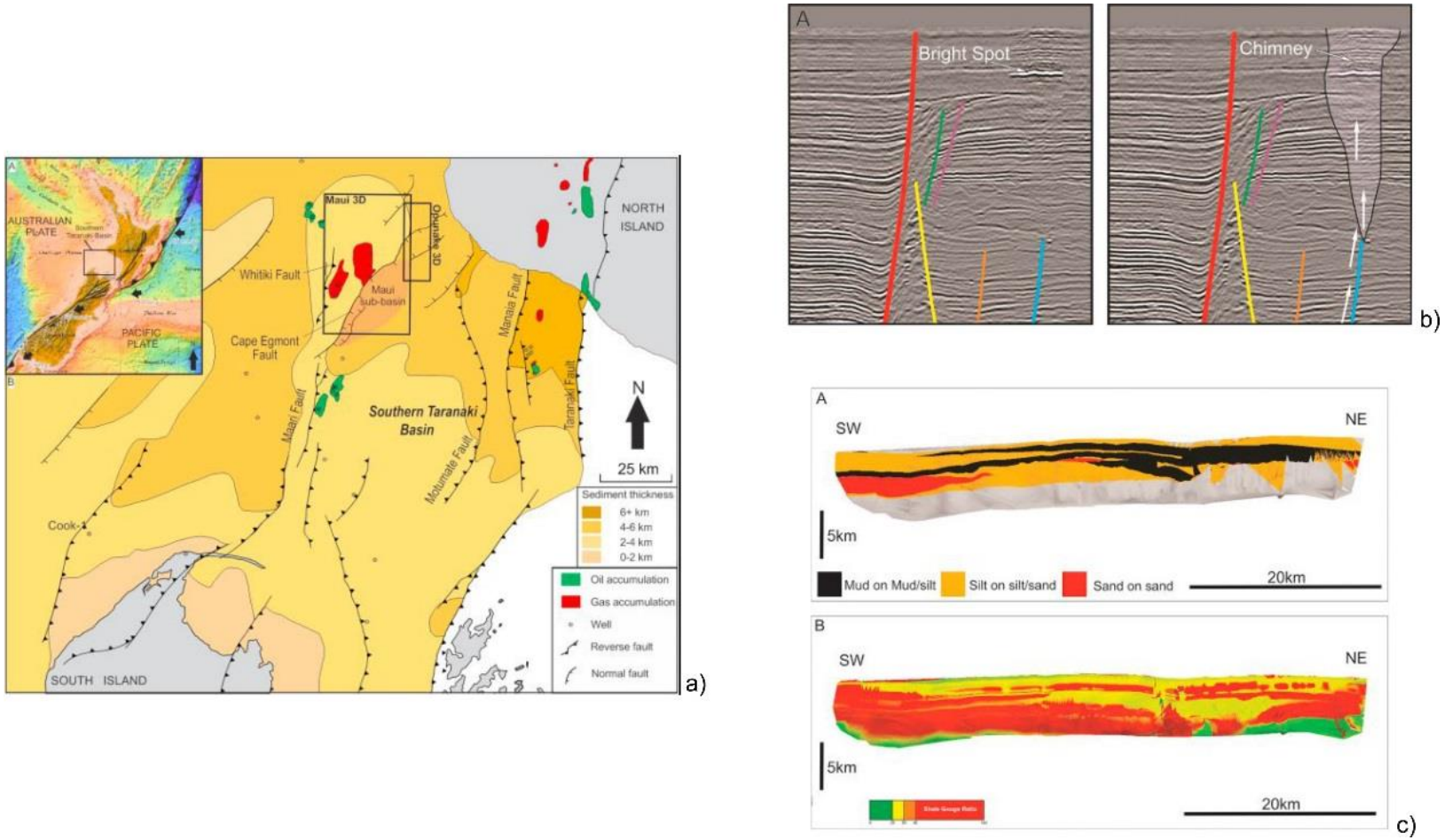

Figure 7-5: Shale Gouge Ratio analysis in the Cape Egmont Fault in the Maui Field, Southern Taranaki Basin. a) Location map of the Maui Field. b) Evidence for fluid flow features in the seismic volume of the Maui Field, adjacently to the Cape Egmont Fault. c) Juxtaposition and Shale Gouge Ratio plotted for the Cape Egmont Fault. The grey areas in the Shale Gouge Ratio plot indicate the zones along the fault most prone to fluid leakage. Modified from Reilly et al. 2016

Contrasts between the southern and northern parts of the Taranaki Basin are clear in tectonic and stratigraphic terms. During the Miocene and Plio-Pleistocene, the Southern Taranaki Basin was subjected to compressional stresses, while extension was taking place in the Northern Taranaki Basin (Giba et al. 2010). The thick and rapidly deposited shales in the Giant Foresets Formation are not found in the Maui Field which, instead, comprises stacked sand reservoirs interbedded with seal intervals (King and Thrasher, 1996). In Chapter 6, no evidence for fluid flow was found in the Parihaka survey, but the study of Reilly et al. (2016) found gas chimneys and bright spots close to the Cape Egmont Fault (Figure 7-5b). Results from this work show that fluid migrated through the CEF during the Pliocene (Figure7-5c), and suggest that the Maui Field hosted larger amounts of hydrocarbon in the recent past (Reilly et al., 2016).

Shale Gouge analyses were not performed in the case studies conducted in this thesis due to the absence of well data constraining lithology across the studied fault systems. However, the thesis nonetheless recognises the importance of Shale Gouge data in the characterisation of the seal competence of faults crossing potential reservoirs, when used together with juxtaposition analyses as presented in Allan (1989).

7.3.4. Deformation bands

Strain localisation in porous rocks results in the generation of deformation bands, which comprise small-scale low-displacement deformation zones (Caine et al., 1996; Knipe et al., 1998). The development of deformation bands is controlled by multiple factors such as confining pressures, tectonic environment, stress states, pore fluid pressure

and the properties of the host rock, such as mineralogy, grain size and shape, and its degree of lithification (Fossen et al., 2007; Solum et al., 2010). For instance, deformation bands consisting of shale smears are associated with a decrease in porosity and permeability relative to the host rock, and tend to form barriers or baffles to fluid-flow (Antonellini et al., 1994; Aydin, 2000; Rotevatn et al., 2013). However, when fault gouge composition is heterogeneous, and the host rock shows marked variations in lithology, a complex 3D volume of rock may thus be formed - composed of conjugate deformation bands that will hinder fluid flow, and porous strata that facilitate it (Fossen et al., 2007). Fault permeability is also dependent on the degree (and styles) of deformation along its surrounding damage zone(s) (Knipe et al., 1998). Damage zones surround the fault core and may enhance permeability relative to the fault core and the non-deformed host rock (Caine et al., 1996).

Deformation bands are recognised in different geological settings, with some key examples of deformation bands in reservoir units being given by Cerveny et al. (2004); Fossen et al. (2017); Gibson (1994); Soliva et al. (2016) and Solum et al. (2010). In these studies, the authors integrate the analyses of outcrop and well cores from hydrocarbon fields to model the spatial distribution of networks of deformation bands, and later estimate the bulk permeability of reservoir units. Solum et al. (2010) investigated the occurrence of deformation bands in the Navajo Sandstone, Utah (USA). Shear bands, noncataclastic shear bands and compaction bands, were found in outcrops of the same host rock for both extensional (Buckskin Gulch) and compressive regimes (Big Hole fault) (Figure 7-6). Compressive stress states applied to the host rock resulted in the creation of a dense network of deformation bands. Consequently, reservoirs were more

prone to be compartmentalised in a reverse-faulting settings than in normal-faulting settings.

Fossen et al. (2017) provide a review of previously published works focusing on the geometry and petrophysical properties of deformation bands different geological settings at outcrop scales. In extensional regimes, deformation bands are clustered at different maturity stages and influence the location and orientation of faults (Figure 7-7a and b), whereas in compressive regimes deformation bands are distributed around the fault cores (Figure 7-7c to e). Whereas deformation bands have a significant role in creating anisotropies in the reservoir, the importance of deformation bands as local reservoir seals is minor. Nevertheless, different factors must be taken into account during the reservoir evaluation such as the type and frequency of deformation bands, the amount of cataclasis experienced by them, and their lateral and vertical continuities (Fossen et al., 2017).

7.4. Pore-fluid pressure and overpressured reservoirs

The analysis of the sealing properties of stratigraphic and structural compartments also benefits from predicting excess pore-fluid pressure, or overpressure (Gao and Flemings, 2017; Mann and Mackenzie, 1990; Mourgues et al., 2011; Webster et al., 2011). Overpressure is defined as the difference between pore pressure and the hydrostatic pressure, and occurs when the reservoir is isolated by low permeability compartments (Mann and Mackenzie, 1990; Mourgues et al., 2011). Overpressures can be generated in a sedimentary basin by different mechanisms such as undercompaction

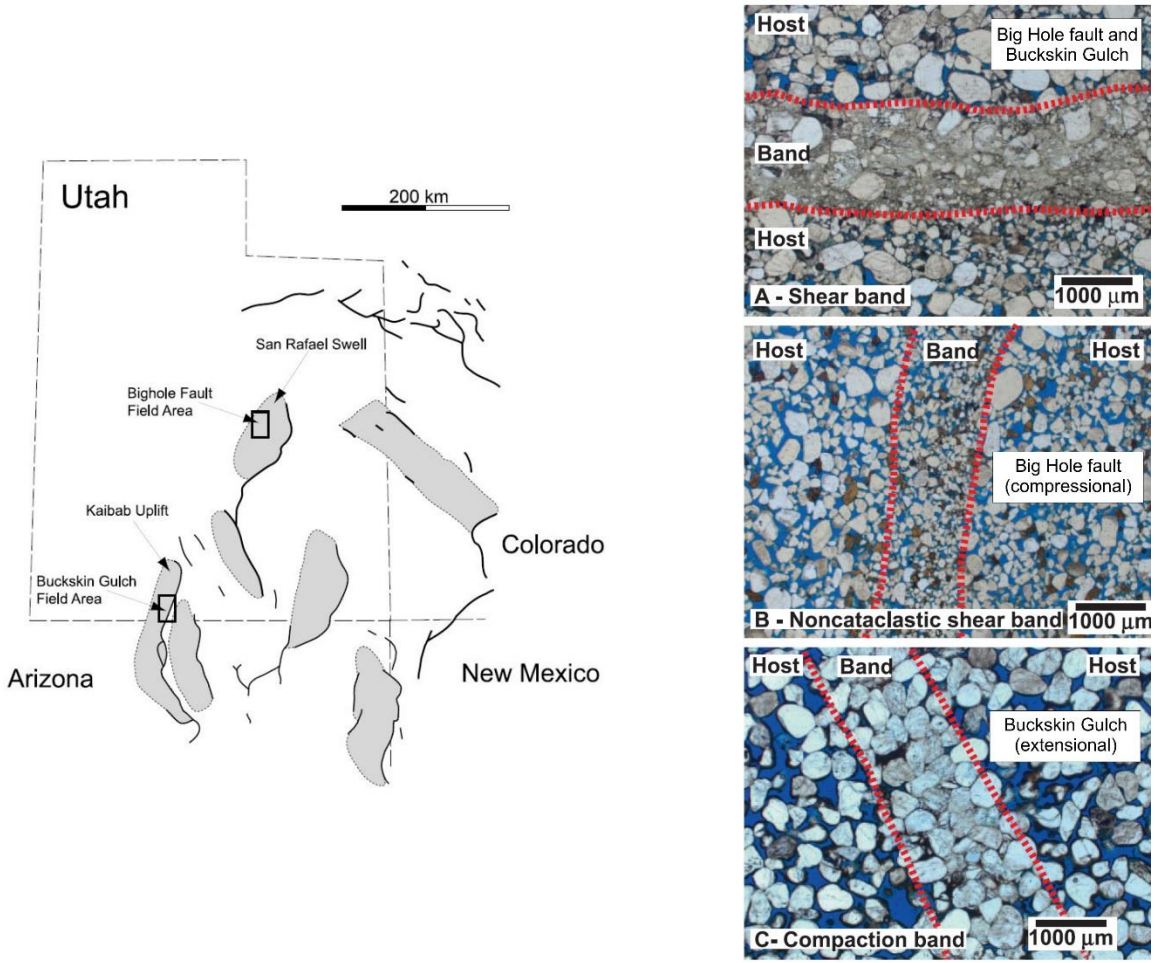

Figure 7-6: Photomicrographs of thin sections representative of the Big Hole fault (compressional) and the Buckskin Gulch (extensional) showing: a) shear bands occurring in both settings; b) noncataclastic shear bands occurring in a reverse-faulting setting and c) compaction bands occurring in a normal-faulting setting. Modified from Solum et al. (2010).

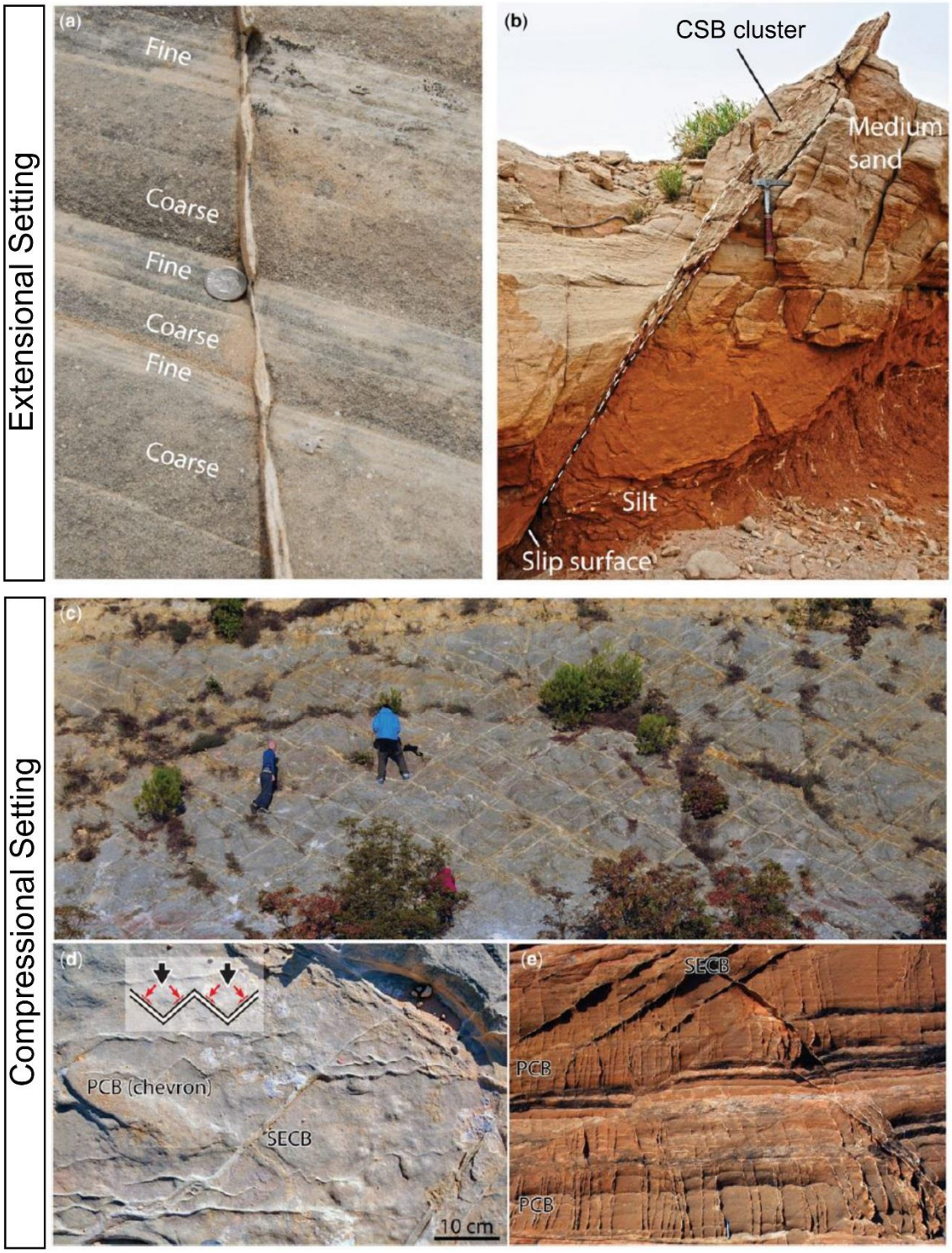

Figure 7-7: Outcrop-scale examples of deformation bands. a) Compactional shear band (CSB) with thickness varying according to the grain size. b) Cluster of CSB located adjacent to the medium sand body. c) Network of CSB occurring distributed in a compressional setting. d) Chevron-type pure compaction bands (PCB) occurring together with shear-enhanced compaction bands (SECB). e) Vertical PCB in highly porous sandstone layers and conjugate set of SECB finer layers. Figures a and b are representative of extensional settings and figures c to e represent a compressional setting. Modified from Fossen et al. (2017).

resulting from the fast transport (and loading) of sediment, tectonic stresses concentrated in specific intervals, hydrocarbon generation, and diagenesis (Mann and Mackenzie, 1990; Osborne and Swarbrick, 1997). An abnormal fluid pressure in a sedimentary sequence affects the porosity of subsurface rocks and can result in the formation of geological features such as mud volcanoes, mud diapirs, pockmarks, pipes, polygonal faults and hydraulic fractures (Berndt, 2005; Cartwright, 2007; Graue, 2000; Moss and Cartwright, 2010; Rovere et al., 2014) (Figure 7-6). Some of these structures can be recognised on seismic data and can comprise an indicator for the fluid-accumulation potential of a basins. In parallel, they can also indicate breaching of reservoir compartments with subsequent leakage of fluids (Løseth et al., 2009).

Stratigraphic units in the Taranaki Basin are predominantly overpressured (Darby, 2002; McAlpine, 2000; Webster et al., 2011). Pressure-depth plots for wells in the Taranaki Basin, based on data obtained from drillstem test (DST), modular dynamic test (MDT) and repeat formation tests (RFT), reveal pressures above hydrostatic values (Figure 7-7; Webster et al., 2011). Overpressures have been attributed to rapid sedimentation and loading of older strata by the Miocene-Pliocene Giant Foresets Formation (Stagpoole et al., 1998; Stagpoole and Funnell, 2001; Darby, 2002; Webster et al., 2011). This latter unit, comprising mudstones and fine-grained channel deposits, is considered to be a proven seal to potential reservoir intervals in the Northern Graben of the Taranaki Basin, together with other Miocene-Pliocene mudstones from the Moki and Mt. Messenger Formations (King and Thrasher, 1996). Disequilibrium compaction can result in a significant increase in the seal competence of these units if the seal is not breached or faulted. Considering this scenario, the distribution of fluids within the studied stratigraphic intervals in the Northern Graben, Taranaki Basin, reflects the importance of

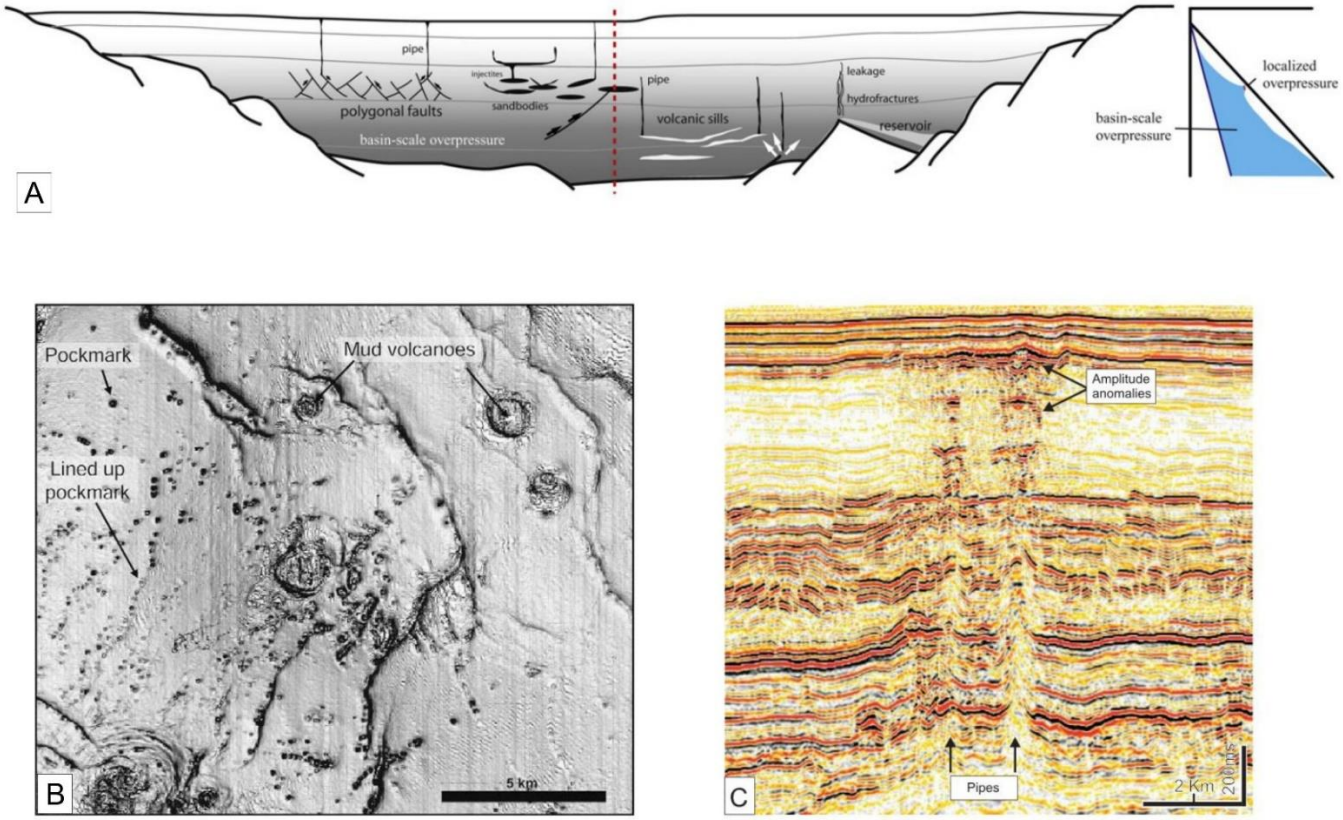

Figure 7-8: a) Geological features formed as a result of an increase in subsurface pore-fluid pressure such as pipes, polygonal faults, fractures, sand bodies and volcanic sills (from Mourgues et al., 2011). b) Dip-azimuth map of the seabed in the Nigerian continental shelf showing the location of mud volcanoes and pockmarks (from Graue, 2000 and Løseth et al., 2009). c) Seismic section offshore Norway highlighting the seismic expression of blowout pipes (from Cartwright, 2007).

faults and associated fractures in transmitting fluids to shallow reservoir units (Webster et al., 2011). The well Arawa-1, located approximately 2.5 km west of theParihaka Fault, recorded three significant dry gas peaks (Arco, 1992). The shallowest gas peak was found at the top of the Moki Formation and, considering the lack of further evidence for hydrocarbon accumulations in the interpreted seismic volume, it is plausible to infer that fluids migrated upwards along the Parihaka Fault.

In order to illustrate the role of overpressure in seal breaching, a pressure-depth profile based on well 7224/7-1, drilled at the crest of the Samson Dome, was compiled using two repeat formation tests (RFT), and compared to the lithostatic and hydrostatic pressure gradients (Figure 7-8). Mud weight data were also included in the analysis, and agrees with the RFT tests. Overpressures for this well are not restricted to specific intervals and might prevent a normal compaction of the sedimentary units around the Samson Dome (see Breivik et al., 1998 for other areas of the Barents Sea). On the Samson Dome, the interval between 902 m and 945 m is marked by the presence of sandstones with good permeability, whereas permeability is reduced at depths below 1672 m (NPD, 2004). This reduction in permeability for the deeper stratigraphic intervals, in well 7224/7-1, can also explain the increase in the seal competence of the Triassic interval crossed by faults above the Samson Dome, as observed in the leakage factor model in Figure 4-12 and discussed in section *4.7.3. Implications for petroleum systems in the Samson Dome and Ottar Basin.*

In the Espírito Santo Basin, Domingues (2008) created a model to evaluate overpressures in five exploration wells drilled on the continental shelf. Three of these wells showed localised overpressures, which were attributed to disequilibrium compaction resulting from rapid sedimentation from the Maastrichtian to the Palaeocene.

Domingues (2008) indicates that fine-grained Paleocene strata can comprise a baffle to fluid circulation, preserving anomalous high pressures in the entire Espírito Santo Basin. The location of these wells, however, is not stated in Domingues (2008), due to confidentiality issues, which makes difficult the integration of the overpressure data in Figure 7-11 with the results from Chapter 5. Nevertheless, the occurrence of a dense fault network around different salt structures can, in the view of this thesis, constitute a preferential pathway to vertical fluid migration from the deepest-seated salt structure to the shallowest salt diapir. This characteristic is recorded by slip tendency and leakage factor models in this thesis, coupled with the juxtaposition diagrams and the recognition of bright-spots on seismic data (Figures 5-6 to 5-9).

The reactivation of faults must also be taken into account when assessing the onset of overpressures in a reservoir interval. Methods to assess the risk of breaching seal units due to the juxtaposition of impermeable strata across faults include detailed assessments of fault geometry and the use of in-situ stresses (Ferrill et al., 2009; Jones and Hillis, 2003; Morris et al., 1996). In Chapter 4 it was possible to constrain the presence of preferential areas of compartmentalisation, and areas of fluid leakage, associated with the dip-linked reactivation of faults in the Samson Dome, using the in-situ stress data from earthquake focal mechanisms from the Finnmark Platform. In this thesis, the present-day stresses these reactivated faults are subjected to seemingly increase the sealing potential of faults with increasing depth. In Chapter 5, however, the absence of wellbore breakouts data for the Espírito Santo Basin made necessary the use of paleostress data, and juxtaposition diagrams, to provide evidence the for strata compartmentalisation associated with fault reactivation.

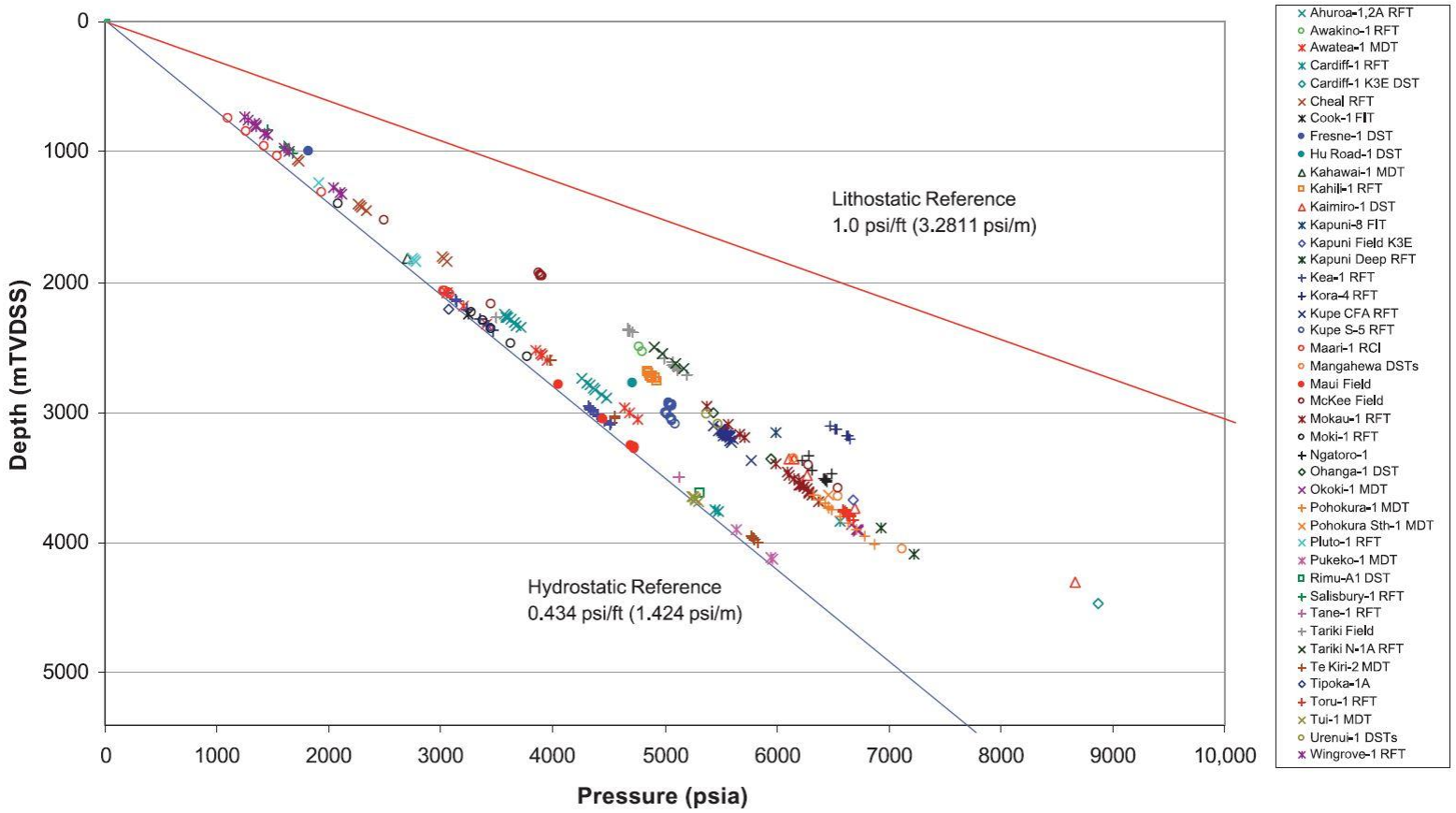

Figure 7-9: Summary plot for water pressure measurements for wells in Taranaki Basin based on data obtained from drill stem (DST), modular dynamic (MDT) and repeat formation tests (RFT), referenced to hydrostatic and lithostatic gradients. Figure from Webster et al. (2011).

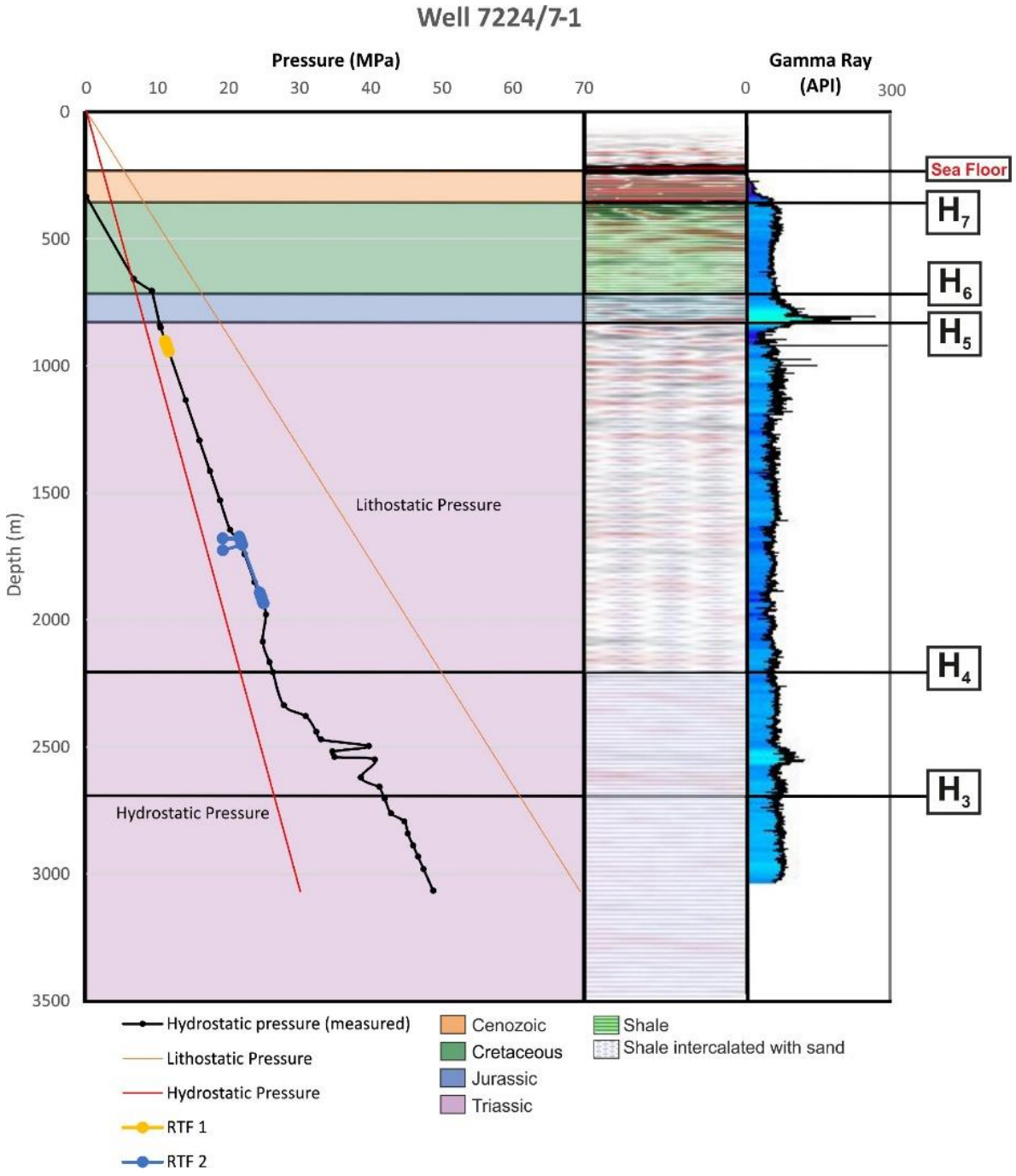

Figure 7-10: Pressure-depth plot based on repeat formation tests (RFT) and mud-weight information for well 7224/7-1, drilled on the crest of the Samson Dome, Barents Sea.

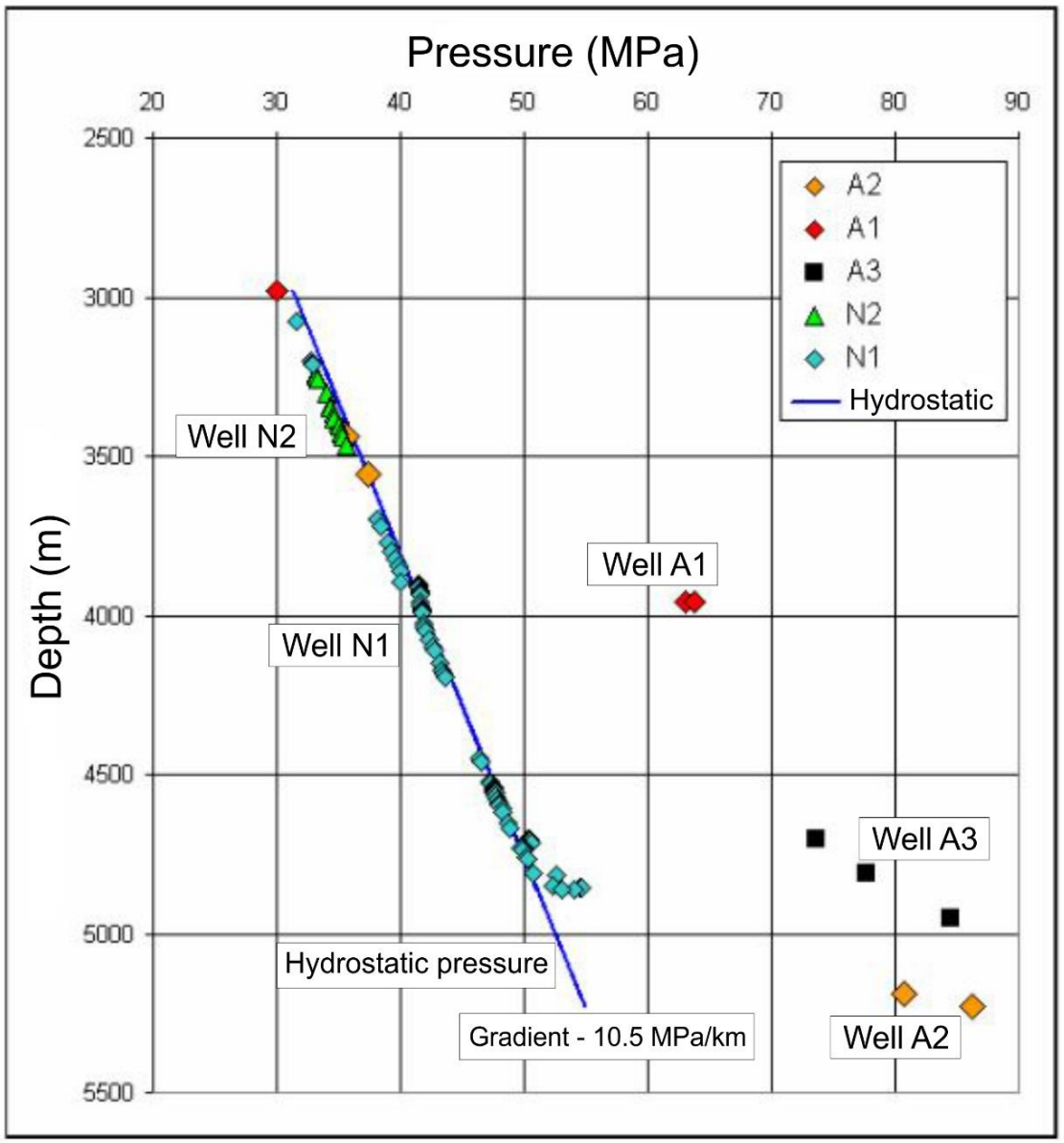

Figure 7-11: Directly measured pressure vs. depth profiles for five wells drilled in the Espírito Santo Basin compared to normal hydrostatic pressure with a gradient of 10.5 MPa/km. Figure from Domingues (2008).

7.5. Limitations of this research

The high quality of the 3D seismic datasets interpreted in three study areas allowed a reliable visualisation and interpretation of key stratigraphic horizons, submarine channels and structures. The major limitations in this thesis are related to the geographical coverage and the resolution of these same 3D seismic datasets. As this thesis has dealt with three different study areas, and data sets, the limitations discussed here focus on each of core chapter separately.

Although the database used for Chapter 4 included a 3D seismic cube, a 2D seismic line and two boreholes, limitations were documented from the significant loss of resolution of the 3D volume with depth. Salt withdrawal in the Samson Dome could not be precisely data due to the low resolution of Paleozoic strata adjacently to this salt anticline. The fault mapping overlying this structure could also be affected by the decrease in resolution.

The main limitations for Chapter 5 consisted in the absence of well data and the vertical extent of the 3D seismic volume. If well data had been available for the Espírito Santo Basin, it would have been possible to correlate the interpreted seismic units with local stratigraphic data, indicating with greater accuracy the lithology of each sub-unit. This would have provided a more reliable lithological framework to perform juxtaposition analyses. The availability of well data would also provide internal velocity (Vp) for sediments in Unit 1 and its five sub-units, allowing the conversion of throw-distribution curves to depth and, consequently, providing a more detailed understanding of the linkage and reactivation histories of faults.

The 3D volume of the Espírito Santo Basin was truncated at a depth of -4000 ms. A greater depth range would have provided a better opportunity to delimit the vertical extent of the Aptian evaporites, correlate the pre-salt units with the regional stratigraphy, and map fault families in pre-salt units to help constraining the timing of salt movements. The research in Chapter 5 would also have benefited from the availability of present-day stress data. Although the paleostress analyses agree with the faulting styles and the evolution of the study area, and the modelling of slip tendency and leakage factor matched with the juxtaposition diagrams, the use of present-day stress data could have provided an updated and more reliable analysis of fluid flow paths, particularly in the vertical direction towards the surface.

The 3D seismic cube used in Chapter 4 is characterised by the reactivation of the Parihaka Fault at the level of the Late Pliocene, and submarine channels have satisfactory resolutions (vertical + horizontal) for the analysis presented in this thesis. However, it was somewhat difficult to resolve small-scale variations in channel geometry over footwall blocks, as well as the occurrence of channels in the hanging-wall block towards the NE of the study area. This could also lead to an inaccurate characterisation of channel sinuosity, especially at depth, and in the plotting of Channel Points (CP) where channel edges were not seismically resolved. The loss of resolution close to the Parihaka Fault segments also provided an obstacle to the interpretation of channels, especially close to the relay ramps. In addition to the loss of resolution, the true extent of geological features such as submarine channels and the two depocentres observed in the hanging-wall block, to the NE of the study area, is compromised by the limited extent of the seismic cube to the north of the Taranaki Basin.

7.6. Further work

During this thesis, it was possible to provide multiple answers to better understand the influence of fault growth and evolution on the seal competence of faults. One of the key questions of this thesis focused on the impact of fault reactivation episodes in the creation of compartments within reservoir units of continental margins. The discussions drawn from this research have wide implications for the understanding of fault growth and its consequences to petroleum systems, as this research considered the different extents in which the magnitude and timing of fault movement, the juxtaposition of reservoir and seal units, and the stress state(s) influence reservoir and seal competence in offshore sedimentary basins. Following the methods applied to this thesis, it would be important to investigate, in more detail, the local processes capable of generating effective fault seals, such as cataclasis, clay smear and diagenesis, considering different pressure scenarios and integrating new information with the high-quality 3D seismic datasets available. This approach would provide a robust model, at a local scale, for hydrocarbon leakage and compartmentalisation.

A feasible continuation for the work developed in this thesis may comprise a detailed investigation of the occurrence of deformation bands in fault zones for areas such as the Barents Sea and the Northern Taranaki Basin, where core data and FMS/FMI data are available. The characterisation of networks of deformation bands would comprise a descriptive documentation of the orientation, thicknesses and density of these deformation bands, followed by a petrographic analysis of the mineralogy of the host rock and associated microstructures. The investigation of deformation bands sets at analogous

outcrops to seismically-imaged (i.e., subsurface) areas would be helpful to a more complete understanding of the impact of deformation bands in reservoir anisotropy.

A further approach could be the development of a model addressing the effects of sediment loading and unloading, halokinesis and faulting on continental crust. This new model would, in a ideal setting, take into account the heterogeneity of strata eroded and deposited in time and space (4D), as well as spatial and temporal variations resulting from consecutive depositional and tectonic events. This model could be integrated with decompaction, thermal subsidence modelling and flexural backstripping analyses performed in seismic cross-sections and well logs. The suggested model would provide accurate information on the mechanisms responsible for reservoir compartmentalisation at different scales of analysis.

8. Conclusions

The core themes of this research have important implications for the topic of fault reactivation on continental margins. The main conclusions of this work are summarised as follows:

8.1. Conclusions of Chapter 4

- The Samson Dome is a salt anticline revealing a three-stage evolution. The first stage took place during the Middle-Late Triassic, as recorded by the occurrence of NE-SW striking faults at this same stratigraphic level. The second stage, corresponding to halokinesis and uplift of the Samson Dome, took place in the Late Cretaceous, and resulted in the reactivation of pre-existing faults and associted formation of crestal faults. The third stage is associated with (salt) dissolution and collapse of the Samson Dome under its own weight.
- The preferential mode of reactivation for the interpreted faults was reactivation by dip-linkage.
- The study area was divided into three zones according to its proximity to the Samson Dome. Zone 1 is located at the north of the Samson Dome, while Zone 2 occurs adjacent to this salt diapir. Zone 3 is located at the southern part of the study area.
- Faults were divided into three fault types according to their geometry and strikes. Type A faults comprise faults developed at the crest of the Samson Dome, whereas Type B faults consist of E-trending faults to the northwest of

the dome. Type C faults comprise small-scale faults found at shallow levels close to the Samson Dome.

- Paleostress analyses reveal that the study area was affected by important extensional events during the inception of the interpreted faults.
- Stress modelling results indicate that Types B and C faults in Zones 1 and 3, respectively, show low slip tendency and high linkage factors. The occurrence of bright-spots close to the interpreted faults indicate Zone 1 as possible conduit for fluids generated at depth.
- In Zone 2, adjacent to the Samson Dome, the leakage factor decreases with depth for modelled faults, indicating the development of closed structural compartments related to the evolution of the Samson Dome. These compartments are capable of retaining fluids in Triassic Strata.

8.2. Conclusions of Chapter 5

- Three salt diapirs and a salt ridge where interpreted in the Espírito Santo Basin and the mapped faults were divided into five families according to their location.
- The evolution of salt structures occurred with different timings during the Late Aptian and the Early Miocene. At least three phases of halokinesis took place in the study area, and were associated with the development of the salt ridge, diapirs 1 to 3, and the faults adjacent to these salt structures.
- The first halokinetic movements in the Espírito Santo Basin took place in the Late Aptian – Early Albian, resulting in the formation of the first few faults.

The first halokinesis-induced reactivation episode took place from the Late Albian to the Early Eocene.

- Based on the detailed interpretation of dated seismic horizons and structures it was possible to establish that halokinesis in the salt ridge ceased during the Early Eocene, culminating with salt dissolution and collapse of this structure. Halokinesis continued until the Early Miocene in diapirs 1 to 3.
- Faults in the study area rarely propagated above the Middle Eocene (horizon H_6). Dip-linkage was found as the preferential mechanism for fault reactivation in the study area. The preferential NE-SW reactivation direction taking place in the study area coincides with paleostress inversion data - which suggests NNE extension.
- Juxtaposition diagrams indicate that faults adjacent to diapirs 2 and 3 show important connections between thick permeable units, coinciding with the preferential location of bright spots on the seismic data. These diagrams also indicate the juxtaposition of seal units, isolating the sand bodies for faults adjacent to diapir 1.
- Slip tendency and leakage factor analyses agree with the juxtaposition diagrams, as the faults with higher leakage factors are located close to diapirs 2 and 3.
- Based on the distribution of faults around the interpreted salt structures, it is here proposed that faults comprise preferential paths for fluid flow from S to NNW.
- Seismic interpretation of horizons and structures, coupled with fault modelling, suggest that halokinesis in Diapir 3 took place for a longer time in

comparison to the other salt structures in the study area. Long-lasting activity in Diapir 3 influenced the geometry (and evolution) of adjacent fault families, and the flow of fluids, in time and space.

8.3. Conclusions of Chapter 6

- The Parihaka Fault is a complex structure developed at the Cape Egmont Fault Zone, and comprises four distinct segments.
- Early Pliocene-Pleistocene extension that affected the Taranaki Basin resulted in the opening of the Northern Graben. Segments S1 and S2 existed prior to this extensional event and were reactivated, whereas segments S3 and S4 were active from that time until the present-day.
- Two depocentres were developed in the hanging-wall block to the NE of the study area.
- Three main drainage types were found in the study area, and reflect the significant interactions with the Parihaka Fault. An oblique drainage system observed to the south of the study area is related to S1, the least active/reactivated segment. Channels initially flowing oblique to the fault were diverted transversally in the proximity of the reactivated segment S2 and the newly formed segment S3. They reveal a close influence of the fault in the geometry of these channel systems. A channel flowing parallel to the fault trace on the footwall block is associated with local uplift caused by the formation of segments S3 and S4.

- The relay ramps developed between the segments of the Parihaka Fault were not a preferential pathway for submarine channels, in contrast to what is commonly expected in such settings.
- Despite no evidence of fluid accumulation(s) in the study area, the rapid deposition of prograding sequences in the Giant Foresets Formation (hanging-wall block) and the vertically- and laterally-stacked channels observed on the footwall block, can comprise important reservoirs in the Taranaki Basin.

References

Abreu, V., Sullivan, M., Pirmez, C., Mohrig, D., 2003. Lateral accretion packages (LAPs): an important reservoir element in deep water sinuous channels. Mar. Pet. Geol. 20, 631–648.

Acocella, V., Funiciello, R., Marotta, E., Orsi, G., de Vita, S., 2004. The role of extensional structures on experimental calderas and resurgence. J. Volcanol. Geotherm. Res. 129, 199–217. doi:10.1016/S0377-0273(03)00240-3

Ainsworth, R.B., 2010. Prediction of stratigraphic compartmentalization in marginal marine reservoirs. Geol. Soc. London, Spec. Publ. 347, 199–218.

Ainsworth, R.B., 2006. Sequence stratigraphic-based analysis of reservoir connectivity: influence of sealing faults - a case study from a marginal marine depositional setting. Pet. Geosci. doi:10.1144/1354-079305-661

Ainsworth, R.B., 2005. Sequence stratigraphic-based analysis of reservoir connectivity: influence of depositional architecture–a case study from a marginal marine depositional setting. Pet. Geosci. 11, 257–276.

Allan, U.S., 1989. Model for hydrocarbon migration and entrapment within faulted structures. Am. Assoc. Pet. Geol. Bull. 73, 803–811.

Allen, P.A., Allen, J.R., 2013. Basin analysis: Principles and application to petroleum play assessment. John Wiley & Sons.

Alsop, G.I., 1996. Physical modelling of fold and fracture geometries associated with salt diapirism. Geol. Soc. London, Spec. Publ. doi:10.1144/GSL.SP.1996.100.01.14

Alsop, G.I., Brown, J.P., Davison, I., Gibling, M.R., 2000. The geometry of drag zones adjacent to salt diapirs. J. Geol. Soc. London. 157, 1019–1029.

Alves, T.M., 2016. Polygonal mounds in the Barents Sea reveal sustained organic productivity towards the P–T boundary. Terra Nov. 28, 50–59.

Alves, T.M., 2012. Scale-relationships and geometry of normal faults reactivated during gravitational gliding of Albian rafts (Espírito Santo Basin, SE Brazil). Earth Planet. Sci. Lett. 331, 80–96.

Alves, T.M., 2010. 3D Seismic examples of differential compaction in mass-transport deposits and their effect on post-failure strata. Mar. Geol. 271, 212–224. doi:10.1016/j.margeo.2010.02.014

Alves, T.M., Cartwright, J., Davies, R.J., 2009. Faulting of salt-withdrawal basins during early halokinesis: effects on the Paleogene Rio Doce Canyon system (Espírito Santo Basin, Brazil). Am. Assoc. Pet. Geol. Bull. 93, 617–652.

Alves, T.M., Fetter, M., Lima, C., Cartwright, J.A., Cosgrove, J., Gangá, A., Queiroz, C.L., Strugale, M., 2017. An incomplete correlation between pre-salt topography, top reservoir erosion, and salt deformation in deep-water Santos Basin (SE Brazil). Mar. Pet. Geol. 79, 300–320.

Anderson, E.M., 1942. The Dynamics of Faulting. Oliver & Boyd, London.

Anderson, J.E., Cartwright, J., Drysdall, S.J., Vivian, N., 2000. Controls on turbidite sand

deposition during gravity-driven extension of a passive margin: examples from Miocene sediments in Block 4, Angola. Mar. Pet. Geol. 17, 1165–1203.

Angelier, J., 1994. Paleostress analysis of small-scale brittle structures, in: Hancock, P. (Ed.), Continental Deformation. Pergamon, Tarrytown, NY, pp. 53–100.

Angelier, J., 1990. Inversion of field data in fault tectonics to obtain the regional stress-III. A new rapid direct inversion method by analytical means. Geophys. J. Int. 103, 363–376. doi:10.1111/j.1365-246X.1990.tb01777.x

Antonellini, M.A., Aydin, A., Pollard, D.D., 1994. Microstructure of deformation bands in porous sandstones at Arches National Park, Utah. J. Struct. Geol. 16, 941–959.

Arco, 1992. Arawa-1 Final Well report.

Armstrong, P.A., Allis, R.G., Funnell, R.H., Chapman, D.S., 1998. Late Neogene exhumation patterns in Taranaki Basin (New Zealand): Evidence from offset porosity-depth trends. J. Geophys. Res. Solid Earth 103, 30269–30282.

Armstrong, P.A., Chapman, D.S., Funnell, R.H., Allis, R.G., Kamp, P.J.J., 1996. Thermal modeling and hydrocarbon generation in an active-margin basin: Taranaki Basin, New Zealand. Am. Assoc. Pet. Geol. Bull. 80, 1216–1241.

Asmus, H.E., Gomes, J.B., Pereira, A.C.B., 1971. Integração geológica regional da bacia do Espírito Santo. Relatório Interno, PETROBRAS.

Athmer, W., Groenenberg, R.M., Luthi, S.M., Donselaar, M.E., Sokoutis, D., Willingshofer, E., 2010. Relay ramps as pathways for turbidity currents: a study combining analogue sandbox experiments and numerical flow simulations. Sedimentology 57, 806–823.

Aydin, A., 2000. Fractures, faults, and hydrocarbon entrapment, migration and flow. Mar. Pet. Geol. 17, 797–814. doi:10.1016/S0264-8172(00)00020-9

Babonneau, N., Savoye, B., Cremer, M., Klein, B., 2002. Morphology and architecture of the present canyon and channel system of the Zaire deep-sea fan. Mar. Pet. Geol. 19, 445–467.

Bacon, M., Simm, R., Redshaw, T., 2007. 3-D seismic interpretation. Cambridge University Press.

Barclay, S.A., Worden, R.H., Parnell, J., Hall, D.L., Sterner, S.M., 2000. Assessment of fluid contacts and compartmentalization in sandstone reservoirs using fluid inclusions: an example from the Magnus oil field, North Sea. Am. Assoc. Pet. Geol. Bull. 84, 489–504.

Barker, P.F., Buffler, R.T., Gambôa, L.A., 1983. A seismic reflection study of the Rio Grande Rise. Initial Reports Deep Sea Drill. Proj. 72, 499–517.

Barnett, J.A.M., Mortimer, J., Rippon, J.H., Walsh, J.J., Watterson, J., 1987. Displacement geometry in the volume containing a single normal fault. Am. Assoc. Pet. Geol. Bull. 71, 925–937.

Barrère, C., Ebbing, J., Gernigon, L., 2009. Offshore prolongation of Caledonian structures and basement characterisation in the western Barents Sea from geophysical modelling. Tectonophysics 470, 71–88. doi:10.1016/j.tecto.2008.07.012

Barton, C.A., Zoback, M.D., Moos, D., 1995. Fluid flow along potentially active faults in crystalline rock. Geology 23, 683–686.

Baudon, C., 2007. Propagation and early growth of normal faults. Cardiff University (United Kingdom).

Baudon, C., Cartwright, J., 2008a. Early stage evolution of growth faults: 3D seismic insights from the Levant Basin, Eastern Mediterranean. J. Struct. Geol. 30, 888–898. doi:10.1016/j.jsg.2008.02.019

Baudon, C., Cartwright, J., 2008b. The kinematics of reactivation of normal faults using high resolution throw mapping. J. Struct. Geol. 30, 1072–1084. doi:10.1016/j.jsg.2008.04.008

Baur, J.R., 2012. Regional seismic attribute analysis and tectono-stratigraphy of offshore south-western Taranaki Basin, New Zealand.

Berndt, C., 2005. Focused fluid flow in passive continental margins. Philos. Trans. R. Soc. London A Math. Phys. Eng. Sci. 363, 2855–2871.

Berner, H., Ramberg, H., Stephansson, O., 1972. Diapirism theory and experiment. Tectonophysics.

Bhullar, A.G., Karlsen, D.A., Holm, K., Backer-Owe, K., Le Tran, K., 1998. Petroleum geochemistry of the Frøy field and Rind discovery, Norwegian Continental Shelf. Implications for reservoir characterization, compartmentalization and basin scale hydrocarbon migration patterns in the region. Org. Geochem. 29, 735–768.

Biddle, K.T., 1985. Glossary—Strike-slip deformation, basin formation, and sedimentation, in: Biddle, K.T., Christie-Blick, N. (Eds.), Strike-Slip Deformation, Basin Formation and Sedimentation. Special Publications of SEPM, Tulsa, pp. 375–386.

Biddle, K.T., Wielchowsky, C.C., 1994. Hydrocarbon Traps: Chapter 13: Part III. Processes.

Bischke, R.E., 1994. Interpreting sedimentary growth structures from well log and seismic data (with examples). Am. Assoc. Pet. Geol. Bull. 78, 873–892.

Bjørlykke, K., 2014. Relationships between depositional environments, burial history and rock properties. Some principal aspects of diagenetic process in sedimentary basins. Sediment. Geol. 301, 1–14.

Bjørlykke, K., Høeg, K., 1997. Effects of burial diagenesis on stresses, compaction and fluid flow in sedimentary basins. Mar. Pet. Geol. 14, 267–276.

Bott, M.H.P., 1959. The Mechanics of Oblique Slip Faulting. Geol. Mag. doi:10.1017/S0016756800059987

Bouma, A.H., 2004. Key controls on the characteristics of turbidite systems. Geol. Soc. London, Spec. Publ. 222, 9–22. doi:10.1144/GSL.SP.2004.222.01.02

Bouroullec, R., Cartwright, J.A., Johnson, H.D., Lansigu, C., Quémener, J.-M., Savanier, D., 2004. Syndepositional faulting in the Grés d'Annot Formation, SE France: high-resolution kinematic analysis and stratigraphic response to growth faulting. Geol. Soc. London, Spec. Publ. 221, 241–265.

Bradley, J.S., Powley, D.E., 1994. Pressure compartments in sedimentary basins: a review.

Breivik, A.J., Faleide, J.I., Gudlaugsson, S.T., 1998. Southwestern Barents Sea margin: late Mesozoic sedimentary basins and crustal extension. Tectonophysics 293, 21–44.

Breivik, A.J., Gudlaugsson, S.T., Faleide, J.I., 1995. Ottar basin, sw Barents sea: A major Upper Palaeozoic rift Basin containing large volumes of deeply Buried salt. Basin Res. 7, 299–312. doi:10.1111/j.1365-2117.1995.tb00119.x

Breivik, A.J., Mjelde, R., Grogan, P., Shimamura, H., Murai, Y., Nishimura, Y., Kuwano, A., 2002. A possible Caledonide arm through the Barents Sea imaged by OBS data.

Tectonophysics 355, 67–97.

Brown, A.R., 2011. Interpretation of three-dimensional seismic data. American Association of Petroleum Geologists and the Society of Exploration Geophysicists.

Brudy, M., Kjørholt, H., 2001. Stress orientation on the Norwegian continental shelf derived from borehole failures observed in high-resolution borehole imaging logs. Tectonophysics 337, 65–84. doi:10.1016/S0040-1951(00)00299-7

Bruhn, C.H.L., Gomes, J.A.T., Del Lucchese Jr, C., Johann, P.R.S., 2003. Campos basin: reservoir characterization and management-Historical overview and future challenges, in: Offshore Technology Conference. Offshore Technology Conference.

Bruhn, C.H.L., Walker, R.G., 1997. Internal architecture and sedimentary evolution of coarse-grained, turbidite channel-levee complexes, Early Eocene Regencia Canyon, Espirito Santo Basin, Brazil. Sedimentology 44, 17–46.

Brun, J.-P., Fort, X., 2011. Salt tectonics at passive margins: Geology versus models. Mar. Pet. Geol. 28, 1123–1145. doi:10.1016/j.marpetgeo.2011.03.004

Brun, J.-P., Fort, X., 2004. Compressional salt tectonics (Angolan margin). Tectonophysics 382, 129–150.

Bugge, T., Elvebakk, G., Fanavoll, S., Mangerud, G., Smelror, M., Weiss, H.M., Gjelberg, J., Kristensen, S.E., Nilsen, K., 2002. Shallow stratigraphic drilling applied in hydrocarbon exploration of the Nordkapp Basin, Barents Sea. Mar. Pet. Geol. 19, 13–37.

Bungum, H., Alsaker, A., Kvamme, L.B., Hansen, R.A., 1991. Seismicity and seismotectonics of Norway and nearby continental shelf areas. J. Geophys. Res. doi:10.1029/90JB02010

Bürgmann, R., Pollard, D.D., Martel, S.J., 1994. Slip distributions on faults: effects of stress gradients, inelastic deformation, heterogeneous host-rock stiffness, and fault interaction. J. Struct. Geol. 16, 1675–1690.

Byerlee, J., 1978. Friction of rocks. Pure Appl. Geophys. 116, 615–626.

Caine, J.S., Evans, J.P., Forster, C.B., 1996. Fault zone architechture and permeability structure. Geology 24, 1025–1028. doi:10.1130/0091-7613(1996)024<1025

Cainelli, C., Mohriak, W.U., 1999. Some remarks on the evolution of sedimentary basins along the Eastern Brazilian continental margin. Episodes-Newsmagazine Int. Union Geol. Sci. 22, 206–216.

Cainelli, C., Mohriak, W.U., 1998. Geology of Atlantic eastern Brazilian basins, in: Brazilian Geology Part. p. 1998.

Carruthers, D., Cartwright, J., Jackson, M.P. a., Schutjens, P., 2013. Origin and timing of layer-bound radial faulting around North Sea salt stocks: New insights into the evolving stress state around rising diapirs. Mar. Pet. Geol. 48, 130–148. doi:10.1016/j.marpetgeo.2013.08.001

Cartwright, J.A., 2007. The impact of 3D seismic data on the understanding of compaction, fluid flow and diagenesis in sedimentary basins. J. Geol. Soc. London. doi:10.1144/0016-76492006-143

Cartwright, J.A., Bouroullec, R., James, D., Johnson, H., 1998. Polycyclic motion history of some Gulf Coast growth faults from high-resolution displacement analysis. Geology 26, 819–822. doi:10.1130/0091-7613(1998)026<0819:PMHOSG>2.3.CO;2

Cartwright, J.A., Mansfield, C.S., 1998. Lateral displacement variation and lateral tip geometry of normal faults in the Canyonlands National Park, Utah. J. Struct. Geol. doi:10.1016/S0191-8141(97)00079-5

Cartwright, J.A., Trudgill, B.D., Mansfield, C.S., 1995. Fault growth by segment linkage: an explanation for scatter in maximum displacement and trace length data from the Canyonlands Grabens of SE Utah. J. Struct. Geol. 17, 1319–1326.

Cerveny, K., Davies, R., Dudley, G., Kaufman, P., Knipe, R.J., Krantz, B., 2004. Reducing uncertainty with fault-seal analysis. Oilf. Rev. 16, 2005.

Chadwick, W.W., Dieterich, J.H., 1995. Mechanical modeling of circumferential and radial dike intrusion on Galapagos volcanoes. J. Volcanol. Geotherm. Res. 66, 37–52.

Chand, S., Mienert, J., Andreassen, K., Knies, J., Plassen, L., Fotland, B., 2008. Gas hydrate stability zone modelling in areas of salt tectonics and pockmarks of the Barents Sea suggests an active hydrocarbon venting system. Mar. Pet. Geol. 25, 625–636. doi:10.1016/j.marpetgeo.2007.10.006

Chand, S., Thorsnes, T., Rise, L., Brunstad, H., Stoddart, D., Bøe, R., Lågstad, P., Svolsbru, T., 2012. Multiple episodes of fluid flow in the SW Barents Sea (Loppa High) evidenced by gas flares, pockmarks and gas hydrate accumulation. Earth Planet. Sci. Lett. 331, 305–314.

Chang, H.K., Kowsmann, R.O., Figueiredo, A.M.F., Bender, A., 1992. Tectonics and stratigraphy of the East Brazil Rift system: an overview. Tectonophysics 213, 97–138.

Chapman, T.J., Williams, G.D., 1984. Displacement-distance methods in the analysis of fold-thrust structures and linked-fault systems. J. Geol. Soc. London. 141, 121–128.

Charalampakis, M., Stefatos, A., Hasiotis, T., Ferentinos, G., 2007. Submarine mass movements on an active fault system in the central Gulf of Corinth. Submar. mass movements their consequences 67–75.

Childs, C., Easton, S.J., Vendeville, B.C., Jackson, M.P. a., Lin, S.T., Walsh, J.J., Watterson, J., 1993. Kinematic analysis of faults in a physical model of growth faulting above a viscous salt analogue. Tectonophysics 228, 313–329. doi:10.1016/0040-1951(93)90346-L

Childs, C., Manzocchi, T., Walsh, J.J., Bonson, C.G., Nicol, A., Schöpfer, M.P.J., 2009. A geometric model of fault zone and fault rock thickness variations. J. Struct. Geol. 31, 117–127. doi:10.1016/j.jsg.2008.08.009

Childs, C., Nicol, A., Walsh, J.J., Watterson, J., 2003. The growth and propagation of synsedimentary faults. J. Struct. Geol. 25, 633–648. doi:10.1016/S0191-8141(02)00054-8

Childs, C., Nicol, A., Walsh, J.J., Watterson, J., 1996. Growth of vertically segmented normal faults. J. Struct. Geol. 18, 1389–1397. doi:10.1016/S0191-8141(96)00060-0

Childs, C., Walsh, J.J., Watterson, J., 1997. Complexity in fault zone structure and implications for fault seal prediction. Nor. Pet. Soc. Spec. Publ. 7, 61–72. doi:10.1016/S0928-8937(97)80007-0

Childs, C., Watterson, J., Walsh, J.J., 1995. Fault overlap zones within developing normal fault systems. J. Geol. Soc. London. doi:10.1144/gsjgs.152.3.0535

Christie-Blick, N., Biddle, K., 1985. Deformation and basin formation along strike-slip faults, in: Biddle, K.T., Christie-Blick, N. (Eds.), Strike-Slip Deformation, Basin Formation and Sedimentation. Society of Economic Paleontologists and Mineralogists, Tulsa, pp. 1–34. doi:10.2110/pec.85.37.0001

Clark, I.R.I.R., Cartwright, J.A.J.A., 2009. Interactions between submarine channel systems and deformation in deepwater fold belts: Examples from the Levant Basin, Eastern Mediterranean sea. Mar. Pet. Geol. 26, 1465–1482. doi:10.1016/j.marpetgeo.2009.05.004

Clark, J.A., Cartwright, J.A., Stewart, S.A., 1999. Mesozoic dissolution tectonics on the west central shelf, UK Central North Sea. Mar. Pet. Geol. 16, 283–300.

Clark, J.D., Pickering, K.T., 1996. Architectural elements and growth patterns of submarine channels: application to hydrocarbon exploration. Am. Assoc. Pet. Geol. Bull. 80, 194–220.

Clark, M.S., Beckley, L.M., Crebs, T.J., Singleton, M.T., 1996. Tectono-eustatic controls on reservoir compartmentalisation and quality—an example from the Upper Miocene of the San Joaquin basin, California. Mar. Pet. Geol. 13, 475–491.

Clausen, O.R., Egholm, D.L., Andresen, K.J., Wesenberg, R., 2014. Fault patterns within sediment layers overlying rising salt structures: A numerical modelling approach. J. Struct. Geol. 58, 69–78. doi:10.1016/j.jsg.2013.11.001

Cobbold, P.R., Meisling, K.E., Mount, V.S., 2001. Reactivation of an obliquely rifted margin, Campos and Santos basins, southeastern Brazil. Am. Assoc. Pet. Geol. Bull. 85, 1925–1944.

Cocks, L.R.M., Torsvik, T.H., 2005. Baltica from the late Precambrian to mid-Palaeozoic times: the gain and loss of a terrane's identity. Earth-Science Rev. 72, 39–66.

Cosgrove, J.W., Ameen, M.S., 1999. A comparison of the geometry, spatial organization and fracture patterns associated with forced folds and buckle folds. Geol. Soc. London, Spec. Publ. 169, 7–21.

Cowie, P.A., Gupta, S., Dawers, N.H., 2000. Implications of fault array evolution for synrift

depocentre development: insights from a numerical fault growth model. Basin Res. 12, 241–261.

Cowie, P.A., Scholz, C.H., 1992a. Displacement-length scaling relationship for faults: data synthesis and discussion. J. Struct. Geol. doi:10.1016/0191-8141(92)90066-6

Cowie, P.A., Scholz, C.H., 1992b. Physical Explanation for the Displacement Length Relationship of Faults Using a Post-Yield Fracture-Mechanics Model. J. Struct. Geol. 14, 1133–1148.

Cowie, P.A., Scholz, C.H., 1992c. Physical explanation for the displacement-length relationship of faults using a post-yield fracture mechanics model. J. Struct. Geol. doi:10.1016/0191-8141(92)90065-5

Cox, S.F., Knackstedt, M.A., Braun, J., 2001. Principles of structural control on permeability and fluid flow in hydrothermal systems. Rev. Econ. Geol. 14, 1–24.

Dalland, A., Worsley, D., Ofstad, K., 1988. A Lithostratigraphic Scheme for the Mesozoic and Cenozoic Succession Offshore Mid- and Northern Norway. Nor. Pet. Dir. Bull. No.4, 87.

Damuth, J.E., Flood, R.D., Kowsmann, R.O., Belderson, R.H., Gorini, M.A., 1988. Anatomy and growth pattern of Amazon deep-sea fan as revealed by long-range side-scan sonar (GLORIA) and high-resolution seismic studies. Am. Assoc. Pet. Geol. Bull. 72, 885–911.

Darby, D., 2002. Seal properties, overpressure and stress in the Taranaki and East Coast Basins, New Zealand, in: 2002 New Zealand Petroleum Conference Proceedings. pp. 24–27.

Davies, R.J., Stewart, S. a., Cartwright, J. a., Lappin, M., Johnston, R., Fraser, S.I., Brown, a. R., 2004. 3D Seismic Technology: Are We Realising Its Full Potential? Geol. Soc. London,

Mem. 29, 1–10. doi:10.1144/GSL.MEM.2004.029.01.01

Davison, I., Alsop, I., Birch, P., Elders, C., Evans, N., Nicholson, H., Rorison, P., Wade, D., Woodward, J., Young, M., 2000. Geometry and late-stage structural evolution of Central Graben salt diapirs, North Sea. Mar. Pet. Geol. 17, 499–522.

Davison, I., Insley, M., Harper, M., Weston, P., 1993. Physical modelling of overburden deformation around salt diapirs. Tectonophysics 228, 255–274.

Dawers, N.H., Anders, M.H., 1995. Displacement-length scaling and fault linkage. J. Struct. Geol. 17. doi:10.1016/0191-8141(94)00091-D

Dawers, N.H., Anders, M.H., Scholz, C.H., 1993. Growth of normal faults: displacement-length scaling. Geology. doi:10.1130/0091-7613(1993)021<1107:GONFDL>2.3.CO;2

Demercian, S., Szatmari, P., Cobbold, P.R., 1993. Style and pattern of salt diapirs due to thin-skinned gravitational gliding, Campos and Santos basins, offshore Brazil. Tectonophysics 228, 393–433. doi:10.1016/0040-1951(93)90351-J

Dengo, C.A., Røssland, K.G., 2013. Extensional tectonic history of the western Barents Sea. Struct. Tecton. Model. its Appl. to Pet. Geol. Nor. Pet. Soc. Spec. Publ. 1, 91–107.

Deptuck, M.E., Steffens, G.S., Barton, M., Pirmez, C., 2003. Architecture and evolution of upper fan channel-belts on the Niger Delta slope and in the Arabian Sea. Mar. Pet. Geol. 20, 649–676.

Deptuck, M.E., Sylvester, Z., Pirmez, C., O'Byrne, C., 2007. Migration–aggradation history and 3-D seismic geomorphology of submarine channels in the Pleistocene Benin-major Canyon, western Niger Delta slope. Mar. Pet. Geol. 24, 406–433.

Dias, J.L., 2005. Tectônica, estratigrafia e sedimentação no Andar Aptiano da margem leste brasileira. Bol. Geociências da PETROBRAS 13, 7–25.

Diegel, F.A., Karlo, J.F., Schuster, D.C., Shoup, R.C., Tauvers, P.R., 1995. Cenozoic structural evolution and tectono-stratigraphic framework of the northern Gulf Coast continental margin.

Domingues, M., 2008. Comparative study of pore pressure estimation methods at Espírito Santo Basin wells, Brazil. Universidade Federal do Rio de Janeiro.

Dooley, T.P., Jackson, M.P.A., Hudec, M.R., 2009. Inflation and deflation of deeply buried salt stocks during lateral shortening. J. Struct. Geol. doi:10.1016/j.jsg.2009.03.013

Doré, A., 1995. Barents Sea geology, petroleum resources and commercial potential. Arctic 48, 207–221.

Doré, A., 1991. The structural foundation and evolution of Mesozoic seaways between Europe and the Arctic. Palaeogeogr. Palaeoclimatol. Palaeoecol. 87, 441–492.

Dorn, G.A., 1998. Modern 3-D seismic interpretation. Lead. Edge 17, 1262–1270.

Duval, B., Cramez, C., Jackson, M.P. a., 1992. Raft tectonics in the Kwanza Basin, Angola. Mar. Pet. Geol. 9, 389–404. doi:10.1016/0264-8172(92)90050-O

Eaton, B.A., 1969. Fracture gradient prediction and its application in oilfield operations. J. Pet. Technol. 21, 1–353.

Ehrenberg, S.N., Nadeau, P.H., 2005. Sandstone vs. carbonate petroleum reservoirs: A global perspective on porosity-depth and porosity-permeability relationships. Am. Assoc. Pet.

Geol. Bull. 89, 435–445.

Ehrenberg, S.N., Nielsen, E., Svånå, T.A., Stemmerik, L., 1998. Depositional evolution of the Finnmark carbonate platform, Barents Sea: results from wells 7128/6-1 and 7128/4-1. Nor. Geol. Tidsskr. 78, 185–224.

Eliet, P.P., Gawthorpe, R.L., 1995. Drainage development and sediment supply within rifts, examples from the Sperchios basin, central Greece. J. Geol. Soc. London. 152, 883–893.

Ellis, M.A., Dunlap, W.J., 1988. Displacement variation along thrust faults: implications for the development of large faults. J. Struct. Geol. doi:10.1016/0191-8141(88)90115-0

Elvebakk, G., Hunt, D.W., Stemmerik, L., 2002. From isolated buildups to buildup mosaics: 3D seismic sheds new light on Upper Carboniferous–Permian fault controlled carbonate buildups, Norwegian Barents Sea. Sediment. Geol. 152, 7–17.

Engelder, T., 2014. Stress regimes in the lithosphere. Princeton University Press, Princeton.

Estrella, G., Mello, M.R., Gaglianone, P.C., Azevedo, R.L.M., Tsubone, K., Rossetti, E., Concha, J., Bruning, I., 1984. The Espirito Santo Basin (Brazil) source rock characterization and petroleum habitat.

Evans, J.P., 1990. Thickness-displacement relationships for fault zones. J. Struct. Geol. 12, 1061–1065.

Fainstein, R., Summerhayes, C.P., 1982. Structure and origin of marginal banks off eastern Brazil. Mar. Geol. 46, 199–215.

Faleide, J.I., Gudlaugsson, S.T., Jacquart, G., 1984. Evolution of the western Barents Sea. Mar.

Pet. Geol. doi:10.1016/0264-8172(84)90082-5

Faleide, J.I., Solheim, A., Fiedler, A., Hjelstuen, B.O., Andersen, E.S., Vanneste, K., 1996. Late Cenozoic evolution of the western Barents Sea-Svalbard continental margin. Glob. Planet. Change. doi:10.1016/0921-8181(95)00012-7

Faleide, J.I., Tsikalas, F., Breivik, A.J., Mjelde, R., Ritzmann, O., Engen, O., Wilson, J., Eldholm, O., 2008. Structure and evolution of the continental margin off Norway and the Barents Sea. Episodes 31, 82–91. doi:10.1016/j.strusafe.2006.11.005

Faleide, J.I., Vågnes, E., Gudlaugsson, S.T., 1993. Late Mesozoic-Cenozoic evolution of the south-western Barents Sea in a regional rift-shear tectonic setting. Mar. Pet. Geol. 10, 186–214. doi:10.1016/0264-8172(93)90104-Z

Faulkner, D.R., Jackson, C.A.L., Lunn, R.J., Schlische, R.W., Shipton, Z.K., Wibberley, C.A.J., Withjack, M.O., 2010. A review of recent developments concerning the structure, mechanics and fluid flow properties of fault zones. J. Struct. Geol. doi:10.1016/j.jsg.2010.06.009

Faulkner, D.R., Jackson, C.A.L., Lunn, R.J., Schlische, R.W., Shipton, Z.K., Wibberley, C.A.J., Withjack, M.O., 2010. A review of recent developments concerning the structure, mechanics and fluid flow properties of fault zones. J. Struct. Geol. 32, 1557–1575. doi:10.1016/j.jsg.2010.06.009

Fejerskov, M., Lindholm, C., Myrvang, a., Bungum, H., 2000. Crustal stress in and around Norway: a compliation of in situ stress observations. Geol. Soc. London, Spec. Publ. 167, 441–449. doi:10.1144/GSL.SP.2000.167.01.18

Ferentinos, G., Papatheodorou, G., Collins, M.B., 1988. Sediment transport processes on an active

submarine fault escarpment: Gulf of Corinth, Greece. Mar. Geol. 83, 43–61.

Ferrill, D.A., Morris, A.P., McGinnis, R.N., 2009. Crossing conjugate normal faults in field exposures and seismic data. Am. Assoc. Pet. Geol. Bull. 93, 1471–1488.

Fiduk, J.C., Brush, E.R., Anderson, L.E., Gibbs, P.B., Rowan, M.G., 2004. Salt deformation, magmatism, and hydrocarbon prospectivity in the Espirito Santo Basin, offshore Brazil, in: Salt-Sediment Interactions and Hydrocarbon Prospectivity: Concepts, Applications, and Case Studies for the 21st Century: Gulf Coast Section SEPM 24th Annual Conference. p. 370.

Figueiredo, A.M.F., Mohriak, W.U., 1984. A tectonica salifera e as acumulacoes de Petroleo da Bacia de Campos, in: Proceedings of the 33rd Brazilian Geological Congress, Sociedada Brasileira de Geologia, Rio de Janeiro. pp. 1380–1394.

Finkbeiner, T., Zoback, M., Flemings, P., Stump, B., 2001. Stress, pore pressure, and dynamically constrained hydrocarbon columns in the South Eugene Island 330 field, northern Gulf of Mexico. Am. Assoc. Pet. Geol. Bull. 85, 1007–1031.

Fisher, Q.J., Knipe, R.J., 2001. The permeability of faults within siliciclastic petroleum reservoirs of the North Sea and Norwegian Continental Shelf. Mar. Pet. Geol. 18, 1063–1081.

Flood, R.D., Damuth, J.E., 1987. Quantitative characteristics of sinuous distributary channels on the Amazon deep-sea fan. Geol. Soc. Am. Bull. 98, 728–738.

Fossen, H., 2010. Structural geology. Cambridge University Press.

Fossen, H., Hesthammer, J., 1997. Geometric analysis and scaling relations of deformation bands in porous sandstone. J. Struct. Geol. 19, 1479–1493.

Fossen, H., Rotevatn, A., 2016. Fault linkage and relay structures in extensional settings—A review. Earth-Science Rev. 154, 14–28. doi:http://dx.doi.org/10.1016/j.earscirev.2015.11.014

Fossen, H., Schultz, R.A., Shipton, Z.K., Mair, K., 2007. Deformation bands in sandstone: a review. J. Geol. Soc. London. 164, 755–769.

Fossen, H., Soliva, R., Ballas, G., Trzaskos, B., Cavalcante, C., Schultz, R.A., 2017. A review of deformation bands in reservoir sandstones: geometries, mechanisms and distribution. Geol. Soc. London, Spec. Publ. 459, SP459-4.

Fox, R.J., Bowman, M.B.J., 2010. The challenges and impact of compartmentalization in reservoir appraisal and development. Geol. Soc. London, Spec. Publ. 347, 9–23.

França, R.L., Del Rey, A.C., Tagliari, C.V., Brandão, J.R., Fontanelli, P. de R., 2007. Bacia do Espírito Santo. Bol. Geociencias da PETROBRAS 15, 501–509.

Frumkin, A., Ezersky, M., Al-Zoubi, A., Akkawi, E., Abueladas, A.-R., 2011. The Dead Sea sinkhole hazard: Geophysical assessment of salt dissolution and collapse. Geomorphology 134, 102–117.

Fugelli, E.M.G., Olsen, T.R., 2007. Delineating confined slope turbidite systems offshore mid-Norway: The Cretaceous deep-marine Lysing Formation. Am. Assoc. Pet. Geol. Bull. 91, 1577–1601.

Funnell, R., Chapman, D., Allis, R., Armstrong, P., 1996. Thermal state of the Taranaki basin, New Zealand. J. Geophys. Res. Solid Earth 101, 25197–25215.

Gabrielsen, P.T., Abrahamson, P., Panzner, M., Fanavoll, S., Ellingsrud, S., 2013. Exploring

frontier areas using 2D seismic and 3D CSEM data, as exemplified by multi-client data over the skrugard and havis discoveries in the barents sea. First Break 31, 63–71. doi:10.3997/1365-2397.2013001

Gabrielsen, R., 1984. Long-lived fault zones and their influence on the tectonic development of the southwestern Barents Sea. J. Geol. Soc. London.

Gabrielsen, R.H., Faerseth, R.B., Jensen, L.N., Kalheim, J.E., Riis, F., 1990. Structural Elements of the Norwegian Continental Shelf Part I: The Barents Sea Region. Nor. Pet. Dir. Bull. No. 6, 45.

Galloway, W.E., 1998. Siliciclastic slope and base-of-slope depositional systems: component facies, stratigraphic architecture, and classification. Am. Assoc. Pet. Geol. Bull. 82, 569–595.

Gamboa, D.A., 2011. An integrated seismic-scale analysis of reservoir compartmentalisation on continental margins: the Espirito Santo Basin, SE Brazil.

Gamboa, D., Alves, T., Cartwright, J., Terrinha, P., 2010. MTD distribution on a "passive" continental margin: The Espírito Santo Basin (SE Brazil) during the Palaeogene. Mar. Pet. Geol. 27, 1311–1324. doi:10.1016/j.marpetgeo.2010.05.008

Gamboa, D., Alves, T.M., 2015. Spatial and dimensional relationships of submarine slope architectural elements: A seismic-scale analysis from the Espírito Santo Basin (SE Brazil). Mar. Pet. Geol. 64, 43–57.

Gamboa, D., Alves, T.M., Cartwright, J., 2012. A submarine channel confluence classification for topographically confined slopes. Mar. Pet. Geol. 35, 176–189. doi:10.1016/j.marpetgeo.2012.02.011

Gao, B., Flemings, P.B., 2017. Pore pressure within dipping reservoirs in overpressured basins. Mar. Pet. Geol. 80, 94–111.

Garcia, A.J. V, 1991. Evolução sedimentar da seqüência pré-rift das bacias costeiras e interiores do Nordeste brasileiro. Pesquisas 18, 3–12.

Gartrell, A., Zhang, Y., Lisk, M., Dewhurst, D., 2004. Fault intersections as critical hydrocarbon leakage zones: integrated field study and numerical modelling of an example from the Timor Sea, Australia. Mar. Pet. Geol. 21, 1165–1179. doi:10.1016/j.marpetgeo.2004.08.001

Gartrell, A., Zhang, Y., Lisk, M., Dewhurst, D., 2003. Enhanced hydrocarbon leakage at fault intersections: an example from the Timor Sea, Northwest Shelf, Australia. J. Geochemical Explor. 78, 361–365.

Gawthorpe, R.L., Fraser, A.J., Collier, R.E.L., 1994. Sequence stratigraphy in active extensional basins: implications for the interpretation of ancient basin-fills. Mar. Pet. Geol. 11, 642–658.

Gawthorpe, R.L., Hurst, J.M., 1993. Transfer zones in extensional basins: their structural style and influence on drainage development and stratigraphy. J. Geol. Soc. London. 150, 1137–1152.

Gawthorpe, R.L., Leeder, M.R., 2000. Tectono-sedimentary evolution of active extensional basins. Basin Res. 12, 195–218. doi:10.1046/j.1365-2117.2000.00121.x

Ge, H., Jackson, M.P.A., 1998. Physical modeling of structures formed by salt withdrawal: Implications for deformation caused by salt dissolution. Am. Assoc. Pet. Geol. Bull. 82, 228–250.

Gee, D.G., Fossen, H., Henriksen, N., Higgins, A.K., 2008. From the early Paleozoic platforms of Baltica and Laurentia to the Caledonide Orogen of Scandinavia and Greenland. Episodes 31, 44–51.

Gee, M.J.R., Gawthorpe, R.L., 2006. Submarine channels controlled by salt tectonics: Examples from 3D seismic data offshore Angola. Mar. Pet. Geol. 23, 443–458.

Gee, M.J.R., Gawthorpe, R.L., Bakke, K., Friedmann, S.J., 2007. Seismic geomorphology and evolution of submarine channels from the Angolan continental margin. J. Sediment. Res. 77, 433–446.

Gernigon, L., Brönner, M., 2012. Late Palaeozoic architecture and evolution of the southwestern Barents Sea: insights from a new generation of aeromagnetic data. J. Geol. Soc. London. 169, 449–459.

Gernigon, L., Brönner, M., Roberts, D., Olesen, O., Nasuti, A., Yamasaki, T., 2014. Crustal and basin evolution of the southwestern Barents Sea: From Caledonian orogeny to continental breakup. Tectonics 33, 347–373. doi:10.1002/2013TC003439

Giba, M., Nicol, A., Walsh, J.J., 2010. Evolution of faulting and volcanism in a back-arc basin and its implications for subduction processes. Tectonics 29.

Giba, M., Walsh, J.J., Nicol, A., 2012. Segmentation and growth of an obliquely reactivated normal fault. J. Struct. Geol. 39, 253–267.

Gibbs, A.D., 1989. Structural styles in basin formation. Extensional tectonics Stratigr. north Atl. Margins. Mem. Am. Assoc. Pet. Geol. 46, 81–93.

Gibson, R.G., 1994. Fault-zone seals in siliciclastic strata of the Columbus Basin, offshore

Trinidad. Am. Assoc. Pet. Geol. Bull. 78, 1372–1385.

Gillespie, P.A., Walsh, J.J. t, Watterson, J., 1992. Limitations of dimension and displacement data from single faults and the consequences for data analysis and interpretation. J. Struct. Geol. 14, 1157–1172.

Glørstad-Clark, E., Faleide, J.I., Lundschien, B.A., Nystuen, J.P., 2010. Triassic seismic sequence stratigraphy and paleogeography of the western Barents Sea area. Mar. Pet. Geol. 27, 1448–1475. doi:10.1016/j.marpetgeo.2010.02.008

Gölke, M., Brudy, M., 1996. Orientation of crustal stresses in the North Sea and Barents Sea inferred from borehole breakouts. Tectonophysics 266, 25–32. doi:10.1016/S0040-1951(96)00181-3

Gölke, M., Cloetingh, S., Coblentz, D., 1996. Finite-element modelling of stress patterns along the Mid-Norwegian continental margin, 62° to 68°N. Tectonophysics 266, 33–53. doi:10.1016/S0040-1951(96)00182-5

Graue, K., 2000. Mud volcanoes in deepwater Nigeria. Mar. Pet. Geol. 17, 959–974.

Green, A.N., 2009. Palaeo-drainage, incised valley fills and transgressive systems tract sedimentation of the northern KwaZulu-Natal continental shelf, South Africa, SW Indian Ocean. Mar. Geol. 263, 46–63.

Guardado, L.R., Spadini, A.R., Brandão, J.S.L., Mello, M.R., 2000. Petroleum System of the Campos Basin, Brazil. AAPG Mem. 73.

Gudlaugsson, S.T.T., Faleide, J.I.I., Johansen, S.E.E., Breivik, A.J.J., 1998. Late Paleozoic structural development of the south-western Barents Sea. Mar. Pet. Geol. 15, 73–102.

doi:10.1016/S0264-8172(97)00048-2

Guerra, M.C.M., Underhill, J.R., 2012. Role of halokinesis in controlling structural styles and sediment dispersal in the Santos Basin, offshore Brazil. Geol. Soc. London, Spec. Publ. 363, 175–206. doi:10.1144/SP363.9

Guerra, M.C.M., Underhill, J.R., 2012. Role of halokinesis in controlling structural styles and sediment dispersal in the Santos Basin, offshore Brazil. Geol. Soc. London, Spec. Publ. 363, 175–206.

Gutierrez, M., Wangen, M., 2005. Modeling of compaction and overpressuring in sedimentary basins. Mar. Pet. Geol. 22, 351–363.

Hansen, R.J., Kamp, P.J.J., 2004a. Late Miocene to early Pliocene stratigraphic record in northern Taranaki Basin: condensed sedimentation ahead of Northern Graben extension and progradation of the modern continental margin. New Zeal. J. Geol. Geophys. 47, 645–662.

Hansen, R.J., Kamp, P.J.J., 2004b. Rapid progradation of the Pliocene-Pleistocene continental margin, northern Taranaki Basin, New Zealand, and implications.

Hansen, R.J., Kamp, P.J.J., 2002. Evolution of the Giant Foresets Formation, northern Taranaki Basin, New Zealand.

Hansen, J.P. V, Cartwright, J.A., Huuse, M., Clausen, O.R., 2005. 3D seismic expression of fluid migration and mud remobilization on the Gjallar Ridge, offshore mid-Norway. Basin Res. 17, 123–139.

Hao, F., Zhu, W., Zou, H., Li, P., 2015. Factors controlling petroleum accumulation and leakage in overpressured reservoirs. Am. Assoc. Pet. Geol. Bull. 99, 831–858.

doi:10.1306/01021514145

Hart, B.S., 1999. Definition of subsurface stratigraphy, structure and rock properties from 3-D seismic data. Earth-Science Rev. 47, 189–218. doi:10.1016/S0012-8252(99)00029-X

Heidbach, O., Tingay, M., Barth, A., Reinecker, J., Kurfeß, D., Müller, B., 2008. The World Stress Map database release 2008. doi:10.1594/GFZ.WSM.Rel2008

Henriksen, E., Bjornseth, H.M., Hals, T.K., Heide, T., Kiryukhina, T., Klovjan, O.S., Larssen, G.B., Ryseth, A.E., Ronning, K., Sollid, K., Stoupakova, A., 2011a. Uplift and erosion of the greater Barents Sea: impact on prospectivity and petroleum systems. Geol. Soc. London, Mem. doi:10.1144/M35.17

Henriksen, E., Ryseth, A.E., Larssen, G.B., Heide, T., Ronning, K., Sollid, K., Stoupakova, A. V., 2011b. Tectonostratigraphy of the greater Barents Sea: implications for petroleum systems. Geol. Soc. London, Mem. doi:10.1144/M35.10

Henstra, G.A., Gawthorpe, R.L., Helland-Hansen, W., Ravnås, R., Rotevatn, A., 2016. Depositional systems in multiphase rifts: seismic case study from the Lofoten margin, Norway. Basin Res.

Holohan, E.P., De Vries, B.V.W., Troll, V.R., 2008. Analogue models of caldera collapse in strike-slip tectonic regimes. Bull. Volcanol. 70, 773–796.

Holt, W.E., Stern, T.A., 1991. Sediment loading on the western platform of the New Zealand continent: Implications for the strength of a continental margin. Earth Planet. Sci. Lett. 107, 523–538.

Hossack, J., 1995. Geometric rules of section balancing for salt structures.

Hudec, M.R., Jackson, M.P.A., 2002. Structural segmentation, inversion, and salt tectonics on a passive margin: Evolution of the Inner Kwanza Basin, Angola. Geol. Soc. Am. Bull. 114, 1222–1244.

Hudec, M.R., Jackson, M.P. a., 2007. Terra infirma: Understanding salt tectonics. Earth-Science Rev. 82, 1–28. doi:10.1016/j.earscirev.2007.01.001

Hull, J., 1988. Thickness-displacement relationships for deformation zones. J. Struct. Geol. 10, 431–435.

Ingram, G.M., Chisholm, T.J., Grant, C.J., Hedlund, C.A., Stuart-Smith, P., Teasdale, J., 2004. Deepwater North West Borneo: hydrocarbon accumulation in an active fold and thrust belt. Mar. Pet. Geol. 21, 879–887.

Jackson, C.A.L., Rotevatn, A., 2013. 3D seismic analysis of the structure and evolution of a salt-influenced normal fault zone: A test of competing fault growth models. J. Struct. Geol. 54, 215–234. doi:10.1016/j.jsg.2013.06.012

Jackson, M.P.A., Talbot, C.J., 1994. Advances in salt tectonics. Cont. Deform. 159–179.

Jackson, M.P.A., Vendeville, B.C., Schultz-Ela, D.D., 1994a. Structural Dynamics of Salt Systems. Annu. Rev. Earth Planet. Sci. 22, 93–117. doi:10.1146/annurev.ea.22.050194.000521

Jackson, M.P.A., Vendeville, B.C., Schultz-Ela, D.D., 1994b. Salt-related structures in the Gulf of Mexico: A field guide for geophysicists. Lead. Edge. doi:10.1190/1.1437040

Jaeger, J.C., Cook, N.G.W., Zimmerman, R., 2009. Fundamentals of rock mechanics. John Wiley & Sons.

Jegou, I., Savoye, B., Pirmez, C., Droz, L., 2008. Channel-mouth lobe complex of the recent Amazon Fan: The missing piece. Mar. Geol. 252, 62–77.

Jensen, L.N., Sørensen, K., 1992. Tectonic framework and halokinesis of the Nordkapp Basin, Barents Sea. Struct. Tecton. Model. its Appl. to Pet. Geol. Nor. Pet. Soc. Spec. Publ. 1, 109–120.

Johansen, S.E., Ostisty, B.K., Birkeland, ø., Fedorovsky, Y.F., Martirosjan, V.N., Christensen, O.B., Cheredeev, S.I., Ignatenko, E.A., Margulis, L.S., 1993. Hydrocarbon potential in the Barents Sea region: play distribution and potential, in: Norwegian Petroleum Society Special Publications. pp. 273–320. doi:10.1016/B978-0-444-88943-0.50024-1

Jolley, S.J., Barr, D., Walsh, J.J., Knipe, R.J., 2007. Structurally complex reservoirs: an introduction. Geol. Soc. London, Spec. Publ. 292, 1–24.

Jolley, S.J., Fisher, Q.J., Ainsworth, R.B., 2010. Reservoir compartmentalization: an introduction. Geol. Soc. London, Spec. Publ. 347, 1–8. doi:10.1144/SP347.1

Jones, R.M., Hillis, R.R., 2003. An integrated, quantitative approach to assessing fault-seal risk. Am. Assoc. Pet. Geol. Bull. 87, 507–524.

Kamp, P.J.J., Vonk, A.J., Bland, K.J., Hansen, R.J., Hendy, A.J.W., McIntyre, A.P., Ngatai, M., Cartwright, S.J., Hayton, S., Nelson, C.S., 2004a. Neogene stratigraphic architecture and tectonic evolution of Wanganui, King Country, and eastern Taranaki Basins, New Zealand. New Zeal. J. Geol. Geophys. 47, 625–644.

Kamp, P.J.J., Vonk, A.J., Nelson, C.S., Hansen, R.J., Tripathi, A.R.P., Hood, S.D., Nagati, M., Hendy, A.J.W., 2004b. Constraints on the evolution of Taranaki Fault from thermochronology and basin analysis: Implications for the Taranaki Fault play.

Kane, I.A., McCaffrey, W.D., Peakall, J., 2008. Controls on sinuosity evolution within submarine channels. Geology 36, 287–290.

Kane, K.E., Jackson, C. a.-L., Larsen, E., 2010. Normal fault growth and fault-related folding in a salt-influenced rift basin: South Viking Graben, offshore Norway. J. Struct. Geol. 32, 490–506. doi:10.1016/j.jsg.2010.02.005

Katz, B.J., Mello, M.R., 2000. Petroleum Systems of South Atlantic Marginal Basins - An Overview. AAPG Mem. 73.

Kearey, P., Brooks, M., Hill, I., 2013. An introduction to geophysical exploration. John Wiley & Sons.

Kelly, P.G., Peacock, D.C.P., Sanderson, D.J., McGurk, A.C., 1999. Selective reverse-reactivation of normal faults, and deformation around reverse-reactivated faults in the Mesozoic of the Somerset coast. J. Struct. Geol. 21, 493–509. doi:10.1016/S0191-8141(99)00041-3

Kettermann, M., Urai, J.L., Vrolijk, P.J., 2017. Evolution of structure and permeability of normal faults with clay smear: Insights from water-saturated sandbox models and numerical simulations. J. Geophys. Res. Solid Earth.

Kim, Y.S., Andrews, J.R., Sanderson, D.J., 2001a. Extension fractures, secondary faults and segment linkage in strike-slip fault systems at Rame Head, Southern Cornwall, in: Geoscience in South-West England. pp. 123–133.

Kim, Y.S., Andrews, J.R., Sanderson, D.J., 2001b. Reactivated strike-slip faults: Examples from North Cornwall, UK. Tectonophysics 340, 173–194. doi:10.1016/S0040-1951(01)00146-9

Kim, Y.S., Sanderson, D.J., 2005. The relationship between displacement and length of faults: A review. Earth-Science Rev. doi:10.1016/j.earscirev.2004.06.003

King, P.R., 2000. Tectonic reconstructions of New Zealand: 40 Ma to the present. New Zeal. J. Geol. Geophys. 43, 611–638.

King, P.R., Thrasher, G.P., 1996. Cretaceous Cenozoic geology and petroleum systems of the Taranaki Basin, New Zealand. Institute of Geological & Nuclear Sciences.

Klausen, T.G., Mørk, A., 2014. The Upper Triassic paralic deposits of the De Geerdalen Formation on Hopen: outcrop analog to the subsurface Snadd Formation in the Barents Sea. Am. Assoc. Pet. Geol. Bull. 98, 1911–1941.

Klausen, T.G., Ryseth, A.E., Helland-Hansen, W., Gawthorpe, R., Laursen, I., 2015. Regional development and sequence stratigraphy of the Middle to Late Triassic Snadd Formation, Norwegian Barents Sea. Mar. Pet. Geol. 62, 102–122.

Klein, R.J., Barr, M.V., 1986. Regional state of stress in western Europe, in: Stephenson, O. (Ed.), Rock Stress and Rock Stress Measurement. Centrek Publ, Stockholm, pp. 33–44.

Knipe, R.J., 1997. Juxtaposition and seal diagrams to help analyze fault seals in hydrocarbon reservoirs. Am. Assoc. Pet. Geol. Bull. 81, 187–195. doi:10.1306/522B42DF-1727-11D7-8645000102C1865D

Knipe, R.J., Fisher, Q.J., Jones, G., Clennell, M.R., Farmer, A.B., Harrison, A., Kidd, B., McAllister, E., Porter, J.R., White, E.A., 1997. Fault seal analysis: successful methodologies, application and future directions. Nor. Pet. Soc. Spec. Publ. 7, 15–38.

Knipe, R.J., Jones, G., Fisher, Q.J., 1998. Faulting, fault sealing and fluid flow in hydrocarbon

reservoirs: an introduction. Geol. Soc. London, Spec. Publ. doi:10.1144/GSL.SP.1998.147.01.01

Knox, G.J., 1982. Taranaki Basin, structural style and tectonic setting. New Zeal. J. Geol. Geophys. 25, 125–140.

Koledoye, B.A., Aydin, A., May, E., 2003. A new process-based methodology for analysis of shale smear along normal faults in the Niger Delta. Am. Assoc. Pet. Geol. Bull. 87, 445–463.

Kolla, V., 2007. A review of sinuous channel avulsion patterns in some major deep-sea fans and factors controlling them. Mar. Pet. Geol. 24, 450–469.

Kolla, V., Bourges, P., Urruty, J.-M., Safa, P., 2001. Evolution of deep-water Tertiary sinuous channels offshore Angola (west Africa) and implications for reservoir architecture. Am. Assoc. Pet. Geol. Bull. 85, 1373–1405.

Kolla, V., Posamentier, H.W., Wood, L.J., 2007. Deep-water and fluvial sinuous channels—Characteristics, similarities and dissimilarities, and modes of formation. Mar. Pet. Geol. 24, 388–405.

Koyi, H., Talbot, C.J., Tørudbakken, B.O., 1993. Salt diapirs of the southwest Nordkapp Basin: analogue modelling. Tectonophysics 228, 167–187.

Labourdette, R., Poncet, J., Seguin, J., Temple, F., Hegre, J., Irving, A., 2006. Three-dimensional modelling of stacked turbidite channels inWest Africa: impact on dynamic reservoir simulations. Pet. Geosci. 12, 335–345.

Langhi, L., Zhang, Y., Gartrell, A., Underschultz, J.R., Dewhurst, D.N., 2009. Fluid flow

behaviour in reactivated hydrocarbon traps: Assessing fluid circulation along natural complex fault systems using numerical fluid flow simulation. J. Geochemical Explor. doi:10.1016/j.gexplo.2008.11.021

Larssen, G.B., Elvebakk, G., Henriksen, L.B., Nilsson, I., Samuelsberg, T.J., Stemmerik, L., Worsley, D., Kristensen, S.E., Svånå, T.A., 2002. Upper Palaeozoic lithostratigraphy of the Southern Norwegian Barents Sea. Nor. Pet. Dir. Bull. 9, 76.

Larue, D.K., Hovadik, J., 2006. Connectivity of channelized reservoirs: a modelling approach. Pet. Geosci. 12, 291–308.

Lee, R.F., 2001. Pitfalls in seismic data flattening. Lead. Edge 20, 160–164.

Lee, Y., Deming, D., 2002. Overpressures in the Anadarko basin, southwestern Oklahoma: Static or dynamic? Am. Assoc. Pet. Geol. Bull. 86, 145–160.

Leeder, M.R., Gawthorpe, R.L., 1987. Sedimentary models for extensional tilt-block/half-graben basins. Geol. Soc. London, Spec. Publ. 28, 139–152.

Leveille, G.P., Knipe, R., More, C., Ellis, D., Dudley, G., Jones, G., Fisher, Q.J., Allinson, G., 1997. Compartmentalization of Rotliegendes gas reservoirs by sealing faults, Jupiter Fields area, southern North Sea. Geol. Soc. London, Spec. Publ. 123, 87–104. doi:10.1144/GSL.SP.1997.123.01.06

Lindholm, C.D., Bungum, H., Hicks, E., Villagran, M., 2000. Crustal stress and tectonics in Norwegian regions determined from earthquake focal mechanisms. Geol. Soc. London, Spec. Publ. 167, 429–439. doi:10.1144/GSL.SP.2000.167.01.17

Lindholm, C.D., Bungum, J., Bratli, R.K., Aadnøy, B.S., Dahl, N., Tørudbakken, B., Atakan, K.,

1995. Crustal stress in the northern North Sea as inferred from borehole breakouts and earthquake focal mechanisms. Terra Nov. 7, 51–59. doi:10.1111/j.1365-3121.1995.tb00667.x

Liner, C.L., 2004. Elements of 3D Seismology, Elements of 3D Seismology. PennWell.

Lomask, J., 2003. Flattening 3-D seismic cubes without picking, in: SEG Technical Program Expanded Abstracts 2003. Society of Exploration Geophysicists, pp. 1402–1405.

Lopez, J.A., 1990. Structural styles of growth faults in the US Gulf Coast Basin. Geol. Soc. London, Spec. Publ. 50, 203–219.

Løseth, H., Gading, M., Wensaas, L., 2009. Hydrocarbon leakage interpreted on seismic data. Mar. Pet. Geol. 26, 1304–1319.

Lowrie, W., 2007. Fundamentals of Geophysics. Cambridge University Press.

Mann, D.M., Mackenzie, A.S., 1990. Prediction of pore fluid pressures in sedimentary basins. Mar. Pet. Geol. 7pore pres, 55–65.

Mansfield, C.S., Cartwright, J.A., 2001. Fault growth by linkage: observations and implications from analogue models. J. Struct. Geol. 23, 745–763. doi:10.1016/S0191-8141(00)00134-6

Mansfield, C.S., Cartwright, J.A., 1996. High resolution fault displacement mapping from three-dimensional seismic data: evidence for dip linkage during fault growth. J. Struct. Geol. 18, 249–263. doi:10.1016/S0191-8141(96)80048-4

Manzocchi, T., Childs, C., Walsh, J.J., 2010. Faults and fault properties in hydrocarbon flow models. Geofluids 10, 94–113.

Martel, S.J., Boger, W.A., 1998. Geometry and mechanics of secondary fracturing around small three-dimensional faults in granitic rock. J. Geophys. Res. Solid Earth 103, 21299–21314.

Mattos, N.H., Alves, T.M., Omosanya, K.O., 2016. Crestal fault geometries reveal late halokinesis and collapse of the Samson Dome, Northern Norway: Implications for petroleum systems in the Barents Sea. Tectonophysics.

Mayall, M., Jones, E., Casey, M., 2006. Turbidite channel reservoirs—Key elements in facies prediction and effective development. Mar. Pet. Geol. 23, 821–841.

Mayall, M., Stewart, I., 2000. The architecture of turbidite slope channels, in: Deep-Water Reservoirs of the World: SEPM, Gulf Coast Section, 20th Annual Research Conference. SEPM, p. 586.

McAlpine, A., 2000. Basin modelling of oil plays northwest of Maui: Results; constraints and calibrations, in: 2000 New Zealand Petroleum Conference Proceedings. p. 9.

McDonnell, A., Loucks, R.G., Dooley, T., 2007. Quantifying the origin and geometry of circular sag structures in northern Fort Worth Basin, Texas: Paleocave collapse, pull-apart fault systems, or hydrothermal alteration? Am. Assoc. Pet. Geol. Bull. 91, 1295–1318.

McFarland, J.M., Morris, A.P., Ferrill, D.A., 2012. Stress inversion using slip tendency. Comput. Geosci. 41, 40–46. doi:10.1016/j.cageo.2011.08.004

McHargue, T., Pyrcz, M.J., Sullivan, M.D., Clark, J.D., Fildani, A., Romans, B.W., Covault, J.A., Levy, M., Posamentier, H.W., Drinkwater, N.J., 2011. Architecture of turbidite channel systems on the continental slope: patterns and predictions. Mar. Pet. Geol. 28, 728–743.

McKie, T., Jolley, S.J., Kristensen, M.B., 2010. Stratigraphic and structural compartmentalization

of dryland fluvial reservoirs: Triassic Heron Cluster, Central North Sea. Geol. Soc. London, Spec. Publ. 347, 165–198.

Meisling, K.E., Cobbold, P.R., Mount, V.S., 2001. Segmentation of an obliquely rifted margin, Campos and Santos basins, southeastern Brazil. Am. Assoc. Pet. Geol. Bull. 85, 1903–1924.

Midland Valley Move Application, 2015.

Milani, E.J., Araújo, L.M. de, Bizzi, L.A., Schobbenhaus, C., Vidotti, R.M., Gonçalves, J.H., 2003. Recursos Minerais energéticos: petróleo. Geol. tectônica e Recur. minerais do Bras. 541–576.

Milani, E.J., Brandão, J.A.S.L., Zalán, P. V., Gamboa, L.A.P., 2001. Petróleo na Margem Continental Brasileira: Geologia, exploração, resultados e perspectivas. Brazilian J. Geophys. 18, 351–396.

Milkov, A. V, Goebel, E., Dzou, L., Fisher, D.A., Kutch, A., McCaslin, N., Bergman, D.F., 2007. Compartmentalization and time-lapse geochemical reservoir surveillance of the Horn Mountain oil field, deep-water Gulf of Mexico. Am. Assoc. Pet. Geol. Bull. 91, 847–876.

Mitchell, T.M., Faulkner, D.R., 2009. The nature and origin of off-fault damage surrounding strike-slip fault zones with a wide range of displacements: A field study from the Atacama fault system, northern Chile. J. Struct. Geol. 31, 802–816. doi:10.1016/j.jsg.2009.05.002

Mohriak, W.U., 2005. Interpretação geológica e geofísica da Bacia do Espírito Santo e da região de Abrolhos: petrografia, datações radiométricas e visualização sísmica das rochas vulcânicas. Bol. Geoc. Petrobrás 14, 133–142.

Mohriak, W.U., 2003. Bacias sedimentares da margem continental Brasileira. Geol. Tectônica e

Recur. Minerais do Bras. 87–165.

Mohriak, W.U., Bassetto, M., Vieira, I.S., 1998. Crustal architecture and tectonic evolution of the Sergipe-Alagoas and Jacuipe basins, offshore northeastern Brazil. Tectonophysics 288, 199–220.

Mohriak, W.U., Nemčok, M., Enciso, G., 2008. South Atlantic divergent margin evolution: rift-border uplift and salt tectonics in the basins of SE Brazil. Geol. Soc. London, Spec. Publ. 294, 365–398.

Moos, D., Zoback, M.D., 1990. Utilization of observations of well bore failure to constrain the orientation and magnitude of crustal stresses: application to continental, Deep Sea Drilling Project, and Ocean Drilling Program boreholes. J. Geophys. Res. Solid Earth 95, 9305–9325.

Moraes, M.A.S., Maciel, W.B., Braga, M.S.S., Viana, A.R., 2007. Bottom-current reworked Palaeocene-Eocene deep-water reservoirs of the Campos Basin, Brazil. Geol. Soc. London, Spec. Publ. 276, 81–94.

Morgans, H.E.G., 2006. Foraminiferal Biostratigraphy of the Early Miocene to Pleistocene Sequences in Witiora-1, Taimana-1, Arawa-1 and Okoki-1. GNS Science.

Mørk, A., Elvebakk, G., 1999. Lithological description of subcropping Lower and Middle Triasic rocks from the Svalis Dome, Barents Sea. Polar Res. 18, 83–104.

Morley, C.K., Guerin, G., 1996. Comparison of gravity-driven deformation styles and behavior associated with mobile shales and salt. Tectonics 15, 1154–1170.

Morris, A., Ferrill, D. a, Henderson, D.B., 1996. Slip-tendency analysis and fault reactivation.

Geology 24, 275–278. doi:10.1130/0091-7613(1996)024<0275

Morse, D.G., 1994. Siliciclastic reservoir rocks. Mem. Assoc. Pet. Geol. 121.

Moss, J.L., Cartwright, J., 2010. 3D seismic expression of km-scale fluid escape pipes from offshore Namibia. Basin Res. 22, 481–501.

Mourgues, R., Gressier, J.B., Bodet, L., Bureau, D., Gay, A., 2011. "Basin scale" versus "localized" pore pressure/stress coupling–Implications for trap integrity evaluation. Mar. Pet. Geol. 28, 1111–1121.

Müller, B., Zoback, M. Lou, Fuchs, K., Mastin, L., Gregersen, S., Pavoni, N., Stephansson, O., Ljunggren, C., 1992. Regional patterns of tectonic stress in Europe. J. Geophys. Res. doi:10.1029/91JB01096

Muraoka, H., Kamata, H., 1983. Displacement distribution along minor fault traces. J. Struct. Geol. 5, 483–495. doi:10.1016/0191-8141(83)90054-8

Mutti, E., Normark, W.R., 1991. An integrated approach to the study of turbidite systems, in: Seismic Facies and Sedimentary Processes of Submarine Fans and Turbidite Systems. Springer, pp. 75–106.

Neall, V.E., Stewart, R.B., Smith, I.E.M., 1986. History and petrology of the Taranaki volcanoes. R. Soc. New Zeal. Bull. 23, 251–263.

Nelson, T.H., Fairchild, L., 1989. Emplacement and evolution of salt sills in the northern Gulf of Mexico.

Neurauter, T.W., Roberts, H.H., 1994. Three generations of mud volcanoes on the Louisiana

continental slope. Geo-Marine Lett. 14, 120–125.

Nicol, A., Gillespie, P.A., Childs, C., Walsh, J.J., 2002. Relay zones between mesoscopic thrust faults in layered sedimentary sequences. J. Struct. Geol. 24, 709–727.

Nicol, A., Stagpoole, V., Maslen, G., 2004. Structure and petroleum potential of the Taranaki fault play, in: New Zealand Petroleum Conference Proceedings. pp. 7–10.

Nicol, A., Walsh, J., Berryman, K., Nodder, S., 2005. Growth of a normal fault by the accumulation of slip over millions of years. J. Struct. Geol. 27, 327–342.

Nicol, A., Watterson, J., Walsh, J.J., Childs, C., 1996. The shapes, major axis orientations and displacement patterns of fault surfaces. J. Struct. Geol. doi:10.1016/S0191-8141(96)80047-2

Nilsen, K., Vendeville, B., Johansen, J., 1995. Influence of regional tectonics on halokinesis in the Nordkapp Basin, Barents Sea, in: In M. P. A. Jackson, D. G. Roberts, and S. Snelson, Eds., Salt Tectonics: A Global Perspective.

Nilsen, K.T., Henriksen, E., Larsen, G.B., 1993. Exploration of the Late Palaeozoic carbonates in the southern Barents Sea—a seismic stratigraphic study. Arct. Geol. Pet. Potential, Norw. Pet. Soc. Spec. Publ 2, 393–404.

Nodder, S.D., 1993. Neotectonics of the offshore Cape Egmont Fault Zone, Taranaki Basin, New Zealand. New Zeal. J. Geol. Geophys. 36, 167–184.

Normark, W.R., Piper, D.J.W., 1991. Initiation processes and flow evolution of turbidity currents: implications for the depositional record.

Normark, W.R., Piper, D.J.W., Hess, G.R., 1979. Distributary channels, sand lobes, and mesotopography of Navy submarine fan, California Borderland, with applications to ancient fan sediments. Sedimentology 26, 749–774.

Normark, W.R., Posamentier, H., Mutti, E., 1993. Turbidite systems: state of the art and future directions. Rev. Geophys. 31, 91–116.

North, F., 1985. Petroleum geology. Springer.

Nøttvedt, A., Cecchi, M., Gjelberg, J.G., Kristensen, S.E., Lønøy, A., Rasmussen, A., Rasmussen, E., Skott, P.H., van Veen, P.M., 1993. Svalbard-Barents Sea correlation: a short review, in: Norwegian Petroleum Society Special Publications. pp. 363–375. doi:10.1016/B978-0-444-88943-0.50027-7

NPD, 2004. Well 7224/7-1 report.

O'Brien, J.J., Lerche, I., 1988. Impact of heat flux anomalies around salt diapirs and salt sheets in the gulf coast on hydrocarbon maturity: models and observations. Gulf Coast Assoc. Geol. Soc. Trans. 38, 231–243.

Ohm, S.E., Karlsen, D.A., Austin, T.J.F., 2008. Geochemically driven exploration models in uplifted areas: Examples from the Norwegian Barents Sea. Am. Assoc. Pet. Geol. Bull. 92, 1191–1223.

Ojeda, H.A.O., 1982. Structural framework, stratigraphy, and evolution of Brazilian marginal basins. Am. Assoc. Pet. Geol. Bull. 66, 732–749.

Omosanya, K., 2014. Seismic character and interaction of intrabasinal mass-transport deposits in deep-water continental margins (Espírito Santo Basin, SE Brazil).

Omosanya, K.O., Alves, T.M., 2014. Mass-transport deposits controlling fault propagation, reactivation and structural decoupling on continental margins (Espírito Santo Basin, SE Brazil). Tectonophysics 628, 158–171. doi:http://dx.doi.org/10.1016/j.tecto.2014.04.045

Omosanya, K.O., Alves, T.M., 2013. A 3-dimensional seismic method to assess the provenance of Mass-Transport Deposits (MTDs) on salt-rich continental slopes (Espírito Santo Basin, SE Brazil). Mar. Pet. Geol. 44, 223–239. doi:10.1016/j.marpetgeo.2013.02.006

Omosanya, K.O., Johansen, S.E., Harishidayat, D., 2015. Evolution and character of supra-salt faults in the Easternmost Hammerfest Basin, SW Barents Sea. Mar. Pet. Geol.

Osagiede, E.E., Duffy, O.B., Jackson, C.A.-L., Wrona, T., 2014. Quantifying the growth history of seismically imaged normal faults. J. Struct. Geol. 66, 382–399.

Osborne, M.J., Swarbrick, R.E., 1997. Mechanisms for generating overpressure in sedimentary basins: a reevaluation. Am. Assoc. Pet. Geol. Bull. 81, 1023–1041.

Ostanin, I., Anka, Z., Di Primio, R., Bernal, A., 2012. Hydrocarbon leakage above the Snøhvit gas field, Hammerfest Basin SW Barents Sea. first Break 30.

Paul, D., Mitra, S., 2013. Experimental models of transfer zones in rift systems. Am. Assoc. Pet. Geol. Bull. 97, 759–780.

Peacock, D.C.P., 2002. Propagation, interaction and linkage in normal fault systems. Earth-Science Rev. 58, 121–142. doi:10.1016/S0012-8252(01)00085-X

Peacock, D.C.P., 1991a. A comparison between the displacement geometries of veins and normal faults at Kilve, Somerset, in: Geoscience in South-West England. pp. 363–367.

Peacock, D.C.P., 1991b. Displacements and segment linkage in strike-slip fault zones. J. Struct. Geol. 13, 1025–1035. doi:10.1016/0191-8141(91)90054-M

Peacock, D.C.P., Sanderson, D.J., 1996. Effects of propagation rate on displacement variations along faults. J. Struct. Geol. 18, 311–320.

Peacock, D.C.P., Sanderson, D.J., 1995. Strike-slip relay ramps. J. Struct. Geol. 17, 1351–1360. doi:10.1016/0191-8141(95)97303-W

Peacock, D.C.P., Sanderson, D.J., 1994. Geometry and development of relay ramps in normal fault systems. Am. Assoc. Pet. Geol. Bull. 78, 147–165.

Peacock, D.C.P., Sanderson, D.J., 1991. Displacements, segment linkage and relay ramps in normal fault zones. J. Struct. Geol. 13, 721–733. doi:10.1016/0191-8141(91)90033-F

Peacock, D.C.P., Xing, Z., 1994. Field examples and numerical modelling of oversteps and bends along normal faults in cross-section. Tectonophysics 234, 147–167.

Peakall, J., Amos, K.J., Keevil, G.M., Bradbury, P.W., Gupta, S., 2007. Flow processes and sedimentation in submarine channel bends. Mar. Pet. Geol. 24, 470–486.

Perez-Garcia, C., Safronova, P.A., Mienert, J., Berndt, C., Andreassen, K., 2013. Extensional rise and fall of a salt diapir in the Sørvestsnaget Basin, SW Barents Sea. Mar. Pet. Geol. 46, 129–143.

Peška, P., Zoback, M.D., 1995. Compressive and tensile failure of inclined well bores and determination of in situ stress and rock strength. J. Geophys. Res. Solid Earth 100, 12791–12811.

Pindell, J.L., 1995. Circum-Caribbean sedimentary basin development and timing of hydrocarbon maturation as a function of Caribbean plate tectonic evolution.

Pirmez, C., Beaubouef, R.T., Friedmann, S.J., Mohrig, D.C., 2000. Equilibrium profile and baselevel in submarine channels: examples from Late Pleistocene systems and implications for the architecture of deepwater reservoirs, in: Global Deep-Water Reservoirs: Gulf Coast Section SEPM Foundation 20th Annual Bob F. Perkins Research Conference. SEPM, pp. 782–805.

Pollard, D.D., Segall, P., 1987. Theoretical displacements and stresses near fractures in rock: with applications to faults, joints, veins, dikes, and solution surfaces. Fract. Mech. rock 277, 277–349.

Posamentier, H.W., Kolla, V., 2003. Seismic geomorphology and stratigraphy of depositional elements in deep-water settings. J. Sediment. Res. 73, 367–388.

Posamentier, H.W., Walker, R.G., 2006. Facies models revisited, in: Posamentier, H.W., Walker, R.G. (Eds.), Facies Models Revisited. SEPM (Society for Sedimentary Geology), Tulsa, pp. 1–17.

Prather, B.E., 2003. Controls on reservoir distribution, architecture and stratigraphic trapping in slope settings. Mar. Pet. Geol. 20, 529–545.

Qin, Y., Alves, T.M., Constantine, J., Gamboa, D., 2017. The Role of Mass Wasting In the Progressive Development Of Submarine Channels (Espírito Santo Basin, Se Brazil). J. Sediment. Res. 87, 500–516.

Qin, Y., Alves, T.M., Constantine, J., Gamboa, D., 2016. Quantitative seismic geomorphology of a submarine channel system in SE Brazil (Espírito Santo Basin): Scale comparison with

other submarine channel systems. Mar. Pet. Geol. 78, 455–473.

Rajan, A., Bünz, S., Mienert, J., Smith, A.J., 2013. Gas hydrate systems in petroleum provinces of the SW-Barents Sea. Mar. Pet. Geol. 46, 92–106.

Ranalli, G., Chandler, T.E., 1975. The Stress Field in the Upper Crust as Determined from In Situ Measurements. Geol. Rundschau 64, 653–674. doi:10.1007/BF01820688

Reilly, C., Nicol, A., Walsh, J.J., Kroeger, K.F., 2016. Temporal changes of fault seal and early charge of the Maui Gas-condensate field, Taranaki Basin, New Zealand. Mar. Pet. Geol. 70, 237–250.

Rippon, J.H., 1984. Contoured patterns of the throw and hade of normal faults in the Coal Measures (Westphalian) of north-east Derbyshire, in: Proceedings of the Yorkshire Geological and Polytechnic Society. Geological Society of London, pp. 147–161.

Ritzmann, O., Faleide, J.I., 2007. Caledonian basement of the western Barents Sea. Tectonics 26. doi:10.1029/2006TC002059

Roberts, D., 2003. The Scandinavian Caledonides: event chronology, palaeogeographic settings and likely modern analogues. Tectonophysics 365, 283–299. doi:10.1016/S0040-1951(03)00026-X

Rotevatn, A., Fossen, H., Hesthammer, J., Aas, T.E., Howell, J.A., 2007. Are relay ramps conduits for fluid flow? Structural analysis of a relay ramp in Arches National Park, Utah. Geol. Soc. London, Spec. Publ. 270, 55–71.

Rotevatn, A., Sandve, T.H., Keilegavlen, E., Kolyukhin, D., Fossen, H., 2013. Deformation bands and their impact on fluid flow in sandstone reservoirs: the role of natural thickness

variations. Geofluids 13, 359–371.

Rovere, M., Gamberi, F., Mercorella, A., Rashed, H., Gallerani, A., Leidi, E., Marani, M., Funari, V., Pini, G.A., 2014. Venting and seepage systems associated with mud volcanoes and mud diapirs in the southern Tyrrhenian Sea. Mar. Geol. 347, 153–171.

Rowan, M.G., Jackson, M.P.A., Trudgill, B.D., 1999. Salt-related fault families and fault welds in the northern Gulf of Mexico. Am. Assoc. Pet. Geol. Bull. 83, 1454–1484.

Rowan, M.G., Jackson, M.P.A., Trudgill, B.D., 1999. Salt-related fault families and fault welds in the northern Gulf of Mexico. Am. Assoc. Pet. Geol. Bull. doi:10.1306/E4FD41E3-1732-11D7-8645000102C1865D

Safronova, P.A., Henriksen, S., Andreassen, K., Laberg, J.S., Vorren, T.O., 2014. Evolution of shelf-margin clinoforms and deep-water fans during the middle Eocene in the Sorvestsnaget Basin, southwest Barents Sea. Am. Assoc. Pet. Geol. Bull. 98, 515–544.

Salazar, M., Moscardelli, L., Wood, L., 2015. Utilising clinoform architecture to understand the drivers of basin margin evolution: a case study in the Taranaki Basin, New Zealand. Basin Res.

Savoye, B., Babonneau, N., Dennielou, B., Bez, M., 2009. Geological overview of the Angola–Congo margin, the Congo deep-sea fan and its submarine valleys. Deep Sea Res. Part II Top. Stud. Oceanogr. 56, 2169–2182.

Schlumberger, 2014. Petrel 2014.

Schmatz, J., Holland, M., Giese, S., Van Der Zee, W., Urai, J.L., 2010. Clay smear processes in mechanically layered sequences—Results of water-saturated model experiments with free

top surface. J. Geol. Soc. India 75, 74–88.

Scholz, C.H., 1987. Wear and gouge formation in brittle faulting. Geology 15, 493–495.

Scholz, C.H., Anders, M.H., 1994. The permeability of faults. Mech. Involv. Fluids Faulting, Ed. S. Hickman, R. Sibson, R. Bruhn, US Geol. Surv. B. LXIII, Rep. 94–228.

Scholz, C.H., Cowie, P.A., 1990. Determination of total strain from faulting using slip measurements.

Schultz-Ela, D.D., Jackson, M.P. a., Vendeville, B.C., 1993. Mechanics of active salt diapirism. Tectonophysics 228, 275–312. doi:10.1016/0040-1951(93)90345-K

Schultz, R.A., Fossen, H., 2002. Displacement-length scaling in three dimensions: The importance of aspect ratio and application to deformation bands. J. Struct. Geol. 24, 1389–1411. doi:10.1016/S0191-8141(01)00146-8

Segall, P., Pollard, D.D., 1983. Nucleation and growth of strike slip faults in granite. J. Geophys. Res. doi:10.1029/JB088iB01p00555

Segall, P., Pollard, D.D., 1980. Mechanics of discontinuous faults. J. Geophys. Res. Solid Earth 85, 4337–4350.

Seni, S.J., Jackson, M.P.A., 1984. Sedimentary Record of Cretaceous and Tertiary Salt Movement, East Texas Basin: Times, Rates, and Volumes of Salt Flow and Their Implications for Nuclear Waste Isolation and Petroleum Exploration. Bureau of Economic Geology, University of Texas of Austin.

Shepard, F.P., Emery, K.O., 1973. Congo submarine canyon and fan valley. Am. Assoc. Pet.

Geol. Bull. 57, 1679–1691.

Sheriff, R.E., Geldart, L.P., 1995. Exploration Seismology, Second Edi. ed. Cambridge University Press, Cambridge. doi:10.1017/CBO9781139168359

Sibson, R.H., 1996. Structural permeability of fluid-driven fault-fracture meshes. J. Struct. Geol. 18, 1031–1042.

Sippel, J., Saintot, A., Heeremans, M., Scheck-Wenderoth, M., 2010. Paleostress field reconstruction in the Oslo region. Mar. Pet. Geol. 27, 682–708.

Slatt, R.M., 2006. Stratigraphic reservoir characterization for petroleum geologists, geophysicists, and engineers. Elsevier.

Smelror, M., Petrov, O. V., Larssen, G.B., Werner, S.C., 2009. Geological history of the Barents Sea. Norges Geol. undersøkelse 1–135.

Smit, J., Brun, J.-P., Fort, X., Cloetingh, S., Ben-Avraham, Z., 2008. Salt tectonics in pull-apart basins with application to the Dead Sea Basin. Tectonophysics 449, 1–16. doi:10.1016/j.tecto.2007.12.004

Smith, D.A., 1980. Sealing and nonsealing faults in Louisiana Gulf Coast salt basin. Am. Assoc. Pet. Geol. Bull. 64, 145–172.

Soliva, R., Ballas, G., Fossen, H., Philit, S., 2016. Tectonic regime controls clustering of deformation bands in porous sandstone. Geology 44, 423–426.

Soliva, R., Schultz, R.A., 2008. Distributed and localized faulting in extensional settings: insight from the North Ethiopian Rift–Afar transition area. Tectonics 27.

Solum, J.G., Brandenburg, J.P., Naruk, S.J., Kostenko, O. V, Wilkins, S.J., Schultz, R.A., 2010. Characterization of deformation bands associated with normal and reverse stress states in the Navajo Sandstone, Utah. Am. Assoc. Pet. Geol. Bull. 94, 1453–1475.

Soper, N.J., Strachan, R.A., Holdsworth, R.E., Gayer, R.A., Greiling, R.O., 1992. Sinistral transpression and the Silurian closure of Iapetus. J. Geol. Soc. London. 149, 871–880.

Spang, J.H., 1972. Numerical method for dynamic analysis of calcite twin lamellae. Geol. Soc. Am. Bull. 83, 467–472.

Spencer, C.W., 1987. Hydrocarbon generation as a mechanism for overpressuring in Rocky Mountain region. Am. Assoc. Pet. Geol. Bull. 71, 368–388.

Sperner, B., Ratschbacher, L., Ott, R., 1993. Fault-striae analysis: A turbo pascal program package for graphical presentation and reduced stress tensor calculation. Comput. Geosci. doi:10.1016/0098-3004(93)90035-4

Sprague, A.R., Patterson, P.E., Hill, R.E., Jones, C.R., Campion, K.M., Van Wagoner, J.C., Sullivan, M.D., Larue, D.K., Feldman, H.R., Demko, T.M., 2002. The physical stratigraphy of fluvial strata: A hierarchical approach to the analysis of genetically related stratigraphic elements for improved reservoir prediction, in: American Association of Petroleum Geologists Annual Meeting, Houston, Texas. p. 167.

Stagpoole, V., Funnell, R., 2001. Arc magmatism and hydrocarbon generation in the northern Taranaki Basin, New Zealand. Pet. Geosci. 7, 255–267.

Stagpoole, V., Nicol, A., 2008. Regional structure and kinematic history of a large subduction back thrust: Taranaki Fault, New Zealand. J. Geophys. Res. Solid Earth 113.

Stemmerik, L., 2000. Late Palaeozoic evolution of the North Atlantic margin of Pangea. Palaeogeogr. Palaeoclimatol. Palaeoecol. 161, 95–126.

Stephansson, O., 1993. Rock stress in the Fennoscandian shield, First Edit. ed, Comprehensive rock engineering. Pergamon Press, Oxford.

Stern, T.A., Stratford, W.R., Salmon, M.L., 2006. Subduction evolution and mantle dynamics at a continental margin: Central North Island, New Zealand. Rev. Geophys. 44.

Stewart, S. a., 2006. Implications of passive salt diapir kinematics for reservoir segmentation by radial and concentric faults. Mar. Pet. Geol. 23, 843–853. doi:10.1016/j.marpetgeo.2006.04.001

Stoupakova, A. V., Henriksen, E., Burlin, Y.K., Larsen, G.B., Milne, J.K., Kiryukhina, T.A., Golynchik, P.O., Bordunov, S.I., Ogarkova, M.P., Suslova, A.A., 2011. The geological evolution and hydrocarbon potential of the Barents and Kara shelves. Geol. Soc. London, Mem. doi:10.1144/M35.21

Straub, K.M., Paola, C., Mohrig, D., Wolinsky, M.A., George, T., 2009. Compensational stacking of channelized sedimentary deposits. J. Sediment. Res. 79, 673–688.

Talbot, C., Rönnlund, P., Schmeling, H., 1991. Diapiric spoke patterns. Tectonophysics 188, 187–201.

Talbot, C.J., 1993. Spreading of salt structures in the Gulf of Mexico. Tectonophysics 228, 151–166. doi:10.1016/0040-1951(93)90338-K

Talbot, C.J., Jackson, M.P.A., 1987. Internal Kinematics of Salt Diapirs. Am. Assoc. Pet. Geol. Bull.

Thorsen, C.E., 1963. Age of growth faulting in southeast Louisiana.

Torabi, A., Berg, S.S., 2011. Scaling of fault attributes: A review. Mar. Pet. Geol. doi:10.1016/j.marpetgeo.2011.04.003

Torsvik, T., Smethurst, M., Meert, J., Vandervoo, R., Mckerrow, W., Brasier, M., Sturt, B., Walderhaug, H., 1996. Continental break-up and collision in the Neoproterozoic and Palaeozoic — A tale of Baltica and Laurentia. Earth-Science Rev. 40, 229–258. doi:10.1016/0012-8252(96)00008-6

Trudgill, B.D., Cartwright, J.A., 1994. Relay-ramp forms and normal-fault linkages, Canyonlands National Park, Utah. Geol. Soc. Am. Bull. 106, 1143–1157.

Vadakkepuliyambatta, S., Bünz, S., Mienert, J., Chand, S., 2013. Distribution of subsurface fluid-flow systems in the SW Barents Sea. Mar. Pet. Geol. 43, 208–221.

van der Zee, W., Urai, J.L., Richard, P.D., 2003. Lateral clay injection into normal faults. Geoarabia Manama 8, 501–522.

Varela, C.L., Mohriak, W.U., 2013. Halokinetic rotating faults, salt intrusions, and seismic pitfalls in the petroleum exploration of divergent margins. Am. Assoc. Pet. Geol. Bull. doi:10.1306/02261312164

Vendeville, B.C., 2002. A new interpretation of Trusheim's classic model of salt-diapir growth.

Vendeville, B.C., Jackson, M.P. a., 1992. The rise of diapirs during thin-skinned extension. Mar. Pet. Geol. 9, 331–354. doi:10.1016/0264-8172(92)90047-I

Viana, A., Figueiredo, A., Faugres, J.-C., Lima, A., Gonthier, E., Brehme, I., Zaragosi, S., 2003.

The São Tomé deep-sea turbidite system (southern Brazil Basin): Cenozoic seismic stratigraphy and sedimentary processes. Am. Assoc. Pet. Geol. Bull. 87, 873–894.

Vieira, R.A.B., Mendes, M.P., Vieira, P.E., Costa, L.A.R., Tagliari, C. V, Bacelar, L.A.P., Feijó, F.J., 1994. Bacias do Espírito Santo e Mucuri. Bol. Geosci. da Petrobrás, Rio Janeiro 8, 191–202.

Vorren, T.O., Richardsen, G., Knutsen, S.-M., Henriksen, E., 1991. Cenozoic erosion and sedimentation in the western Barents Sea. Mar. Pet. Geol. doi:10.1016/0264-8172(91)90086-G

Wallace, R.E., 1951. Geometry of Shearing Stress and Relation to Faulting. J. Geol. doi:10.1086/625831

Walsh, J.J., Bailey, W.R., Childs, C., Nicol, A., Bonson, C.G., 2003. Formation of segmented normal faults: a 3-D perspective. J. Struct. Geol. 25, 1251–1262.

Walsh, J.J., Nicol, A., Childs, C., 2002. An alternative model for the growth of faults. J. Struct. Geol. 24, 1669–1675. doi:10.1016/S0191-8141(01)00165-1

Walsh, J.J., Watterson, J., 1989. Displacement gradients on fault surfaces. J. Struct. Geol. doi:10.1016/0191-8141(89)90070-9

Walsh, J.J., Watterson, J., 1988. Analysis of the relationship between displacements and dimensions of faults. J. Struct. Geol. doi:10.1016/0191-8141(88)90057-0

Walsh, J.J., Watterson, J., 1987. Distributions of cumulative displacement and seismic slip on a single normal fault surface. J. Struct. Geol. doi:10.1016/0191-8141(87)90012-5

Walsh, J.J., Watterson, J., Heath, A.E., Childs, C., 1998. Representation and scaling of faults in fluid flow models. Pet. Geosci. doi:10.1144/petgeo.4.3.241

Walter, T.R., Troll, V.R., 2001. Formation of caldera periphery faults: an experimental study. Bull. Volcanol. 63, 191–203.

Warren, J.K., 2006. Evaporites: sediments, resources and hydrocarbons. Springer Science & Business Media.

Watterson, J., 1986. Fault dimensions, displacements and growth. Pure Appl. Geophys. 124, 365–373.

Webster, M., O'Connor, S., Pindar, B., Swarbrick, R., 2011. Overpressures in the Taranaki Basin: Distribution, causes, and implications for exploration. Am. Assoc. Pet. Geol. Bull. 95, 339–370.

Weijermars, R., Jackson, M.P. a., Vendeville, B., 1993. Rheological and tectonic modeling of salt provinces. Tectonophysics 217, 143–174. doi:10.1016/0040-1951(93)90208-2

Wilkins, S.J., Gross, M.R., 2002. Normal fault growth in layered rocks at Split Mountain, Utah: influence of mechanical stratigraphy on dip linkage, fault restriction and fault scaling. J. Struct. Geol. 24, 1413–1429.

Willemse, E.J.M., Pollard, D.D., Aydin, A., 1996. Three-dimensional analyses of slip distributions on normal fault arrays with consequences for fault scaling. J. Struct. Geol. 18, 295–309.

Williams, G., Chapman, T., 1983. Strains developed in the hangingwalls of thrusts due to their slip/propagation rate: a dislocation model. J. Struct. Geol. 5, 563–571.

Wiprut, D., Zoback, M., 2002. Fault reactivation, leakage potential, and hydrocarbon column heights in the northern North Sea. Nor. Pet. Soc. Spec. Publ. 11, 203–219.

Wiprut, D., Zoback, M.D., 2000. Fault reactivation and fluid flow along a previously dormant normal fault in the northern North Sea. Geology 28, 595–598.

Withjack, M., Scheiner, C., 1982. Fault patterns associated with domes - an experimental and analytical study. Am. Assoc. Pet. Geol. Bull. 66, 302–316.

Wood, L.J., 2007. Quantitative seismic geomorphology of Pliocene and Miocene fluvial systems in the northern Gulf of Mexico, USA. J. Sediment. Res. 77, 713–730.

Worrall, D.M., Snelson, S., 1989. Evolution of the northern Gulf of Mexico. Geol. North Am. an Overv. Geol. Soc. Am. v. A 97–138.

Worsley, D., 2008. The post-Caledonian development of Svalbard and the western Barents Sea, in: Polar Research. pp. 298–317. doi:10.1111/j.1751-8369.2008.00085.x

Wynn, R.B., Kenyon, N.H., Masson, D.G., Stow, D.A. V, Weaver, P.P.E., 2002. Characterization and recognition of deep-water channel-lobe transition zones. Am. Assoc. Pet. Geol. Bull. 86.

Yeats, R.S., 1986. Faults related to folding with examples from New Zealand. R. Soc. New Zeal. Bull. 24, 273–292.

Yielding, G., 2002. Shale gouge ratio—Calibration by geohistory. Nor. Pet. Soc. Spec. Publ. 11, 1–15.

Yielding, G., Freeman, B., Needham, D.T., 1997. Quantitative fault seal prediction. Am. Assoc.

Pet. Geol. Bull. 81, 897–917.

Yilmaz, Ö., 2001. Seismic data analysis. Society of Exploration Geophysicists Tulsa.

Yin, A., 2004. Gneiss domes and gneiss dome systems. Geol. Soc. Am. Spec. Pap. 380, 1–14.

Yin, H., Groshong, R.H., 2007. A three-dimensional kinematic model for the deformation above an active diapir. Am. Assoc. Pet. Geol. Bull. 91, 343–363. doi:10.1306/10240606034

Young, M.J., Gawthorpe, R.L., Hardy, S., 2001. Growth and linkage of a segmented normal fault zone; the Late Jurassic Murchison–Statfjord North Fault, northern North Sea. J. Struct. Geol. 23, 1933–1952.

Žalohar, J., Vrabec, M., 2007. Paleostress analysis of heterogeneous fault-slip data: the Gauss method. J. Struct. Geol. 29, 1798–1810.

Ze, T., Alves, T.M., 2016. The role of gravitational collapse in controlling the evolution of crestal fault systems (Espírito Santo Basin, SE Brazil). J. Struct. Geol. 92, 79–98.

Zhang, Y., Gartrell, A., Underschultz, J.R., Dewhurst, D.N., 2009. Numerical modelling of strain localisation and fluid flow during extensional fault reactivation: Implications for hydrocarbon preservation. J. Struct. Geol. 31, 315–327. doi:10.1016/j.jsg.2008.11.006

Zhou, H.-W., 2014. Practical Seismic Data Analysis. Cambridge University Press.

Zoback, M.D., 2010. Reservoir geomechanics. Cambridge University Press.

Zoback, M.D., Barton, C.A., Brudy, M., Castillo, D.A., Finkbeiner, T., Grollimund, B.R., Moos, D.B., Peska, P., Ward, C.D., Wiprut, D.J., 2003. Determination of stress orientation and

magnitude in deep wells. Int. J. Rock Mech. Min. Sci. 40, 1049–1076.

Zoback, M.D., Zoback, M. Lou, Mount, V.S., Suppe, J., Eaton, J.P., Healy, J.H., Oppenheimer, D., Reasenberg, P., Jones, L., Raleigh, C.B., 1987. New evidence on the state of stress of the San Andreas fault system. Science (80-.). 238, 1105–1111.